

23 November 2012 | \$10

Science

EDITORIAL

- 1009** Combating Hunger
M. S. Swaminathan

NEWS OF THE WEEK

- 1014** A roundup of the week's top stories

NEWS & ANALYSIS

- 1016** Genetic Influences on Disease Remain Hidden
- 1017** DOE Shifts Money From Research Grants to New Projects
- 1018** As Open Access Explodes, How to Tell the Good From the Bad and the Ugly?
- 1019** Genome Study Helps Contain MRSA Outbreak—And Breeds New Questions

NEWS FOCUS

- 1020** In Search of the Wild Chicken From Farmyard to the Lab
>> Science Podcast
- 1025** Making Sense of a Senseless Act Korea Tackles a Mushrooming Problem

LETTERS

- 1028** Barry Commoner's Place in History
M. Egan
- Climate Change—Induced Salinity Threatens Health
P. Vineis and A. Khan
- Journals: Increase Revisions, Not Rejections
E. K. Bowers
>> Report p. 1065

- 1029** CORRECTIONS AND CLARIFICATIONS

BOOKS ET AL.

- 1030** Spillover
D. Quammen, reviewed by D. G. Streicker and A. B. Pedersen

POLICY FORUM

- 1031** The Contribution of Private Industry to Agricultural Innovation
K. Fuglie et al.

PERSPECTIVES

- 1033** A Golden Era of Nobel Laureates
J. L. Goldstein and M. S. Brown
- 1034** Carbon Storage with Benefits
S. P. Sohi
- 1035** Can One Cell Influence Cancer Heterogeneity?
A. V. Krivtsov and S. A. Armstrong
>> Report p. 1080
- 1037** Imaging the Deep Earth
G. A. Prieto
>> Report p. 1063
- 1038** Plant Gametes Do Fertilization with a Twist
W. J. Snell
>> Report p. 1093
- 1039** Algae Under Pressure and in Hot Water
P. E. Savage
- 1040** The Origin of the Moon
A. N. Halliday
>> Research Article p. 1047; Report p. 1052

CONTENTS continued >>



page 1020



page 1030



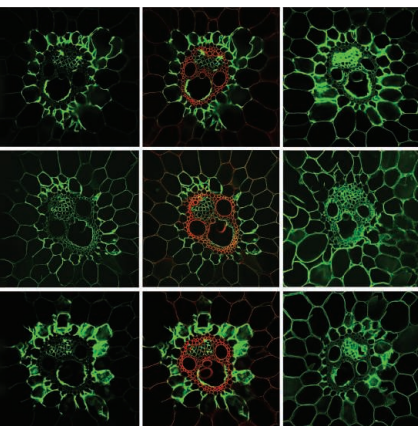
COVER

The lower hemisphere of a fast-spinning Earth shown 2 hours after a giant impact. Colors denote the silicate mantles and iron cores of Earth and the impactor. The debris evolves into a Moon-forming disk composed primarily of material from Earth's mantle, explaining the isotopic similarity between Earth and the Moon. In this model, the fast-spinning Earth is slowed by an orbital resonance between the Moon and the Sun. See pages 1040, 1047, and 1052.

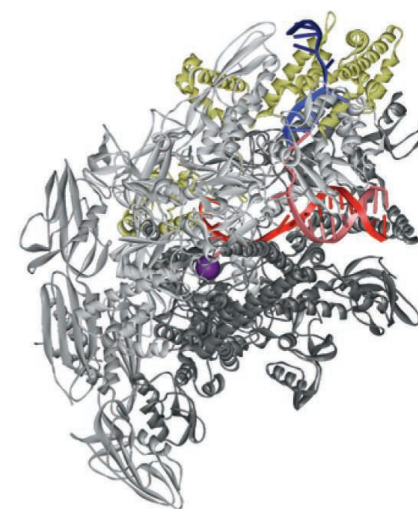
Image: Sarah T. Stewart

DEPARTMENTS

- 1006** This Week in *Science*
- 1010** Editors' Choice
- 1012** *Science* Staff
- 1101** New Products
- 1102** *Science* Careers



page 1055



page 1076

REVIEW

- 1042** The Protein-Folding Problem,
50 Years On
K. A. Dill and J. L. MacCallum
>> *Science Podcast*

RESEARCH ARTICLE

- 1047** Making the Moon from a Fast-Spinning
Earth: A Giant Impact Followed by
Resonant Despinning
M. Čuk and S. T. Stewart
Computer simulations show that a giant
impact on early Earth could lead to a Moon
with a composition similar to Earth's.
>> *Perspective p. 1040; Report p. 1052*

REPORTS

- 1052** Forming a Moon with an Earth-like
Composition via a Giant Impact
R. M. Canup
Computer simulations show that a giant
impact on early Earth could lead to a Moon
with a composition similar to Earth's.
>> *Perspective p. 1040; Research Article p. 1047*
- 1055** How Does Plant Cell Wall Nanoscale
Architecture Correlate with Enzymatic
Digestibility?
S.-Y. Ding et al.
Microscopy techniques uncover the distinct
mechanisms of different enzyme classes in
breaking down cellulose for biofuels.
- 1060** Quantum-State Resolved Bimolecular
Collisions of Velocity-Controlled OH
with NO Radicals
M. Kirste et al.
Precise experiments on bimolecular collisions
show that simplifications rendering theory
tractable confer reasonable accuracy.
- 1063** Body-Wave Imaging of Earth's Mantle
Discontinuities from Ambient Seismic
Noise
P. Poli et al.
Correlated seismic waves reveal that the mantle
boundary at 410 kilometers is three times the
thickness of the deeper one at 660 kilometers.
>> *Perspective p. 1037; Science Podcast*
- 1065** Flows of Research Manuscripts Among
Scientific Journals Reveal Hidden
Submission Patterns
V. Calcagno et al.
A large-scale study of biological manuscript
submission history reveals how authors
strategically submit their research.
>> *Letter by E. K. Bowers p. 1028*

- 1069** SAICAR Stimulates Pyruvate Kinase
Isoform M2 and Promotes Cancer Cell
Survival in Glucose-Limited Conditions
K. E. Keller et al.
A metabolite is identified that may help
cancer cells coordinate their mode of energy
generation with nutrient conditions.
- 1072** The *Legionella* Effector RavZ Inhibits
Host Autophagy Through Irreversible
Atg8 Deconjugation
A. Choy et al.
An intracellular pathogen disrupts autophagy
by targeting an essential host protein on the
early autophagosome.
- 1076** Structural Basis of Transcription Initiation
Y. Zhang et al.
The bacterial transcription initiation complex
preorganizes promoter DNA for nucleotide
binding and RNA synthesis.
- 1080** Dedifferentiation of Neurons and
Astrocytes by Oncogenes Can Induce
Gliomas in Mice
D. Friedmann-Morvinski et al.
Murine brain tumors do not necessarily
originate from neural stem cells but can arise
from mature neurons and astrocytes.
>> *Perspective p. 1035*
- 1085** A Global Pattern of Thermal Adaptation
in Marine Phytoplankton
M. K. Thomas et al.
Optimal growth rates for phytoplankton
correlate with local temperature and predict
movement toward the poles with warming.
- 1088** Decoding Human Cytomegalovirus
N. Stern-Ginossar et al.
A closer look at the human cytomegalovirus
genome uncovers many new open reading
frames.
- 1093** Egg Cell-Secreted EC1 Triggers Sperm Cell
Activation During Double Fertilization
S. Sprunck et al.
The cysteine-rich proteins of *Arabidopsis* egg
and central cells enable fusion with just one
sperm each.
>> *Perspective p. 1038*
- 1097** Content-Specific Fronto-Parietal
Synchronization During Visual
Working Memory
R. F. Salazar et al.
Short-term memories are represented by
large-scale patterns of synchronous activity
across the fronto-parietal network.

SCIENCEEXPRESS

www.sciencexpres.org

Publication Ahead of Print

Crystal Structure of the Calcium Release-Activated Calcium Channel Orai

X. Hou et al.

10.1126/science.1228757

Organization of the Influenza Virus Replication Machinery

A. Moeller et al.

10.1126/science.1227270

The Structure of Native Influenza Virion Ribonucleoproteins

R. Arranz et al.

10.1126/science.1228172

Visualizing the Influenza Genome

Y. J. Tao and W. Zheng

10.1126/science.1231588

The Spatial and Temporal Origin of Chandelier Cells in Mouse Neocortex

H. Taniguchi et al.

10.1126/science.1227622

Phase Transformations and Metallization of Magnesium Oxide at High Pressure and Temperature

R. S. McWilliams et al.

10.1126/science.1229450

SCIENCENOW

www.sciencenow.org

Highlights From Our Daily News Coverage

Why Einstein Was a Genius

New photographs show unusual features in the great physicist's brain.

http://scim.ag/Einstein_Genius

Rainforest Insects Hear Like Humans

Katydid may listen with their legs, but their ears are almost human.

http://scim.ag/Katydid_Ears

Bdelloids Surviving on Borrowed DNA

The secret to the rotifers' success may be their "genetic mosaic."

<http://scim.ag/Genetic-Mosaic>

SCIENCE SIGNALING

www.sciencesignaling.org

The Signal Transduction Knowledge Environment

20 November issue: <http://scim.ag/ss112012>

RESEARCH ARTICLE: Attractor Landscape Analysis Reveals Feedback Loops in the p53 Network that Control the Cellular Response to DNA Damage

M. Choi et al.

State-space analysis of the p53 network identifies a therapeutic strategy for treating cancer.

RESEARCH ARTICLE: Sumoylation Silences Heterodimeric TASK Potassium Channels Containing K2P1 Subunits in Cerebellar Granule Neurons

L. D. Plant et al.

Potassium channels that respond to the anesthetic halothane are electrically silent when sumoylated.

RESEARCH ARTICLE: GPRC5B Activates Obesity-Associated Inflammatory Signaling in Adipocytes

Y. Kim et al.

Mice lacking an orphan G protein-coupled receptor show reduced inflammatory signaling and obesity.

PERSPECTIVE: Sequential Conformational Rearrangements Dictate the Dynamics of Class C GPCR Activation

J. R. Lane and M. Canals

Fluorescent probes reveal the roles of domain rearrangement and dimerization in GPCR activation.

PODCAST

R. J. Lefkowitz and A. M. VanHook

ST NETWATCH: The Nobel Prize in Chemistry 2012

The Nobel Prize Committee honors work on the structure and function of G protein-coupled receptors.

SCIENCE TRANSLATIONAL MEDICINE

www.sciencetranslationalmedicine.org

Integrating Medicine and Science

21 November issue: <http://scim.ag/stm112112>

FOCUS: Treating Epilepsy with a Light Potassium Diet

C. Bernard

RESEARCH ARTICLE: Optogenetic and Potassium Channel Gene Therapy in a Rodent Model of Focal Neocortical Epilepsy

R. C. Wykes et al.

Light-activated gene therapy suppresses seizures in a rodent model of epilepsy.

RESEARCH ARTICLE: Mesenchymal Stem Cells Regulate Blood-Brain Barrier Integrity Through TIMP3 Release After Traumatic Brain Injury

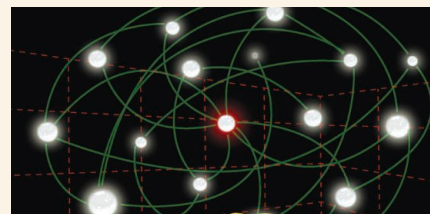
T. Menge et al.

TIMP3 mediates the beneficial effects of mesenchymal stem cells on blood-brain barrier integrity after brain injury.

RESEARCH ARTICLE: Modulation of Vigilance in the Primary Hypersomnias by Endogenous Enhancement of GABA_A Receptors

D. A. Rye et al.

A cerebrospinal fluid component in excessively sleepy people mimics the actions of sedatives.



SCIENCE SIGNALING

Charting a deadly landscape.

SCIENCE CAREERS

www.sciencereers.org/career_magazine

Free Career Resources for Scientists

<http://scim.ag/SciCareers23November2012>

Experimental Error: Does Scientific Research Need a Purpose?

A. Ruben

Not all research is easily justified—but what do you do when you can't even justify it to yourself?

Successful Careers: A Matter of Confidence

S. A. Holgate

Identifying and addressing confidence issues can help early-career scientists make swifter progress.

SCIENCE PODCAST

www.sciencemag.org/multimedia/podcast

Free Weekly Show for 23 November 2012

Listen to stories on ambient seismic noise, 50 years of protein folding, the origins of the chicken, and more.

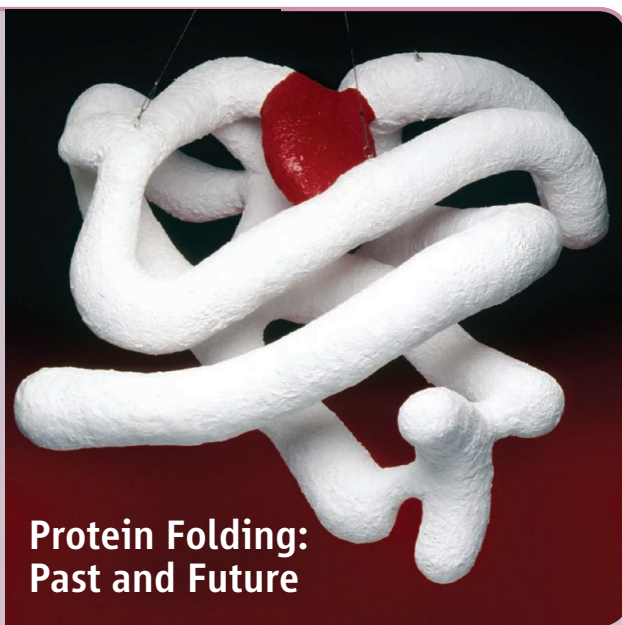
SCIENCE (ISSN 0036-8075) is published weekly on Friday, except the last week in December, by the American Association for the Advancement of Science, 1200 New York Avenue, NW, Washington, DC 20005. Periodicals Mail postage (publication No. 484460) paid at Washington, DC, and additional mailing offices. Copyright © 2012 by the American Association for the Advancement of Science. The title SCIENCE is a registered trademark of the AAAS. Domestic individual membership and subscription (51 issues): \$149 (\$74 allocated to subscription). Domestic institutional subscription (51 issues): \$990; Foreign postage extra: Mexico, Caribbean (surface mail) \$55; other countries (air assist delivery) \$85. First class, airmail, student, and emeritus rates on request. Canadian rates with GST available upon request, GST #1254 88122. Publications Mail Agreement Number 1069624. Printed in the U.S.A.

Change of address: Allow 4 weeks, giving old and new addresses and 8-digit account number. **Postmaster:** Send change of address to AAAS, P.O. Box 96178, Washington, DC 20090-6178. **Single-copy sales:** \$10.00 current issue, \$15.00 back issue prepaid includes surface postage; bulk rates on request. **Authorization to photocopy** material for internal or personal use under circumstances not falling within the fair use provisions of the Copyright Act is granted by AAAS to libraries and other users registered with the Copyright Clearance Center (CCC) Transactional Reporting Service, provided that \$30.00 per article is paid directly to CCC, 222 Rosewood Drive, Danvers, MA 01923. The identification code for Science is 0036-8075. Science is indexed in the Reader's Guide to Periodical Literature and in several specialized indexes.



ADVANCING SCIENCE. SERVING SOCIETY

Fifty years ago the Nobel Prize in chemistry was awarded to Max Perutz and John Kendrew for determining the structure of globular proteins. Since first viewing their structure of myoglobin, scientists have sought to understand protein folding. **Dill and MacCallum** (p. 1042) review the progress that has been made on three central questions: What is the code that relates sequence to structure? How do proteins fold so fast? Can protein structure be computationally predicted? While we have come some way toward answering these questions, new questions have been generated. It is no longer useful to talk about “solving the protein-folding problem”—protein folding has grown into a field of research where the next 50 years promise to be as exciting as the last.



Protein Folding: Past and Future

Forming the Moon from Earth

It is thought that the Moon formed after a Mars-sized planet hit Earth about 4.5 billion years ago. Computer simulations of this event predict that the Moon was produced primarily from material from the impacting planet. However, the Moon has a similar composition to that of Earth, and the impacting planet would likely have had a different composition. Prior models assumed that the impact left the Earth-Moon system with the same angular momentum as it has today (see the Perspective by **Halliday**). **Čuk and Stewart** (p. 1047, published online 17 October; see the cover) show that the angular momentum of the Earth-Moon system could have decreased by half after the Moon-forming impact, opening the door to new impact models. For example, simulations suggest that high-velocity impacts onto a fast-spinning early Earth can lead to a Moon formed primarily from Earth's mantle. **Canup** (p. 1052, published online 17 October) considered instead lower-velocity impacts by planets comparable in mass to the proto-Earth, which could generate a Moon and an Earth with similar compositions.

Watching a Breakdown

One of the key challenges in scaling up biofuels manufacturing is development of a cost-effective way to break down cellulose into sugars for

subsequent fermentation. **Ding et al.** (p. 1055) applied several different types of microscopy to understand the details of how cellulase enzymes perform this task, in the interest of ultimately optimizing the procedure. After lignin removal, fungal cellulases penetrated the remaining cellulose pore structure more efficiently than did bacteria-derived multienzyme complexes. However, this behavior hinges on a lignin extraction scheme that preserves the native architecture of the cellulose.

When Molecules Collide

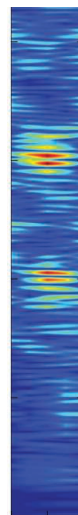
As advances in computing power and algorithm design parallel the increasing sophistication of experimental apparatus, theory and measurement are perpetually trading places as to which can detail the dynamics of molecular interactions more precisely. At present, collisions of an atom with a diatomic molecule can be studied comparably in both domains. In contrast, collisions of two diatomics each bearing an unpaired electron manifest too many degrees of freedom for computational quantum mechanics. **Kirste et al.** (p. 1060) have now experimentally resolved the rotational dynamics of one such case—the inelastic scattering of $\text{NO} + \text{OH}$ —and find that a simplified theoretical model focusing on long range interactions predicts the outcome surprisingly well. Such approximations could render many analogous systems moderately predictable.

Fathoming Publication Strategies

While many studies have tracked numbers of citations after publication, such studies cannot reveal how prepublication dynamics affects subsequent citation history. **Calcagno et al.** (p. 1065, published online 11 October) surveyed the submission history of more than 80,000 articles published in 16 fields of biology in 2006–2008 and constructed a social network based on manuscript flows among scientific journals. High-impact journals occupied central positions in the network. A majority of manuscripts were published in the first journal to which they were submitted. However, submission history affected the post-publication impact (citation count) of articles, with manuscripts requiring resubmission eventually receiving more citations.

Exploiting Seismic Noise

Typically, seismic imaging has been based on examining the seismic waves that traveled from a known source, usually an earthquake, to a seismograph. **Poli et al.** (p. 1063; see the Perspective by **Prieto**) now show that correlations of body waves in seismic noise can yield information about Earth's deep interior. An array in Finland, supplemented by other stations, was used to examine reflections from two major seismic boundaries within Earth's mantle at depths of about 410 and 660 km thought to be associated with mineralogical changes in Earth's interior. The data imply that the upper discontinuity extends over about 15 kilometers whereas the deeper one is only about 4 km thick.



Axing Autophagy

When intracellular pathogens like *Legionella pneumophila* take up residence in mammalian host cells, they must combat the efforts of the host cell to attack them. Autophagy is a process by which cells digest their own constituents, often involved in response to starvation or pathogen attack. **Choy et al.** (p. 1072, published online 25 October) now describe how *L. pneumophila* can inhibit the autophagy pathway in eukaryotic cells, and provide a detailed description of the biochemical mechanism. A *Legionella* effector protein, RavZ, acts as a very potent enzyme that specifically deconjugates a key autophagy protein, Atg8, from autophagosomal membranes, thus blocking autophagy.

CREDITS (TOP TO BOTTOM): DILL ET AL.; POLI ET AL.

Getting the Feel of DNA

To transcribe a gene, RNA polymerase (RNAP) must unwind the promoter DNA to form a “transcription bubble” and the RNAP-promoter open complex (RPO). The activity of RPO is critical for the regulation of gene expression. **Zhang *et al.*** (p. 1076, published online 18 October) describe crystal structures of bacterial RPO, together with the transcription initiation factor σ , from *Thermus thermophilus*, variously in complex with promoter DNA and an RNA primer. RNAP and σ recognize the promoter through sequence-specific contacts with transcription-bubble, nontemplate-strand DNA. Critical interactions occur through the unstacking of DNA bases and their insertion into pockets on the surfaces of the two proteins, allowing direct sensing of the DNA sequence.

Cancer Stem Cells: A Moving Target?

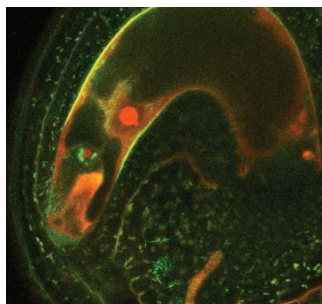
Glioblastoma multiforme (GBM) is a highly aggressive human brain tumor. The prevailing “cancer stem cell hypothesis” posits that GBMs arise primarily from neuronal stem cells. Now, **Friedmann-Morvinski *et al.*** (p. 1080, published online 18 October; see the Perspective by **Krivtsov and Armstrong**) suggest that this hypothesis may be too restrictive. In mouse models, brain tumors resembling human GBMs could form from fully differentiated cells such as astrocytes and neurons. Upon acquiring certain genetic alterations, mature brain cells may thus be capable of dedifferentiating into a progenitor-like cell, which could then initiate and maintain tumor growth.

Local Optima for Plankton

Recent ocean warming has changed the seasonality and composition of the marine phytoplankton. **Thomas *et al.*** (p. 1085, published online 25 October) investigated the direct effect of temperature on phytoplankton. By fitting published data to reaction temperature norms for 194 phytoplankton strains isolated from a wide latitudinal range, the resultant temperature-related traits (maximum growth rate, temperature optimum, and thermal niche width) reveal latitudinal trends in temperature optima and diversity. Biogeographical differences indicate an increased susceptibility of tropical strains to further warming, and modeling predicts poleward shifts of tropical strains and a loss of phytoplankton diversity in the tropics within the next hundred years.

Double Delivery During Plant Fertilization

Double fertilization is a defining feature of flowering plants and involves two nonmotile male gametes (sperm cells) and two female gametes (egg cell and central cell). Both fertilization events are necessary for reproductive success. It is not clear how flowering plants ensure the reliable and on-time fusion of the two pairs of gametes, while preventing polyspermy. **Sprunck *et al.*** (p. 1093; see the Perspective by **Snell**) now show that gamete interactions in *Arabidopsis* depend on small cysteine-rich EGG CELL 1 (EC1) proteins that accumulate in storage vesicles of the egg cell and that are released during sperm-egg interaction. EC1 peptides trigger the delivery of a fusogen to the sperm cell surface. An intercellular link connects the two sperm cells throughout the gamete fusion process and could play a role in preventing the spontaneous fusion of activated sperm cells.



Synchronous Brain Activity

Synchronization of neuronal activity across different brain areas varies according to working memory load or the locus of attention. It is thought that synchronization serves as a general mechanism for increasing effective cross-area communication during memory and attention tasks. However, it is not known if synchronization carries specific content. **Salazar *et al.*** (p. 1097, published online 1 November) recorded from multiple electrodes across parietal and prefrontal cortices of monkeys and found content-specific synchronization for both location and object identity in a working memory task. The findings suggest that the contents of working memory could be maintained through site-specific synchrony across brain areas.

CREDIT: STEFANIE SPRUNCK

AAAS Travels



Wild Iceland

June 13-22, 2013

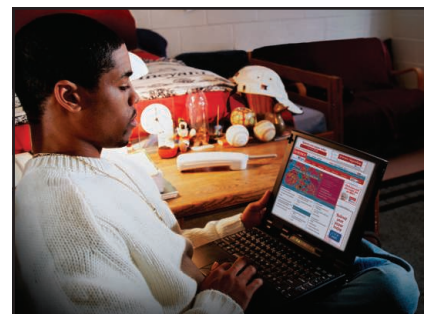
Land of Fire & Ice
& Nature's Paradise!

Grab your binoculars and cameras and discover Iceland—the world's oldest democracy. Its wildlife and natural wonders are truly magical! Join naturalist **Siggi Tomasson** for a tremendous introduction to the heritage of Iceland, from geology to history and wildlife! \$3,995 + air

For a detailed brochure, please call (800) 252-4910

All prices are per person twin share + air


BETCHART EXPEDITIONS inc.
 17050 Montebello Rd, Cupertino, CA 95014
 Email: AAASInfo@betchartexpeditions.com
www.betchartexpeditions.com



AAAS is here – preparing minority students for careers in science.

Part of AAAS's mission is to diversify and strengthen the scientific work force. To help achieve this goal, AAAS partners with NSF to present the Historically Black Colleges and Universities Undergraduate Program, a conference where students from HBCUs get experience presenting their research, networking with peers, meeting with representatives from graduate schools, and learning about career opportunities. If you're not yet a AAAS member, join us. Together we can make a difference.

To learn more, visit
aaas.org/plusyou/hbcuup





M. S. Swaminathan is the emeritus chairman of the M S Swaminathan Research Foundation, Chennai, India. E-mail: swami@mssrf.res.in.

Combating Hunger

AT THE CLOSE OF THE RECENT LONDON OLYMPICS, THE UNITED KINGDOM ANNOUNCED A PROGRAM designed to rescue 25 million children worldwide from malnutrition by the time of the next Olympics in Brazil. In May 2012, the World Health Assembly agreed to a target of reducing the number of stunted children by 40% (a reduction of about 70 million children) by 2025. To meet these targets and nourish the 870 million hungry people in the world,* the world's leaders will need to prioritize an innovative science-based marriage of nutrition and agriculture.

The problem of hunger is not simply a lack of sufficient quantities of food. The chronic hunger caused by protein and calorie undernutrition is exacerbated by malnutrition (the "hidden" hunger caused by the deficiency of micronutrients, which include iron, iodine, zinc, vitamin A, and vitamin B12) and sometimes by human diseases that disable the body's ability to absorb what micronutrients it receives. To address such intertwined problems, there must be synergy among national programs dealing with the availability, access to, and absorption of food. These nutrition security programs should be based on a life-cycle approach that starts with the "first 1000 days" from pregnancy to 2 years old, the critical period when stunting can cause irreversible damage.†

In September, a High Level Panel of Experts to the United Nations (UN) Committee on World Food Security, which I chaired, released a comprehensive report on *Social Protection for Food Security*, with recommendations for combating chronic childhood hunger.‡ One of its recommendations—the concept of a "food security floor"—is particularly worthy of mention. The food security floor recognizes that freedom from hunger is a fundamental human right, defining the minimal steps needed for hunger elimination. These include nutrition literacy, clean drinking water, sanitation, and primary health care.

In some "hunger hot spots" of the world where agriculture is the backbone of survival, as in sub-Saharan Africa and South Asia, mainstreaming nutrition in agriculture programs is the most effective and low-cost method of eliminating malnutrition. This requires greater attention to the net income of smallholder farmers, whose women food producers have particular needs that require specific policies and support. As an example, the M S Swaminathan Research Foundation in Chennai, India, has designed a Farming System for Nutrition initiative, comprising specific steps. They include carrying out a nutritional survey of the area and identifying the major causes of chronic and hidden hunger, and redesigning the farming system so that specific agricultural remedies are introduced for each nutritional malady, such as the cultivation of biofortified crops and crop-livestock integration. Thanks to the work carried out since 2004 under the Harvest Plus program of the Consultative Group on International Agricultural Research, micronutrient-enriched varieties are becoming available in several crops, such as iron- and zinc-rich rice; iron-rich beans and pearl millet; zinc-rich wheat; and vitamin A-rich cassava, sweet potato, and maize. The year 2014 has been designated the International Year of Family Farming by the UN, and every effort should be made by developing countries to make each family farm a biofortified farm. We also should aim to train one woman and one man in every village in nutrition literacy to serve as Community Hunger Fighters.

The Olympic spirit stimulates efforts to achieve what may appear unachievable. There are already encouraging examples of speedy progress, with Brazil leading the way through its Zero Hunger (Fome Zero) program initiated in 2003 by then-President Luiz Inácio Lula da Silva, which has helped to cut the number of Brazilians living in extreme poverty by more than half. If synergy can be created among scientific know-how, political do-how, and farmers' participation, it should be possible to achieve the goal of overcoming chronic and hidden hunger in large sections of the population of developing countries during this decade.

— M. S. Swaminathan

10.1126/science.1231305

*www.fao.org/publications/sofi/en. †<http://reliefweb.int/report/world/nutrition-first-1000-days-state-worlds-mothers-2012>. ‡www.fao.org/cfs/cfs-hlpe/en.

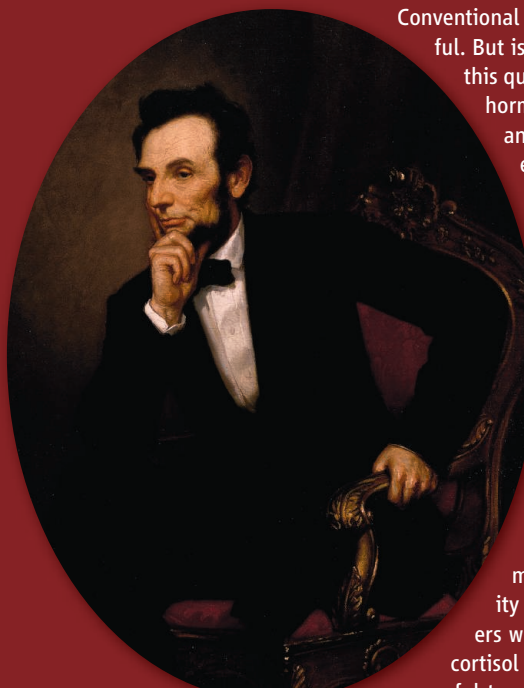


PSYCHOLOGY

Low-Stress Leaders?

Conventional wisdom suggests that being a leader is stressful. But is that actually true? Sherman *et al.* addressed this question by measuring the amount of the stress hormone cortisol in the saliva of participants in an executive education program, which included corporate, government, and industry leaders. They also measured the anxiety levels of participants using surveys. Leaders had lower amounts of cortisol and reported experiencing less anxiety than people not in leadership positions, and individuals further up the chain had less cortisol and anxiety than individuals in lower positions. The authors hypothesized that a greater sense of control by leaders may explain this difference and a second study in which leaders provided information about how many subordinates they had, how many directly reported to them, and how much decision-making autonomy and authority they had relative to the subordinates. Leaders who had more of a sense of control had lower cortisol levels and less anxiety. Sherman *et al.* were careful to note that their study was purely correlational and could not demonstrate which came first—the leadership or the lower levels of markers for stress. — BJ

Proc. Acad. Natl. Sci. U.S.A. **109**, 17903 (2012).



the potential energy landscape is mapped as a three-dimensional surface in which depressions represent stable states or “attractors.” These attractors represent alternative cell fates. With a simplified network analyzed with a Boolean network model, the authors identified key network components that together could force cells to undergo apoptosis rather than proliferation or cell cycle arrest. Experiments verified that modulation of these two components effectively promoted cell death. The approach may provide a way to address complex system-level data and models to more accurately predict ways to steer cells to adopt a desired physiological state. — LBR

Sci. Signal. **5**, ra83 (2012).

CHEMISTRY

A Stable Route to Selectivity

In general, the purpose of catalysis is to speed up reactions that otherwise proceed too slowly. Asymmetric catalysis is something of a special case though: When the catalyst's role is to bias a reaction toward one particular product isomer, problems arise if the background reaction is too fast on its own. This circumstance limited a prospectively promising route to chiral allylic amines. Specifically, decades-old chemistry established that adducts of terminal olefins and imido-sulfur compounds quickly rearrange to form carbon-nitrogen bonds. Bao and Tambar realized that stabilization of such adducts could slow down the bond-forming event sufficiently for a catalyst to dictate stereoselectivity. Benzenesulfonyl sulfurdiumide proved the optimal reagent, affording an adduct so slow to rearrange that

it persisted for days below 0°C. The authors could then introduce a palladium catalyst coordinated by a chiral ligand to coax the adducts toward allylic amine products with enantioselectivities exceeding 90%. The reaction tolerated electrophilic substituents on the olefin framework, such as aldehydes, nitriles, and halides. — JSY

J. Am. Chem. Soc. **134**, 10.1021/ja307851b (2012).

PLANETARY SCIENCE

The Two Faces of the Moon

The nearside and farside of the Moon look very different. The farside, which we cannot see from Earth but has been imaged by satellites, almost completely lacks the large basaltic

GENETICS

Acquiring the Essentials

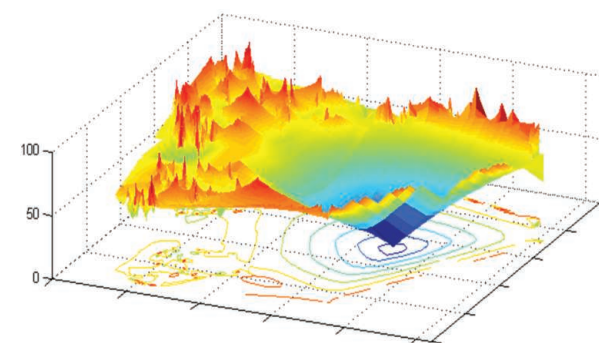
Bdelloid rotifers are microinvertebrates that have garnered much interest because of their long history of asexual reproduction (tens of millions of years), high rates of horizontal gene transfer, and ability to withstand extreme desiccation. Boschetti *et al.* have examined the transcriptome of hydrated and dehydrated *Adineta ricciae* bdelloid rotifers and identified genes that have probably undergone horizontal gene transfer. They found that approximately 9.7% of transcripts appeared to be from genes that have undergone horizontal gene transfer, of which half appeared to be of prokaryotic origin. The remaining half were of eukaryotic origin. These foreign transcripts are probably functional. In fact, 39% of enzymatic activity in bdelloid rotifers may be the result of acquired genes. The presence of genes of prokaryotic origin in their genome allowed bdelloid rotifers to degrade toxic compounds. Thus, the authors conclude that extreme horizontal gene transfer may have increased bdelloid stress tolerance and competitiveness, and might have also facilitated their long-term persistence in the absence of sex. — LMZ

PLoS Genet. **8**, e1003035 (2012).

CELL SIGNALING

Viewing the Cancer Landscape

The cellular signaling pathways that control cell physiology are key targets of therapeutic strategies, like those aimed at killing cancer



cells. But agents that cause DNA damage in cancer cells lead to cell death through a complicated network of pathways, including positive and negative feedback loops, that control the activity of the tumor suppressor p53. To help clarify more effective strategies to promote cell death in cancer cells, Choi *et al.* used a computational approach in which



plains (mare) that are so prominent on the nearside. A giant impact early in the Moon's history is one of the possible explanations for this asymmetry, which manifests itself not only in mare basalt distribution but also in crustal thickness and concentrations of radioactive elements. Nakamura *et al.* used spectral data from the Japanese Kaguya mission to look for the signatures of such an impact. Specifically, they searched for low-calcium pyroxene, a mineral that can be associated with a large impact, because it would either be excavated from the upper mantle and exposed at the surface or produced by the melting of a mixture of crust and mantle materials after the impact. Concentrations of low-calcium pyroxene were found to occur around the two largest impact basins on the Moon: the South Pole–Aitken basin, on the farside, and the Imbrium basin, on the nearside. The mineral was also found around the Procellarum basin, a 3000-kilometer-diameter basin on the nearside, whose origin has been equivocal. A large impact on the Procellarum region could explain the asymmetry between the two faces of the Moon. — MJC

Nat. Geosci. **5**, 775 (2012).

EDUCATION

Quality Assurance

Measuring teacher quality is a contentious topic; everyone agrees it should be done, but few can agree on how best to do it. Multiple-choice assessments are easy and cost-effective, but are they accurate enough to determine

teacher certification and promotion? Hill *et al.* investigated this question by evaluating 10 elementary and 24 middle-school teachers in the United States on a written math assessment, during their mathematics instruction, and on their students' performance on a state assessment. Although the written math assessment did identify teachers below a minimum competence criterion, it failed to identify all of the weak teachers, suggesting that the written test could be more reliable if expanded to detect the types of difficulties observed during classroom teaching. In contrast, the written test identified most teachers with strong observational scores, suggesting that it could be used as a screen for teacher promotions. Taken together, these results indicate that multiple-choice exams can be predictive of classroom practice. To verify the reliability of these exams, future research should include comparing preservice teachers' scores with their later practice and student outcomes scores. — MM

Am. J. Educ. **118**, 489 (2012).

ECOLOGY

A One-Two Punch

Climate change is expected to shift the ranges of many species as they attempt to follow the thermal envelope to which they are presumably adapted. As the planet warms, this may produce novel communities and interactions between species. This is because species do not exist in isolation but as parts of large communities of interacting species. Milazzo *et al.* now report one such example by studying two closely related species of wrasse (rainbow and ornate) in the Mediterranean Sea. Rather than shift their ranges, they found that the cool-water species of fish shifted to a less-preferred seagrass habitat and reduced its level of activity when the density of the warmer-water species within the same enclosure was high. Interestingly, these shifts were not seen at cooler water temperatures and were only observed at high water temperatures when the ratio of the warm-water to cool-water species was high. Thus, in this particular example, the cooler-water species make these changes only when faced with the dual injury of both warmer water and interspecific competition. Furthermore, as species individually begin to respond to their changing environments, unexpected interactions and impacts among species are likely to occur. As the climate changes, we should begin to expect the unexpected. — SNV

J. Anim. Ecol. 10.1111/

j.1365-2656.2012.02034.x (2012).

\$14,626.79*

in savings.

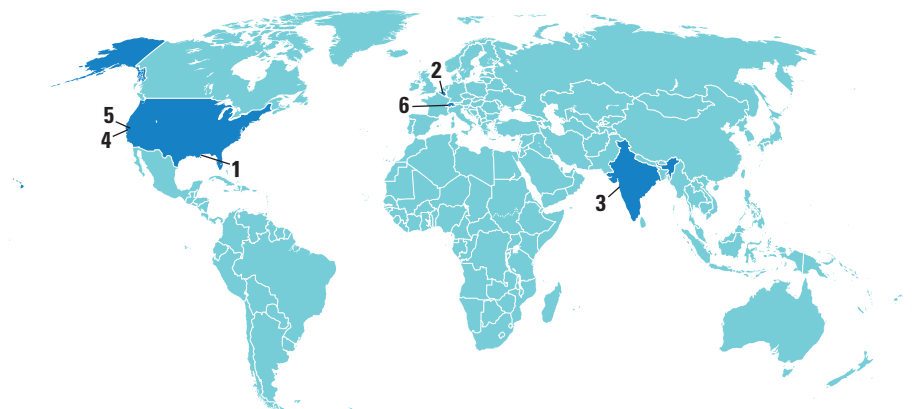
One more data point on why it's worth investing in a membership at membercentral.aaas.org. There you can enjoy videos, webinars, blogs and downloads while you calculate the potential members-only savings from all our Apple hardware and software discounts combined.

*The combined member discount when purchasing one of each item at the Apple Store.



membercentral.aaas.org

AROUND THE WORLD



New Orleans, Louisiana 1

Research, Restoration Get Share Of Record BP Oil Spill Fine

Environmental restoration projects and scientific research will get a major windfall from a 15 November decision by oil giant BP to pay a record \$4 billion to settle U.S. criminal



Louisiana marsh grass impacted by Deepwater Horizon oil spill.

charges related to the 2010 *Deepwater Horizon* oil spill in the Gulf of Mexico. More than half of the total, \$2.4 billion, will go to a congressionally chartered foundation for ecological restoration projects along the Gulf Coast. Another \$350 million will go to the U.S. National Academy of Sciences to establish a 30-year research effort focused on reducing the risk of future spills and improving environmental monitoring. The payments are unlikely to be BP's last; the company still faces other penalties, including up to \$25 billion in civil fines for oil pollution.

Brussels 2

Scientists Lobby E.U. Presidents To Prevent Budget Cuts

A delegation led by Nobel laureates Tim Hunt and Jules Hoffmann on 15 November met with the European Union's three presidents—European Parliament President

Martin Schulz, European Council President Herman Van Rompuy, and European Commission President José Manuel Barroso—to lobby them to spare research funding from looming cuts in the European Union's budget.

A growing chorus of scientists and research organizations across Europe has been arguing that research funding should be protected from cuts because it offers a path out of the crisis and a way to strengthen the European Union's economy in the long term.

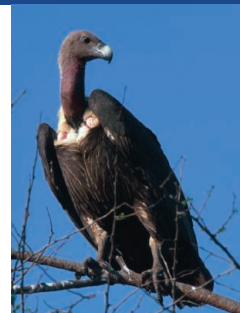
"They're on our side, no question about that," Hunt says, referring to the three presidents. "Van Rompuy said he'd do his best to protect [research funds]" in upcoming negotiations, Hunt adds. Van Rompuy's support may matter most in the short term, as the European Council—the body representing the governments of the member states—has the most power over spending. <http://scim.ag/EUSciBdgt>

Mumbai, India 3

Vultures Soar in India

There's good news for South Asian vulture populations, possibly thanks to a 2006 ban on veterinary use of the painkiller diclofenac, used to treat livestock. Researchers surmised that the drug induced kidney failure in vultures that ingested it while feeding on dead livestock recently treated with the drug. A 2011 population survey of the oriental white-backed vulture, long-billed vulture, and slender-billed vulture found a slowdown in the rapid decline seen in all three species since the early 1990s, researchers report online this month in *PLOS ONE*. The team notes that this is the first sign of recovery for these endangered birds.

The results are encouraging, said con-



servation scientist and study co-author Richard Cuthbert of the United Kingdom's Royal Society for the Protection of Birds in a state-

ment. But he added: "A lot of hard work still remains to ensure that the small surviving populations can now begin to recover across South Asia and other toxic veterinary drugs do not cause similar impacts."

Mountain View, California 4

Millions of Dollars For Extraterrestrial Hunt

A generous gift has breathed new life into the search for extraterrestrial intelligence. The SETI Institute in Mountain View, California—whose future was looking bleak a year ago because of a lack of funding—has received a \$3.5 million donation from Franklin Antonio, co-founder and chief scientist of Qualcomm. The institute will use the new money to improve the sensitivity of its Allen Telescope Array, which searches the cosmos for signals from alien civilizations.

Sacramento 5

Cap-and-Trade for California

The cap-and-trade system that California launched last week to cut greenhouse gas emissions is the first such comprehensive scheme in the United States. It began with an auction on emissions permits for the electric-



ity sector, the first to be regulated. The sale includes a price floor of \$10 per ton of carbon dioxide to prevent a crash of emissions prices. The system will expand in 2015 to cover transportation, commercial, and residential fuels, regulating 85% of California's total greenhouse gas pollution.

The system was set up as part of a landmark 2006 state law and survived a voter referendum to suspend it in 2010. Other

emissions control schemes already in place include one established in Europe in 2005—which covers electricity and industry—and in the northeastern United States, which covers only electricity.

Geneva, Switzerland **6**

Major Changes Afoot At Global Fund

In dizzying but unrelated decisions last week, the board of the Global Fund to Fight AIDS, Tuberculosis and Malaria hired a new executive director, fired its inspector general, and made a controversial decision about financing malarial drugs. The fund, which has spent \$23 billion since 2002 to finance treatment and prevention of these three diseases in resource-limited countries, announced on 15 November that Mark Dybul would take the helm. Dybul formerly ran the President's Emergency Plan for AIDS Relief, a multi-billion-dollar program financed by the U.S. government. John Parsons, the fund's inspector general for the past 5 years, was dismissed for "unsatisfactory" work, the board said. And finally, the board decided to fold the Affordable Medicines Facility-malaria (AMFm)—a controversial program that aims to improve access to more effective malarial medicines by enlisting the private market—into the fund's regular activities. Backers of AMFm say the move threatens the scheme's survival. http://scim.ag/_GFund

NEWSMAKERS

Computer Graphics, Cellular Processes Win Kyoto Prize

American computer scientist **Ivan Sutherland** and Japanese biologist **Yoshinori Ohsumi** have won the Kyoto Prize, which encourages a balance between scientific progress and spiritual depth. The prize, administered by the Inamori Foundation, was awarded for their lifetime achievements. Sutherland, 74, the "Father of Computer Graphics" now at Portland State University in Oregon, won the advanced technology prize for developing progenitors of the graphical user interfaces now ubiquitous in many devices, such as smart phones and personal computers.

Science LIVE

Join us on Thursday, 29 November, at 3 p.m. EST for a live chat on the imminent "end of the world." <http://scim.ag/science-live>

Double Whammy for Threatened Salamander

The threatened California tiger salamander is losing ground on its native turf. This black and yellow-spotted amphibian interbreeds with the introduced barred tiger salamander. Hybrid larvae outcompete the native young, making the smaller natives more vulnerable to environmental insults, says evolutionary ecologist Maureen Ryan, of the University of Washington, Seattle. One month into a study on the effects of habitat and hybrid-native interactions on salamander survival, all of the native tiger salamander larvae and about half of the hybrid larvae suddenly died in four of the six ponds containing the experiments. Ryan and colleagues ruled out fungal and viral infections and strongly suspect pesticide runoff killed the salamanders' invertebrate food supply, starving them, they reported online 9 November in *Conservation Biology*. The more hybrids in the enclosures, the smaller the natives were, they noted. The team speculates that the natives weren't big enough to switch to larger prey, such as tadpoles, when the invertebrates disappeared. Further study would be needed to verify the pesticide connection, Ryan adds.



Sutherland



Ohsumi

Ohsumi, 67, of Tokyo Institute of Technology, won the basic sciences prize for unraveling the mechanisms and demonstrating the significance of autophagy, the phenomenon by which a cell degrades and recycles its own components. Autophagy plays a central role in cell growth, development, and homeostasis. Understanding autophagy could lead

to future treatments for neurodegenerative diseases and cancer.

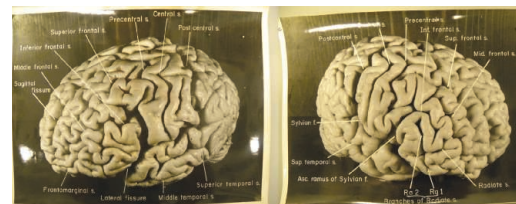
Each laureate received a medal, a diploma, and about \$630,000 at a ceremony in Kyoto on 10 November.

FINDINGS

Einstein's Brain Reveals Genius

It took a special brain to come up with the theory of relativity. Newly discovered photographs of Albert Einstein's brain reveal many extra folds and convolutions—but it's not clear how they translated into his amazing abilities.

When Einstein died in 1955, the examining pathologist, Thomas Harvey, photographed the scientist's brain and cut it into 240 blocks. Now, in a study published online on 15 November in *Brain*, researchers led by anthropologist Dean Falk of Florida State University in Tallahassee analyzed 14 photographs of the whole brain from the Harvey collection that have never before been made public.



Singular mind. A new analysis of Einstein's brain yields clues to his genius.

When compared with 85 human brains in the scientific literature, Einstein's brain is special, the team found. Although average in size, the brain has several regions with unusual twists and folds. For example, regions on the left side of the brain connected to the face and tongue are much larger than normal, as is his prefrontal cortex, which is linked to planning, focused attention, and perseverance. <http://scim.ag/Einsteinbrain>



HUMAN GENETICS

Genetic Influences On Disease Remain Hidden

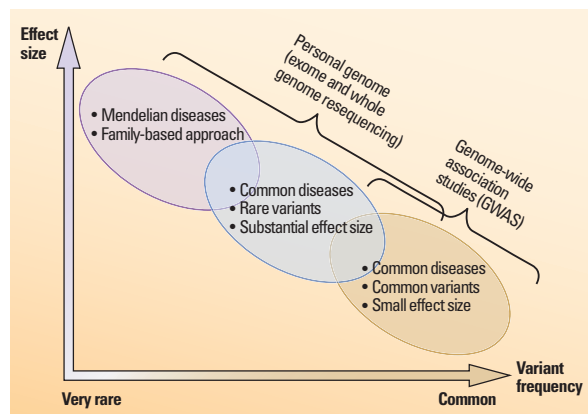
SAN FRANCISCO, CALIFORNIA—The quest to find genes that strongly influence whether people will develop common diseases is turning out to be even more difficult than some researchers had expected. This month, at the annual meeting of the American Society of Human Genetics here, several large DNA sequencing studies aimed at ferreting out genetic variants behind diseases such as diabetes and heart disease reported initial findings. This work shows that a popular hypothesis in the field—that the general population carries somewhat rare variants that greatly increase or decrease a person's disease risk—is not yet panning out.

“People were overly optimistic,” says Suzanne Leal of Baylor College of Medicine in Houston, Texas, a co-leader of one of the reported studies. Instead, it seems that the variants conferring high risks for common diseases—assuming they exist—are so rare that pinning down these variants will be an enormous challenge. Some researchers say the results aren't surprising, however, and that the predicted variants will eventually be unearthed. “We're still in the foothills, really. We need larger sample sizes,” says another gene hunter, Mark McCarthy of the University of Oxford in the United Kingdom.

The new studies are the latest efforts to apply data on the human genome to personalized medicine by identifying the multiple genes under-

lying complex, common diseases, ones unlike the Mendelian disorders caused by a defect in a single gene. Soon after the human genome was sequenced in 2003, researchers created a map of common markers scattered along the genome. By comparing markers carried by at least 5% of the population in healthy people and those with various diseases, they found many associated with disease risk. These genome-wide association studies (GWAS) have now uncovered hundreds of common variants, known as single-nucleotide polymorphisms (SNPs), that point to genes that raise the risk of diseases such as cancer, diabetes, and heart disease.

But for most diseases, individual SNPs only raise the risk by a modest amount, perhaps 20% or 40%, which isn't very use-



Hole in the middle. New studies are failing to find many rare genetic variants with large influences on common diseases (blue).

Elusive. Genetic variants that sharply raise a person's risk for type 2 diabetes haven't been found yet.

ful for predicting whether someone will develop the illness. And in combination, these markers account for only a fraction of a disease's heritability, a measure of how much genes are responsible for the condition. (For instance, twin studies indicate that a person's genes determine 26% of their risk of developing type 2 diabetes, with the rest governed by environment.)

Many researchers have postulated that the so-called missing heritability for many common diseases lies in rarer variants carried by less than 2% of the population. These variants might have larger effects on risk, somewhere between the common variants of small influence and the extremely rare Mendelian gene mutations (see graph). To look for such medium-rare risk variants, researchers have now used next-generation DNA sequencing and other methods to quickly analyze the exome—the 1% of the genome that codes for proteins—of thousands of people.

But as many talks here showed, these rare variants with a large influence on common diseases remain elusive. One project, the National Heart, Lung and Blood Institute Exome Sequencing Project (ESP), has sequenced about 6700 exomes of people of European or African ancestry who have specific heart, lung, or blood diseases or traits such as high blood pressure. As Leal reported, the majority of variants linked to those conditions turned out to be extremely rare: Often, only one person in the study group carried them. So the researchers looked at disease associations for a group of variants in the same gene. This firmed up some known connections, for example between the gene *APOC3* and lower blood triglyceride levels. ESP has also linked a set of variants in the *APOA5* gene, previously implicated in triglyceride levels, to a 2.3-fold higher risk for early-onset heart attack. But in general, for other gene variants being linked to heart disease or its risk factors, “effect sizes are not as large as initially believed,” Leal says.

Two large diabetes studies examining exomes have also come up short. The T2D-GENES Consortium, which has analyzed 5300 of a planned 10,000 exomes of type 2 diabetes patients and controls from five ancestry groups, has yielded an intriguing SNP in the *PAX4* gene that's associated with the disease in East Asians,

Tanya Teslovich of the University of Michigan, Ann Arbor, reported. But the study hasn't yet found any low-frequency variants with large effects. Researchers with another diabetes study, GoT2D, which has exome and whole genome data for 2700 patients, have not yet found any new rare variants above 1.5% in frequency with a strong effect on diabetes risk, reported Jason Flannick, a postdoctoral researcher at the Broad Institute in Cambridge, Massachusetts.

"The view that there would be lots of low frequency variants with really big effects does not look to be well supported at the moment," says McCarthy, a principal investigator of GoT2D. This may not be a surprise, he says, because as several

groups reported earlier this year, sequencing studies have revealed that the human population underwent an explosive expansion 5000 years ago (*Science*, 11 May, p. 740; 6 July, p. 64, p. 100). This produced many very rare gene variants that, according to one hypothesis, are often disease-influencing but haven't yet been weeded out through natural selection. Tying these scarce variants to disease risks could require scouring tens of thousands of people's genomes.

Some geneticists are eager to move on to these massive analyses by pooling exome data sets. It's also sometimes possible to look for rare variants found in exome studies in people whose DNA was analyzed for

GWAS, thereby increasing a study's overall sample, Leal points out. Another promising avenue is to look for rare variants in families or isolated populations.

Some scientists, such as Harry Dietz of Johns Hopkins University in Baltimore, Maryland, suspect that much of the missing heritability lies in gene-gene interactions. Dietz cites his work with Marfan syndrome, a Mendelian disorder which turned out to involve one main gene acting in concert with other gene variants, including one that has pointed to a new treatment. To find such interactions for common diseases, researchers may need "huge sample sizes" of hundreds of thousands of people, Dietz says.

—JOCELYN KAISER

HIGH-ENERGY PHYSICS

DOE Shifts Money From Research Grants to New Projects

The U.S. Department of Energy (DOE) has decided to cut funding for high-energy physics research to free up money for new projects. The shift will reduce the number of researchers it supports on the teams working with the world's largest atom smasher—the Large Hadron Collider (LHC) at the European particle physics laboratory, CERN, near Geneva, Switzerland.

The \$792 million within DOE's high-energy physics program, whose budget has remained flat for more than a decade, is divided into three main pieces. The proportion going to research grants (see chart) has nearly doubled in the past 15 years, to 57%, while the size of the pot for new projects has shrunk by half, to roughly 12%. DOE officials would like to grow that slice to 20%, picking up roughly \$40 million a year. To do that, they plan to pare back support for research grants by 2% per year for several years.

"We certainly are not targeting the LHC, but we are going to try to reduce some of our research grant money so we can do [new] projects with the budgets we are getting," says William Brinkman, director of DOE's Office of Science. "We are doing a careful review and will cut the weakest grants."

DOE spends roughly \$80 million a year to sponsor 1270 senior researchers, postdocs, and graduate students working on one

or the other of two huge particle detectors, called ATLAS and CMS, that are fed by the LHC. (Most researchers are not stationed at CERN.) Four months ago, the LHC scored the biggest discovery in particle physics in 30 years when researchers spied the long-sought Higgs boson—or something like it.

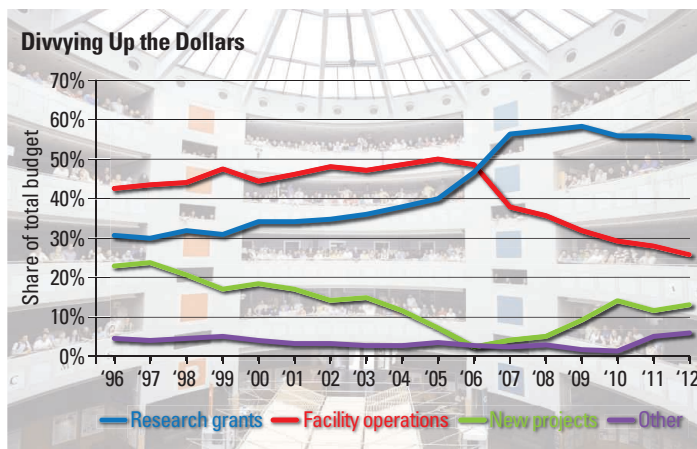
gest experiment based at the Fermi National Accelerator Laboratory (Fermilab) in Batavia, Illinois—the NOvA neutrino experiment—has a total of 180 collaborators.

DOE would plow the savings back into new projects. Researchers at Fermilab want to build a \$789 million experiment to study neutrinos. Their counterparts at SLAC National Accelerator Laboratory in Menlo Park, California, plan to build a \$160 million, 3.2-gigapixel camera for the National Science Foundation's proposed \$457 million Large Synoptic Survey Telescope. And U.S. researchers hope to contribute to upgrades of particle detectors at the LHC.

But will an extra \$40 million a year enable DOE to fit such big-ticket items into its budget? "We've been struggling with this question, and we've asked [DOE officials] to come up with some data," says Gordon, who will become chair of the ATLAS collaboration board in January. "They claim that they have a plan that will make it work."

It's ironic that DOE is scaling back on its LHC effort so soon after the discovery of the Higgs, says Nick Hadley, a physicist at the University of Maryland, College Park, who chairs the U.S. CMS collaboration board. "What if we hadn't been so successful?" Hadley asks. "Would they have cut our budget by 5% per year?"

—ADRIAN CHO



Thinning the herd. The U.S. contingent to the LHC, part of which gathered for a photo at CERN, will shrink as DOE reduces spending on research.

But that success doesn't make the U.S. LHC program invulnerable. "We're a larger target because so many groups are working on the LHC," says Howard Gordon, an LHC collaborator from Brookhaven National Laboratory in Upton, New York. "There are not a lot of other places to find money."

The teams working on U.S.-based particle physics experiments are much smaller than the LHC contingent. For example, the big-

SCIENTIFIC PUBLISHING

As Open Access Explodes, How to Tell The Good From the Bad and the Ugly?

ROTTERDAM, THE NETHERLANDS—Would you submit a paper to the *Electronic Journal of Biology*? Does *Aquatic Biosystems* have good editors? Should your grad student, whose career may be riding on it, send her paper to the *International Journal of Computer Science and Network*?

Picking the right journal has always been difficult, but the plethora of new open access (OA) journals—and the increasing pressure from funders to publish in them—has made the choice even more daunting. The titles above are three of the 76 that

Almost everyone agreed that scientists could use some help. Funders are increasingly pushing scientists to publish in OA journals, which offer their content online for free and charge authors a publication fee rather than bill for subscriptions. Many scientists say they support the idea of open access, SURF's Marc Dupuis says—but more importantly, they want to publish in journals where their papers get noted and cited. Because they are so young, most OA journals don't yet have an impact factor, a controversial but well-established indicator of journal quality published by Thomson Reuters.

Meanwhile, the OA industry is becoming increasingly diverse; it includes traditional powerhouses, such as Germany's Springer, which now publishes about 300 OA titles, as well as a vast array of newcomers. OA publishers have a built-in incentive to lower the bar, Dupuis says, because in contrast to subscription journals, an OA title earns more revenue with every paper its editors accept.

Moreover, many so-called predatory publishers—which often eschew peer review, use fake editors, or contain plagiarized papers—have flooded the market, says Jeffrey Beall, a librarian at the University of

whether it was possible to predict a journal's impact factor based on the scientific output of its editorial board, the underlying assumption being that a journal run by people who perform well themselves is probably a better journal than one with mediocre editors.

Based on a study of 286 existing journals, Wouters found such a correlation, but the predictive power of models based on his data wasn't impressive, and meeting participants saw various problems with their use as an indicator; for instance, journals could game the system by getting good scientists on their boards without changing anything else.

Research by Jelte Wicherts, a psychology researcher at Tilburg University, suggests that transparency could be an indicator of quality. Journals that very clearly explain things such as scope, target readership, peer-review procedures, and rejection rates on their Web sites tend to be better than journals that don't, Wicherts says. During the meeting, he asked participants to go to the Web sites of selected journals and rank them on their transparency on a range of issues using a five-star system—as if they were rating hotels or movies. The experiment clearly separated the predatory journals from well-established ones, Wicherts says.

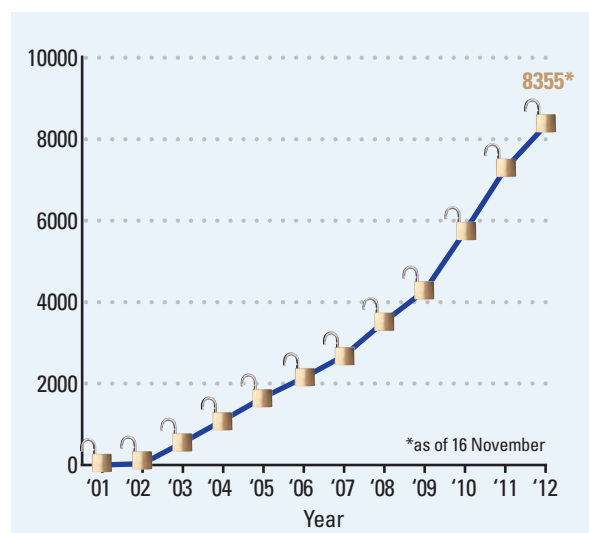
Although most of his criteria were seen as sound, Wicherts's proposal, too, ran into various practical objections, and the meeting ended without a consensus to support the further development or refinement of either indicator, as the organizers had hoped. Beall, who attended the meeting, says he was disappointed by the outcome and that the idea of devising a quality indicator should be pursued. Springer Executive Vice President of Corporate Strategy Wim van der Stelt says the Open Access Scholarly Publishers Association (OASPA) would be a natural candidate to promote quality in OA publishing.

Paul Peters, who will take over as president of OASPA in March, agrees that his group can do more; so far, the organization, founded in 2008, has had no staff and very little budget, he says. But Peters questions

the need for a numerical indicator or a rating system. OASPA vets its members carefully, he says, and guarantees that they are decent publishers. He suggests the association should make its membership known to scientists

to help them evaluate which publishers to trust: "The idea is that we are the good OA publishers—the opposite of Beall's list."

—MARTIN ENSERINK



Open questions. More than 1000 new open access journals hit the market every year, but gauging their quality is difficult.

made their debut in just the past 4 weeks in an online registry called the Directory of Open Access Journals (DOAJ). In the past year alone, the directory has added almost 1200 titles in all scientific fields; as of last week, the total was 8355.

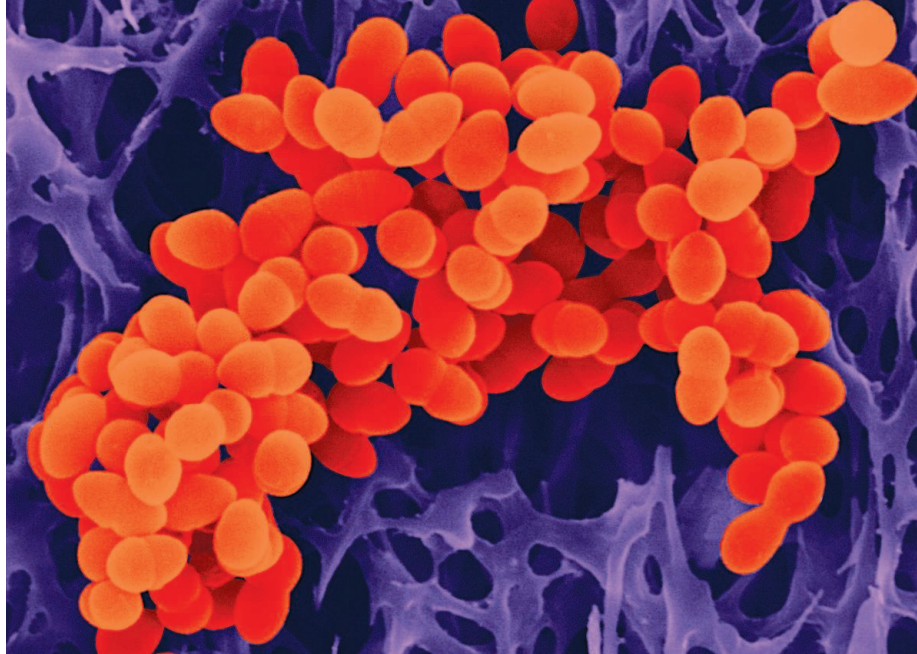
So how to tell which are the best? At a meeting here last month, about two dozen representatives from science funding agencies, publishers, librarians, and journal editors discussed ways of helping befuddled scientists with that question—including two proposed yardsticks for quality, developed by Dutch researchers. But the meeting, organized by the Netherlands Organisation for Scientific Research (NWO) and SURF, a partnership that provides information and communication technology to Dutch universities, failed to come up with clear answers.

Colorado, Denver, who keeps an online list of these dodgy outfits. (The latest publisher added to his list just launched 141 new medical journals.) "Anybody can set up a publishing company in a matter of hours," Beall says. Many of the shady journals aren't even on the DOAJ, he adds, which means that the actual number of OAs journal far exceeds that tally.

To help bring order to the chaos, the meeting's organizers had commissioned preliminary studies of possible quality indicators for OA journals from two Dutch researchers. One came from Paul Wouters of the Centre for Science and Technology Studies at Leiden University, who wondered

"Anybody can set up a publishing company in a matter of hours."

—JEFFREY BEALL,
UNIVERSITY OF COLORADO,
DENVER



INFECTIOUS DISEASES

Genome Study Helps Contain MRSA Outbreak—And Breeds New Questions

When Julian Parkhill, a bacterial geneticist at the Wellcome Trust Sanger Institute in Hinxton, U.K., started sequencing the whole genomes of bacteria isolated from infants at a special care baby unit, it was a matter of scientific curiosity, he says. Three babies had become infected with methicillin-resistant *Staphylococcus aureus* (MRSA) at Cambridge's Rosie Hospital at the same time, and he wanted to know if their cases were isolated incidents or part of a bigger outbreak.

Parkhill didn't realize that the study would help discover an asymptomatic MRSA carrier working in the hospital—and eventually stop the outbreak in its tracks. His study, published last week in *The Lancet Infectious Diseases*, is the latest in the burgeoning field dubbed genomic epidemiology, which uses full-genome sequencing of microbes to trace the path that a pathogen took—and, increasingly, to help stop transmission.

By fully sequencing bacteria from different patients and comparing the sequences, researchers can find out where an outbreak originated and, in some cases, who infected whom. In August, scientists at the U.S. National Institutes of Health Clinical Center in Bethesda, Maryland, described how they used a similar method to halt an outbreak of drug-resistant *Klebsiella pneumoniae*. Parkhill's study of MRSA, a scourge of hospitals worldwide, is "another great example of the potential of whole-genome sequencing in managing outbreaks," says Dag Harmsen of the University Clinic of Münster in Germany. But the paper also raises

questions that researchers in the new field have yet to answer.

Parkhill sequenced bacteria from the three babies as well as 13 cases that had occurred in the preceding 6 months. Testing the isolates for their susceptibility to a battery of antibiotics suggested that six of these additional MRSA cases were part of the same outbreak. "But because there were long gaps between some of the cases, you couldn't really be sure that these belonged together," Parkhill says.

The genomic data clearly showed that the six older cases were related to the three recent ones. And two other cases that had been deemed unrelated to the rest, also based on antibiotic tests, turned out to be part of the outbreak as well. The remaining five other cases turned out to have a different origin.

But the most interesting finding was still to come. After sterilization of the whole hospital ward and 64 days without a new MRSA case, another baby became infected. The researchers sequenced the strain immediately and found it to be almost identical to the outbreak strain. "It was seeing that strain reappear that made us think there must be a carrier," Parkhill says. The team then screened 154 staff members, and one member was found to carry the outbreak strain, making it very likely that he was responsible for reintroducing the bacterium, Parkhill says. The man was treated with antibiotics, became MRSA-free, and the outbreak strain has not come back there since.

Harmsen believes the paper may be remembered as a milestone in the field. "They managed to use this information to

Staph story. Genomic sleuthing led to a hidden source of resistant *Staphylococcus aureus*.

change the course of an outbreak, which is great," adds Edward Feil, a geneticist at the University of Bath in the United Kingdom. But Feil is skeptical of the paper's conclusion that the hospital employee infected the babies, instead of vice versa.

The researchers sequenced 20 different MRSA isolates from the staff member and found a great deal of genetic variation; this led them to conclude he had been infected for a long time, based on the simple idea that if a microbial population is around longer, it has more time to diversify. But this does not necessarily hold true, Feil says. In HIV-infected people, for instance, the virus evolves over time, but genetic diversity does not usually increase. And because the researchers didn't assess multiple isolates from the babies, they don't really know whether the variation seen in the staff member is larger than that of the babies.

Parkhill agrees that this is a weakness of the study, but says that only single isolates were available for the other patients. Although he agrees that there is no proof the health worker infected the babies rather than the other way around, he says the circumstances strongly suggest it.

Meanwhile, Feil says the MRSA diversity seen within one person raises another question that goes to the heart of genomic epidemiology. Usually, when comparing bacterial genomes, scientists pick and sequence only one bacterial clone from each patient, essentially treating a patient as if all of his microbes were genetically identical, and only one type could be transmitted. That's probably not true, Feil says: "If we have a whole zoo of microorganisms on our skin or up our noses, it is fairly likely that a reasonable proportion of that zoo will be transmitted." (He has a name for the genetic material going from one patient to the next: the transmissome.) That means that two patients whose bacterial genomes look different may have been infected by the same person. How big the difference could be is unclear even though it is critically important to the field.

Parkhill agrees that these are fascinating questions. To answer them, the field will have to take the next plunge: Sequence not just a single microbe from each patient but a bunch of them. That adds another layer of complexity, Harmsen says—a curse and a blessing at the same time: "Suddenly we can see things we couldn't before, but now we need to make sense of this data too."

—KAI KUPFERSCHMIDT



In Search of the Wild Chicken

Researchers are melding genetics and archaeology to close in on the origin of the world's most common bird—and potentially help protect a major source of animal protein

IN THE 1950s, BIRD HUNTERS IN THE SOUTHERN United States were eager to bag more exotic prey than quail, and so their representatives in Washington agitated for the introduction of foreign varieties. A U.S. Fish and Wildlife Service biologist dutifully went to a remote area in India's Himalayan foothills and collected dozens of red jungle fowl, a colorful, shy, and tasty wild bird that also happens to be the primary progenitor of today's domestic chicken. Bred at research stations across the South, nearly 10,000 of the birds were released in the 1960s. They failed to thrive, and the program introducing an alien species was quietly cancelled. The few remaining penned jungle fowl were slated for slaughter in 1969.

But a young ecologist named I. Lehr Brisbin rescued five birds. The biologist who had originally imported them warned him that someday these birds might be the last ones left. "I didn't understand what he meant at the time," recalls Brisbin, who works at the University of Georgia's Savannah River Ecology Laboratory in Aiken, South Carolina. "Now I do." Over the intervening decades, South Asia's wild red jungle fowl has suffered from development and crossbreeding with village chickens, while Brisbin's flock quietly flourished in an aviary in Alabama. Today, there are more than 100 birds, carefully isolated from other varieties, that may be among the closest living wild ancestors of the modern chicken.

Their genes, and those of other isolated populations, are now being sequenced (see sidebar, p. 1022) as part of a larger effort to

understand the world's most common bird and biggest source of animal protein. In 2009, Americans ate 36 billion pounds of chicken, and the numbers keep growing, especially in developing countries in Asia and Africa. That importance is highlighted by the fact that the chicken was the first farm animal to have its genome published, back in 2004. Since then, the proliferation of factory farms, mass bird deaths from avian influenza, and dwindling diversity in chickens have raised concerns about this critical source of food.

A key thrust of research in the past decade has been to track the genetic changes that turned a remarkably shy creature into today's meat-and-eggs dynamo, with an eye to protecting and improving breeds. But this research has also given scientists the opportunity to unravel a long-standing mystery that

Online

sciencemag.org
Podcast interview
with Andrew
Lawler (http://scim.ag/pod_6110).

fascinated Charles Darwin: Where, when, and how was the chicken domesticated?

Researchers agree that the red jungle fowl gave rise to the barnyard chicken somewhere in South Asia. But they agree on little else.

Some contend that domestication took place 8000 years ago; others suggest that tame chickens are only 4000 years old. Some say the bird was domesticated only once; others look to several independent centers of domestication. And since Darwin's day, scholars have disputed whether the three other jungle fowl subspecies contributed to the modern bird. There isn't even accord over whether the truly wild red jungle fowl remains numerous or has long gone extinct, leaving only mixtures of wild and domesticated birds. "There has been more noise than signal," says Greger Larson, an archaeologist at Durham University in the United Kingdom.

The sudden surge in chicken studies across several disciplines may soon help answer these fundamental questions, however. One recent paper claims that two subspecies contributed to today's chicken, while another paper published this week suggests

Rooster's riddle. The chicken emerged from the red jungle fowl, shown here, but how, when, and where still perplexes scientists.



His and hers. Unlike domesticated chickens, female (left) and male red jungle fowl don't share traits such as wattles and combs.

that the bird was domesticated separately in several regions. Researchers are tracking red jungle fowl populations across South Asia and searching for older specimens in museums for DNA sequencing. Archaeologists, meanwhile, have begun to extract DNA from ancient chicken bones to determine the genetic profile of prehistoric barnyard birds. "Now we are getting the data," Larson says. "And we may be getting to the answers."

Identifying the chicken's wild cousins and preserving their genetic diversity may one day prove critical for improving the stock, some researchers say. Genes from wild birds may help breed birds resistant to avian influenza and other illnesses, for example. "This is the most important bird to humans," says A. Townsend Peterson, an ornithologist at the University of Kansas, Lawrence. "And we can potentially make chickens better."

The indispensable bird

Humans have been shaping the chicken for millennia. Darwin's grandfather Erasmus was one of the first to suggest that the red jungle fowl was the ancestor of the chicken, *Gallus gallus domesticus*. His grandson, who studied chickens as he formulated his theory of evolution, backed this up with detailed observation of the jungle fowl's physical characteristics and postulated that the chicken was domesticated in India and then spread around the world. But he also complained that "sufficient materials do not exist for tracing the history" of the bird.

The red jungle fowl—*Gallus gallus*—ranges from the western foothills of the Himalaya Mountains to the tip of Sumatra (see map, p. 1022). Unlike modern-day chickens, all roosters sport elaborate plumage, the females lack a comb, and both genders have thin, dark legs and can fly considerable distances. The fowl is also generally half the size of a White Leghorn domesticated chicken, but it can produce fertile offspring with domestic chickens.

Domestication couldn't have been easy given the bird's extremely shy nature. However, its habits ultimately made it a natural domesticate. It lives by day on the forest floor, eating insects, seeds, and fruits, and it nests in trees at night to avoid its myriad predators. Life spent pecking in a barnyard during the day and safe in a coop at night is not so removed from the fowl's natural condition, says anthropologist Naomi Sykes of the University of Nottingham in the United Kingdom. Once domesticated, the chicken proved remarkably versatile. It could eat almost anything and provided not just meat and eggs but medicines, sacrifices for religious ritual, and entertainment in the form of cockfighting. Humans carried the easily portable bird around the world.

How this began remains controversial. Archaeological finds of chicken bones were rare until recently. Bones and artifacts at Indus River valley sites south of the red jungle fowl's range revealed domesticated birds by 2000 B.C.E., bolstering Darwin's view of a single domestication in India. Then a hotly disputed Chinese find in 1988 pushed the date back to 6000 B.C.E.

The advent of sequencing tools in the 1990s promised a new line of evidence that went beyond physical characteristics. The results, however, have only heightened the controversy. A draft of the chicken genome, for example, isn't enough to trace the bird's evolution: Researchers need ancestral birds for comparison. Geneticists first used mitochondrial DNA (mtDNA) to trace the female line of the species back to its origin. Akishinomiya Fumihito, an ornithologist and

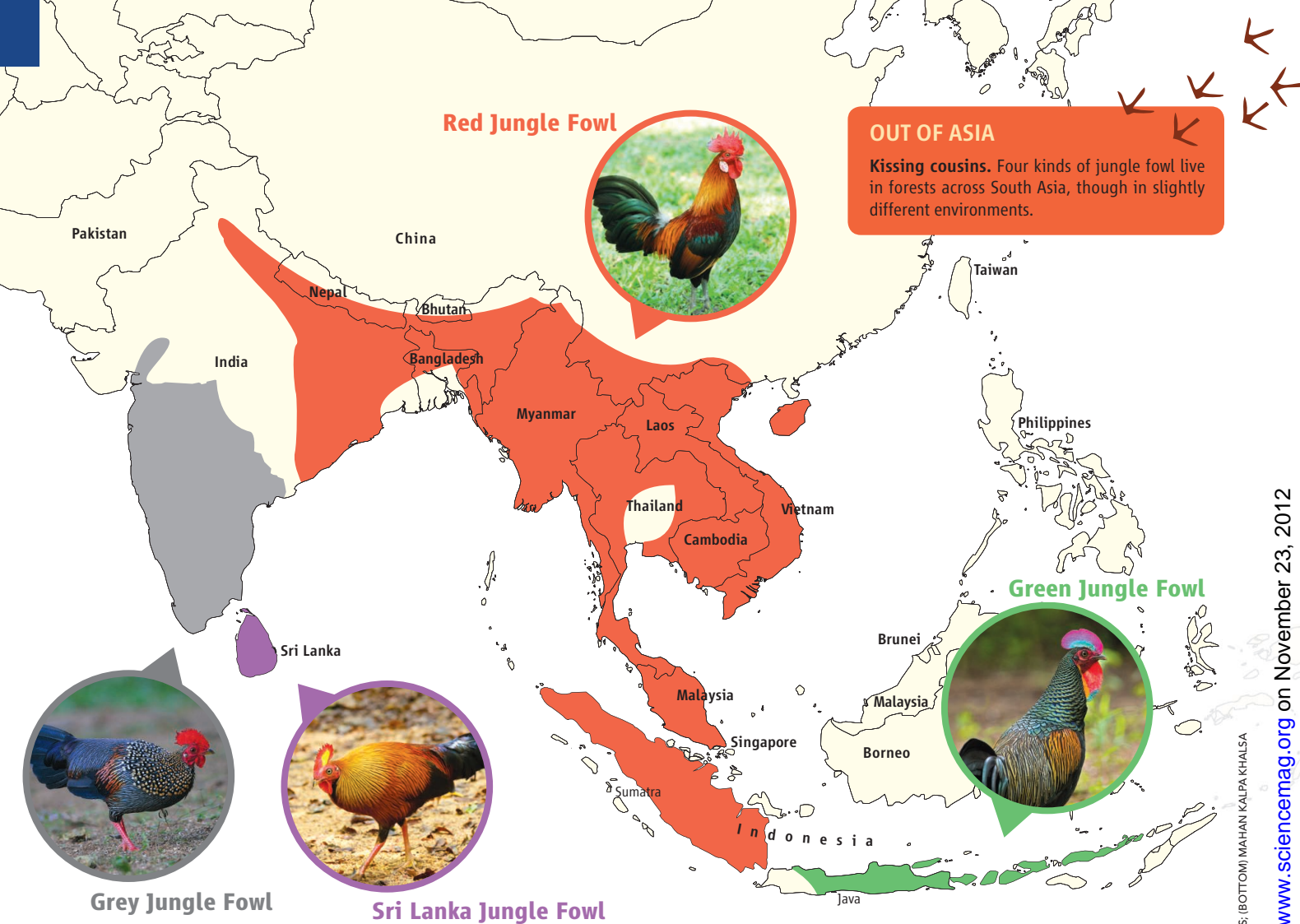
prince in Japan's royal family, extracted sections of mtDNA from Thai red jungle fowl and asserted in a 1994 paper that the findings suggested a single domestication in Thailand. Eight years later, another team used mtDNA from native Chinese chickens to support that idea.

In 2006, however, a team led by Yi-Ping Liu of China's Kunming Institute of Zoology found nine separate clades—that is, groups descended from a common ancestor—in the mtDNA of a large sample of wild and domestic modern birds. The distribution of the clades suggests a distinct and separate expansion of lineages in southern China, Southeast



Jungle game. To entice shy jungle fowl from the bush, locals in Southeast Asia often use a live bird as bait.

CREDITS (CLOCKWISE FROM LEFT): J.J. HARRISON/WIKIMEDIA COMMONS; TONY HIGSETT/WIKIMEDIA COMMONS; A. LAWLER/SCIENCE



From Farmyard to the Lab

SON LA, VIETNAM—On a tidy farm in the mountains of northwest Vietnam, Chinese biologist Jianlin Han expertly grabs a nervous red jungle fowl recently captured in this region's quickly disappearing forest. The bird—which sports a long and dangerously sharp spur—is part of Han's hands-on effort to breed better animals to benefit the rural poor, while at the same time gathering a massive data set to understand the genetic underpinnings of the domestic chicken.

Han, who grew up raising chickens in rural China, is as comfortable in the lab as in the barnyard. Although the chicken's genome was sequenced in 2004, traditional livestock research around the world has been decidedly low-tech. Different chicken varieties are still described by physical traits and behavior rather than by genetic heritage. Researchers like Han, trained in genetics but interested in agricultural applications, are increasingly using DNA tools to see how genotype affects a bird's phenotype.



Making a flap. Jianlin Han examines a red jungle fowl at a farm in Vietnam's mountains.

They also hope that these data will help them get at fundamental questions such as when and where the chicken was domesticated (see p. 1020).

The chicken, which grows quickly and is the most intensely bred of domestic animals, provides an intriguing model for understanding those issues, says Han, who works for the International Livestock Research Institute based in Nairobi but spends most of his time in his Beijing lab and in the field across South Asia. He recently took a bone-jarring 8-hour trip from Hanoi to check up on an experiment to breed the red jungle fowl—generally acknowledged as the primary progenitor of the chicken—with both local and foreign breeds. The goal is to produce a domesticated chicken that caters to local tastes while providing more meat and eggs. Han is also investigating the unusually high number of local varieties found in surrounding villages—many more than elsewhere in South Asia—which may be a hint that the chicken was originally domesticated in this rugged area.

Han has an ambitious plan to catalog the genetic makeup of today's jungle fowl, charting its diversity in different regions and also reveal-

CREDITS: (MAP CLOCKWISE FROM TOP) ISTOCKPHOTO; © ERIC TAN; © THIMINDU GOONATILLAKE; © CLEMENT FRANCIS; (BOTTOM) MAHAN KALPA KHALLA

Asia, and the Indian subcontinent, supporting a multiple origins theory. Another team published a study this week in *Heredity* based on nuclear DNA, which is not limited to the maternal line, supporting that view.

"It shows the complex history of the chicken," says Michèle Tixier-Boichard, a geneticist at the French National Institute for Agricultural Research in Paris, who was not part of the *Heredity* research but is familiar with the results. "And their sampling is impressive."

The implications are important for capturing genetic diversity, because if the chicken really did have multiple origins, researchers will have to carefully sample wild birds across many areas. The find also suggests that early peoples were operating largely independently, and that new technologies were homegrown rather than diffused.

But others insist that the old debate is far from over. "We need to reconcile all the data," says Olivier Hanotte, a geneticist at the University of Nottingham. He favors a single origin in northern Southeast Asia, based on the enormous diversity of chicken breeds there.

Whether domestication originally diffused from a single region or from multiple points, other genetic evidence suggests that more than one subspecies contributed to the modern chicken along the way. In 2008, Larson, geneticist Leif Andersson of Uppsala University in Sweden, and others claimed "the first

conclusive evidence for a hybrid origin of the domestic chicken." The results made headlines for contradicting Darwin's assertion that the red jungle fowl was the sole ancestor. Using single-nucleotide polymorphisms (SNPs) in nuclear DNA, the team found that the chicken's yellow skin allele likely comes from the grey jungle fowl, not the red. Domestication, they concluded, had many stages—and continues today.

Despite the power of these genetic approaches, some researchers say that decades of studies comparing red jungle fowl and modern birds may be fatally flawed, because wild and domesticated populations have mixed across South Asia for millennia. "The chicken is like a sponge, sucking up genes wherever humans take them," Larson says. Travelers, hunters, and merchants carrying hens for eggs and meat and breeding them with wild or hybrid roosters—all likely scenarios—would, over millennia, have muddled the wild fowl's gene pool.

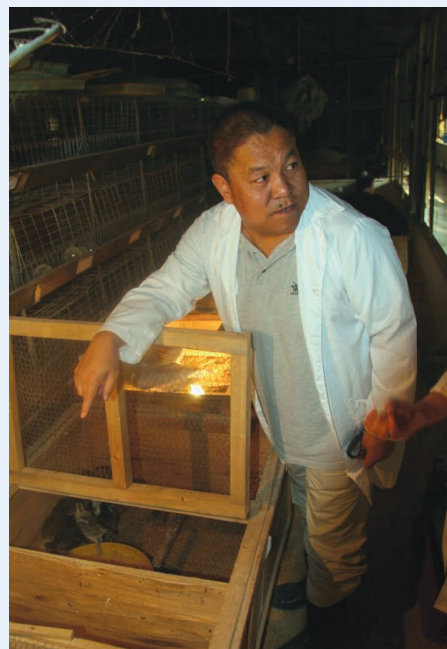
Thus, no one knows the genetic makeup of a pure wild red jungle fowl. Biologist Sambandam Sathyakumar of the Wildlife Institute of India in Dehradun, near where Brisbin's birds were collected a half-century ago, says genetic studies show that more than 95% of their birds are "relatively pure." But Brisbin and other researchers note ominous signs of morphological and behavioral changes in the fowl. For example, biologists have mapped the gradual loss of the male

red jungle fowl's eclipse plumage—a long black feather across the middle of his back and slender red-orange plumes on the rest of his body—which is absent in chickens. This plumage started to vanish in wild Southeast Asian birds a century ago and was gone in most Indian birds by the 1960s. And many red jungle fowl hens in zoo collections—often the source of scientific samples—have combs, though the purely wild birds do not. "All the work done to date is inconclusive, and our colleagues around the world have not been careful about the provenance of their material," Peterson says. "Our studies have been done without any idea what is a pure red jungle fowl."

Brisbin and Peterson hope that sequencing the birds brought from India to the United States in the 1960s, now being done by Andersson's lab, may create a genetic baseline for the wild bird, as well as provide "a reservoir of potentially invaluable genetic variation," says Tomas Condon, a biologist who studied at Georgia Southern University in Statesboro and researched the history of Brisbin's flock. Others are combing museum collections for DNA from pre-1900 birds that might be of purer strain. But some warn that the outcome could prove disappointing. "I'm not convinced [Brisbin's birds] are wild," says Hanotte, who also has samples from the birds but has not yet published a sequence. "I think they are related to domestic birds in Southeast Asia." He and Larson believe that

ing whether it includes genes from domestic chickens. In the past 7 years, he and collaborators around the world have sampled blood from more than 200 birds belonging to the four types of jungle fowl, including more than 120 red jungle fowl, from Pakistan, Bangladesh, Indonesia, Vietnam, and China. Those from China's Hainan Island—which harbors a red jungle fowl population that has been largely isolated from domestic varieties—could prove particularly intriguing, Han says.

He and his colleagues have analyzed the birds' mitochondrial DNA as well as microsatellites: short, repeating sequences in the nuclear DNA that could reveal what parts of the chicken genome differ from that of the jungle fowl. Starting early next year, he hopes to analyze single-nucleotide polymorphisms in selected parts of the genome. "We won't be the first to do this with the red jungle fowl, but we will be the first to use this large number of samples," he says. Han wants to compare wild birds from a wide array of regions to see the larger picture of genetic change among the many subspecies in order to gauge the impact of



Breeding a better bird. Han oversees experiments at a livestock facility in Hanoi.

domestication on specific parts of the genome. "Jianlin's brute-force approach definitely has its merits," says archaeologist Greger Larson of Durham University in the United Kingdom. "I suspect we can't possibly know what all the variation is out there unless you go and sequence a ton of stuff." Geneticist Olivier Hanotte of the University of Nottingham in the United Kingdom agrees, though he adds that ultimately full-genome sequencing of the jungle fowl—a far larger, expensive, and complicated task—would provide more definitive answers. But no such grand plans are in the works at the moment.

Han is also curious about what happens when chickens go feral. Natural selection reasserts itself when humans no longer make breeding decisions or provide regular food and protection. "This will help us understand how the genome works, and how plastic it is," Han says. "This is the most fundamental biological question." The lowly chicken may one day provide humans with more than just a cheap joke or a fast meal.

—A.L.

introgression has been going on for millennia and that the search for a pure wild bird, even if the genetic material is more than a century old, may prove fruitless.

Chicken tracks

Ancient chicken bones could provide data that circumvent the complexities of today's birds. But information on the chicken's prehistory is remarkably scant. "Until 20 years ago, no one bothered to analyze chicken bones," says Melinda Zeder, an archaeozoologist at the Smithsonian Institution's National Museum of Natural History in Washington, D.C. "Finally, that is starting to change."

Larger species like sheep and goat left behind more evidence, and they were domesticated in the Middle East, an area closely studied by archaeologists. By contrast, chicken bones are hard to find and the birds were domesticated in a region largely untouched by excavators' spades. "The chicken has been woefully neglected," Larson says. He and others have begun to use fine-meshed sieves to recover even tiny bone fragments, an effort that is paying off, but only after many false starts.

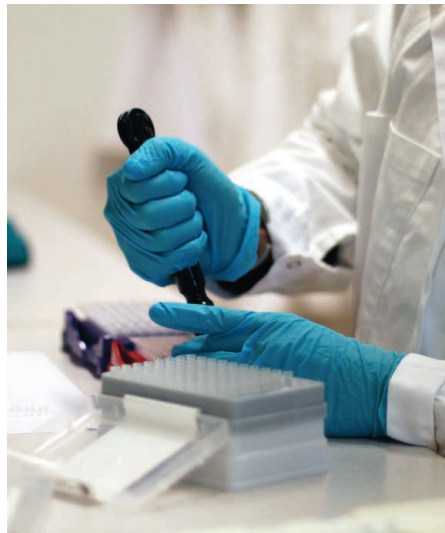
A stunning 1988 claim of very ancient domesticated chicken bones in central China, for example, implied that the bird was carried 2000 kilometers north of the jungle fowl's range as early as 6000 B.C.E. That suggested at least two centers of domestication, the Indian subcontinent and China. But these and many other bones have been seriously misdated, says paleozoologist Joris Peters of Ludwig Maximilian University of Munich in Germany. He has embarked on a laborious effort to ascer-



Early bird. This clay chicken figurine from Pakistan is one of the first solid signs of domesticated birds.

tain the age of ancient bird bones around the world, and his early conclusions offer a sobering lesson. "The problem with chicken bones is that they move around," Peters says. Small and lightweight, they easily slip lower in the soil—appearing to be older than they really are—and rodents and other animals can readily shift them around.

That appears to be the case with the Chinese chickens. After cursorily examining the evidence last year in Beijing, Peters says the bones more likely date to the settlement layer of the Han Dynasty—6 millennia later than claimed. By then, the chicken had already spread across both Asia and Europe. Although chicken bones may move around in sediment, they can be carbon-dated directly,



Hands-on. Geneticists around the world, including here at Uppsala University in Sweden, are tracking the mutations that created domesticated chickens.

and Peters is doing just that, starting with a collection of ancient Near Eastern and Greek bones. Preliminary results suggest they are centuries younger than once thought.

Ultimately, researchers hope to get ancient DNA from well-dated bones. But "replicable DNA has been as rare as hen's teeth," Zeder says, thanks to contamination issues and tropical climes that degrade DNA. One team recently claimed to have mtDNA from an ancient Polynesian chicken bone in Chile—a dramatic find that would prove Polynesians reached the Americas before Columbus—but the find has been questioned as possibly contaminated (*Science*, 11 June 2010, p. 1344). Techniques are improving, however. Larson hopes to sequence Thai bones dated to as early as 1500 B.C.E. It's a long shot, because the DNA is likely to have degraded in the humid Thai climate. "But we don't need a huge number of successes," he says. "Just one will tell us a lot."

Other genetic studies are beginning to identify traits involved in domestication. For example, a 2010 paper in *Nature* reported the sequence of more than 7 million SNPs in the genome of the chicken and the red jungle fowl. The team, led by Uppsala's Carl-Johan Rubin and including Andersson as a co-author, pinpointed a thyroid-stimulating hormone receptor that is shared by all domesticated birds but not the wild fowl, and presumably spurs growth. "This shows what traits were being selected" during domestication, says Wes Warren, a geneticist with Washington University in St. Louis.

But Hanotte notes that growing genetic evidence suggests small populations in the early phase of domestication, which may point to cockfighting as an initial driver rather than eggs and meat. Even today the red jungle fowl is known as a small but fierce fighter in South Asia. In Vietnam, for example, trapping the bird is an illegal but widespread practice. A single cock can net well over \$100.

Such pressures could soon render the truly wild bird extinct, if it is not already. That worries biologists, who note that conservationists don't have the jungle fowl on their radar. There is no guarantee that saving the red jungle fowl and its wild genes will pay off in the future, but they insist that it would be tragic to let the opportunity slip away. For Condon, the young biologist, the genetic information in truly wild fowl could kill two birds with one stone, unraveling the chicken's past while potentially ensuring its future. "This is the most important bird in the world," he says. "We need to preserve the original."

—ANDREW LAWLER

CREDITS (TOP TO BOTTOM): © J.M. KENOYER/HARAPPA.COM/COURTESY OF DEPT. OF PAKISTAN; PREYIA ISLAND (2)

Downloaded from www.sciencemag.org on November 23, 2012



PUBLIC HEALTH

Making Sense of a Senseless Act

Research from Asia is overturning long-held notions about the factors that drive people to commit suicide

SHANGHAI, CHINA—Mrs. Y's death would have stumped many experts. A young mother and loyal wife, the rural Chinese woman showed none of the standard risk factors for suicide. She was not apparently depressed or mentally ill. Villagers said she exuded happiness and voiced few complaints. But when a neighbor publicly accused Mrs. Y of stealing eggs from her henhouse, the shame was unbearable. Mrs. Y rushed home and downed a bottle of pesticide. "A person cannot live without face," she cried before she died. "I will die to prove that I did not steal her eggs."

Decades of research in Western countries have positioned mental illness as an overwhelming predictor of suicide, figuring in more than 90% of such deaths. Another big risk factor is gender: Men commit suicide at much higher rates than women, by a ratio of nearly 4 to 1 in the United States, according to the U.S. Centers for Disease Control and Prevention. Other common correlates include city life and divorce. But in China, says Jie Zhang, a sociologist at the State University of New York, Buffalo State, the case of Mrs. Y is "a very typical scenario."

Zhang oversaw interviews with Mrs. Y's family and acquaintances while researching the prevalence of mental illness among suicide victims aged 15 to 34 in rural China. Through psychological autopsies—detailed assessments after death—Zhang and co-authors found that only 48% of 392 victims had a mental illness, they reported in the July 2010 issue of the *American Journal of Psychiatry*. An earlier study of Chinese suicide

victims put the prevalence of mental disorders at 63%—still nowhere near as high as accepted models of suicide prevention would predict. Meanwhile, other standard risk factors simply don't hold true, or are even reversed, in China. Chinese women commit suicide at unusually high rates; rural residents kill themselves more frequently than city dwellers do; and marriage may make a person more, rather than less, volatile.

Such differences matter because China accounts for an estimated 22% of global suicides, or roughly 200,000 deaths every year. In India, meanwhile, some 187,000 people took their own lives in 2010—twice as many as died from HIV/AIDS. By comparison, the World Health Organization (WHO) estimates that suicides in high-income countries total only 140,000 a year. Suicide rates in Japan and South Korea, however, are similar to



Suicide sleuth. Sociologist Jie Zhang is investigating the roots of suicide in rural China.

Hidden scourge. Despite accounting for a sizable share of Asia's mortality burden, suicide has been overlooked.

China's (see p. 1026), suggesting that this is a regional public health issue. And yet suicide in Asia is poorly understood. "Suicide has not gotten the attention it deserves vis-à-vis its disease burden," says Prabhat Jha, director of the Centre for Global Health Research in Toronto, Canada.

Emerging research from developing countries like China and India is now filling that gap—and overturning prevailing notions. "The focus of the study of suicide in the West is psychiatry," Zhang says. While mental illness remains an important correlate in Asia, he says, researchers may learn more from a victim's family, religion, education, and personality. New findings, Zhang says, suggest that some researchers may have misread correlation as causation: In both the East and the West, "mental illness might not be the real cause of suicide."

Distressing data

Reliable data on suicide across Asia were once maddeningly scarce. In Thailand until 2003, there was no requirement that the reported cause of death be medically validated—a flaw that rendered the country's suicide data inaccurate. In India, suicide is a crime, which means it often goes unreported. But the Thai government now has a more accurate reporting system for mortality figures, while Indian researchers are benefiting from the Million Death Study, an effort to catalog causes of death for 1 million Indians in a 16-year survey relying on interviews with family members (*Science*, 15 June, p. 1372). The study has already produced a disturbing revelation about reported suicide rates. "When we compare our data with police reports, you find undercounts of at least 25% in men and 36% in women," says Jha, the study's lead investigator.

New insights from China are particularly instructive. Because suicide carries a stigma, the Chinese government withheld data on the topic until the late 1980s. When information finally came out, it quickly became clear that the country had a serious problem. In 1990, for example, the World Bank's Global Burden of Disease Study estimated there were 343,000 suicides in China—or 30 per 100,000 people. The U.S. rate for the same year was 12 per 100,000.

But other reports gave different figures, prompting a debate on sources. WHO's extrapolated total was based on data that China had reported from stations covering



Korea Tackles a Mushrooming Problem

After a popular South Korean actress hung herself on 2 October 2008, news reports included lurid details about the act. Choi Jin-sil became a grim role model: Suicides jumped 66% in South Korea that month and continued at high rates for months. Young hanging victims accounted for most of the increase.

In the gloomy realm of suicide research, South Korea stands out. "Korea is unusual in the high number of young women killing themselves," says Ha Kyooseb, a psychiatrist at Seoul National University. Another eye-catching pattern is a high suicide rate among the elderly. But perhaps the most alarming feature about the trend is how quickly the suicide rate has accelerated, from fewer than 10 suicide deaths per 100,000 people in 1990 to 31.2 per

Words of encouragement.

A statue offers a message of hope on Seoul's Mapo Bridge, a notorious spot for suicide attempts.

100,000 in 2010—the world's second-highest rate after Lithuania and nearly triple the average of advanced industrialized nations. Suicide leapt from the 10th most frequent cause of death in South Korea to fourth; it is now the leading killer of those aged 10 to 39.

"Nobody knows the exact cause of the surge in suicide in Korea," says Park Jong-Ik, a psychiatrist at Kangwon National University in Chuncheon. But there are hints that rapid socioeconomic changes, a burgeoning elderly population, and cultural influences all play roles, both in South Korea and elsewhere in the region. For example, China and India also have high rates of suicide among young women. And, as in South Korea, suicide rates rose sharply as economies grew in Japan, Hong Kong, and Taiwan. With neighbors facing similar challenges, "there may be something that could be learned" from the South Korean experience, says Wang Xiangdong, a psychiatrist who heads mental health efforts for the World Health Organization's Western Pacific office in Manila.

Research on suicides in the West may not shed much light on the Asian experience (see p. 1025). In North America and Europe, men take their own lives two to three times more often than women do. But in South Korea, suicide rates of men and women in their 20s and 30s are nearly the same. Ha blames this on the popularity of hanging, which more often results in death than

only 10% of the population, skewed toward urban residents. As researchers focused on the problem, they arrived at more reliable figures—but also unearthed more mysteries. In an analysis in *The Lancet* in 2002, a group led by Michael Phillips of Shanghai Mental Health Center and Emory University School of Medicine in Atlanta estimated that from 1995 to 1999, Chinese women killed themselves more frequently than men—by a ratio of 5 to 4. "There was originally disbelief about the very different gender ratio in China," Phillips says, although later it was accepted.

Today, the suicide sex ratio in China is roughly 1 to 1, still a significant departure from the overall U.S. male-to-female ratio of 4 to 1. In India, the male-to-female suicide ratio is 1.5 to 1, although in the 15 to 29 age group it is close to equal. And yet, WHO estimates the global sex ratio at three men to one woman. (With colleague Cheng Hui, Phillips recently used Chinese and Indian figures to lower that estimate to 1.67 to 1.) Among young adults in India, suicide is second only to maternal mortality as a cause of death for women, according to the Million Death Survey.

In both China and India, cases like Mrs. Y's involving no apparent mental illness are common. In India, suicide is most prevalent among teenagers and young adults—the cohort that is entering the workforce, marrying, and facing new life stresses. This contrasts with the Western pattern of high suicide rates among the middle-aged, suggesting that although "there might well be some underlying psychiatric conditions, the main drivers of [suicide in India] are probably chiefly

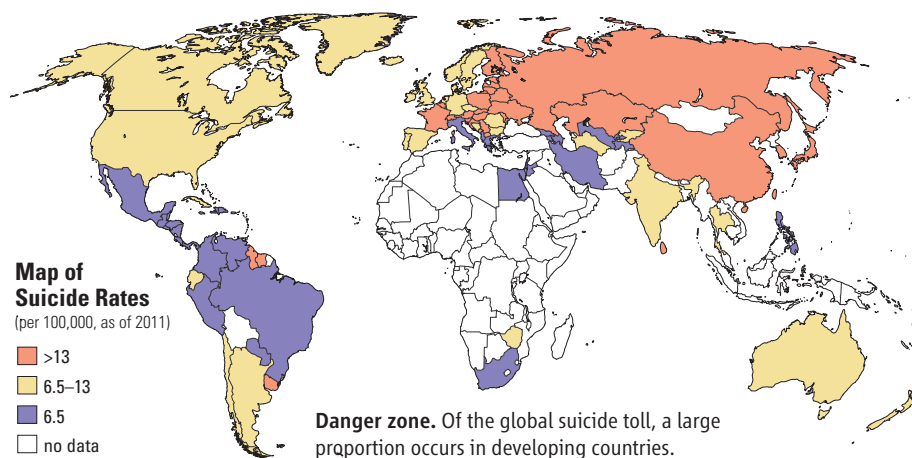
social conditions," Jha says. While cautioning that detailed psychological autopsies are still needed in India, he says, "it's a reasonable assumption that many of these young folks are not mentally ill."

Convincing researchers outside Asia may prove an uphill battle. Matthew Miller, a suicide researcher at the Harvard Injury Control Research Center in Boston, says that mental illness may be underdiagnosed in Asia for reasons that aren't fully understood. That could

victims, he adds, are "most certainly severely distressed, but they don't meet the criteria of a formal mental illness."

Lethal weapons

Assuming that suicide risk is shaped by different factors in Asia, researchers are striving to uncover the roots. One clue may lie in the high proportion of unplanned Chinese suicides. In a 2002 survey of 306 Chinese patients who had been hospitalized for at least 6 hours follow-



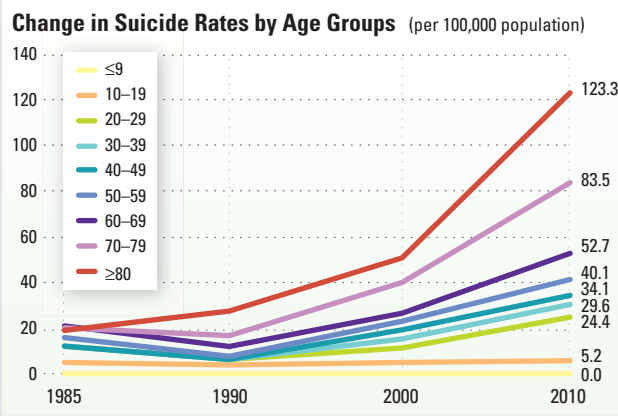
throw off correlation studies. Phillips, who has worked in China for over 20 years, agrees that underdiagnosis is a problem, and that "many Western researchers still believe that we are just missing cases." But he rejects that explanation. Even accounting for underdiagnosis, he says, the finding of a lower rate of mental illness among suicide victims has held up in multiple studies. Many Chinese suicide

ing a suicide attempt, Phillips and colleagues found that 35% had contemplated suicide for less than 10 minutes—and 54% for less than 2 hours. Impulsiveness among suicide victims in Asia "tends to be higher than in the West," says Paul Yip, director of the Hong Kong Jockey Club Centre for Suicide Research and Prevention at the University of Hong Kong and one of the authors of a recent WHO report on

wrist-slashing or pill overdoses—the preferred methods of women in the West. Ha believes that hanging is common because it has been used by most of the dozen or so entertainers who have killed themselves in the last decade.

A particularly disturbing trend in South Korea is the rise of suicides among the elderly (see graph). It coincides with the disintegration of support networks in rural areas as young people flock to the cities. Rural South Koreans who want to do away with themselves have ready access to pesticides. Last December, the government banned sales of Gramoxone, one of the most lethal pesticides. That could halve the roughly 3000 deaths each year attributed to pesticides, Ha says.

In addition to mental illness, South Koreans and even police statistics cite job loss, financial difficulty, academic pressure, and physical illness as factors behind suicides. Ha, however, wanted to base interventions on better evidence, so in 2010 he organized the country's first professional survey of suicide-attempt survivors. It revealed that mental illnesses, particularly depression, accounted for about one-third of unsuccessful suicide attempts. In the



Worrisome trend. Suicide rates in South Korea have risen in all age groups, but most alarmingly among the elderly.

other two-thirds, the most commonly cited reason for attempting suicide was interpersonal conflict: children at odds with parents or teachers, school bullying, and failed relationships. In a pilot program, psychiatric nurses contact survivors during the year after a suicide attempt, a step that Ha believes has cut the rate of second

attempts. To deter copycats, the media has been urged to cover celebrity suicides with restraint. And earlier this year, the government established the Korea Suicide Prevention Center to gather data and develop intervention programs.

Wang says other countries should pay heed and address suicide before it becomes a major societal problem. Given the complexity of the factors underlying suicide, he says, a community-wide response should emphasize a simple message: Suicide is preventable.

—DENNIS NORMILE

suicide in Asia. Although impulsive personality traits are sometimes linked to illnesses like bipolar disorder, studies in China have not uncovered full-fledged personality disorders in impulsive suicide victims.

In a tragic twist, impulsive victims in Asia tend to favor highly fatal methods. After interviewing family members and friends of 505 Chinese suicide victims, Kenneth Conner, a psychiatric researcher at the University of Rochester Medical Center in New York, and colleagues reported in 2005 that those who had ingested pesticides were more likely to have acted rashly than were those who used other methods such as hanging or drowning. Pesticides are a leading cause of suicide death in China and India, and the cause of roughly half of suicides worldwide. Pesticides may also explain Asia's unusual suicide sex ratio, Jha says. In the West, women attempt suicide just as frequently as men do, but they tend to down sleeping pills—and often survive.

The trends in Asia point to a need for innovative prevention strategies. Zhang believes efforts should focus less on mental illness and more on “educating people to have realistic goals in life and teaching them to cope with crisis.” Front and center should be universities and rural women's organizations, both of which already have active suicide prevention programs in China, he says. Such community-based approaches appear to have been effective in Hong Kong, Yip says. Over the past decade, the territory has rolled out programs for schoolchildren on dealing with stress and outreach groups for older adults. Its suicide rate has fallen 27% since 2003.

But resources in many Asian countries are limited. The vast majority of cities in China and India still do not have 24-hour suicide prevention hotlines. That may make what scholars call means restriction—reducing access to tools commonly used in suicide—a better goal. In Sri Lanka, pesticides once accounted for two-thirds of suicide deaths. Then in 1995, the government took steps to ban the most toxic pesticides. The suicide rate plummeted by 50% in the following decade.



Mortality review. India's Million Death Study has given researchers a more accurate suicide rate.

The varying degrees to which mental illness and suicide correlate in East and West may ultimately be beside the point, argues Zhang, who believes a third factor may be the trigger in both regions. Strain theory, which posits that societal pressures, rather than inborn traits, contribute to crime, can help explain suicide, he believes. “Psychological strains usually precede a suicidal behavior, and they also happen before an individual becomes mentally ill.”

When a person is pulled by two or more conflicting pressures, Zhang says, as with “a girl who receives Confucian values at home and then goes to school and learns about modern values and gender equality,” she may be more prone to suicide. Other situational stresses may include a sudden crisis faced by a rural woman lacking coping mechanisms—such as the case of Mrs. Y—or an incident that forces a young man to confront a gap between his aspirations and reality. Zhang found that strain theory held up for his study subjects in rural China. He plans to probe whether it also applies to older Chinese.

Ultimately, Zhang hopes to test strain theory on Americans. The U.S. National Institutes of Health “spends millions and millions of dollars every year on treating mental illness to prevent suicide,” he says. “But no matter how much money we spend, how many psychiatrists we train, or how much work we do in psychiatric clinics, the U.S. suicide rate doesn't decrease.” It has hovered around 10 to 12 suicides per 100,000 people since 1960.

Such research may be the tip of the iceberg when it comes to debunking long-held ideas about behavior disorders. Alcoholism is another area ripe for exploration, Cheng says: The profile of alcoholics in China contrasts sharply with that in the West. Because of social pressure to drink, Chinese alcoholics are far more likely to be working and married than American counterparts, who are often unemployed and divorced, she says. Suicide, Cheng muses, “is just another example of how environment can change behavior.”

—MARA HVISTENDAHL



LETTERS

edited by Jennifer Sills

Barry Commoner's Place in History

THE BRIEF ANNOUNCEMENT ON THESE PAGES OF DR. BARRY COMMONER'S PASSING ECHOED those of mainstream media outlets, which lauded his work in environmental politics ("Early leader of environmental movement dies," *News of the Week*, 5 October, p. 23). More important, Commoner's life in science offers a crucial perspective on the development of science and public life through the 20th century.



Barry Commoner.

In addition to receiving the 1953 Newcomb Cleveland Prize for his work on the tobacco mosaic virus (1) and conducting groundbreaking work on free radicals (2), Commoner was at the vanguard of the science information movement, an early effort to promote science literacy and to engage the public in the importance of science to public life and policy. Commoner sought to stress that the scientist's primary obligation was to society, and he practiced that belief in his professional work. He worked tirelessly through the 1950s to affirm AAAS's integrity and relevance. As early as 1953, Warren Weaver recruited him to revitalize the society's examination of science's social integration (3). He became a member of the Social Aspects of Science Committee and subsequently chaired the Committee on Science in the Promotion of Human Welfare. During the 1955 conference in segregated Atlanta, Commoner worked as a catalyst with former AAAS president Detlev Bronk and Margaret Mead to push for a AAAS Council anti-segregation resolution (4).

Commoner was prominently involved in raising public awareness about the threats inherent in nuclear fallout. Linus Pauling's 1957 petition to the United Nations to end nuclear weapons testing (5) was drafted in Commoner's office at Washington University in St. Louis. In addition, Commoner helped to direct the Greater St. Louis Committee for Nuclear Information, whose studies on strontium-90 absorption by primary teeth were reported in *Science* (6). This work was cited by President Lyndon Johnson as an important influence for the decision to ban above-ground nuclear weapons testing (7).

Commoner would later claim that his efforts to stop nuclear weapons testing made him an environmentalist. He dedicated his career to promoting greater awareness of the risks to public health derived from certain industrial practices, and remained an outspoken critic of both

the petrochemical and nuclear industries. In 1966, he founded the Center for the Biology of Natural Systems, which continues to work at the intersections of science and policy to advocate more environmentally sustainable solutions to continuing pollution and health-related problems. This work remained consistent with his early devotion to informing the public, providing them with an accessible vernacular body of scientific information on the environmental crisis.

Commoner's Four Laws of Ecology (8) (everything is connected to everything else, everything must go somewhere, nature knows best, and there is no such thing as a free lunch) are perhaps of more social consequence than scientific, but by the 1970s Commoner was—as *TIME* magazine rightly observed—a scientist "with a classroom of millions" (9). His life and career constitute a model for science activism and social engagement. He should be remembered for his deep-seated belief in the scientist's social responsibility, his duty to the public, and his unwavering faith in an informed citizenry.

MICHAEL EGAN

Department of History, McMaster University, Hamilton, ON L8S 4L9, Canada. E-mail: egan@mcmaster.ca

References

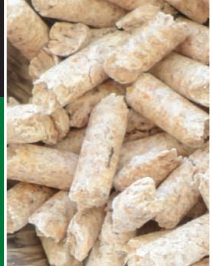
1. About AAAS, History & Archives, Barry Commoner (http://archives.aaas.org/people.php?p_id=460).
2. B. Commoner, *Nature* **174**, 689 (1954).
3. M. Egan, *Barry Commoner and the Science of Survival: The Remaking of American Environmentalism* (Massachusetts Institute of Technology, Cambridge, MA, 2007).
4. About AAAS, History & Archives, AAAS: AAAS Annual Meetings and Freedom from Racial Segregation (http://archives.aaas.org/docs/resolutions.php?doc_id=249).
5. Linus Pauling and the International Peace Movement, The Right to Petition (<http://osulibrary.oregonstate.edu/specialcollections/coll/pauling/peace/narrative/page27.html>).
6. L. Z. Reiss, *Science* **134**, 1669 (1961).
7. L. Johnson, Televised Address, 12 October 1964.
8. B. Commoner, *The Closing Circle: Nature, Man, and Technology* (Knopf, New York, 1971).
9. *TIME*, "Environment: Paul Revere of ecology" (2 February 1970); www.time.com/time/magazine/article/0,9171,878180,00.html.

Climate Change–Induced Salinity Threatens Health

SEA-LEVEL RISE, STORM SURGES, AND cyclones exacerbated by climate change have begun to severely affect coasts and river estuaries in low-income countries. The resulting increased salinity in soil and drinking water has health implications for large populations.

Letters to the Editor

Letters (~300 words) discuss material published in *Science* in the past 3 months or matters of general interest. Letters are not acknowledged upon receipt. Whether published in full or in part, Letters are subject to editing for clarity and space. Letters submitted, published, or posted elsewhere, in print or online, will be disqualified. To submit a Letter, go to www.submit2science.org.



The value
of biochar

1034



Cell of origin
and cancer

1035

In coastal Bangladesh, natural drinking water sources such as rivers and groundwater are threatened by saltwater intrusion from the Bay of Bengal (1). The U.S. Environmental Protection Agency's recommended water sodium level for human consumption is 0.02 parts per thousand (ppt), and the World Health Organization's drinking water standard, above which sodium may affect the taste of drinking water, is 0.2 ppt. However, river salinity in some southwest coastal districts of Bangladesh reaches as high as 4 ppt in the rainy season and 13 ppt in the dry season (2).

The increased salinity in drinking water will likely affect health over the long term. Excreting more than 100 mmol/day of sodium over a 30-year period is associated with an increase in systolic blood pressure by 3.1 to 6.0 millimeters of mercury (mmHg) and in diastolic blood pressure by 0.1 to 2.5 mmHg in an average man or woman of 20 to 59 years (3). In a coastal Bangladeshi rural population, the mean urinary sodium excretion among healthy pregnant women in 2011 was 170 mmol/day of sodium (2), twice the recommended level (4). Extrapolating forward 30 years, this level of sodium will significantly increase systolic and diastolic blood pressure, potentially leading to a substantial rise in cases of hypertension, as well as other associated health problems. Indirect estimates of salinity are available

for other areas, such as the Pearl River Delta, China (5); the San Joaquin Delta, California (6); and in the Netherlands (7), Australia (8), and Brazil (9). These estimates show that salinity may be an increasing problem in a number of coastal areas affected by intrusion of salty water into rivers.

To mitigate the risk of high blood pressure, cardiovascular disease, and other associated health problems caused by climate change-induced salt intrusions, we must take immediate action. Adaptation measures, including rainwater harvesting and solar distillation, require coordination among governments and nongovernmental organizations. Putting these prevention plans in place will be far less expensive than treating the disease that will occur later if salt intrusions continue unabated.

PAOLO VINEIS* AND ANEIRE KHAN

MRC-HPA Centre for Environment and Health, Imperial College, London, SW7 2AZ, UK.

*To whom correspondence should be addressed. E-mail: p.vineis@imperial.ac.uk

References

1. M. L. Parry, O. F. Canziani, J. P. Palutikof, P. J. van der Linden, C. E. Hanson, Eds., *Climate Change 2007: Impacts, Adaptation and Vulnerability. Contribution of Working Group II to the Fourth Assessment Report of the Intergovernmental Panel on Climate Change* (Cambridge Univ. Press, Cambridge, 2007).
2. A. E. Khan *et al.*, *Environ. Health Perspect.* **119**, 1328 (2011).

CORRECTIONS AND CLARIFICATIONS

Reports: "Corals chemically cue mutualistic fishes to remove competing seaweeds" by D. L. Dixon and M. E. Hay (9 November, p. 804). The genus and species names of the goby were spelled incorrectly in the abstract. The correct names are used throughout the Report *Gobiodon histrio* and *Paragobiodon echinocephalus*. The names have been corrected in the HTML and PDF versions online.

Perspectives: "Quantum procrastination" by S. Lloyd (2 November, p. 621). In references 1 and 2, the year should be 2012, not 2007. The PDF and HTML versions online have been corrected.

Table of Contents: (26 October, p. 433). On page 435, the title of the Report by J. L. Garrison *et al.* was incorrect. The correct title is "Oxytocin/vasopressin-related peptides have an ancient role in reproductive behavior." The title is correct online.

Review: "Anticipating critical transitions" by M. Scheffer *et al.* (19 October, p. 344). In the print article, reference 44 was incorrect and reference 45 was mistakenly omitted. Reference 44 should be: T. M. Lenton, V. N. Livina, V. Dakos, E. H. van Nes, M. Scheffer, *Philos. Trans. R. Soc. London Ser. A* **370**, 1185 (2012). Reference 45 should be: J. M. T. Thompson, J. Sieber, *IMA J. Appl. Math.* **76**, 27 (2011). The references are correct in the HTML version online.

News & Analysis: "Oh, baby: Fight brews over U.S. import of beluga whales" by E. Underwood (12 October p. 180). The last request to the U.S. government for a permit to import wild-caught cetaceans was in 1993, not 1988.

News & Analysis: "Calling all baby boomers: Get your hepatitis C test" by J. Cohen (24 August, p. 903). The article incorrectly stated that the hepatitis C test was first introduced in 1992. The first test was licensed in 1990. In 1992, a much improved test came to market.

3. P. Elliott *et al.*, *Br. Med. J.* **312**, 1249 (1996).
4. World Health Organization/Food and Agriculture Organization, "Diet, nutrition, and the prevention of chronic diseases: Report of a joint WHO/FAO expert consultation" (Technical Report Series 916, World Health Organization, Geneva, 2003).
5. Xinhua News Agency, "Salt Tide in Pearl River Estuary Receding" (March, 2006).
6. W. Fleenor, E. Hanak, J. Lund, J. Mount, "Delta Hydrodynamics and Water Salinity with Future Conditions: Technical Appendix C" (Public Policy Institute of California, San Francisco, 2008).
7. M. Bonte, J. J. Zwolsman, *Water Res.* **44**, 4411 (2010).
8. S. K. Merz, "Evaluation of salinity outcomes of regional investment" (Department of the Environment and Heritage and Department of Agriculture, Fisheries and Forestry, Australian Government, 2006).
9. A. M. Medeiros, J. E. Barbosa, P. R. Medeiros, R. M. Rocha, L. F. Silva, *Braz. J. Biol.* **70**, 551 (2010).

Journals: Increase Revisions, Not Rejections

IN THEIR REPORT "FLOWS OF RESEARCH manuscripts among scientific journals reveal hidden submission patterns" (this issue, p. 1065; published online 11 October), V. Calcagno *et al.* discuss an enlightening and unexpected finding about the path that manuscripts often follow in the publication process. Among other insights, they show that previously rejected manuscripts that are submitted to other journals ultimately receive more citations, once published, than papers in the same journal that were not previously rejected. In light of this result, a feature on this Report in *Nature* (1) quotes physicist Michael Schreiber from the Technical University of Chemnitz in Germany, who suggests that journal editors should reject more manuscripts because that improves their citation count. I argue that editors should do the opposite to improve their own journal's citation impact.

According to Calcagno *et al.*'s findings, rejecting to improve the quality of papers, as suggested by the *Nature* article (1), will not directly benefit the journal that rejects the paper. Journal editors could increase the quality of papers published in their own journals by exacting more rigorous standards for revision without rejecting them. Providing authors more opportunities to revise and resubmit manuscripts following peer review, while being clear to authors that substantial improvement must be made before a final decision is reached, would increase the citation impact of an editor's own journal.

E. KEITH BOWERS

Behavior, Ecology, Evolution, and Systematics Section, School of Biological Sciences, Illinois State University, Normal, IL 61761, USA. E-mail: ekbowers@ilstu.edu

Reference

1. P. Ball, *Nature News* (11 October 2012); 10.1038/nature.2012.11583.

ECOLOGY AND MEDICINE

On the Origins of Zoonoses

Daniel G. Streicker¹ and Amy B. Pedersen²

Imagine being asked in a job interview: When was the last time you stalked a gorilla with a tranquilizer dart in the Congo, caught a giant fruit bat atop a building in Malaysia, or even trapped a mouse in New England? Would it bother you if the point of handling these animals was to find pathogens that, if present, could kill you? And did we mention that there might be political unrest, civil war, and farmed rats for dinner? These are not questions that often yield long lines of volunteers, but David Quammen's book *Spillover* argues if we are going to save ourselves from new infectious diseases that spill over from non-human animals into people and threaten our existence, maybe they should.

However, *Spillover* is not your typi-



Crucial studies. The detection of the zoonotic origins of emerging diseases depends on long-term field investigations of wild animals such as chimpanzees.

cal sensationalist scare-a-thon about new deadly viruses that will turn us all into goo. Instead, it chronicles Quammen's 6-year, global exploration of the origins of new diseases, which led him from remote forests to sophisticated laboratories. The book hybridizes the rigor of an investigative report with the suspense of a mystery novel, making for a page-turner that will have readers pondering the answers before the questions are even raised. Through a series of interconnected case studies of disease emergence, Quammen describes a remarkable breadth

of epidemiological and evolutionary concepts, from the basic reproductive number (R_0) and phylogenetic inference to immunology and viral replication. The author accomplishes much through clever and insightful analogies: antibody assays are "like splashing holy water at a witch" and DNA sequence analysis makes sense of long runs of nucleotides "strung out in unpronounceable streaks as though typed by a manic chimpanzee."

Quammen introduces an eclectic mix of field and laboratory adventurers, who range from "judiciously empirical" to "jumping around" ... [with] insane jubilation" but are all driven by a common unquenchable curiosity. His scientists dress like rock stars, stake out monkeys in temples, and sneak beers into federal laboratories for quarantined colleagues. Even historical figures, previously known to most of us only from textbooks and their eponymous equations, come to life through vivid storytelling. For example, Ronald Ross, discoverer of the malaria transmission cycle and a pioneer in the application of mathematics to epidemics, also "wrote poetry, plays, music, [and] bad novels." These tales diversify our concepts of scientists and demystify the scientific process (showing it is not solely theory and experiments but also trial and error, dedication, and, sometimes, serendipity).

The book diverges from earlier popular science presentations of emerging human diseases [e.g., (1)] by defining infectious disease in ecological terms: a natural interspecific interaction, analogous to "what lions do to wildebeests and zebras, or what owls do to mice." Pathogens emerge when "[e]cological circumstance provides opportunity" and evolution seizes it and "helps convert spill-overs to pandemics." Moreover, Quammen accurately points out that emergence is not simply something that happens to us as guiltless victims but often a response to human activities such as agricultural intensification and ever-increasing encroachment into forests. Concisely: "Shake a tree, and things fall out."

Surprisingly, despite the ecological definition of parasitism as antagonistic, on the

notoriously challenging topic of zoonotic origins (2) *Spillover* echoes the conventional biomedical wisdom that a reservoir "carries the pathogen, harbors it chronically, while suffering little or no illness," as ancient host-parasite associations should evolve to become benign. Yet, ecological and evolutionary theory and numerous well-studied diseases (e.g., polio, measles, malaria, rabies, brucellosis, *Cordyceps*, and anther smut) show that pathogens often harm their hosts owing to trade-offs between transmission and

virulence (3, 4). Especially when mortality isn't dramatic, detecting it in wild animal populations is a serious endeavor, as illustrated best by Quammen's case study of simian immunodeficiency virus in chimpanzees. There, it took years of detailed field observations, linked to infection status and pathology, to reveal the 10- to 16-fold

greater mortality and numerous sublethal effects from the presumably harmless chimpanzee virus that seeded the HIV pandemic (5). Such longitudinal studies of disease in zoonotic reservoirs remain exceptional, so it is perhaps not surprising that a dead mouse underground or a sick bat in a cave might go unnoticed; just because something is hard to see doesn't mean it's not happening. In the end, some pathogens cause severe disease in their reservoirs while others do not, so this criterion may not tell us much when it comes to discovering the origin of zoonoses.

Regardless of any shortcomings, the book is a remarkable achievement born of tenacious investigation and masterful writing. Quammen's account firmly establishes emerging infectious diseases as the realm of not only physicians, veterinarians, and public health workers but also ecologists and evolutionary biologists. If integrating these historically disparate fields is our main hope for combating new pandemics, *Spillover* will undoubtedly help inspire a new generation of scientists to achieve a holistic vision of pathogen emergence.

References

1. L. Garrett, *The Coming Plague* (Farrar, Straus and Giroux, New York, 1994).
2. D. T. Haydon, S. Cleaveland, L. H. Taylor, M. K. Laurenson, *Emerg. Infect. Dis.* **8**, 1468 (2002).
3. R. M. Anderson, R. M. May, *Infectious Diseases of Humans: Dynamics and Control* (Oxford Univ. Press, Oxford, 1991).
4. J. C. de Roode, A. J. Yates, S. Altizer, *Proc. Natl. Acad. Sci. U.S.A.* **105**, 7489 (2008).
5. B. F. Keele et al., *Nature* **460**, 515 (2009).

10.1126/science.1230791

¹Odum School of Ecology, University of Georgia, Athens, GA 30603, USA. E-mail: dstrike@uga.edu. ²Centre for Immunity, Infection, and Evolution, University of Edinburgh, Edinburgh EH9 3JT, UK. E-mail: amy.pedersen@ed.ac.uk

RESEARCH FUNDING

The Contribution of Private Industry to Agricultural Innovation

Led by seed biotechnology, private-sector spending in agricultural R&D grew 43% from 1994 to 2010.

Keith Fuglie,¹ Paul Heisey,¹ John King,² Carl E. Pray,³ David Schimmelpennig^{1*}

Most of the increase in global agricultural production over the past half-century has come from raising crop and livestock yields rather than through area expansion. This growth in productivity is attributed largely to investments in research and innovation (1). Since around 1990, there has been a decline in the rate of growth in yield per area harvested for several important crops (2). In parallel, the rate of growth in public spending on agricultural research and development (R&D) has also fallen, which may account for declining crop yield growth and may be contributing to rising food prices (3).

Absent from this picture has been the role of the private sector in contributing innovations for food and agriculture. There is evidence that innovations in some manufacturing industries (machinery and chemicals, especially) have benefited agriculture (4) but little systematic evidence on the level and trend in private-sector R&D investments targeting applications to the agricultural sector (5). There is little quantitative evidence of private R&D's contribution to agricultural productivity. Our understanding of how different factors may induce or hinder incentives for private R&D—like government investments in public research and policies concerning intellectual property (IP), taxes, and regulations—is limited by the lack of data.

To fill in this data gap, we surveyed global agricultural R&D investment by industries supplying inputs to agriculture, as well as R&D in biofuel and food manufacturing (6). We present some results of this survey and preliminary analysis of causes and implications of the observed growth in private R&D.

Private R&D Growing Faster than Public

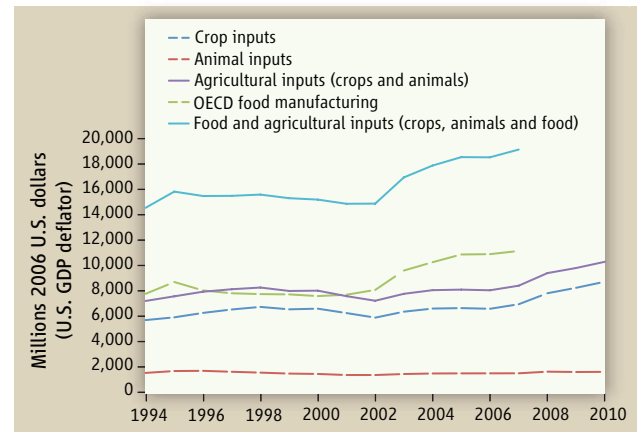
Between 1981 and 2000, the absolute increase in private-sector spending on food and agriculture research in the Organization for Economic Cooperation and Development

(OECD) countries, where the majority of private research has taken place, was nearly three times as great as the increase in real public-sector research; by 2000, 54% of total food and agricultural R&D in OECD countries and 39% globally was private (7). These estimates do not break out food manufacturing from agriculturally related R&D, and the relevance of this for the agricultural sector is not clear. From more detailed information available for the

United States, only about half appears to be agriculturally related, with food manufacturing research focused primarily on the development of new consumer food products (8).

Our survey provides 1994–2010 annual estimates of global private R&D in seven industries supplying agricultural inputs to farms, as well as the food manufacturing industry through 2007 and the biofuel industry for 2009 (6). World inflation-adjusted R&D spending in the seven agricultural input industries combined increased by 43% between 1994 and 2010 (6). All of this growth, however, occurred in industries supplying inputs for crop production, led by the seed-biotechnology and farm machinery industries, whereas R&D related to livestock remained essentially unchanged (see the first chart).

Global private investment in food manufacturing research was U.S. \$11.5 billion in 2007 and in agricultural input research was \$11.0 billion in 2010 (with \$8.7 billion of this oriented to crops). Within the agricultural input industries, there have been striking changes in the composition of research investment. This is best illustrated for the United States, which accounts for a little over one-third of global private agricultural input research. In the 1960s and 1970s, agricultural chemicals and farm machinery dominated private agricultural R&D; as late as 1980, these two sectors accounted for more than three-fourths of the total (6). In the 1980s and



Global private investment in food and agricultural input research. For 1994–2010; see (6) for data and methods.

1990s, private investment in crop-related seed and biotechnology research began to grow rapidly and, by 1998, surpassed other industries' agricultural R&D spending (see the second chart) (6). For the United States and globally, private R&D spending on crop seed and biotechnology grew rapidly in the 1990s; leveled off in real terms from the late 1990s until about 2005; then accelerated again, reaching \$3.7 billion by 2010.

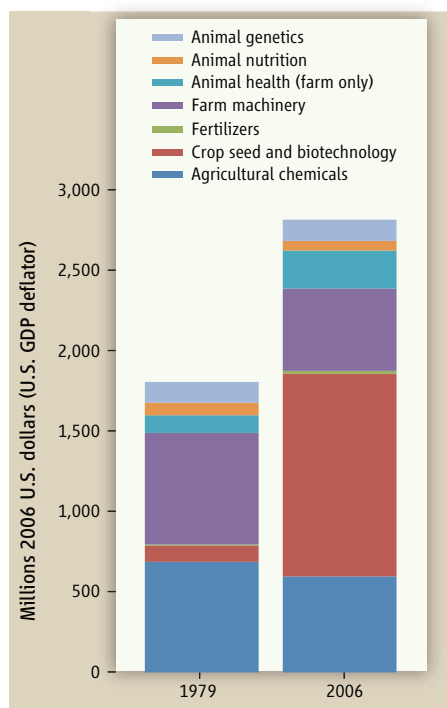
In recent years, research into biofuels, a new agriculturally related research area, has become increasingly important. In 2009, private companies spent ~\$1.47 billion on biofuels-related research globally. More than 75% of these expenditures were in the energy sector, but about \$340 million was spent by crop seed–biotechnology companies to improve biofuel feedstocks (9).

Drivers of Private R&D

Factors influencing returns to investment in R&D by private, for-profit firms include market size, technological opportunity, appropriability (the ability of firms to appropriate economic benefits of research), and costs of R&D inputs (10). Across agricultural input industries, market size does not appear to be a good predictor of the amount of R&D invested, as research intensity (research spending as a percentage of net sales) varies widely, from 10.5% in seeds to 0.25% in fertilizers. Research intensity within each industry, how-

¹Economic Research Service, U.S. Department of Agriculture (USDA), Washington, DC 20472, USA. ²Office of the Chief Scientist, USDA, Washington, DC 20250, USA. ³Rutgers, The State University of New Jersey, New Brunswick, NJ 08901, USA.

*Author for correspondence. E-mail: des@ers.usda.gov.



Private agricultural input research in the United States. For 1979 and 2006; see (6) for data and methods.

ever, has remained fairly constant over time. Thus, for some industries in which sales have grown rapidly, e.g., the seed industry, R&D also has grown rapidly.

Advances in molecular genetics opened up new technological opportunities in biotechnology and, together with strengthened patent protection over biological inventions (one form of appropriability), stimulated growth in private-sector investment in crop improvement. The public sector, through research at universities, national laboratories, and international centers, contributed to this process by developing improved genetic resources, genomic information, and molecular tools (11, 12). Universities have also contributed to private research through training the science and technology (S&T) workforce. A larger supply of S&T workers reduces R&D input costs for private firms, raising returns to their R&D investments.

Although, in most industrialized countries, patent protection has been available for mechanical, chemical, and pharmaceutical inventions for a century or more, patent protection for biological inventions has been more recent and gradual, beginning in the United States only in 1980 (13, 14). Most countries now provide patent protection for novel biological organisms and plant breeder's rights for novel plant varieties—provisos for membership in the World Trade Organization. Plant breeder's rights offer considerably

weaker IP protection than patents, and some countries have begun to offer patent protection for novel plant varieties as well. This strengthening of patent protection increased appropriability for private firms and likely induced more agricultural R&D.

More stringent environmental and safety regulations have also exerted influence on food and agricultural R&D. Regulations on new chemical and biotechnologies may have increased overall R&D spending by firms in order to meet these requirements but may have diminished rates of innovation, as a larger proportion of R&D funds was redirected from discovery research (15–17). In addition, regulations may create barriers to entry for new firms. In crop biotechnology, high fixed costs and long time lags in meeting regulatory requirements reduce incentives for private firms to develop new traits for small, heterogeneous markets, such as horticulture (18).

Implications

Growth of private R&D spending for agriculture in the face of slowing or stagnant public R&D resources raises the question of whether private R&D can substitute for public R&D. If so, long-term productivity growth in agriculture may be maintained or revived even as public R&D spending wanes. However, to the extent that technology opportunities created through basic research and the training of the S&T labor force are largely public-sector functions, reduced public-sector capacity may eventually reduce returns to private R&D as well and lead to lower aggregate investments in innovation (19–21). In addition, agricultural biotechnology may need public investment to achieve wide international dissemination, especially in poor countries with limited IP or regulatory capacity (22).

Another issue is whether the concentration in agricultural input industries may have adverse consequences for market performance. In several input industries, a few firms dominate global market sales, account for most of the industry R&D spending, and hold large patent portfolios. These factors may be creating possibly major barriers to entry of new firms and may be limiting market competition (23).

Not only is private agricultural input R&D concentrated among a few firms, it also appears to be focused on fewer commodities, technologies, and markets than public R&D (24). Areas that the private sector has avoided are generally those where profitable opportunities are perceived to be low. However, private R&D appears to be responsive to changing technological opportunities

when market and regulatory conditions are favorable, as evidenced by the rapid growth in crop biotechnology and biofuel R&D. Policies to strengthen IP, streamline regulatory procedures, and offer favorable tax treatment for R&D investment can encourage private investment in agricultural innovation. However, lack of sufficient market competition or barriers to entry by new firms could constrain the potential contribution of industry to agriculture.

References and Notes

1. J. Piesse, C. Thirtle, *Philos. Trans. R. Soc. London Ser. B* **365**, 3035 (2010).
2. World Bank, World development report 2008: Agriculture for development (World Bank, Washington, DC, 2007).
3. J. M. Alston *et al.*, *Science* **325**, 1209 (2009).
4. C. E. Pray, K. Fuglie, D. K. N. Johnson, in *Handbook of Agricultural Economics*, R. Evenson, P. Pingali, Eds. (Elsevier, Amsterdam, 2007), vol. 3, chap. 49.
5. P. Pardey *et al.*, Agricultural research: A growing global divide? (Food Policy Report, International Food Policy Research Institute, Washington, DC, 2006).
6. K. Fuglie *et al.*, Research investments and market structure in the food processing, agricultural input, and biofuel industries worldwide [Economic Res. Rep. 130, Economic Research Service, U.S. Department of Agriculture (USDA), Washington, DC, 2011]; www.ers.usda.gov/publications/err-economic-research-report/err130.aspx.
7. J. M. Alston, M. Andersen, J. James, P. Pardey, *Persistence Pays: U.S. Agricultural Productivity Growth and the Benefits from Public R&D Spending* (Springer, New York, 2010).
8. C. Klotz, K. Fuglie, C. E. Pray, Private sector agricultural research expenditures in the United States, 1960–1992 (Staff paper AGE5-9525, Economic Research Service, USDA, Washington, DC, 1995).
9. This \$340M of estimated biofuels R&D expenditure is reflected in estimates for crop seed and/or biotechnology. The eight largest energy research spenders invested more than \$6 billion total in R&D in 2009, primarily on fossil fuels. See (6) for details.
10. P. Dasgupta, J. Stiglitz, *Econ. J.* **90**, 266 (1980).
11. K. D. Rubenstein, M. Smale, M. P. Widrtecher, *Crop Sci.* **46**, 1021 (2006).
12. J. I. Cohen, *Nat. Biotechnol.* **23**, 27 (2005).
13. In 1980, the U.S. Supreme Court ruled in (14) that living material was patentable.
14. *Diamond v. Chakrabarty*, 447 U.S. 303 (1979).
15. Health and environmental risk assessments, product registration, patenting, and regulatory affairs required 34% of agricultural chemical R&D costs (16) and 18% of crop biotechnology trait development costs (17).
16. P. McDougall, The cost of new agrochemical product discovery, development, and registration in 1995, 2000, and 2005–8 (R&D study, CropLife International, Brussels, 2010).
17. P. McDougall, The cost and time involved in the discovery, development and authorisation of a new plant biotechnology derived trait (R&D study, CropLife International, Brussels, 2011); www.croplife.org/PhillipsMcDougallStudy.
18. J. M. Alston, *Calif. Agric.* **58**, 80 (2004).
19. K. Fuglie, T. Walker, *J. Agric. Appl. Econ.* **33**, 459 (2001).
20. W. E. Huffman, R. E. Evenson, *Science for Agriculture: A Long-Term Perspective* (Blackwell, Boston, 2006).
21. C. Wang *et al.*, *Am. J. Agric. Econ.* **91**, 374 (2009).
22. C. E. Pray, D. Umali-Deininger, *World Dev.* **26**, 1127 (1998).
23. D. Schimmelpennig, *Choices (N.Y. N.Y.)* **2004**, 19 (2004).
24. P. Pingali, G. Traxler, *Food Policy* **27**, 223 (2002).

Acknowledgments: The authors thank the Economic Research Service of USDA for support and representatives of agricultural companies for information. The views expressed are not necessarily those of the USDA.

10.1126/science.1226294

HISTORY OF SCIENCE

A Golden Era of Nobel Laureates

Joseph L. Goldstein and Michael S. Brown

What conditions in the 1960s enabled nine physicians who trained at NIH to win Nobel Prizes?

The award of the 2012 Nobel Prize in Chemistry to Robert Lefkowitz brings to nine the number of Nobel laureates who trained in research at the United States National Institutes of Health (NIH) between 1964 and 1972—a remarkable outpouring over such a short period from a single biomedical institution (see the figure). Was there something particular about these recipients, the time, and the place that account for this unprecedented record?

We were among the nine, and the parallels in our experiences are striking. All of us graduated from medical school before entering NIH, and all (except Alfred Gilman) took residency training. Gilman and Ferid Murad were the only M.D.-Ph.D.s in the group. For the rest of us, NIH provided our first intense research experience. Some of our mentors were Ph.D.s and some were M.D.s, but they all worked in reductionist systems focused on fundamental mechanisms. The nine of us studied problems ranging from protein synthesis in bacteria to hormone receptors in animal cells. Despite our clinical training and the fact that some of us had patient care duties, our science was far removed from the bedside. The sharp contrast between the uncertainties of the bedside and the relatively “pristine” world of the laboratory provided the stimulus that drove us to pursue careers in fundamental research.

The research experience at NIH in the 1960s was intense. Distractions were few. Many of us knew each other, had heated discussions about our research, and wondered whether we had the ability to succeed in a laboratory-based career.

After finishing our training, it is surprising that none of us stayed at NIH. We either joined clinical departments or basic science departments in medical schools. Regardless, we all addressed fundamental problems that were relevant to medicine, making primary use of the tools of biochemistry, supplemented with molecular biology as those methods became available. It is noteworthy that four of us received our prizes for discovery of receptors [low-density lipoprotein

Nobel laureate	NIH mentor	Institute	Year of Nobel Prize	Discovery
Michael S. Brown	Earl Stadtman	NHLBI	1985	LDL receptors
Joseph L. Goldstein	Marshall Nirenberg	NHLBI	1985	LDL receptors
J. Michael Bishop	Leon Levintow	NIAID	1989	Cellular oncogenes
Harold E. Varmus	Ira Pastan	NIDDK	1989	Cellular oncogenes
Alfred G. Gilman	Marshall Nirenberg	NHLBI	1994	G proteins
Stanley B. Prusiner	Earl Stadtman	NHLBI	1997	Prions
Ferid Murad	Martha Vaughan	NHLBI	1998	Nitric oxide signaling
Richard Axel	Gary Felsenfeld	NIDDK	2004	Odorant receptors
Robert J. Lefkowitz	Jesse Roth and Ira Pastan	NIDDK	2012	G protein-coupled receptors

The Nobel nine. Listed are the Nobel Prize winners who trained at NIH in the years 1964 to 1972. NHLBI, National Heart, Lung, and Blood Institute; NIAID, National Institute of Allergy and Infectious Diseases; NIDDK, National Institute of Diabetes and Digestive and Kidney Diseases.

(LDL) receptors, G protein-coupled receptors, and odorant receptors], and two were honored for discovery of receptor-signaling mechanisms (G proteins and nitric oxide). In the nonreceptor arena, two laureates elucidated a basic mechanism of cancer, and one discovered a new form of infectious neurologic disease. Although none of us performed “translational research,” as currently in vogue, our discoveries influenced drug discovery, medical practice, and human health.

It is not a coincidence that the 1960s was the decade of the Vietnam War and the doctor draft. Service at NIH substituted for military service in Vietnam, which led some of us to apply to NIH instead of an academic institution. The draft exemption evoked a huge increase in the number of applicants for NIH fellowships. As a result, NIH had its pick of fellows with the strongest academic records. While these factors were important, they would have amounted to nothing if we had not encountered the excitement and rigor then in place at NIH.

As research fellows at NIH, we trained with brilliant scientists who had been appointed in previous years. Credit is due to the courageous leaders of the various institutes who chose to appoint basic scientists even when their work did not deal directly with the disease-oriented mission of the institute. Five NIH-career scientists have

been honored with Nobel Prizes: Marshall Nirenberg (1968), Julius Axelrod (1970), Christian Anfinsen (1972), D. Carlton Gajdusek (1976), and Martin Rodbell (1994). Four of them were Ph.D. basic scientists, and one (Gajdusek) was a physician-scientist. All five were dominant forces at NIH when we nine were there.

Scores of distinguished scientists were trained at NIH in the 1960s, including many who earned election to the U.S. National Academy of Sciences. Others achieved distinction in other ways. Indeed, a substantial portion of the faculties of American medical schools trained at NIH in this remarkable period.

Will a single biomedical institution ever again train nine Nobel laureates in a single decade? Under the current conditions, it seems unlikely. The focus of medical schools in the United States has changed. In the 1960s, basic science was at the core of medical education. The brightest graduates were expected to advance their discipline through scientific investigation. Today, medical school curricula tend to condense basic science teaching to a few months instead of the traditional two preclinical years, and the courses focus on a restricted set of disease-relevant “facts” with little to no discussion about where those facts came from or that facts will change as science advances. The

joy of finding new facts or overturning old ones is no longer transmitted to students.

As well, clinical departments have expanded geometrically as medical schools compete with private hospitals by amassing huge clinical programs. The few scientifically oriented faculty in clinical departments have been diluted to irrelevance by pure clinicians. No wonder that few medical students are choosing to follow paths in basic research.

The research emphasis of NIH has gradually shifted. The primary focus is no longer on acquisition of knowledge in basic bio-

logical mechanisms. Current emphasis on “translational research” relegates basic science to a back burner. What has been lost is the conviction that progress in medicine rests ultimately on a fundamental understanding of physiology. Individual curiosity-driven science has been replaced by large consortia dedicated to the proposition that gathering vast amounts of correlative data will somehow provide the answer to life’s fundamental questions.

Is it likely that the best and brightest medical students can be funneled into settings where they can reinforce each other

and be inspired by brilliant mentors? If it were to happen, it would require NIH to support teaching and research at a concentrated depth in the basic sciences to open the eyes of medical school graduates to the joy of scientific study.

There is a lesson from this golden era of NIH: Ambitious young physicians juxtaposed to cutting-edge basic scientists can themselves make fundamental discoveries. Hopefully, this lesson will help to reconfigure the future.

10.1126/science.1231699

AGRICULTURE

Carbon Storage with Benefits

Saran P. Sohi

Biochar—a material related to charcoal—has the potential to benefit farming as well as mitigate climate change.

Biochar is the solid, carbon-rich product of heating biomass with the exclusion of air (pyrolysis or “charring”). If added to soil on a large scale, biochar has the potential to both benefit global agriculture and mitigate climate change. It could also provide an income stream from carbon abatement for farmers worldwide. However, biochar properties are far from uniform, and biochar production technologies are still maturing. Research is beginning to point the way toward a targeted application of biochar to soils that maximizes its benefits.

Incentives for using biomass to mitigate climate change currently focus on replacing fossil fuels in combustion. Biochar production seeks a different route to carbon abatement. By stabilizing carbon that has already been captured by plants from the atmosphere into a form resembling charcoal, it can prevent the carbon from degrading and returning to the air. A key attraction of biochar is that it can enhance the fertility and resilience of crop land. If biochar production could be made profitable through its use in agriculture, this would distinguish it from costly geoengineering measures to mitigate climate change.

At least one-third of net plant growth globally is thought to be now managed by



Biochar variation. The diverse properties of biochar have led to widely varying results. A more systematic understanding is now emerging, helping to define its value in crop production and carbon storage.

humans (1). Diverting a few percent of this growth into biochar production could sustainably expand biosphere carbon stocks by a gigatonne [10^9 metric tons (t)] each year (2). In contrast, the addition of fresh or composted plant material would have a small effect on carbon storage: Only around 10% of the carbon becomes stabilized (3) and after reequilibration, higher levels of organic inputs to the soil are matched by more decomposition. Conversion of biomass to biochar through pyrolysis creates a product that is highly resistant to biological attack. The finite capacity of soils to store decomposing organic matter therefore does not apply to biochar. Exactly how long biochar remains stable in the soil is still not completely resolved, however.

Calculations show that cleanly creating biochar from diffuse, seasonal sources of biomass such as rice husk should provide a clear carbon benefit. However, biomass can often equally be used to create bioenergy

and displace the use of fossil fuel. For biochar to become the better option, the efficient stabilization of carbon into biochar must be combined with the recovery of energy from pyrolysis gases and residual heat (2, 4). Pyrolysis systems that connect continuous biochar production (for example, in rotating kilns) with power generation from coproducts remain scarce.

Without financial incentives for carbon abatement by stabilization, biochar has to be worth money in the soil. However, biochar materials are diverse (see the figure), and maximizing the benefits gained from their use depends on matching them to the right situation (5). This diversity is the reason for the startling variety of results from early observational studies that aimed to demonstrate benefits to plant productivity. Although one study reported an eight-fold increase in crop yield through the use of biochar (6), a meta-analysis of 16 glasshouse and field studies showed a mean impact of only 10 to 15% on plant productivity (7). The highest productivity increases were seen in soils of medium texture and low pH.

Many of these early studies used readily available charcoal, which is one form of biochar. Increasingly, biochar with particular properties is selected to address an identified soil constraint, such as water storage or flow, pH or retention of crop nutrients, or even a biological purpose (8). Suitable screening methods allow biochar to be compared for properties such as physical and material sta-

UK Biochar Research Centre, School of GeoSciences, University of Edinburgh, Edinburgh EH9 3JN, UK. E-mail: saran.sohi@ed.ac.uk

bility, macroporosity, release of entrained ash, and labile carbon (9–11).

To understand the long-term value of biochar addition for both soil improvement and carbon storage, methods to assess and predict biochar durability and changes in its properties are required. Beyond real-time observation (12) and experimental manipulation (13), insight can be gained from the study of old wildfire charcoal as a naturally aged analog (14). Focusing effort toward these strategic goals could later explain much-studied but less predictable effects on native soil carbon (priming) and nitrous oxide emission.

Positive effects on soils and crop production cannot alone confirm the viability of producing and deploying biochar, however. In many situations, there will be limited technology options for pyrolysis and constraints on affordable or available feedstock (2). Strategies for deploying biochar must also consider the practical and logistical issues of storage, transport, and incorporation into soil.

Doses of application should reflect such constraints. In the United Kingdom, for example, the projected break-even cost of deploying biochar from fresh or clean waste biomass exceeds \$150/t, suggesting that only annual doses at the lowest experimental rates would currently be economic (15). Understanding the relative merits of regular low-

dose applications as part of a nutrient management regime, versus larger one-off applications, is therefore a priority; establishing protocols for the safe use of biochar derived from low-cost waste streams is another.

Future applications may include broad-acre crops, high-value vegetable production, and management of liquid manures, and there is already niche usage in horticultural growing media and fertilizer products. Such diverse modes and scales of deployment require a generalized understanding of biochar function. Using biochar to enhance existing products, even as a relatively minor ingredient, could build familiarity and reliable supply chains for potential future scale-up. Other functions of biochar worthy of consideration include provision of compounds that promote plant growth and resistance to disease (16, 17) or the modification of nutrient dynamics at the plant-soil interface (18). There may also be synergistic effects between biochar and manure (19), compost, and fertilizer.

Integrated understanding of biochar function and deployment will support expanding use patterns that are economic and environmentally attractive. Over decades, the use of biochar could create soils that in management and function begin to resemble the fertile terra preta (famed charcoal-rich soils in Amazonia). Full realization of these benefits

requires rewards and incentives at a national level that reflect the global value of both agriculture and climate.

References and Notes

1. S. W. Running, *Science* **337**, 1458 (2012).
2. D. Woolf, J. E. Amonette, F. A. Street-Perrott, J. Lehmann, S. Joseph, *Nat. Commun.* **1**, 1 (2010).
3. M. W. Schmidt *et al.*, *Nature* **478**, 49 (2011).
4. J. Hammond *et al.*, *Energy Policy* **39**, 2646 (2011).
5. S. P. Sohi, E. Krull, E. Lopez-Capel, R. Bol, *Adv. Agron.* **105**, 47 (2010).
6. C. Steiner *et al.*, *Plant Soil* **291**, 275 (2007).
7. S. Jeffery *et al.*, *Agric. Ecosyst. Environ.* **144**, 175 (2011).
8. C. E. Brewer *et al.*, *Bioenergy Res.* **4**, 312 (2011).
9. K. A. Spokas, *Carbon Manage.* **1**, 289 (2010).
10. M. I. Bird *et al.*, *J. Archaeol. Sci.* **35**, 2698 (2008).
11. A. Cross, S. P. Sohi, *Soil Biol. Biochem.* **43**, 2127 (2011).
12. R. S. Quilliam *et al.*, *Agric. Ecosyst. Environ.* **158**, 192 (2012).
13. S. E. Hale *et al.*, *Environ. Sci. Technol.* **45**, 10445 (2011).
14. A. C. Scott, F. Damblon, *Palaeogeogr. Palaeoclimatol. Palaeoecol.* **291**, 1 (2010).
15. S. Shackley *et al.*, *Carbon Manage.* **2**, 335 (2011).
16. Y. Elad *et al.*, *Phytopathol. Mediterr.* **50**, 335 (2011).
17. K. A. Spokas *et al.*, *Plant Soil* **333**, 443 (2010).
18. M. T. Prendergast-Miller, M. Duvall, S. P. Sohi, *Soil Biol. Biochem.* **43**, 2243 (2011).
19. B. O. Dias *et al.*, *Bioresour. Technol.* **101**, 1239 (2010).

Acknowledgments: The UK Biochar Research Centre (UKBRC) was established in 2009 under a Science and Innovation funding award to S. Haszeldine by the Engineering and Physical Sciences Research Council, with additional funding from the Scottish Funding Council and the University of Edinburgh. Discussions with all UKBRC colleagues are acknowledged in particular S. Shackley and O. Mašek.

10.1126/science.1225987

CANCER

Can One Cell Influence Cancer Heterogeneity?

Andrei V. Krivtsov and Scott A. Armstrong

Gliomas are the most common form of malignant brain tumor in adults and have generally poor clinical outcomes. Patients with the most aggressive form of glioma, glioblastoma multiforme (GBM), have a low 5-year survival rate (1). Progress has been made in characterizing the genetic lesions and cells of origin in GBM, both of which may contribute to disease pathogenesis. On page 1080 in this issue, Friedmann-Morvinski *et al.* (2) show that differentiated neuronal cells and glial cells in the mouse brain can revert to less mature states upon acquiring these genetic lesions. Thus,

multiple different cell types in the central nervous system, and not just neural stem cells, can be transformed into GBM in an animal model that recapitulates important aspects of the human disease.

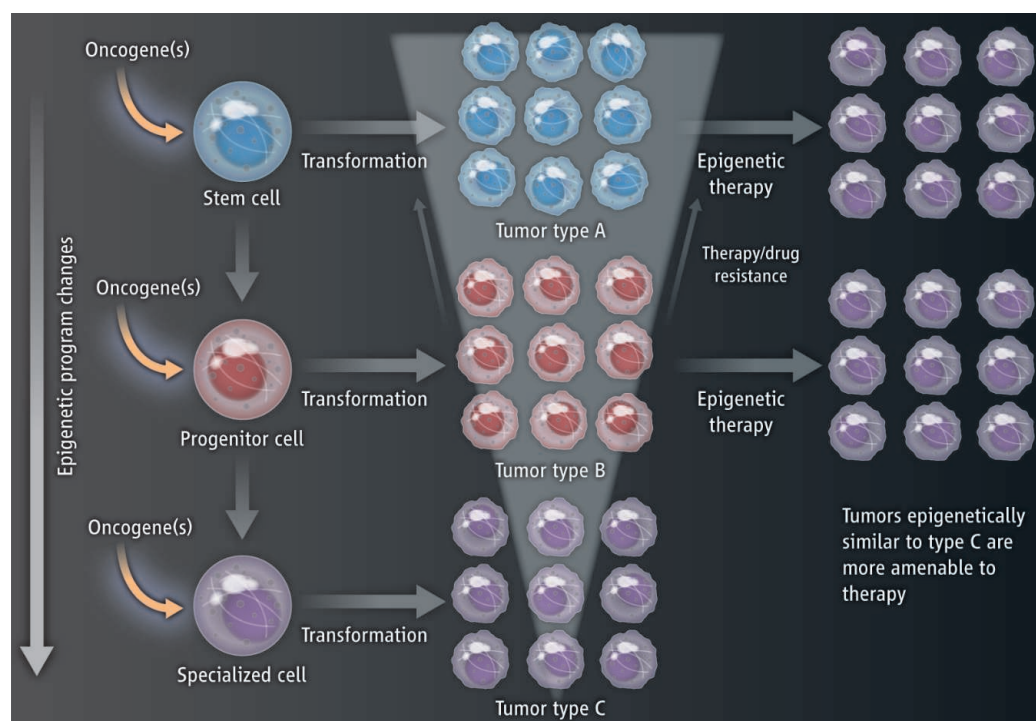
The cellular background (the chemical modifications of chromatin, or the epigenetic state) in which a transforming genetic lesion occurs (cell of origin) may contribute to the complexity of cancer. The potential importance of the cell of origin and the transformability of multiple cell types raises questions about hierarchical relationships between cells and the properties of tumor-initiating cancer stem cells (thought to be cells within a tumor that can self-renew and give rise to heterogeneous populations of cancer cells that constitute the tumor). In mouse models of glioblas-

Genetic lesions allow mature brain cells in mice to revert to immature forms that can give rise to tumors.

toma, genetic lesions introduced in both neural stem cells and more mature glial cells may lead to tumor formation (3, 4). Although glial progenitor cells and differentiated astrocytes both have the potential to contribute to GBM, the tumors develop differently, depending on the cell of origin (5). Specific subtypes of human GBM show some relation to normal brain cell types (6) based on gene expression, suggesting that the cell of origin may influence the final GBM subtype.

Friedmann-Morvinski *et al.* examined this possibility in mice using a highly targeted method (stereotaxic injection of lentivirus vectors into cells that allows transduction of oncogenes or deletion of tumor suppressor genes) to induce genetic lesions in specific central nervous system cell types in vivo. The

Human Oncology and Pathogenesis Program and Department of Pediatrics, Memorial Sloan-Kettering Cancer Center, New York, NY 10065, USA. E-mail: armstrong@mskcc.org



Cell of origin. Cellular differentiation and specialization are accompanied by gradual changes in epigenetic programs. Genetic lesions can initiate tumorigenic transformation of tissue stem cells, differentiated progenitors, and more specialized cells. The cell of origin may influence the epigenetic state of the resulting tumor. Cancers expressing stem cell programs have an adverse prognosis. Modulating the epigenetic state of more aggressive tumors (epigenetic therapy) may sensitize them to treatment with current therapies.

authors demonstrate that multiple normal cell types within the central nervous system can be transformed into tumors, consistent with findings that multiple hematopoietic cells types can be transformed in leukemia development (7, 8). However, which hematopoietic cell types can be transformed is determined by the initiating oncogene, demonstrating an interaction between the epigenetic state of the cell of origin and the initiating oncogene (9, 10). The study by Friedmann-Morvinski *et al.* indicates that both neuronal and glial cells, upon loss of the tumor suppressor proteins p53 and neurofibromatosis-1 (NF1), reactivated expression of markers normally found in immature cells of the nervous system. The transformed cells expressing the immature markers then gave rise to tumors. Therefore, cancer cells may not follow the same strict relationships and directionality that normal cells follow during lineage development.

The finding of Friedmann-Morvinski *et al.* does not rule out a hierarchical relationship between cells in a fully developed cancer, with some cells being more tumorigenic than others. However, if more differentiated cells can be transformed and revert to more immature states, markers of normal differentiation will not consistently identify the most tumorigenic populations. Indeed, mouse models of

leukemia have demonstrated this possibility (11). Therefore, markers that are inextricably linked to cellular signaling pathways that control extensive cancer cell proliferation and self-renewal should be more predictably associated with tumor-initiating potential than markers associated with normal differentiation. However, most studies assessing cellular permissiveness to transformation have been performed on mouse cells, which are easier to transform than human cells. Further studies are required to define the permissiveness of various human cell types. Furthermore, studies such as that of Friedmann-Morvinski *et al.* introduce multiple genetic abnormalities simultaneously, so mutations could accumulate in tissue-specific stem cells until the final lesion necessary for tumor development is acquired in one of many transformable cell types; that cell type then becomes the cell of origin for that cancer.

The genetic makeup of a malignancy correlates with clinical outcome and can therefore be useful in predicting prognosis and planning treatment. In addition to the impact of the genetic lesions themselves, the epigenetic state of cells within the cancer, perhaps influenced by the cell of origin, likely contributes to the clinical properties, including drug resistance (12). Gene expression profiling of

multiple different types of cancer have identified different subtypes that are not clearly defined by genetic abnormalities, and thus may be defined by epigenetic mechanisms (13). Indeed, Friedmann-Morvinski *et al.* show that specific subtypes of mouse GBM are developed on the basis of the cell of origin. Further studies are required in multiple cancers to determine the extent to which the cell of origin influences epigenetic heterogeneity.

As our understanding of cancer genetics broadens, the opportunities to apply that knowledge to individualize therapy for cancer patients with more targeted therapies will continue to increase as well. However, molecularly targeted therapies have shown that cancers are remarkably adept at developing resistance, and some of the mechanisms of resistance are likely a result of either pre-existing (cancer stem cells) or acquired (adaptation) epigenetic differences. These studies raise the possibility that influencing the epigenetic state of cancer

cells may sensitize cancers to concurrent treatments and/or restrict cancer cell adaptation to therapeutic intervention (see the figure). Emerging classes of therapeutics aimed at enzymes that catalyze chemical modifications of DNA and chromatin-associated proteins (and thereby modify the epigenetic states of cells) are currently entering clinical trials (14). There is hope that a combination of therapies that target genetic abnormalities, epigenetic properties, immune mechanisms, and resistance to programmed cell death (apoptosis) will usher in better treatments to deal with difficult-to-cure cancers like GBM.

References

1. J. Chen, R. M. McKay, L. F. Parada, *Cell* **149**, 36 (2012).
2. D. Friedmann-Morvinski *et al.*, *Science* **338**, 1080 (2012); 10.1126/science.1226929.
3. R. M. Bachoo *et al.*, *Cancer Cell* **1**, 269 (2002).
4. C. Liu *et al.*, *Cell* **146**, 209 (2011).
5. L. Lei *et al.*, *PLoS ONE* **6**, e20041 (2011).
6. R. G. Verhaak *et al.*, *Cancer Cell* **17**, 98 (2010).
7. A. V. Krivtsov *et al.*, *Nature* **442**, 818 (2006).
8. A. Cozzio *et al.*, *Genes Dev.* **17**, 3029 (2003).
9. B. J. Huntly *et al.*, *Cancer Cell* **6**, 587 (2004).
10. Y. Wang *et al.*, *Science* **327**, 1650 (2010).
11. K. D. Gibbs Jr. *et al.*, *Cell Stem Cell* **10**, 210 (2012).
12. S. V. Sharma *et al.*, *Cell* **141**, 69 (2010).
13. M. E. Figueroa *et al.*, *Cancer Cell* **17**, 13 (2010).
14. <http://clinicaltrials.gov/ct2/show/NCT01684150>

10.1126/science.1231594

GEOPHYSICS

Imaging the Deep Earth

German A. Prieto

Insights into Earth's thermal and chemical structure, from the inner core to the crust, have historically been gained from analyzing seismic waves excited by earthquakes (1). However, the resolution of these methods is limited because nearly all earthquakes occur along tectonic plate boundaries, leaving large areas that are seismically quiet. Recent developments in seismic noise tomography have shown great potential for high-resolution imaging of Earth's interior structure (2). This approach yields data wherever a seismic instrument can be deployed, but the seismic noise signals (3) used to image the crustal and upper mantle structures often lack resolution for most of the remaining mantle. On page 1063 of this issue, Poli *et al.* (4) overcome some of these limitations, enabling the imaging of deep-Earth structures.

Ambient seismic noise is a ubiquitous signal that is recorded at seismic stations globally, even in the interior of continents. At periods below 30 s, microseismic noise is generated by pressure fluctuations on the ocean bottom in coastal waters and by nonlinear interactions of ocean waves traveling in opposite directions (5, 6) (see the figure, panel A). Microseismic noise is dominated by surface waves, which travel in the top 10 to 100 km of Earth's interior. However, storms over the oceans can also generate global body waves (7), which propagate through Earth's mantle and can be reflected from major interfaces (see the figure, panel B).

Geosciences, Universidad de los Andes, Bogotá, Colombia.
E-mail: gprieto@mit.edu

More than 50 years ago, Aki (8) showed how the ambient seismic noise can be used to estimate the propagation speed of surface waves underneath a seismic array. Soon after, Claerbout (9) suggested that Earth's reflection response (that is, the imaging of interfaces at depth) could be extracted from carefully treated seismic signals. But it was not until the advent of continuously recorded high-density seismic networks that these proposals could be put in practice.

In 2005, Shapiro *et al.* presented a tomographic model of the velocity structure of Earth's crust and upper mantle, based on ambient seismic noise records (2). The main idea behind this approach (10) is that a coherent signal can be extracted from apparently random noise by cross-correlation between multiple seismic stations. The signal extracted is used to calculate the propagation speed of surface waves between each pair of stations (see the figure, panel A). Since then, several seismic noise imaging methods have been developed, most of them based on surface-wave measurements (11–13). Because of the ubiquitous nature of the ambient seismic noise, continuous monitoring of the subsurface is possible (14).

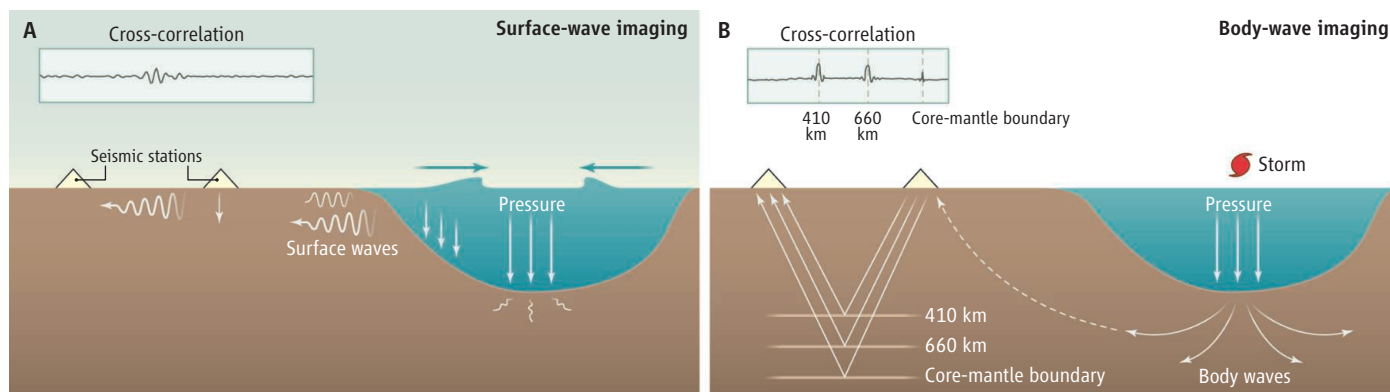
Body waves have also been observed in the ambient seismic noise (7), but only in a limited number of cases have station-to-station body wave arrivals been reported (3). Most reported noise-derived body waves have been related to reflections from the Moho (the discontinuity between Earth's crust and mantle) or other shallow crustal interfaces. A substantial portion of

Improved processing of seismic noise data enables detailed imaging of deep Earth structures.

Earth's mantle thus remained out of reach for noise imaging.

Poli *et al.* are now able to extract global station-to-station body-waves from the noise and to determine the thickness of the transition zone and the fine structure of its interfaces in the area of study. The authors carefully processed the ambient seismic field of a yearlong continuously recording seismic experiment (POLENET/LAPNET) in northern Finland. They removed earthquake signals and other glitches in the data (for example, when stations were offline or reported large spikes), using shorter signals for cross-correlation and stacking (averaging) over the entire time span of the experiment. As in many other seismic noise studies, the cross-correlations of the signals show clear surface waves but no evident body waves. Only after “muting” these surface waves (that is, setting their amplitudes to zero) and summing the cross-correlations over the entire network, did evidence for vertically propagating body waves from the mantle transition interfaces emerge (see the figure, panel B). The authors further corroborated this interpretation with theoretical predictions based on a standard Earth model.

The results are a major advance in seismic noise tomography. There have been multiple seismic deployments in the past 10 to 20 years over continents; analysis of these data with Poli *et al.*'s technique should reveal further evidence for body waves from the deep Earth. The combined results may help to resolve the topography of the mantle transition zone at the global scale and place



Surface and body waves in ambient noise tomography. (A) Microseismic noise is mostly generated in the ocean basins by wave-wave interactions and occasionally during strong storm activity. The resulting microseismic surface waves are recorded at seismic stations and cross-correlated for surface-wave tomography.

(B) Signals from body waves generated in the ocean basins are recorded at one seismic station, travel back into the deep Earth, are reflected from any interfaces encountered, and are registered at a second seismic station. Poli *et al.* use this approach to image the thickness and structure of the mantle transition zone.

constraints on the thermodynamics of mantle transition minerals (15).

With improved signal processing and data from seismic networks with high station density, it may become possible to obtain detailed information not only about the lithosphere and the mantle transition zone, but also about the core-mantle boundary (16). Seismic noise will likely become a key ingredient in imaging efforts to discern Earth's structures, independent of the presence of earthquakes.

References

1. G. Masters *et al.*, *Geophys. Monogr. Ser.* **117**, 63 (2000).
2. N. M. Shapiro *et al.*, *Science* **307**, 1615 (2005).
3. Z. Zhan *et al.*, *Geophys. J. Int.* **182**, 408 (2010).
4. P. Poli *et al.*, *Science* **338**, 1063 (2012).
5. M. S. Longuet-Higgins, *Philos. Trans. R. Soc. Lond. A* **243**, 1 (1950).
6. K. Hasselmann, *Rev. Geophys.* **1**, 177 (1963).
7. P. Gerstoft *et al.*, *Geophys. Res. Lett.* **35**, L23306 (2008).
8. K. Aki, *Bull. Earthq. Res. Inst. Univ. Tokyo* **35**, 415 (1957).
9. J. F. Claerbout, *Geophysics* **33**, 264 (1968).
10. R. L. Weaver, *Science* **307**, 1568 (2005).
11. M. P. Moschetti *et al.*, *Nature* **464**, 885 (2010).
12. G. A. Prieto, G. C. Beroza, *Geophys. Res. Lett.* **35**, L14304 (2008).
13. J. F. Lawrence, G. A. Prieto, *J. Geophys. Res.* **116**, B06302 (2011).
14. F. Brenguier *et al.*, *Nat. Geosci.* **1**, 126 (2008).
15. L. Stixrude, C. Lithgow-Bertelloni, *Geophys. J. Int.* **184**, 1180 (2011).
16. P. Wang *et al.*, *Geophys. J. Int.* **175**, 103 (2008).

10.1126/science.1231290

DEVELOPMENT

Plant Gametes Do Fertilization with a Twist

William J. Snell

A new generation in eukaryotes begins with fusion between sperm and egg, but we know little about the mechanisms involved. Sperm-egg interactions have been studied most thoroughly in animals, but on page 1093 of this issue, Sprunck *et al.* (1) have pushed our understanding of gamete interactions in plants to the head of the model organisms class. They discovered that plants do the fertilization dance similarly to animals, but with a twist. In animals, the egg remains quiescent until fused with the sperm, but in *Arabidopsis* the egg leads. The egg cell responds to sperm discharged from a newly arrived pollen tube by secreting a cloud of sperm-activating proteins. The aroused sperm redistributes a previously cryptic putative membrane fusogen to its plasma membrane to prepare for fusion.

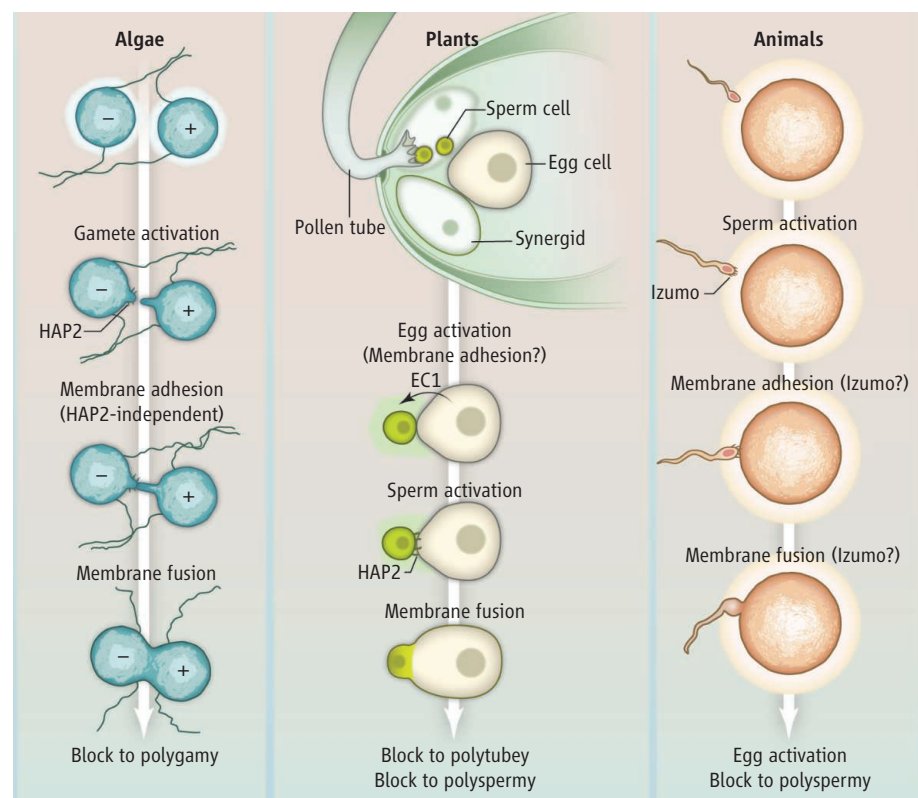
In most animals, the sperm is activated for fusion after binding to the outer vestments of the egg (the zona pellucida in mammals) (2, 3). After penetrating the zona, the sperm fuses with the egg plasma membrane, which triggers the egg to release contents of secretory vesicles and undergo surface modifications (blocks to polyspermy) to prevent fusion of additional sperm (4). Animal fertilization is particularly resistant to genetic studies (2). In mammals, only the sperm protein Izumo-1 is exclusive to gametes and shown by gene disruption to be essential for an unknown step in membrane fusion (5, 6).

Studying higher plant fertilization is challenging because the female gametophyte is

inaccessible and more players are involved: the pollen cell with two sperm and two dimorphic eggs with adjacent synergid cells (see the figure). The most thorough understanding of fertilization is in the model plant *Arabidopsis*. The pollen tube is drawn to an embryo sac within an ovule by attractants produced by

Identification of key regulatory mechanisms of higher plant gametes advances our understanding of fertilization.

the synergids (7). Upon pollen tube arrival at a synergid, the synergid degenerates and two sperm are discharged, which then travel to the egg cell. After a brief pause, one sperm fuses with the egg cell to form the zygote, and the other fuses with the central cell to form the endosperm (8). Fusion activates a block to



Fertilization across phyla. As in algae and animals, *Arabidopsis* gametes undergo mutual activation. Upon sperm arrival, the egg cell secretes EC1 proteins that trigger sperm to display previously cryptic HAP2. Adhesion between *Chlamydomonas* gametes also triggers exposure of cryptic HAP2, and in mammals, sperm binding to egg triggers exposure of Izumo-1. Only in the two plant systems are both gametes activated before fusion.

Cell Biology Department, University of Texas Southwestern Medical School, Dallas, TX 75390, USA. E-mail: william.snell@utsouthwestern.edu

“polytubey” (i.e., more than one pollen tube reaching the plant ovule) (9, 10) as well as a block to polyspermy (11).

Higher plants, a unicellular green alga, and a unicellular malaria pathogen all contain a conserved, gamete-specific, integral membrane protein, HAP2 (GSC1), present on only one gamete and essential for the membrane fusion reaction (12–14). The HAP2 family is conserved throughout plants and protists and is present in some multicellular animals (12, 15). In higher plants, it was unclear whether sperm HAP2 was required for membrane adhesion or fusion (13, 14). In *Chlamydomonas* and *Plasmodium*, HAP2 is required after adhesion during lipid bilayer fusion (12), suggesting that HAP2 is an ancestral “fusogen” in all three groups (16). Paradoxically, HAP2 is on internal membranes in plant sperm in pollen tubes and undetectable on the surface where it is needed (13, 14).

The solution to this conundrum was sparked when Sprunck *et al.* discovered that arrival of sperm near the egg cell triggers the

release of a protein cloud containing Egg Cell 1 (EC1). Knockdown of all five EC1 proteins led to inhibition of sperm-egg fusion and reduced seed set. Egg cells were surrounded by as many as four unfused sperm, consistent with other fusion-defective *Arabidopsis* mutants in which the second, persistent synergid in ovules that received fusion-defective sperm (*hap2* or *duo1* sperm) continued to attract pollen tubes (9, 10).

Mouse sperm respond to the egg contact by redistributing Izumo-1, and *Chlamydomonas* minus gametes uncover HAP2 when they meet their mates (10). Sprunck *et al.* found that in sperm incubated with S1 and S2 peptides derived from EC1 proteins, HAP2 redistributed to the plasma membrane. Thus, the ancient cellular mechanism of restricting accessibility of membrane-active, fusion-essential gamete proteins until their possessors perceive their partners is also preserved in plants.

It will be interesting to determine whether the sole function of egg cell activation is to

secrete EC1 for sperm, or whether activation also brings about fusion-essential changes in the egg cell. Gaining new insights about the molecular details of sperm-egg interactions in plants likely will be simpler once in vitro methods become more advanced.

References

1. S. Sprunck *et al.*, *Science* **338**, 1093 (2012).
2. J. P. Evans, *Annu. Rev. Physiol.* **74**, 477 (2012).
3. B. Baibakov *et al.*, *J. Cell Biol.* **197**, 897 (2012).
4. J. L. Wong, G. M. Wessel, *Curr. Top. Dev. Biol.* **72**, 1 (2005).
5. N. Inoue *et al.*, *Nature* **434**, 234 (2005).
6. D. A. Ellerman *et al.*, *Mol. Reprod. Dev.* **76**, 1188 (2009).
7. S. Sprunck, *Biochem. Soc. Trans.* **38**, 635 (2010).
8. Y. Hamamura *et al.*, *Curr. Biol.* **21**, 497 (2011).
9. R. D. Kasahara *et al.*, *Curr. Biol.* **22**, 1084 (2012).
10. K. M. Beale *et al.*, *Curr. Biol.* **22**, 1090 (2012).
11. R. J. Scott *et al.*, *Mol. Plant* **1**, 611 (2008).
12. Y. Liu *et al.*, *Genes Dev.* **22**, 1051 (2008).
13. T. Mori *et al.*, *Nat. Cell Biol.* **8**, 64 (2006).
14. K. von Besser *et al.*, *Development* **133**, 4761 (2006).
15. R. E. Steele, C. E. Dana, *PLoS ONE* **4**, e7680 (2009).
16. J. L. Wong, M. A. Johnson, *Trends Cell Biol.* **20**, 134 (2010).

10.1126/science.1231259

CHEMISTRY

Algae Under Pressure and in Hot Water

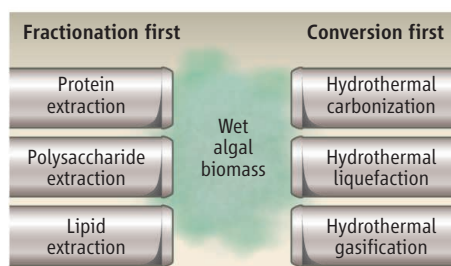
Phillip E. Savage

Algae grow quickly, can be cultivated to have a high oil (triacylglyceride) content, and can be grown on nonarable land with brackish or salt water. These characteristics make them an attractive source of biomass for renewable biofuels. The U.S. Navy and commercial airlines have demonstrated the use of algal biofuel in ships and planes; blending algal biofuel with ultralow-sulfur diesel fuel reduced the pollutants and particulate matter and improved fuel economy during the operation of a marine vessel on the Great Lakes (1). Algae-derived fuel is very expensive, however, and most of the cost is associated with producing the biomass. The U.S. Navy has contracted to pay \$12 million for 450,000 gallons (1.7 million liters) of biofuel, which works out to about \$27/gallon or 10 times the U.S. cost of petroleum-derived fuel [see, for example, (2)]. Chemical reactions in hot, compressed water (hydrothermal reactions) and in super-

critical fluids can provide new, potentially cheaper paths to renewable fuels from wet algal biomass (3).

The methods used to make large quantities of liquid fuels from algae involve extracting the oil with an organic solvent such as hexane and converting the oil to either biodiesel by catalyzed transesterification with alcohol or to green diesel by catalytic hydrotreating. Drying the algae before extracting

Strategies are being developed to convert algae into high-value products and fuels without expensive drying of raw biomass.



Processing strategies. Hydrothermal and supercritical fluid processing approaches for transformation of wet algal biomass into fuels and other products fractionate the biomass first or process the entire biomass first.

the oil takes time, consumes energy, and adds expense. Processes that can produce fuel directly from wet algal biomass could improve the economics and environmental sustainability of algal biofuels.

This realization has prompted a flurry of research into alternative approaches, including use of hydrothermal and solvothermal processes (4). Hydrothermal processing is energy efficient and favors the reactions required (5). Hot, compressed water (e.g., 300°C, 8.6 MPa) readily dissolves organic compounds, and its elevated ion product ($\sim 10^{-11}$ versus 10^{-14} for ambient water) can accelerate the acid-catalyzed, hydrolytic decomposition of algal biomacromolecules (5, 6). Algal biomass contains macromolecular proteins, polysaccharides, and lipids, along with inorganic components. The lipid fraction is generally targeted for fuels, but the protein and polysaccharide fractions also have heating value. Thus, conversion of the whole biomass into fuel can lead to biocrude yields exceeding the lipid content of the algae and a greater partitioning of the heating value

Chemical Engineering Department, University of Michigan, Ann Arbor, MI 48109, USA. E-mail: psavage@umich.edu

originally resident in the biomass into the final fuel product. Hydrothermal processing also facilitates reuse of nitrogen (N) and phosphorus needed for a sustainable process.

Hydrothermal conversion of biomass to fuels was described in the 1940s (7), and Shell developed a hydrothermal upgrading process in the 1980s (5). Approaches being developed for making fuels from wet algal biomass generally either first complete chemical conversion of the whole biomass and then separate the product fractions, or first fractionate the biomass and then convert the lipid fraction into fuel (see the figure). Hydrothermal treatment of algal biomass at temperatures of ~200°C generates carbonized solids (hydrochar) that can be filter-separated from water and contain nearly all of the lipids (8). The lipids exist as free fatty acids and mono-, di-, and triglycerides; the relative amounts depend on the extent of hydrolysis. The hydrochar can be dried and used directly as a solid fuel (9), or the lipids can be converted to biodiesel fuel by reacting the carbonized solids, either wet or dried, with an alcohol in a process called *in situ* transesterification.

Traditional base-catalyzed transesterification is not suitable because the hydrochar contains fatty acids that would form soaps. Acid-catalyzed transesterification is slower and typically requires higher temperatures than base-catalyzed reactions. Levine *et al.* (8) demonstrated that *in situ* transesterification proceeds readily in supercritical ethanol with no added catalyst and has promise as a route to biodiesel. Direct supercritical transesterification of lipids in freshly harvested wet algal biomass without any prior carbonization step has also been attempted, but the high moisture content [>90 weight (wt) %] presents challenges (10).

Hydrothermal treatment of algal biomass in liquid water at a higher temperature (~300° to 350°C) produces a viscous crude bio-oil that can contain 60 to 80% of the heating value of the biomass (4, 5, 11). This biocrude has a hydrogen to carbon ratio similar to that of the vacuum gas oil cut of a heavy petroleum crude oil, but it is richer in heteroatoms [N at ~3 to 5 wt % and oxygen (O) at ~8 to 10 wt %] that are unwanted in final products and that would not be removed if coprocessed with crude oil.

The biocrude from hydrothermal liquefaction can be upgraded thermally (12) or catalytically (13) to produce a crude bio-oil that is free-flowing at room temperature and has a reduced total heteroatom content. Removal of N atoms from the oil remains a challenge. This hydrothermal liquefaction path to renewable liquid fuels

does not require algae with a high lipid content, although such algae do tend to produce higher yields of crude bio-oil.

Hydrothermal treatment of algae at higher temperatures (e.g., 400° to 600°C) and pressures (e.g., 25 MPa) converts wet algal biomass to gaseous products that are useful as fuels or chemicals. Gasifying part of the algal biomass entering the biorefinery could provide CH₄ for thermal energy and H₂ for catalytic processes such as hydrotreating, hydrocracking, or hydrogenation. Supported ruthenium catalysts have achieved complete gasification of the carbon in algae (14, 15), but catalyst deactivation presents challenges.

The high N content in algal biocrudes from hydrothermal liquefaction, and the potential economic value of proteins and amino acids in some algae species, have motivated work on the extraction of these coproducts. Moscoso and Kumar report that proteins or amino acids can be extracted from algal biomass in subcritical water on a time scale of seconds (16); the balance of the biomass can then be converted to biocrude or biodiesel. Likewise, polysaccharides can be extracted hydrothermally from algae and the extracted biomass then liquefied to make bio-crude (17).

Supercritical CO₂ has been used to remove lipids first from wet algal biomass (18) at temperatures of ~100°C, which are lower than those used for hydrothermal extraction and processing, but the optimal pressure is much higher (e.g., 40 MPa). Moreover, the

conditions used are far from the critical point of CO₂, so some of the solubility advantages of supercritical fluid extraction vanish.

Finally, it is likely that optimal processing conditions will vary with the biochemical content of the alga. Research is moving toward elucidating the chemistry of biomolecules in these rich and complex reaction systems.

References

1. M. Y. Khan *et al.*, *Energy Fuels* **26**, 6137 (2012).
2. www.reuters.com/article/2012/07/05/usa-navy-green-fleet-idUSL2E8157HE20120705
3. U.S. DOE 2010, *National Algal Biofuels Technology Roadmap*, U.S. Department of Energy, Office of Energy Efficiency and Renewable Energy, Biomass Program; <http://biomass.energy.gov>.
4. P. Biller, A. B. Ross, *Biofuels* **3**, 603 (2012).
5. P. E. Savage, R. B. Levine, C. M. Huelsman, in *Thermochemical Conversion of Biomass to Liquid Fuels and Chemicals*, M. Crocker, Ed. (Royal Society of Chemistry, Cambridge, UK, 2010), pp. 195–221.
6. N. Akiya, P. E. Savage, *Chem. Rev.* **102**, 2725 (2002).
7. E. Berl, *Science* **99**, 309 (1944).
8. R. B. Levine *et al.*, *Energy Fuels* **24**, 5235 (2010).
9. S. M. Heilmann *et al.*, *Biomass Bioenergy* **34**, 875 (2010).
10. P. D. Patil *et al.*, *Bioresour. Technol.* **102**, 118 (2011).
11. P. J. Valdez *et al.*, *Biomass Bioenergy* **46**, 317 (2012).
12. S. G. Roussis *et al.*, *Energy Fuels* **26**, 5294 (2012).
13. P. Duan, P. E. Savage, *Bioresour. Technol.* **102**, 1899 (2011).
14. S. Stucki *et al.*, *Energy Environ. Sci.* **2**, 535 (2009).
15. Q. Guan *et al.*, *Energy Fuels* **26**, 4575 (2012).
16. http://abstracts.acs.org/chem/243nm/program/view.php?pub_num=98&par=1%26EC
17. M. Chakraborty *et al.*, *Fuel* **95**, 63 (2012).
18. L. Soh, J. Zimmerman, *Green Chem.* **13**, 1422 (2011).

10.1126/science.1224310

PLANETARY SCIENCE

The Origin of the Moon

Alex N. Halliday

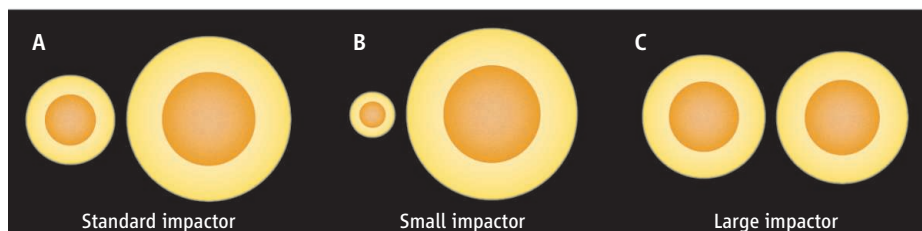
Model simulations provide a new picture of how the Earth-Moon system may have formed.

The Apollo program radically changed our understanding of the origin of Earth and the Moon. The return of a large number of samples for analysis, allowing the determination of isotopic, chemical, and mineralogical compositions of lunar rocks, resulted in a “scientific giant leap” and also posed a particular challenge. Samples from the Moon have primordial isotopic compositions identical to those of Earth, whereas current models predict that they should be distinct, like other solar system

materials. On pages 1047 and 1052 of this issue, Ćuk and Stewart (1) and Canup (2) provide simulations that offer differing solutions to the problem.

Any successful model of lunar origin has to explain the Moon’s angular momentum and its slightly lower density (than Earth). With the return of samples, a number of other constraints became apparent. First, the Moon formed relatively late given its size. Tungsten isotopic data (3) require that the Moon formed more than 30 million years after the start of the solar system, whereas most objects this size are predicted to have formed in the first few hundred thousand years (4). Second, the oldest rocks appear to have

Department of Earth Sciences, Oxford University, South Parks Road, Oxford, OX1 3AN UK. E-mail: alexh@earth.ox.ac.uk



Collision scenarios. Examples of the three new models of the Moon-forming Giant Impact, each of which allows more angular momentum to be lost and thereby achieves oxygen isotopic compositions that cannot be resolved between Earth and the Moon. (A) “Standard” impactor, 10% of Earth’s final mass, works with “hit and run” collision (14). (B) “Small” impactor, 2.5% of Earth’s final mass (1). (C) “Large” impactor, 45% of Earth’s final mass (2).

formed from a magma ocean (5), implying an intensely energetic fiery start at a time when heat-producing short-lived nuclides (^{26}Al and ^{60}Fe) were extinct. Third, the oxygen isotopic composition of the Moon is identical to that of Earth (6) to within 5 parts per million, whereas that of nearly all asteroidal and planetary objects are different.

The Giant Impact Theory is the resultant widely accepted current explanation for the Moon’s late, molten start as a low-density object that now contributes most of the angular momentum in the Earth-Moon system. Following an early similar model (7), dynamic models using smooth particle hydrodynamic code have been deployed (8, 9) to track the temperature and fate of silicate and dense iron metal resulting from the oblique collision of two planets. In most models, this has been an Earth when it was about 85 to 90% formed and another planet, sometimes called Theia, that was about 10 to 15% of the mass of Earth or roughly the size of Mars (see the figure, panel A). Simulations of this catastrophic glancing blow show that most of the material from Theia was added to Earth, with a small fraction of silicate-rich material left as a disk from which the Moon accreted.

In nearly all “successful” Giant Impact simulations, the material that ends up in the Moon is mainly derived from Theia. To account for the identical isotopic composition, it was proposed that Theia and Earth must have formed at similar heliocentric distances—but then it is difficult to explain why the Giant Impact was so late. Perhaps at the high temperatures achieved during the Giant Impact, Earth’s mantle and lunar accretion disk would have remained in vapor and liquid form long enough to achieve isotopic equilibration by mixing and diffusion (10). This would work for elements as volatile as oxygen. However, refractory elements such as tungsten and titanium are also isotopically identical (3, 11). Further mixing of refractory elements might have occurred during rainout of condensates (12). However, the identical

silicon isotopic composition of Earth and the Moon (13) is not readily explained; the rain-out process is expected to generate a silicon isotopic difference, so the problem persists.

The papers by Ćuk and Stewart and by Canup remove the major constraint that the initial angular momentum was generated by the Giant Impact. Ćuk and Stewart propose instead that after the Moon formed the system was rotating far faster, that Earth could also have been doing so beforehand, and that it has been slowed subsequently as a consequence of a resonance in tidal forces with the Sun. This opens up the possibility of different impact scenarios. Earth itself could have been left spinning rapidly after its prior accretion history, such that a relatively small proportion of the angular momentum of the Earth-Moon system today is the result of the Giant Impact. Without this constraint, it is then possible to investigate a broader array of impact scenarios, and this is where the two papers diverge.

Ćuk and Stewart investigate solutions with a relatively small Theia (less than 10% of Earth’s mass) and a pre-impact angular momentum two to three times that of today. In one example with a mass of Theia of only 2% of Earth’s final mass (see the figure, panel B), they achieve formation of a lunar mass of material in orbit with only 8% being derived from Theia, which compares with a final Earth with as little as 2%. This small proportion of impactor material in both objects limits the possibilities for there being Earth-Moon isotopic differences.

Canup goes to the opposite extreme with models exploring the possibility that Theia was 30 to 45% of the current Earth (see the figure, panel C). As Theia gets bigger, the proportions of the proto-Earth:Theia mix become closer in the two objects. The result is tested using assumptions of isotopic diversity, the strongest constraint for which comes from oxygen that a Theia of more than 40% of the total mass appears to satisfy.

Another class of models has been proposed simultaneously (14), arguing for very

energetic hit-and-run collisions between a Theia with the more conventional 10% Earth mass and removal of angular momentum by loss of material from the system (see the figure, panel A). As with the Ćuk and Stewart model, most of the material in the Moon is derived from the proto-Earth.

Distinguishing among these three models is going to involve further simulation and debate. Geochemical constraints may again prove decisive in three ways.

First, tungsten isotopes are sensitive to equilibration between incoming metal from the impactor’s core and tungsten in the silicate Earth (15). Such equilibration will vary with impact angle (16) and should lead to different isotopic compositions between silicate Earth and Moon after further post-impact equilibration and core formation. This will be less of an issue with a small impactor.

Similarly, the silicon isotopic composition of Earth and the Moon are identical (13), and this is a signature of high-pressure core formation that has been transferred to the Moon. If there is a major increase in the size of Earth, as in the Canup model, it might be expected to further fractionate silicon isotopes relative to the Moon.

Finally, for the particularly energetic models (2, 14), this would be expected to lead to widespread melting and mixing. Yet recent results (17) provide evidence of deep reservoirs with noble gas isotopic heterogeneities that have been preserved since about the time of the Giant Impact. It is not known whether these are localized or widespread, but their presentation is intriguing in a planet that supposedly was built by repeated highly energetic accretion.

References

1. M. Ćuk, S. T. Stewart, *Science* **338**, 1047 (2012); 10.1126/science.1225542.
2. R. M. Canup, *Science* **338**, 1052 (2012); 10.1126/science.1226073.
3. M. Touboul, T. Kleine, B. Bourdon, H. Palme, R. Wieler, *Nature* **450**, 1206 (2007).
4. J. E. Chambers, *Earth Planet. Sci. Lett.* **223**, 241 (2004).
5. G. J. Taylor, *Elements* **5**, 17 (2009).
6. U. Wiechert et al., *Science* **294**, 345 (2001).
7. W. K. Hartmann, D. R. Davis, *Icarus* **24**, 505 (1975).
8. A. G. W. Cameron, W. Benz, *Icarus* **92**, 204 (1991).
9. R. M. Canup, E. Asphaug, *Nature* **412**, 708 (2001).
10. K. Pahlevan, D. J. Stevenson, *Earth Planet. Sci. Lett.* **262**, 438 (2007).
11. J. Zhang, N. Dauphas, A. M. Davis, I. Leya, A. Fedkin, *Nat. Geosci.* **5**, 251 (2012).
12. K. Pahlevan, D. J. Stevenson, J. M. Eiler, *Earth Planet. Sci. Lett.* **301**, 433 (2011).
13. R. M. G. Armytage, R. B. Georg, H. M. Williams, A. N. Halliday, *Geochim. Cosmochim. Acta* **77**, 504 (2012).
14. A. Reufer, M. M. M. Meier, W. Benz, R. Wieler, *Icarus* **221**, 296 (2012).
15. A. N. Halliday, *Nature* **427**, 505 (2004).
16. T. W. Dahl, D. J. Stevenson, *Earth Planet. Sci. Lett.* **295**, 177 (2010).
17. S. Mukhopadhyay, *Nature* **486**, 101 (2012).

10.1126/science.1229954

The Protein-Folding Problem, 50 Years On

Ken A. Dill^{1,2,3*} and Justin L. MacCallum¹

The protein-folding problem was first posed about one half-century ago. The term refers to three broad questions: (i) What is the physical code by which an amino acid sequence dictates a protein's native structure? (ii) How can proteins fold so fast? (iii) Can we devise a computer algorithm to predict protein structures from their sequences? We review progress on these problems. In a few cases, computer simulations of the physical forces in chemically detailed models have now achieved the accurate folding of small proteins. We have learned that proteins fold rapidly because random thermal motions cause conformational changes leading energetically downhill toward the native structure, a principle that is captured in funnel-shaped energy landscapes. And thanks in part to the large Protein Data Bank of known structures, predicting protein structures is now far more successful than was thought possible in the early days. What began as three questions of basic science one half-century ago has now grown into the full-fledged research field of protein physical science.

Protein molecules embody a remarkable relationship between structure and function at the molecular level. Proteins perform many different functions in biochemistry. A protein's biological mechanism is determined by its three-dimensional (3D) native structure, which in turn is encoded in its 1D string of amino acid monomers.

This year marks the 50th anniversary of the 1962 Nobel Prize in Chemistry awarded to Max Perutz and John Kendrew for their pioneering work in determining the structure of globular proteins (1–3). That work laid the foundation for structural biology, which interprets molecular-level biological mechanisms in terms of the structures of proteins and other biomolecules. Their work also raised the question of how protein structures are explained by physical principles. Upon seeing the structure of myoglobin (Fig. 1) at 6 Å resolution (1), Kendrew *et al.* said,

“Perhaps the most remarkable features of the molecule are its complexity and its lack of symmetry. The arrangement seems to be almost totally lacking in the kind of regularities which one instinctively anticipates, and it is more complicated than has been predicated by any theory of protein structure. Though the detailed principles of construction do not yet emerge, we may hope that they will do so at a later stage of the analysis.”

The protein-folding problem came to be three main questions: (i) The physical folding code: How is the 3D native structure of a protein determined by the physicochemical properties that are encoded in its 1D amino-acid sequence? (ii)

The folding mechanism: A polypeptide chain has an almost unfathomable number of possible conformations. How can proteins fold so fast? (iii) Predicting protein structures using computers: Can we devise a computer algorithm to predict a protein's native structure from its amino acid sequence? Such an algorithm might circumvent the time-consuming process of experimental protein-structure determination and accelerate the discovery of protein structures and new drugs.

Here, we give our perspective on these questions at the broad-brush level. More detailed reviews can be found elsewhere (4–8).

The Physical Code of Protein Folding

What forces drive a protein to its 3D folded structure? Much insight comes from the Protein Data Bank (PDB), a collection of now more than 80,000 protein structures at atomic detail (9). The following factors appear to contribute (10): (i) Hydrogen bonds. Protein structures are composed of α -helices and β -sheets, as was predicted by Linus Pauling on the basis of expected hydrogen bonding patterns (11). (ii) van der Waals interactions. The atoms within a folded protein are tightly packed, implying the importance of the same types of close-ranged interactions that govern the structures of liquids and solids. (iii) Backbone angle preferences. Like other types of polymers, protein molecules have preferred angles of neighboring backbone bond orientations. (iv) Electrostatic interactions. Some amino acids attract or repel because of negative and positive charges. (v) Hydrophobic interactions. Proteins ball up into well-packed folded states in

which the hydrophobic (H) amino acids are predominantly located in the protein's core and the polar (P) amino acids are more commonly on the folded protein's surface. Theory and experiments indicate that folding is governed by a predominantly binary code based on interactions with surrounding water molecules: There are few ways a given protein sequence of H and P residues can configure to bury its hydrophobic amino acids optimally (12, 13). (vi) Chain entropy. Opposing the folding process is a large loss in chain entropy as the protein collapses into its compact native state from its many open denatured configurations (12).

These physical forces are described approximately by “forcefields” (14). Forcefields are models of potential energies that are used in computer simulations. They are widely applied to studies of protein equilibria and dynamics. In computer modeling, a protein molecule is put into an initial configuration, often random. Conformations change over the course of the simulation by repeatedly solving Newton's dynamical laws of motion for the atoms of the protein molecule and the solvent by using the forcefield energies. According to the laws of thermodynamics, systems tend toward their states of lowest free energy. Computational protein folding explores the process by which the protein proceeds through conformational states to states of lower free energies. As shown in Fig. 2, the thermodynamically stable states of 12 small protein structures can be reached fairly successfully by means of extensive molecular dynamics (MD) simulations in a bath of



Fig. 1. In 1958, Kendrew and co-workers published the first structure of a globular protein: myoglobin at 6 Å resolution (1). Its puzzlingly complex structure lacked the expected symmetry and regularity and launched the protein-folding problem. [With permission from the Medical Research Council Laboratory of Molecular Biology]

¹Laufer Center for Physical and Quantitative Biology, Stony Brook University, Stony Brook, NY 11794–5252, USA. ²Department of Physics, Stony Brook University, Stony Brook, NY 11794–3800, USA. ³Department of Chemistry, Stony Brook University, Stony Brook, NY 11794–3400, USA.

*To whom correspondence should be addressed. E-mail: dill@laufercenter.org

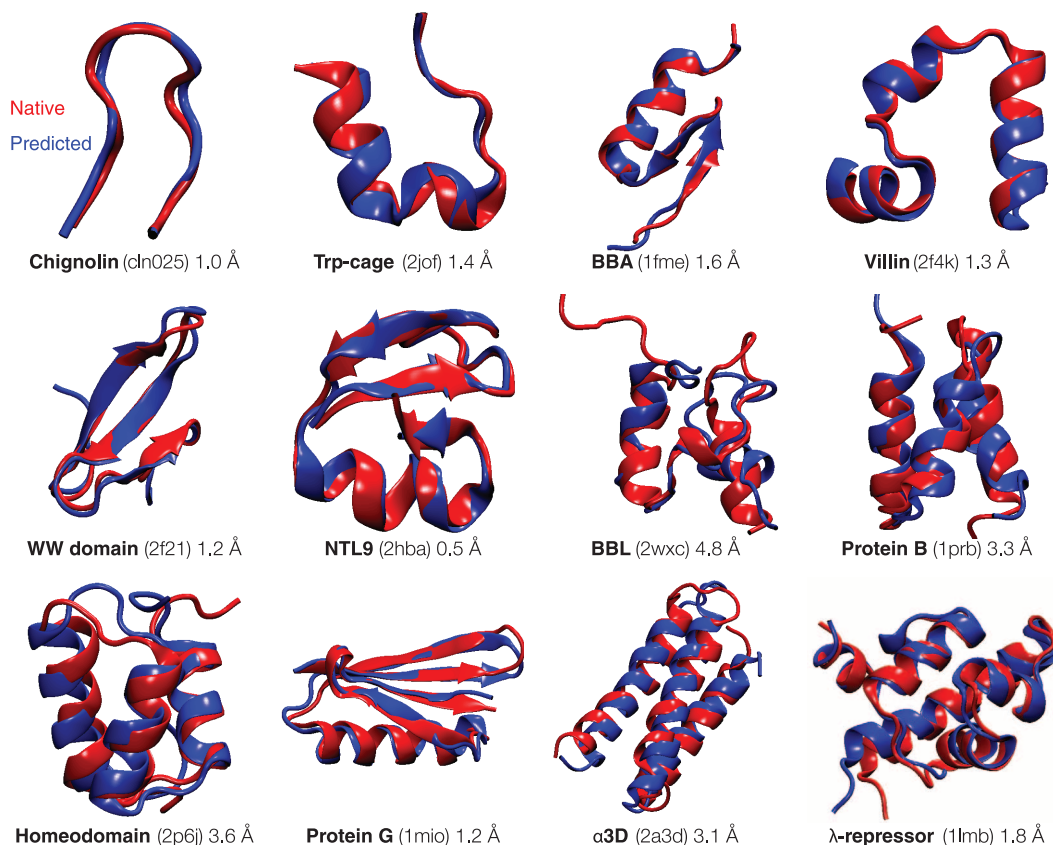


Fig. 2. Modern physical models can compute the folded structures of some small proteins. Using a high-performance custom computer called Anton (48), Shaw and co-workers observed reversible folding and unfolding in more than 400 events across 12 small proteins to structures within 4.5 Å of the experimental structure (15). The experimental structures are shown in red, and the computed structures are blue. Shown are the name, PDB identifier, and RMSD (root-mean-square deviation between alpha carbon atoms) between the predicted and experimental structures. [Adapted with permission (15)]

explicit water molecules (15). However, such successes, important as they are, are limited. So far, such modeling succeeds only on a limited set of small simple protein folds (16). And, it does not yet accurately predict protein stabilities or thermodynamic properties. Opportunities for the future include better forcefields, better models of the protein-water interactions, and faster ways to sample conformations, which are far too limited, even with today's most powerful computers.

The early days saw hopes of finding simple sequence patterns—say of hydrophobic, polar, charged, and aromatic amino acids—that would predict protein structures and stabilities. That has not materialized. Nevertheless, the results of the detailed atomic simulations described above give optimism that atomically detailed modeling is systematically improving and is contributing to our understanding of protein sequence-structure relationships.

The Rate Mechanism of Protein Folding

At a meeting in Italy in 1968, Cyrus Levinthal raised the question (17) of how, despite the huge number of conformations accessible to it, a protein molecule can fold to its one precisely defined native structure so quickly (microseconds, for some proteins). How does the protein “know” what conformations not to search?

This question led to a major experimental quest to characterize the kinetics of protein folding and to find folding intermediates, which are partially structured states along the “folding pathway” (18, 19). The hope was that snapshots of the chain caught in the act of folding would give insights into folding “mechanisms,” the rules by which nature performs conformational searching. The experimental challenge was not just to measure atom-by-atom contacts within the heterogeneous interior of a protein molecule, but to do it on the fly, over microsecond-to-second time scales. This drove development of a powerful arsenal of new experimental methods, including mutational studies, hydrogen exchange, fluorescence labeling, laser temperature jumps, and single-molecule methods [reviewed elsewhere (7)].

The general-principles solution of the needle-in-a-haystack conundrum emerged from polymer statistical thermodynamics. Studies of the chain entropies in models of foldable polymers showed that more compact, low-energy conformational ensembles have fewer conformations (12, 20–23), indicating that protein-folding energy landscapes are funnel-shaped (Fig. 3). Protein folding landscapes are narrower at the bottom; there are few low-energy, native-like conformations and many more open unfolded structures. A protein folds by

taking random steps that are mostly incrementally downhill in energy. Steps need only be favorable by one to two times the thermal energy to reach the native structure rapidly (24). Insights from funnels, however, have not yet been sufficient to improve computer search methods. A landscape that appears smooth and funnel-shaped on a global scale can be rough on the local scales that are sampled in computer simulations.

But we are still missing a “folding mechanism.” By mechanism, we mean a narrative that explains how the time evolution of a protein's folding to its native state derives from its amino acid sequence and solution conditions. A mechanism is more than just the sequences of events followed by any one given protein in experiments or in computed trajectories. We do not yet have in hand a general principle that is applicable to a broad range of proteins, that would explain differences and similarities of the folding routes and rates of different proteins in advance of the data, and that properly average, in some meaningful way, over “irrelevant” thermal motions. One difficulty has been reconciling our “macroscopic” understanding of kinetics (mass-action models) that

result from ensemble-averaged experiments with our “microscopic” understanding of the angstrom-by-angstrom changes of each protein conformation in computer simulations (energy landscapes). However, there are a few general conclusions (25). Proteins appear to fold in units of secondary structures. A protein's stability increases with its growing partial structure as it folds. And, a protein appears to first develop local structures in the chain (such as helices and turns) followed by growth into more global structures. Even though the folding process is blind, nevertheless it can be fast because native states can be reached by this divide-and-conquer, local-to-global process (26, 27). Funneled landscapes predict that the different individual molecules of the same protein sequence may each follow microscopically different routes to the same native structure. Some paths will be more populated than others.

Computing Protein Structures from Amino Acid Sequences

A grand challenge has been to develop a computer algorithm that can predict a protein's 3D native structure from its amino acid sequence. On the one hand, knowledge of native structures is a starting point for understanding biological mechanisms and for discovering drugs that can

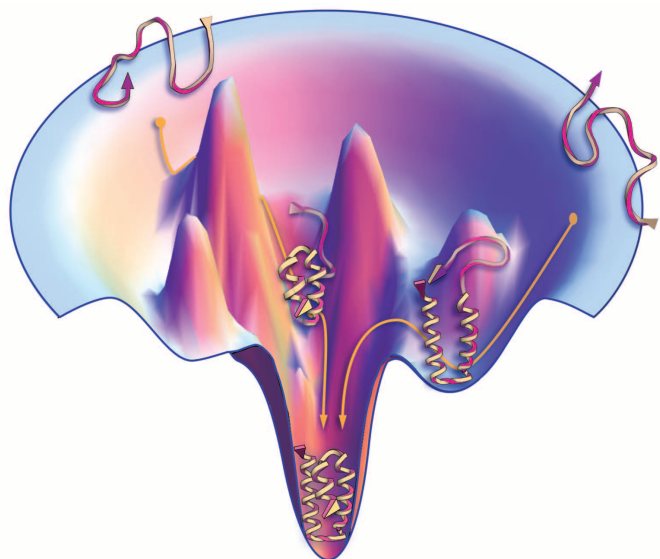


Fig. 3. Proteins have a funnel-shaped energy landscape with many high-energy, unfolded structures and only a few low-energy, folded structures. Folding occurs via alternative microscopic trajectories.

inhibit or activate those proteins. On the other hand, we know 1000-fold more sequences than structures, and this gap is growing because of developments in high-throughput sequencing. So, there is considerable value in methods that could accurately predict structures from sequences.

Computer-based protein-structure prediction has been advanced by Moulton and colleagues, in an event initiated in 1994 called CASP: Critical Assessment of protein Structure Prediction (28, 29). Held every second summer, CASP is a community-wide blind competition in which typically more than 100 different “target sequences” (of proteins whose structures are known but not yet publicly available) are made available to a community that numbers more than 150 research groups around the world. Each participating group applies some algorithmic scheme that aims to predict the 3D structures of these target proteins. After each CASP event, the true experimental structures are then revealed, group performances are evaluated, and community evaluations are published.

Currently, all successful structure-prediction algorithms are based on assuming that similar sequences lead to similar structures. These methods draw heavily on the PDB, which now contains more than 80,000 structures. However, many of these structures are similar, and the PDB contains only ~4000 structural families and 1200 folds (30).

CASP-wide progress over the past 18 years is summarized in Fig. 4A. Prediction accuracies improved from CASP1 (1994) to CASP5 (2002) on the basis of several advances: (i) PDB expanded from ~1600 structures to 19,000 during that time. (ii) Better sequence search and alignment tools, such as Position-Specific Iterated Basic Local Alignment Search Tool (PSI-BLAST) (31), enabled the detection of more remote evolutionary relationships and more accurate sequence alignments. (iii) A strategy, called the

“fragment assembly approach” (32–35), was developed that can often improve predictions when a similar sequence cannot be found in the PDB.

If the target protein’s sequence is related to a sequence that is already in the PDB, predicting its structure is usually easy (Fig. 4). In such cases, target protein structures are predicted by using “template-based modeling” (also called homology modeling or comparative modeling). But when there is no protein in the PDB with a sequence resembling the target’s, accurately predicting the structure of the target is much more difficult. These latter predictions are called “free modeling” (also called *ab initio* or *de novo* prediction). One of the most successful free-modeling techniques is fragment assembly, described below. Many prediction methods are hybrids, combining template-based modeling, fragment assembly, and other strategies.

In fragment assembly (32–35), a target protein sequence is deconstructed into small, overlapping fragments. A search of the PDB is performed to identify known structures of similar fragment sequences, which are then assembled into a full-length prediction. The qualities of fragments and their assemblies are assessed by using some form of scoring function that aims to select more native-like protein structures from among the many possible combinations. Problems of folding physics described above share more commonality with free modeling than with template-based modeling.

Since CASP6, although overall progress has slowed (Fig. 4A), there has been systematic, incremental progress (36). The best groups can now on average produce models that are better than the single best template from the PDB. Progress has been made toward successfully combining multiple templates into a single prediction. Substantial improvements have been observed for free-modeling targets shorter than 100 amino acids, although no single group yet consistently produces accurate models. Larger free-modeling targets remain challenging. Several recent algorithmic developments—to predict residue-residue contacts from sequence alone (37–39) and to more sensitively and accurately identify remote homologs (40)—promise to further improve prediction accuracy.

The performance of two of the best fully automated server predictors during CASP9 (41) are shown in Fig. 4B: HHPred, a pure template-based modeling tool (42), and ROSETTA, a hybrid tool

that combines fragment assembly and template-based modeling with all-atom refinement (43). For some fraction of CASP targets [~10%, based on a cutoff of 85 Global Distance Test–Total Score (GDT-TS) (44), which is defined in Fig. 4, legend], the best predictions are now accurate enough to interpret biological mechanisms, to guide biochemical studies, or to initiate a drug-discovery program (which requires structural errors of less than 2 to 3 Å). However, it remains a challenge to predict the other 90% of protein structures this accurately. In addition, it is critical to also improve physics-based technologies and to reduce our dependence on knowledge of existing structures, so that we can ultimately study protein motions, intrinsically disordered proteins, induced-fit binding of drugs, and membrane proteins and foldable polymers, for which databases are too limited.

Protein Folding: The Legacy of a Basic Science

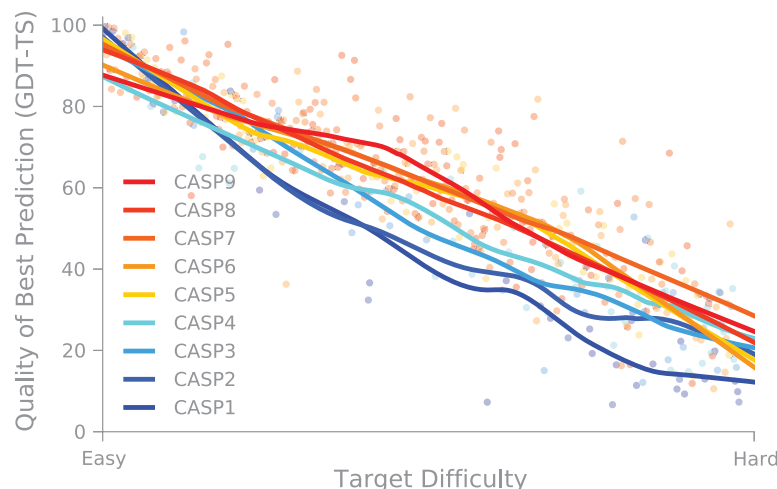
Protein folding is a quintessential basic science. There has been no specific commercial target, yet the collateral payoffs have been broad and deep. Specific technical advances are reviewed elsewhere (7); below, we describe a few general outgrowths.

Growth of protein-structure databases. Today, more than 80,000 protein structures are known at atomic detail and publically available through the PDB. New structures are being added at a rapid pace, supported by the National Institutes of Health (NIH)–funded Protein Structure Initiative, which was developed in part to inform protein structure prediction.

Advances in computing technology. Understanding protein folding was a key motivation for IBM’s development of the Blue Gene supercomputer (45), now also used to study the brain, materials, weather patterns, and quantum and nuclear physics. Protein folding has also driven key advances in distributed-grid computing, such as in Folding@home, developed by Pande at Stanford, in which computer users all over the world donate their idle computer time to perform physical simulations of protein systems (46). Folding@home, which now has more than one million registered users and an average of 200,000 user-donated CPUs available at any one time, provided some of the earliest simulations showing that MD simulations can accurately predict folding rates (47). The Anton computer from DE Shaw Research, custom designed to simulate biomolecules, gives several orders of magnitude better performance than conventional computers (48). Advances in computer technology have led to major advances in forcefields and to more reliable atomic-level insights into biological mechanisms.

Improvements in biomolecular forcefields. Computer processing power has advanced at the Moore’s law rate, doubling every ~2 years. But equally important, forcefields have kept pace. Increased computer power leads to longer computed time scales, which puts more stringent demands on the accuracies of biomolecular forcefields. In a pioneering paper in 1977, McCammon *et al.*

A Historical CASP Performance



B Performance in CASP9

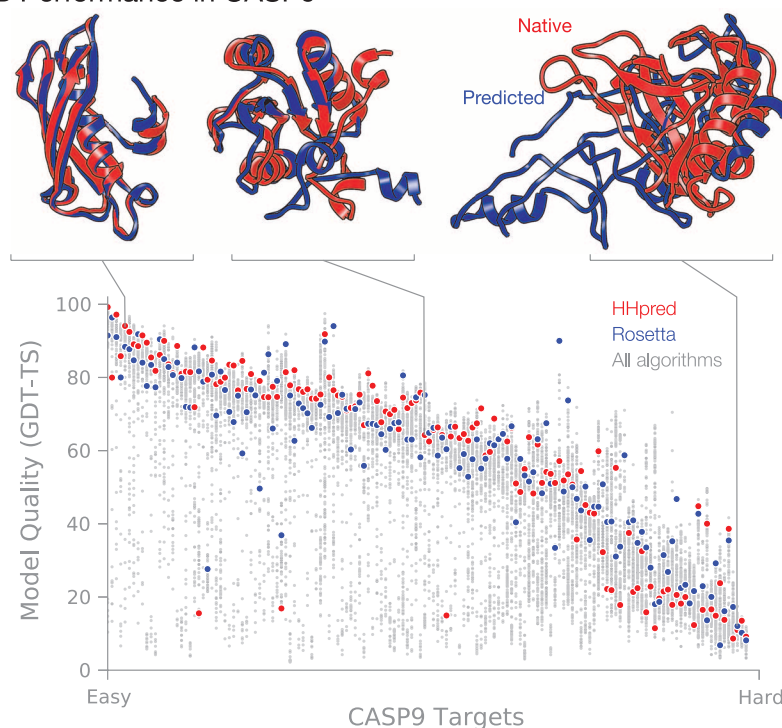


Fig. 4. Historical and present performance in CASP. Model quality is judged by using GDT-TS (44), which is approximately the percentage of residues that are located in the correct position. **(A)** Evolution of accuracy over the history of CASP, spanning 18 years. Each target is classified according to an approximate measure of difficulty that incorporates both the structural and sequence similarity to proteins of known structure (36). Each dot represents the best prediction (across all participants) for a given target. **(B)** Summary of prediction accuracy in CASP9 (41). We highlight the performance of two of the best automated server algorithms. Selected predictions are superimposed on the corresponding native structures to give a visual sense of the accuracy level that can be expected.

showed that the BPTI protein was stable in computer simulations during a computed time of 10 ps (49). Today, small proteins are typically stable in explicit-water simulations for 5 to 8 orders of magnitude longer—microseconds to milliseconds of computed time (50). Achieving such advances has required continuous improvements in force-field accuracy.

New sociological structures in the scientific enterprise. Protein folding has driven innovations in how science is done. CASP was among the first community-wide scientific competitions/collaborations, a paradigm for how grand-challenge science can be advanced through an organized communal effort. Other such competitions have followed, including Critical As-

essment of Prediction of Interactions (CAPRI) (predicting protein-protein docking) (51), SAMPL (predicting small-molecule solvation free energies, and ligand binding modes and affinities) (52), and GPCR-Dock (predicting structures for G-protein coupled receptors, a pharmaceutically important category of membrane proteins) (53), among many others. Protein folding has also pioneered “citizen science,” such as in Folding (46) and Robetta@home and in a computer game called Foldit (54), in which the public engages in protein folding on their home computers.

New materials: Sequence-specific foldable polymers. The principles and algorithms developed for protein folding have led to nonbiological, human-made proteins and to new types of polymeric materials. In particular, proteins have been designed that bind to and inhibit other proteins (fig. 5A) (55), have new folds (56), have new enzymatic activities (57), and act as potential new vaccines (58). Also, a class of nonbiological polymers has emerged, called “foldamers,” that are intended to mimic protein structures and functions (59–62). Foldamers already have broad-ranging applications (63–67) as inhibitors of protein-protein interactions, broad-spectrum antibiotics, lung surfactant mimics, optical storage materials, a zinc-finger-like binder, an RNA-protein binding disrupter for application in muscular dystrophy, gene transfection agents, and “molecular paper” (Fig. 5B). Although such materials have potential applications in biomedicine and materials science, they also provide a way for us to test and deepen our understanding of protein folding.

Protein-folding diseases. Protein-folding research began before it was known that there are diseases of protein folding. Before 1972, it was assumed that all infectious diseases were transmitted through the DNA and RNA carried by viruses and bacteria. But Prusiner’s studies of a patient with Creutzfeldt-Jakob disease (CJD) led to a previously unrecognized disease mechanism—namely, protein misfolding (68). Protein misfolding is now known to be important in many diseases, including CJD and type II diabetes, as well as neurodegenerative diseases such as Alzheimer’s, Parkinson’s, Huntington’s, and amyotrophic lateral sclerosis. The protein-folding enterprise has provided important underpinnings for our understanding of folding diseases.

Unsolved Problems of Protein Physical Science

Is the protein-folding problem “solved” yet (69)? We believe it is no longer useful to frame the question this way. Protein folding is now a whole field of research—a large, growing, and diverse enterprise. A field of science—such as physics, chemistry, or biology—is bigger than any individual research question. A field is self-perpetuating; a few old puzzles generate more new puzzles. For the field of protein physical science, the future is at least as compelling as the past. Here are some of the unsolved problems:

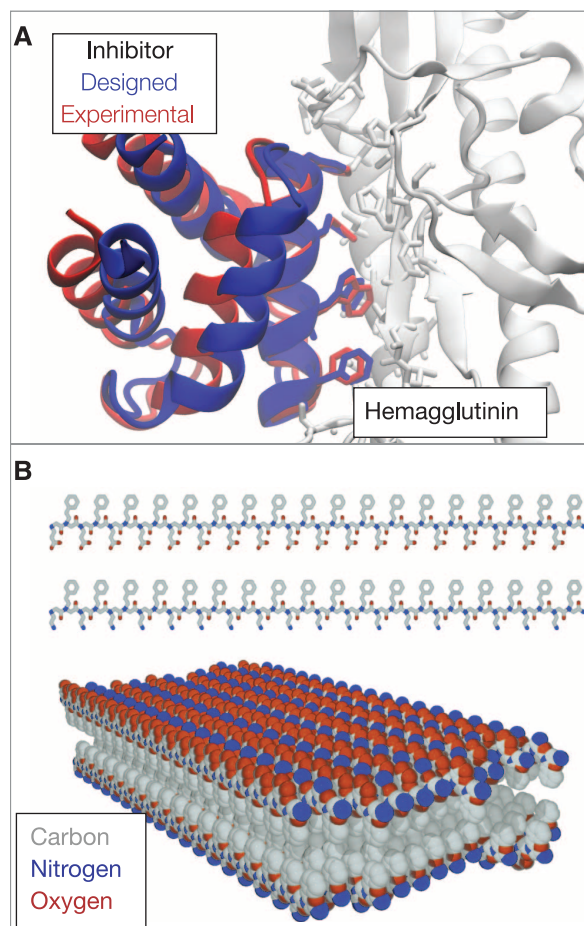


Fig. 5. Designed proteins and foldamers. **(A)** A protein inhibitor that was designed by computer to bind to hemagglutinin, an influenza protein. After design, the inhibitor was crystallized in a complex with hemagglutinin. The designed structure is in remarkably good agreement with experiment, particularly for the side chains involved in binding. [Adapted with permission (55)] **(B)** Peptoids are synthetic, foldable, protein-inspired polymers that have various applications. Shown here are peptoids that were designed as chains of alternating hydrophobic (gray) and either positively (blue) or negatively (red) charged side chains that spontaneously form a thin 2D structure called molecular paper. [Reprinted by permission (67)]

We have little experimental knowledge of protein-folding energy landscapes.

We cannot consistently predict the structures of proteins to high accuracy.

We do not have a quantitative microscopic understanding of the folding routes or transition states for arbitrary amino acid sequences.

We cannot predict a protein's propensity to aggregate, which is important for aging and folding diseases.

We do not have algorithms that accurately give the binding affinities of drugs and small molecules to proteins.

We do not understand why a cellular proteome does not precipitate, because of the high density inside a cell.

We know little about how folding diseases happen, or how to intervene.

Despite their importance, we still know relatively little about the structure, function, and folding of membrane proteins (70, 71).

We know little about the ensembles and functions of intrinsically disordered proteins (72), even though nearly half of all eukaryotic proteins contain large disordered regions. This is sometimes called the “protein nonfolding problem” or “unstructural biology.”

Summary

Fifty years ago, the protein-folding problem was born as a grand challenge of basic science. Since then, our understanding has advanced considerably. And, outgrowths of protein folding include the commercial development of new computers, such as IBM's Blue Gene; new modes of citizen science, including Folding@Home and Foldit; the development of communal scientific competitions, such as CASP; a database of now more than 80,000 protein structures; the Moore's-Law advancement in biomolecular simulation forcefields; new areas of materials science based on foldable polymers; and a foundation for understanding whole new classes of diseases—such as Alzheimer's, Parkinson's, and type II diabetes, called folding diseases—that were not even known when the protein-folding problem was first identified.

In times when there are pressures on science budgets for immediate payoffs, it is worth repeating the well-worn point that untargeted basic science often pays off in unexpected ways.

References and Notes

1. J. C. Kendrew *et al.*, *Nature* **181**, 662 (1958).
2. J. C. Kendrew *et al.*, *Nature* **185**, 422 (1960).
3. M. F. Perutz *et al.*, *Nature* **185**, 416 (1960).
4. C. M. Dobson, *Nature* **426**, 884 (2003).
5. A. R. Fersht, *Nat. Rev. Mol. Cell Biol.* **9**, 650 (2008).
6. J. E. Shea, C. L. Brooks III, *Annu. Rev. Phys. Chem.* **52**, 499 (2001).
7. K. A. Dill *et al.*, *Annu. Rev. Biophys.* **37**, 289 (2008).
8. G. R. Bowman *et al.*, *Curr. Opin. Struct. Biol.* **21**, 4 (2010).
9. H. M. Berman *et al.*, *Nucleic Acids Res.* **28**, 235 (2000).
10. K. A. Dill, *Biochemistry* **29**, 7133 (1990).
11. L. Pauling *et al.*, *Proc. Natl. Acad. Sci. U.S.A.* **37**, 205 (1951).
12. K. A. Dill, *Biochemistry* **24**, 1501 (1985).
13. S. Kamtekar *et al.*, *Science* **262**, 1680 (1993).
14. J. W. Ponder, D. A. Case, *Adv. Protein Chem.* **66**, 27 (2003).
15. K. Lindorff-Larsen *et al.*, *Science* **334**, 517 (2011).
16. A. Raval *et al.*, *Proteins* **80**, 2071 (2012).
17. C. Levinthal, *J. Chim. Phys.* **65**, 44 (1968).
18. P. S. Kim, R. L. Baldwin, *Annu. Rev. Biochem.* **59**, 631 (1990).
19. C. R. Matthews, *Annu. Rev. Biochem.* **62**, 653 (1993).
20. J. D. Bryngelson, P. G. Wolynes, *Proc. Natl. Acad. Sci. U.S.A.* **84**, 7524 (1987).
21. P. E. Leopold *et al.*, *Proc. Natl. Acad. Sci. U.S.A.* **89**, 8721 (1992).
22. J. D. Bryngelson *et al.*, *Proteins* **21**, 167 (1995).
23. K. Dill, H. S. Chan, *Nat. Struct. Biol.* **4**, 10 (1997).
24. R. Zwanzig *et al.*, *Proc. Natl. Acad. Sci. U.S.A.* **89**, 20 (1992).
25. S. W. Englander *et al.*, *Q. Rev. Biophys.* **40**, 287 (2008).
26. J. Hockenmaier *et al.*, *Proteins* **66**, 1 (2006).
27. V. A. Voelz, K. A. Dill, *Proteins* **66**, 877 (2007).
28. J. Moulton, *Curr. Opin. Struct. Biol.* **15**, 285 (2005).
29. J. Moulton *et al.*, *Proteins* **79**, (suppl. 10), 1 (2011).
30. A. G. Murzin *et al.*, *J. Mol. Biol.* **247**, 536 (1995).
31. S. F. Altschul *et al.*, *Nucleic Acids Res.* **25**, 3389 (1997).
32. D. T. Jones, *Proteins* **45**, 127 (2001).
33. D. T. Jones, L. J. McGuffin, *Proteins* **53**, (Suppl 6), 480 (2003).
34. K. T. Simons *et al.*, *Proteins* **37**, 171 (1999).
35. R. Bonneau *et al.*, *Proteins* **45**, 119 (2001).
36. A. Kryzhanovych *et al.*, *Proteins* **79**, (suppl. 10), 196 (2011).
37. F. Morcos *et al.*, *Proc. Natl. Acad. Sci. U.S.A.* **108**, E1293 (2011).
38. D. S. Marks *et al.*, *PLoS ONE* **6**, e28766 (2011).
39. D. T. Jones *et al.*, *Bioinformatics* **28**, 184 (2012).
40. M. Remmert *et al.*, *Nat. Methods* **9**, 173 (2011).
41. V. Mariani *et al.*, *Proteins* **79**, (suppl. 10), 37 (2011).
42. J. Söding *et al.*, *Nucleic Acids Res.* **33**, (Web Server), W244 (2005).
43. P. Bradley *et al.*, *Science* **309**, 1868 (2005).
44. A. Zemla, *Nucleic Acids Res.* **31**, 3370 (2003).
45. F. Allen *et al.*, *IBM Syst. J.* **40**, 310 (2001).
46. M. Shirts, V. S. Pande, *Science* **290**, 1903 (2000).
47. C. D. Snow *et al.*, *Nat. Struct. Mol. Biol.* **420**, 102 (2002).
48. D. E. Shaw *et al.*, *Commun. ACM* **51**, 91 (2008).
49. J. A. McCammon *et al.*, *Nature* **267**, 585 (1977).
50. D. E. Shaw *et al.*, *Science* **330**, 341 (2010).
51. J. Janin *et al.*, *Proteins* **52**, 2 (2003).
52. J. P. Guthrie, *J. Phys. Chem. B* **113**, 4501 (2009).
53. M. Michino *et al.*, *Nat. Rev. Drug Discov.* **8**, 455 (2009).
54. S. Cooper *et al.*, *Nature* **466**, 756 (2010).
55. S. J. Fleishman *et al.*, *Science* **332**, 816 (2011).
56. B. Kuhlman *et al.*, *Science* **302**, 1364 (2003).
57. J. B. Siegel *et al.*, *Science* **329**, 309 (2010).
58. M. L. Azoitei *et al.*, *Science* **334**, 373 (2011).
59. S. H. Gellman, *Acc. Chem. Res.* **31**, 173 (1998).
60. W. S. Horne, S. H. Gellman, *Acc. Chem. Res.* **41**, 1399 (2008).
61. K. Kirshenbaum *et al.*, *Curr. Opin. Struct. Biol.* **9**, 530 (1999).
62. B.-C. Lee *et al.*, *J. Am. Chem. Soc.* **127**, 10999 (2005).
63. S. A. Fowler, H. E. Blackwell, *Org. Biomol. Chem.* **7**, 1508 (2009).
64. M. T. Dohm *et al.*, *Curr. Pharm. Des.* **17**, 2732 (2011).
65. B.-C. Lee *et al.*, *J. Am. Chem. Soc.* **130**, 8847 (2008).
66. N. H. Shah, K. Kirshenbaum, *Org. Biomol. Chem.* **6**, 2516 (2008).
67. K. T. Nam *et al.*, *Nat. Mater.* **9**, 454 (2010).
68. S. B. Prusiner, *Proc. Natl. Acad. Sci. U.S.A.* **95**, 13363 (1998).
69. R. F. Service, *Science* **321**, 784 (2008).
70. Y. Arinaminpathy *et al.*, *Drug Discov. Today* **14**, 1130 (2009).
71. J. L. MacCallum, D. P. Tieleman, *Trends Biochem. Sci.* **36**, 653 (2011).
72. V. N. Uversky, A. K. Dunker, *Biochim. Biophys. Acta* **1804**, 1231 (2010).

Acknowledgments: We thank the NIH for support from NIH GM34993. We thank D. Baker, H. S. Chan, J. Chodera, W. Englander, D. Farrell, C. Fennell, S. Gellman, L. Gierasch, C. R. Matthews, D. Mobley, J. Moulton, G. Rocklin, G. Rollins, and R. Zuckermann for helpful comments.

10.1126/science.1219021

Making the Moon from a Fast-Spinning Earth: A Giant Impact Followed by Resonant Despinning

Matija Ćuk*† and Sarah T. Stewart

A common origin for the Moon and Earth is required by their identical isotopic composition. However, simulations of the current giant impact hypothesis for Moon formation find that most lunar material originated from the impactor, which should have had a different isotopic signature. Previous Moon-formation studies assumed that the angular momentum after the impact was similar to that of the present day; however, Earth-mass planets are expected to have higher spin rates at the end of accretion. Here, we show that typical last giant impacts onto a fast-spinning proto-Earth can produce a Moon-forming disk derived primarily from Earth's mantle. Furthermore, we find that a faster-spinning early Earth-Moon system can lose angular momentum and reach the present state through an orbital resonance between the Sun and Moon.

The origin of the Moon by a giant impact (1, 2) is the leading theory to explain multiple features of the Earth-Moon system (3), including the current angular momentum, the Moon's small core compared with those of rocky planets, and the compositional similarity between the Moon and Earth. In the canonical scenario (4), a ~ 0.1 Earth-mass (M_E) body obliquely strikes the proto-Earth near the escape velocity to generate a circumterrestrial debris disk from which the Moon accretes. Since the formulation of the giant impact hypothesis, ever-improving analytical techniques have revealed that the Moon and Earth are identical in their oxygen, tungsten, chromium, and titanium isotopes (5–8). These isotope systems show considerable variations between planetary bodies and most meteorite groups; thus, the simplest explanation for the isotopic similarity is that the Moon was formed from Earth's mantle (9). In contrast, giant impact simulations find that the lunar disk is predominantly [>60 weight percent (wt %)] composed of material originating from the impactor (4, 10, 11), which is expected to have a different isotopic signature than Earth.

To reconcile the impact simulations with the observations, post-impact isotopic equilibration by mixing material between the lunar disk and Earth has been suggested as a means to mitigate an initial compositional difference (12, 13). However, based on recent isotopic data from the deep mantle, the whole mantle was not completely mixed at the end of accretion (14, 15). Second, recent simulations find that increasing the impactor mass and velocity combined with a steeper impact angle could reduce the impac-

tor mass fraction in the lunar disk to ~ 40 wt % at the expense of a small excess in the final angular momentum (16), but the isotopic similarity requires more efficient mixing of impactor and target material (9). Third, one could invoke the special case of an impactor with identical isotopes as Earth, but such a body is unlikely to also satisfy other geochemical constraints such as the relative abundances of moderately siderophile elements [for example, see (17)]. To date, none of the proposed variations on the giant impact model satisfy all of the geochemical observations.

All previous giant impact scenarios were constrained by the present angular momentum of the Earth-Moon system. The Moon accreted from the disk just beyond Earth's Roche radius [$R_{\text{Roche}} \sim 2.9$ Earth radii (R_E)] (18), the distance at which tidal forces no longer disrupt a satellite. Subsequent tidal interactions between the two bodies (19–21) expanded the lunar orbit to its current $60R_E$. During this process, angular momentum was transferred from Earth to the Moon, but the total angular momentum of the system did not change. Tides raised by the Sun have a minor effect on the Earth-Moon system, changing the angular momentum by, at most, $\sim 1\%$ (10). Thus, the present spin of Earth and the orbit of the Moon imply that the post-impact Earth could not have spun faster than once every 4 hours. However, simulations of the accretion of Earth-mass planets produce final spin periods much faster than 4 hours due to multiple giant impacts (22–24). Starting with a fast-spinning proto-Earth, simulations of giant impacts that reduced Earth's angular momentum to the present value did not produce disks massive enough to form the Moon (11).

Here, we present a different model for the origin of the Earth-Moon system. An erosive giant impact onto a fast-spinning proto-Earth produced a disk that was massive enough to form the Moon and was composed primarily

of material from Earth, but the system had more angular momentum than is the case today. Subsequently, the excess angular momentum was lost during tidal evolution of the Moon via a resonance between Earth's orbital period and the period of precession of the Moon's perigee.

Impacts onto a fast-spinning proto-Earth. We define successful Moon-forming impact scenarios by the following observational constraints: (i) the isotopic similarity between the Moon and Earth, (ii) the mass of the Moon ($M_M = 0.012M_E$), and (iii) the mass of the lunar core. First, the isotopic data limit the difference in the projectile mass fraction between the silicate Earth and the silicate portion of the lunar disk, but the maximum difference depends on the projectile composition. If the impactor had the same isotopic composition as Mars, the difference in projectile mass fraction (Δ^{proj}) is limited to only a few to several weight percent (6, 8, 9). Because the projectile may have been more similar to Earth than Mars, impact scenarios in which $\Delta^{\text{proj}} \leq 15$ wt % are considered successful, although a wider range may be permitted. Second, the mass of the satellite that accretes from the disk must be greater than or equal to one lunar mass ($M_M = 0.012M_E$). We did not model the accretion of the Moon from the disk. Instead, we used the results from previous simulations of lunar accretion (18, 25), which found that the satellite mass is approximated by

$$M_S \approx 1.9L_{\text{disk}}/\sqrt{GM_ER_{\text{Roche}}} - 1.1M_{\text{disk}} - 1.9M_{\text{esc}} \quad (1)$$

where L_{disk} and M_{disk} are the angular momentum and mass of the disk, and G is the gravitational constant. As in (11), we neglected the mass that escapes during disk evolution, M_{esc} . We also estimated the satellite mass by angular momentum conservation ($M_{S,\text{AM}}$) and found values within $\sim 10\%$ of Eq. 1 (26). Third, the mass of the lunar core was estimated to be only a few weight percent (27, 28). Following (10, 11), we required ≤ 10 wt % of the disk be composed of material originating from the iron cores of the impactor and target.

We used a smooth particle hydrodynamics (SPH) code (29, 30) to model high-velocity collisions between differentiated planets [2/3 silicate mantle and 1/3 iron core (26)]. We assumed that Earth was nearly fully formed at the time of the Moon-forming impact, or subsequent accretion would increase any compositional difference between the planet and satellite. Hence, we modeled impacts onto a $\sim 1M_E$ target. At the end of accretion, the average angular momentum of Earth-mass planets is estimated to be ~ 2.7 times the present value (L_{EM}), with possible spin periods up to the instability limit of ~ 2 hours (24). The minimum stable spin period achieved for the SPH model Earth-mass planets was ~ 2.3 hours. Our model proto-Earths began with initial spin

Department of Earth and Planetary Sciences, Harvard University, 20 Oxford Street, Cambridge, MA 02138, USA.

*To whom correspondence should be addressed. E-mail: cuk@eps.harvard.edu

†Present address: Carl Sagan Center, SETI Institute, 189 North Bernardo Avenue, Mountain View, CA 94043, USA.

periods from 2.3 to 2.7 hours, corresponding to angular momenta from 1.9 to $3.1L_{\text{EM}}$. The characteristics of the projectiles were constrained by terrestrial planet-formation simulations, where the typical last giant impactor onto Earth-mass bodies had a mass $\leq 0.10M_{\text{E}}$ and an impact velocity of one to three times the mutual escape velocity (V_{esc}) (31). We calculated the properties of a circumterrestrial disk 1 to 2 days after impact (Table 1).

An example of a successful impact scenario is shown in Fig. 1. The post-impact planet has a hot, massive atmosphere that grades into a rotationally supported vapor-dominated disk. The disk is defined by SPH particles that have sufficient angular momentum such that the equivalent circular Keplerian orbital radius is outside the equatorial radius of the planet. The disk is compact with 85% of its mass within the Roche radius. The planet's post-impact equatorial and polar radii are estimated by a density contour of 1 g cm^{-3} . The post-impact silicate atmosphere, approximated by lower-density material lacking the angular momentum to remain in orbit, has a mass of several weight percent of the planet (Table 1). In this example, the iron core material in the disk is $<1 \text{ wt } \%$, and the predicted satellite mass is $1.0M_{\text{M}}$. The mass fraction of projectile in the disk ($\delta_{\text{disk}}^{\text{proj}}$) is only 8 wt %, and the projectile mass fraction in the silicate Earth is 2 wt %. Hence, the compositional difference between the silicate portions of the disk and Earth is only 6 wt % and is within the range allowed by the isotopic data.

A wide range of probable terminal giant impacts onto an Earth-mass planet with a 2.3-hour rotation period produces potential Moon-forming disks that are composed primarily of material derived from Earth (Fig. 2 and Table 1). We find that these giant impacts typically result in partial accretion of the impactor and net erosion from the proto-Earth (a small final mass deficit is neglected in the Moon-formation criteria, as a larger initial planet mass can compensate for the difference). Head-on and slightly retrograde impacts with impact velocities of ~ 1.5 to $\sim 2.5V_{\text{esc}}$ generated the most successful Moon-forming disks. In these cases, the impactor mantle is distributed between Earth and disk, and less material escapes compared with prograde impacts, which tend to deposit more impactor mantle in the disk and put more Earth mantle material on escaping trajectories. A wide range of impact angles and velocities produced potential Moon-forming disks with properties very close to the desired traits (Table 1, also bold numbers in Fig. 2). For the impact velocities and projectile masses considered here, oblique impacts at angles of 45° and greater were hit-and-run events (32) that did not create disks massive enough to form the Moon. Head-on impacts with velocities above $3V_{\text{esc}}$ begin to substantially decrease the final mass of the planet (32).

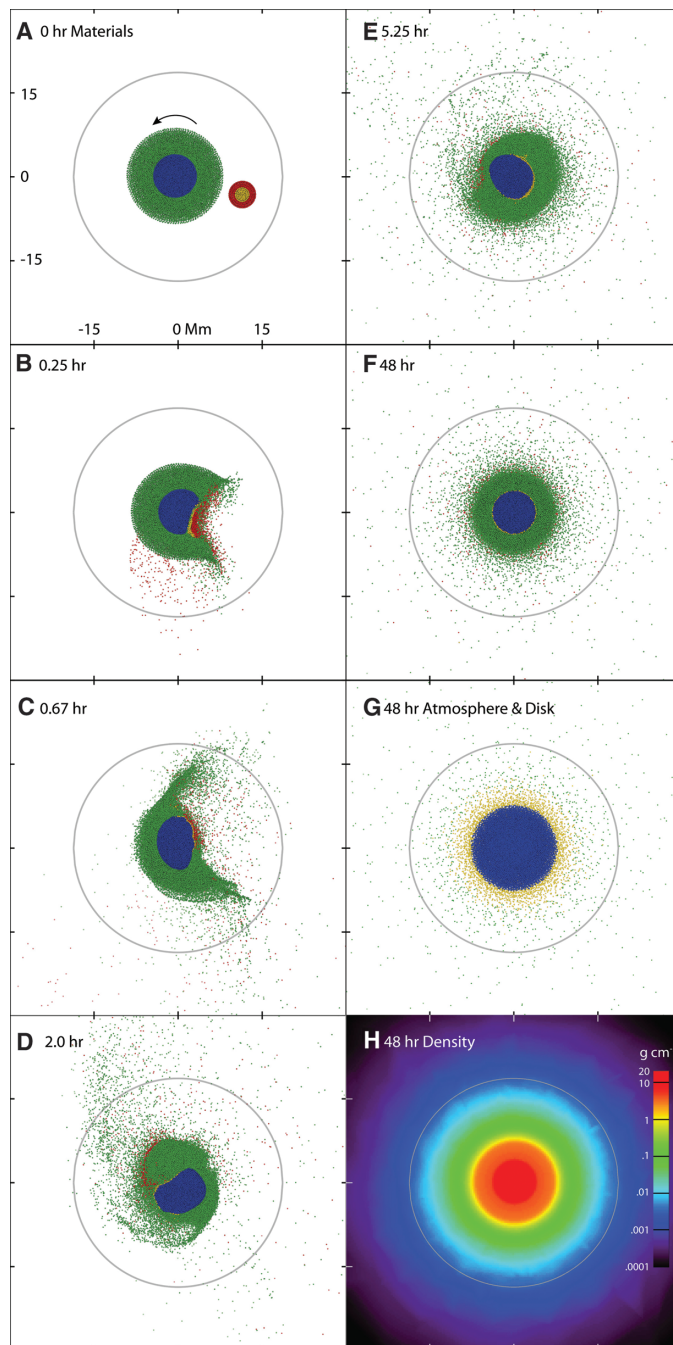
Giant impacts onto planets with spin periods of 2.5 and 2.7 hours produced smaller disk

masses compared with the 2.3-hour cases. In addition, prograde impacts onto the slower-spinning planets have larger iron core mass fractions in the disk (table S1). The results imply a more narrow range for potential Moon-formation events for impact scenarios with less angular momentum. Increasing the total angular momentum by adding spin to the impactors generated successful disks from the slower-spinning planets. Because angular momentum is carried away with debris from these erosive giant impacts, the spin period of the planet decreases. Thus, the spin state of Earth is not required to be near fission before or after the Moon-forming impact in our scenario (for example, last entry in Table 1). However,

our simulations suggest that the impact-driven formation of a sufficiently massive disk derived primarily from Earth's mantle is easiest when the total angular momentum of the event (from the spin of each body and the impact geometry) is near the stability limit.

Our candidate Moon-forming events have more than double the kinetic energy of previous scenarios, and the impact velocities were sufficient to substantially vaporize silicates (33). As a result, the silicate atmosphere and vapor-rich disk are more massive and hotter than found in previous work (34). At the resolution of the simulations, the projectile-to-target mass ratio is uniform from the atmosphere to the Roche radius.

Fig. 1. Formation of the lunar disk from Earth's mantle. Example impact of a $0.05M_{\text{E}}$ impactor at 20 km s^{-1} and $b = -0.3$ onto a $1.05M_{\text{E}}$ Earth spinning with a period of 2.3 hours (\ddagger in Table 1). Gray circles denote the Roche radius. (A to F) View of SPH particles in the lower hemisphere looking down the counterclockwise spin axis, where colors denote the silicate mantles and iron cores of the Earth and the impactor. The disk is dominated by material originating from Earth's mantle near the impact site (fig. S1 and movie S1). (G) Lower hemisphere view with particle colors denoting the planet (blue), atmosphere (yellow), and disk (green). (H) Density in the equatorial plane of the disk and planet, which is stably stratified.



The disk contains both volatile and refractory components from the mantles of the colliding bodies, and the observed depletion of volatile elements in the Moon is a result of the separation of volatile and refractory material during lunar accretion from the disk (35, 36). Detailed comparisons between our Moon-formation scenario with the isotopic data require modeling lunar accretion coupled to the chemical evolution of a disk with our calculated initial conditions.

Tidal evolution and angular momentum loss.

The successful Moon-forming impacts onto a fast-spinning proto-Earth leave the Earth-Moon system with excess angular momentum (Table 1). To test if our lunar origin scenario can be reconciled with the present angular momentum, we simulated the early tidal evolution of the Earth-Moon system using a custom-made orbital integrator based on a symplectic mapping method commonly used in solar system dynamics (21, 37), which includes mutual precession, both Earth and Moon tides, and solar perturbations (26).

We find that the evection resonance between the Moon and the Sun (38, 39), which occurs when the period of precession of lunar perigee equals the period of Earth's orbit, can substantially reduce the angular momentum of the Earth-Moon system. After capture into this resonance,

the long axis of lunar orbit librates around 90° from the Earth-Sun line, and the lunar perigee precession period is fixed at 1 year. The evection resonance is encountered soon after lunar formation, and the efficiency of capture is a strong function of the lunar semimajor axis at which the resonance happens, which increases with increased flattening of Earth. At larger distances from Earth, solar gravitational perturbations are stronger, and more importantly, lunar tidal recession is slower, enabling more efficient capture. It has been found that capture is possible even for an Earth spinning once every 5 hours (39), as long as tidal evolution is very slow (implying a large tidal quality factor Q of $\sim 10^4$ for Earth; Q is an inverse measure of the dissipation of tidal energy as heat within a body).

In our simulations (Fig. 3), robust capture into the evection resonance happened at $\sim 7R_E$, for a standard tidal quality factor of $Q \simeq 100$, 2.5-hour rotation and a simplified flattening model for Earth. After the Moon was captured in the resonance, the lunar orbit continued to evolve outward while keeping a constant precession period, which led to a rapid increase of eccentricity (39). The eccentricity increased until a balance between Earth and lunar tides was reached, but the exact eccentricity at which this happened is

model-dependent because the mechanical properties of both Earth and the Moon are uncertain. We used a standard satellite tidal parameter for the Moon in Fig. 3, but other values for Q give us similar outcomes (Fig. 4).

There was always a substantial period of balance between Earth and Moon tides, where the Moon stayed in the evection resonance with a roughly constant eccentricity. During this period, Earth tides were transferring angular momentum to the Moon, and Earth's rotation was slowing down (movies S2 and S3). Satellite tides cannot remove angular momentum from lunar orbit, but the Sun can absorb angular momentum through the evection resonance. Because the resonance couples lunar perigee and eccentricity with Earth's orbital period, angular momentum of the lunar orbit can be transferred to the angular momentum of Earth's orbit around the Sun. Earth tides pass angular momentum to lunar orbit, and the resonance-locked lunar orbit transfers angular momentum to the heliocentric orbit of Earth. Our integrator keeps Earth's orbit stationary, but in reality, this process makes the Earth-Sun distance slightly larger.

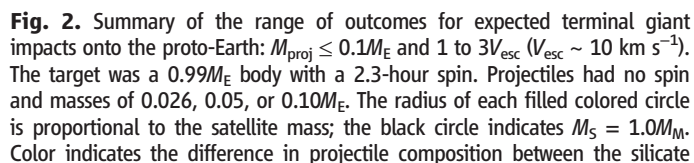
As Earth lost its spin, Earth's flattening decreased, and the position of the evection resonance for the equilibrium eccentricity slowly

Table 1. Potential Moon-forming giant impacts onto a fast-spinning proto-Earth. M_{proj} , projectile mass; V_i , impact velocity in kilometers per second; b , impact parameter (negative value indicates retrograde impact; all impacts in the equatorial plane); M_{planet} , mass of post-impact planet including atmosphere; R_{eq} ,

estimated equatorial radius of post-impact planet in kilometers; f , flattening of post-impact planet ($R_{\text{eq}} - R_{\text{pole}}/R_{\text{eq}}$ (where R_{pole} is the polar radius); T , spin period of post-impact planet in hours; L_z , z-component of angular momentum of planet and disk; M_{atm} , mass of the atmosphere; $M_{\text{iron}}/M_{\text{disk}}$, iron core mass fraction in disk.

$\frac{M_{\text{proj}}}{M_E}$	V_i	b	$\frac{M_{\text{planet}}}{M_E}$	R_{eq}	f	T	$\frac{L_z}{L_{EM}}$	$\frac{M_{\text{atm}}}{M_M}$	$\frac{M_{\text{disk}}}{M_M}$	$\frac{M_S}{M_M}$	$\frac{M_{S,AM}}{M_M}$	$\delta_{\text{disk}}^{\text{proj}}$	Δ^{proj}	$\frac{M_{\text{iron}}}{M_{\text{disk}}}$	Result
<i>0.99M_E target with 2.3 hours spin and 3.0L_{EM}</i>															
0.026	20.0	−0.30	0.96	7700	0.39	2.6	2.43	4.0	1.54	0.82	0.85	0.064	0.052	0.003	*
0.026	25.0	−0.30	0.94	7500	0.37	2.6	2.32	5.6	2.07	0.87	0.96	0.049	0.039	0.010	*
0.026	30.0	−0.30	0.91	7300	0.36	2.7	2.22	6.8	2.33	0.90	1.01	0.046	0.038	0.049	*
0.026	20.0	0.30	0.96	8100	0.45	2.4	2.76	2.9	1.59	0.88	0.79	0.167	0.157	0.037	*
0.050	15.0	−0.30	0.98	7800	0.42	2.5	2.56	4.5	1.81	0.91	0.93	0.113	0.087	0.002	*
0.050	20.0	−0.30	0.94	7500	0.38	2.6	2.40	6.6	2.45	0.96	1.09	0.086	0.064	0.008	*
0.050	25.0	−0.30	0.90	7300	0.38	2.7	2.22	8.0	2.54	0.91	1.06	0.077	0.059	0.034	*
0.050	15.0	−0.15	0.98	7900	0.43	2.5	2.67	4.5	1.84	0.93	0.90	0.122	0.093	0.007	*
0.050	20.0	−0.15	0.94	7600	0.40	2.6	2.52	6.4	2.62	1.14	1.22	0.090	0.067	0.024	†
0.050	15.0	0.00	0.98	8100	0.46	2.5	2.84	4.2	1.97	1.02	0.95	0.176	0.147	0.015	†
0.050	20.0	0.00	0.94	7800	0.42	2.5	2.68	6.0	2.85	1.33	1.36	0.115	0.091	0.054	†
0.100	15.0	−0.30	0.98	7400	0.38	2.8	2.30	8.1	2.16	0.89	0.90	0.121	0.069	0.021	*
0.100	20.0	−0.30	0.93	7100	0.35	2.9	2.07	10.4	2.22	0.81	0.86	0.103	0.056	0.078	*
0.100	10.0	0.00	1.04	8100	0.43	2.5	2.90	4.5	1.60	0.91	0.74	0.255	0.187	0.014	*
0.100	15.0	0.00	0.99	7800	0.43	2.6	2.79	7.4	2.81	1.32	1.23	0.168	0.111	0.083	†
<i>1.05M_E target with 2.3 hours spin and 3.1L_{EM}</i>															
0.050	20.0	−0.30	1.01	7500	0.37	2.7	2.47	7.0	2.20	1.02	1.02	0.081	0.059	0.005	††
0.050	22.5	−0.30	0.99	7400	0.36	2.8	2.40	7.9	2.32	0.90	0.97	0.070	0.050	0.007	*
0.050	25.0	−0.30	0.97	7300	0.35	2.8	2.31	8.7	2.37	0.93	0.95	0.066	0.048	0.019	*
<i>1.05M_E target with 2.5 hours spin and 2.5L_{EM}</i>															
0.050	25.0	0.00	0.98	7200	0.30	3.1	2.15	8.7	2.14	1.29	1.09	0.084	0.061	0.092	†
0.050	20.0	0.15	1.03	7500	0.35	2.8	2.42	6.3	1.67	1.01	0.81	0.187	0.161	0.076	*
<i>1.05M_E target with 2.7 hours spin and 2.1L_{EM}</i>															
0.050	20.0	0.30	1.03	7400	0.35	2.8	2.25	5.1	1.26	0.91	0.70	0.196	0.174	0.098	*
0.050	25.0	0.00	1.00	7100	0.29	3.4	1.94	9.9	1.77	1.24	0.82	0.101	0.076	0.084	†

*Potential Moon-forming simulations with more relaxed criteria of $0.8 \leq M_S/M_M \leq 1.5$, $\delta_{\text{proj}}^{\text{proj}} \leq 0.20$, and $M_{\text{iron}}/M_{\text{disk}} \leq 0.1$. †Successful Moon-forming simulations with $M_S \geq 1.0M_M$, $\delta_{\text{proj}}^{\text{proj}} \leq 0.15$, and $M_{\text{iron}}/M_{\text{disk}} \leq 0.1$. ††Example in Fig. 1. ‡Projectile with a 2.9-hour prograde spin; other projectiles have no spin. Targets have 1 to 2×10^5 SPH particles [additional simulation results and methods in (26)].



A high spin rate during the giant impact phase of planet formation would affect all major

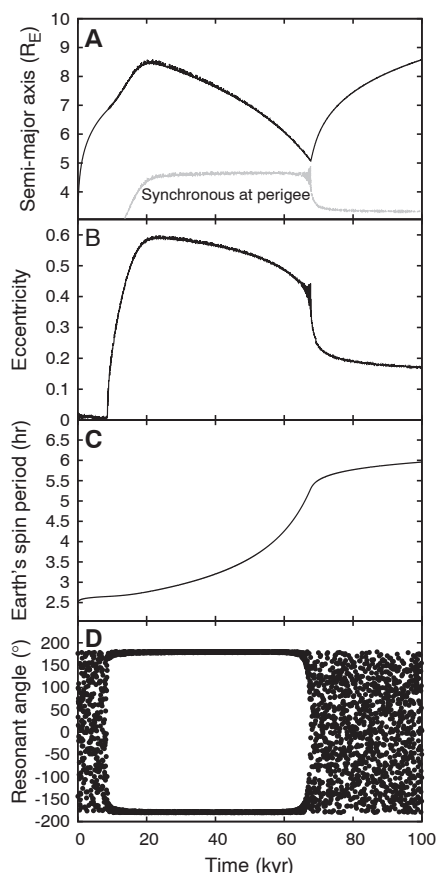


Fig. 3. Tidal evolution of the Moon through the evection resonance, starting with an Earth spin period of 2.5 hours. The Moon is captured into the resonance at ~ 9 thousand years (kyr) [at a semi-major axis of $6.8R_E$ in (A)] and stays in the resonance until ~ 68 thousand years, when the Moon almost reaches an orbit that is geosynchronous at perigee (gray line). During this time, the long axis of lunar orbit is locked to 90° from the Earth-Sun line. At first, the Moon keeps evolving outward (A) in the resonance while the eccentricity (B) increases, until the eccentricity stabilizes and a slower inward migration ensues, ending at $\sim 5R_E$. During the resonance lock, Earth's rotation slows down dramatically (C), with the spin period increasing from just over 2.5 hours to almost 6 hours. During resonance capture, resonant argument $\Psi = 2\lambda_{\text{Sun}} - 2\omega_{\text{Moon}} - \lambda_{\text{Sun}} - \lambda_{\text{perigee}}$ (the Sun's mean longitude; ω_{Moon} , longitude of perigee) librates around 180° (D). Also see movie S2.

processes on the growing Earth, including mantle convection patterns and overturn rates. Within 100 million years of solar system formation, major chemical reservoirs were established in Earth's lower mantle that were not destroyed by a Moon-forming impact (14, 15). The isotopic constraints require the Moon's formation to occur at the end of Earth's accretion, but the exact timing remains uncertain (41). Although the SPH technique generally underestimates the mixing of materials, our simulations show that the relatively cooler and denser material from the lower mantle in the hemisphere opposite the impact is

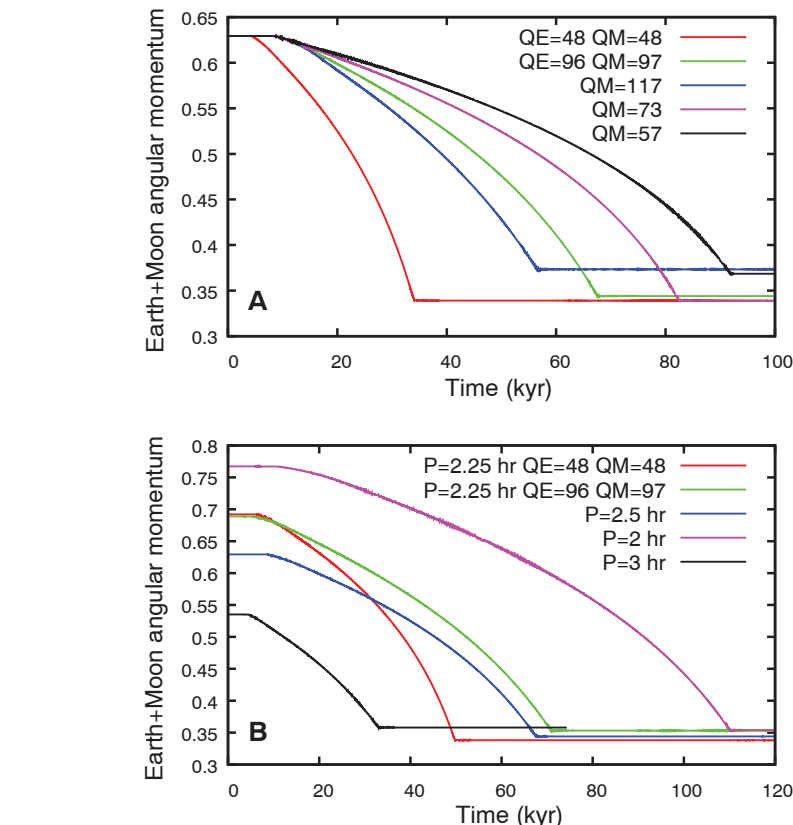


Fig. 4. Change in total angular momentum of the Earth-Moon system during tidal evolution of the Moon for different simulation parameters. (A) Simulations starting with Earth's spin period of 2.5 hours with different tidal quality factors for Earth ($Q_E = 96$, where not noted otherwise) and the Moon (Q_M). (B) Simulations starting with 2-, 2.25-, 2.5-, and 3-hour spin periods for Earth ($Q_E = 96$ and $Q_M = 97$, where not noted otherwise). The current angular momentum of the Earth-Moon system is 0.35 in our units [$\alpha M \sqrt{GMR}$; α , dimensionless moment of inertia; M , mass; R , radius (26)], where a spherical Earth spinning at the break-up rate would have an angular momentum of 1.

not well mixed with material from the impacted hemisphere and upper mantle during gravitational reequilibration (fig. S1). The post-impact planet is stably stratified with the entropy of the upper mantle higher than the entropy of the lower mantle, which would inhibit deep convective mixing. Hence, our Moon-formation scenario need not destroy preexisting chemical differentiation within the proto-Earth.

Our model for the origin of the Moon blends aspects of the original impact hypothesis, in which material was ejected from Earth by a late large impact (1), and the fission hypothesis first proposed by Darwin (19), in which Earth lost material via spin instability. We show that an erosive giant impact onto a fast-spinning proto-Earth followed by despinning during passage through the evection resonance can reproduce the isotopic homogeneity and present angular momentum of the Earth-Moon system.

References and Notes

- W. K. Hartmann, D. R. Davis, *Icarus* **24**, 504 (1975).
- A. G. W. Cameron, W. R. Ward, *Proc. Lunar Planet. Sci. Conf.* **7**, 120 (1976).
- D. J. Stevenson, *Annu. Rev. Earth Planet. Sci.* **15**, 271 (1987).
- R. M. Canup, E. Asphaug, *Nature* **412**, 708 (2001).
- G. W. Lugmair, A. Shukolyukov, *Geochim. Cosmochim. Acta* **62**, 2863 (1998).
- U. Wiechert et al., *Science* **294**, 345 (2001).
- M. Touboul, T. Kleine, B. Bourdon, H. Palme, R. Wieler, *Nature* **450**, 1206 (2007).
- J. Zhang, N. Dauphas, A. M. Davis, I. Leya, A. Fedkin, *Nat. Geosci.* **5**, 251 (2012).
- M. M. Meier, *Nat. Geosci.* **5**, 240 (2012).
- R. M. Canup, *Icarus* **168**, 433 (2004).
- R. M. Canup, *Icarus* **196**, 518 (2008).
- K. Pahlevan, D. J. Stevenson, *Earth Planet. Sci. Lett.* **262**, 438 (2007).
- K. Pahlevan, D. J. Stevenson, J. M. Eiler, *Earth Planet. Sci. Lett.* **301**, 433 (2011).
- M. Touboul, I. S. Puchtel, R. J. Walker, *Science* **335**, 1065 (2012).
- S. Mukhopadhyay, *Nature* **486**, 101 (2012).
- A. Reufer, M. M. Meier, W. Benz, R. Wieler, *Icarus* **221**, 296 (2012).
- A. E. Ringwood, *Earth Planet. Sci. Lett.* **95**, 208 (1989).
- S. Ida, R. M. Canup, G. R. Stewart, *Nature* **389**, 353 (1997).
- G. H. Darwin, *Philos. Trans. R. Soc. London* **170**, 447 (1879).
- P. Goldreich, *Rev. Geophys.* **4**, 411 (1966).
- J. Touma, J. Wisdom, *Astron. J.* **108**, 1943 (1994).
- C. B. Agnor, R. M. Canup, H. F. Levison, *Icarus* **142**, 219 (1999).
- E. Kokubo, S. Ida, *Astrophys. J.* **671**, 2082 (2007).
- E. Kokubo, H. Genda, *Astrophys. Lett.* **714**, L21 (2010).

25. E. Kokubo, S. Ida, J. Makino, *Icarus* **148**, 419 (2000).
 26. Supplementary materials are available on Science Online.
 27. R. C. Weber, P.-Y. Lin, E. J. Garnero, Q. Williams, P. Lognonné, *Science* **331**, 309 (2011).
 28. M. A. Wieczorek et al., *Rev. Mineral. Geochem.* **60**, 221 (2006).
 29. V. Springel, *Mon. Not. R. Astron. Soc.* **364**, 1105 (2005).
 30. R. A. Marcus, S. T. Stewart, D. Sasselov, L. Hernquist, *Astrophys. Lett.* **700**, L118 (2009).
 31. S. T. Stewart, Z. M. Leinhardt, *Astrophys. J.* **751**, 32 (2012).
 32. Z. M. Leinhardt, S. T. Stewart, *Astrophys. J.* **745**, 79 (2012).
 33. R. G. Kraus et al., *J. Geophys. Res.* **117**, E09009 (2012).
 34. It is difficult to accurately calculate the mass of the atmosphere and the vapor fraction of the disk, as current numerical methods lack equations of state for multiple silicate phases in the mantle and multiphase flow of partially vaporized material (26). Although early work on

the accretion of the Moon focused on a gas-poor disk (18, 25), recent studies indicate that the Moon may also accrete from a more vapor-rich atmosphere-disk structure (35, 36).
 35. R. Machida, Y. Abe, *Astrophys. J.* **617**, 633 (2004).
 36. W. R. Ward, *Astrophys. J.* **744**, 140 (2012).
 37. J. Wisdom, M. Holman, *Astron. J.* **102**, 1528 (1991).
 38. W. M. Kaula, C. F. Yoder, *Proc. Lunar Planet. Sci. Conf.* **7**, 440 (1976).
 39. J. Touma, J. Wisdom, *Astron. J.* **115**, 1653 (1998).
 40. W. R. Ward, R. M. Canup, *Nature* **403**, 741 (2000).
 41. G. Yu, S. B. Jacobsen, *Proc. Natl. Acad. Sci. U.S.A.* **108**, 17604 (2011).

Acknowledgments: This work, which was supported by NASA's Origins of Solar Systems program and Harvard's Daly and Smithsonian's Clay Fellowships, was improved by helpful discussions with S. Jacobsen, J. Melosh, D. Minton, S. Mukhopadhyay, D. Stevenson, J. Wisdom, and comments

from the anonymous reviewers. The impact simulations were run on the Odyssey cluster supported by the Harvard Faculty of Arts and Sciences Research Computing Group. S.T.S. conducted the impact simulations, M.C. calculated the tidal evolution, and both wrote the paper. Numerical codes are available as supplementary materials.

Supplementary Materials

www.sciencemag.org/cgi/content/full/science.1225542/DC1
 Supplementary Text
 Figs. S1 to S7
 Table S1
 References (42–52)
 Movies S1 to S3
 Computer Codes

4 June 2012; accepted 26 September 2012
 Published online 17 October 2012;
 10.1126/science.1225542

REPORTS

Forming a Moon with an Earth-like Composition via a Giant Impact

Robin M. Canup*

In the giant impact theory, the Moon formed from debris ejected into an Earth-orbiting disk by the collision of a large planet with the early Earth. Prior impact simulations predict that much of the disk material originates from the colliding planet. However, Earth and the Moon have essentially identical oxygen isotope compositions. This has been a challenge for the impact theory, because the impactor's composition would have likely differed from that of Earth. We simulated impacts involving larger impactors than previously considered. We show that these can produce a disk with the same composition as the planet's mantle, consistent with Earth-Moon compositional similarities. Such impacts require subsequent removal of angular momentum from the Earth-Moon system through a resonance with the Sun as recently proposed.

The oblique, low-velocity impact of a roughly Mars-mass planet with Earth can produce an iron-depleted disk with sufficient mass and angular momentum to later produce our iron-poor Moon while also leaving the Earth-Moon system with roughly its current angular momentum (1–3). A common result of simulations of such impacts is that the disk forms primarily from material originating from the impactor's mantle. The silicate Earth and the Moon share compositional similarities, including in the isotopes of oxygen (4), chromium (5), and titanium (6). These would be consistent with prior simulations if the composition of the impactor's mantle was comparable with that of Earth's mantle. It had been suggested that this similarity would be expected for a low-velocity impactor with an orbit similar to that of Earth (4, 7, 8). However, recent work (9) finds that this is improbable given the degree

of radial mixing expected during the final stages of terrestrial planet formation (10). Explaining the Earth-Moon compositional similarities would then require post-impact mixing between the vaporized components of Earth and the disk before the Moon forms (9), which is a potentially restrictive requirement (11).

A recent development is the work of Ćuk and Stewart (12, 13), who find that the angular momentum of the Earth-Moon system could have been decreased by about a factor of 2 after the Moon-forming impact because of the evection resonance with the Sun. This would allow for a broader range of Moon-forming impacts than previously considered, including those involving larger impactors.

Prior works (1–3, 14) focus primarily on impactors that contain substantially less mass than that of the target, with impactor masses $M_{\text{imp}} \sim 0.1$ to $0.2M_T$, where $M_T \approx M_\oplus$ is the total colliding mass and M_\oplus is Earth's mass. If the target and impactor have different isotopic compositions, creating a final disk and planet with similar compositions then requires that the disk

be formed overwhelmingly from material derived from the target's mantle. However, gravitational torques that produce massive disks tend to place substantial quantities of impactor material into orbit (2, 3).

We considered a larger impactor that is comparable in mass with that of the target itself. A final disk and planet with the same composition are then produced if the impactor contributes equally to both, which for large impactors is possible even if the disk contains substantial impactor-derived material because the impactor also adds substantial mass to the planet. For example, in the limiting case of an impactor whose mass equals that of the target and in the absence of any pre-impact rotation, the collision is completely symmetric, and the final planet and any disk that is produced will be composed of equal parts impactor and target-derived material and can thus have the same silicate compositions even if the original impactor and target did not.

We describe the impactor and target as differentiated objects with iron cores and overlying silicate mantles (15). We simulated impacts using smooth particle hydrodynamics (SPH) (Fig. 1) as in (1–3, 15, 16), representing the impactor and target with 300,000 SPH particles. Each particle was assigned a composition (either iron for core particles or dunite for mantle particles) and a corresponding equation of state (17, 18), and its evolution was tracked with time as it evolved owing to gravity, pressure forces, and shock dissipation.

We simulated a given impact for approximately 1 day of simulated time. We used an iterative procedure (1–3, 15) to determine whether each particle at the end of the simulation is in the planet, in bound orbit around the planet (in the disk), or escaping. Given the calculated disk mass M_D and angular momentum L_D , we estimated the mass of the moon that would later form from the disk, M_M , using a conservation of mass and angular momentum argument (19, 20). Assuming that the disk would later accumulate

Planetary Science Directorate, Southwest Research Institute, 1050 Walnut Street, Suite 300, Boulder, CO 80302, USA.

*To whom correspondence should be addressed. E-mail: robin@boulder.swri.edu

Fig. 1. An SPH simulation of a moderately oblique, low-velocity ($v_{\infty} = 4 \text{ km s}^{-1}$) collision between an impactor and target with similar masses (Table 1, run 31). Color scales with particle temperature in kelvin, per color bar, with red indicating temperatures $>6440 \text{ K}$. All particles in the three-dimensional simulation are overplotted. Time is shown in hours, and distances are shown in units of 10^3 km . After the initial impact, the planets recollided, merged, and spun rapidly. Their iron cores migrated to the center, while the merged structure developed a bar-type mode and spiral arms (24). The arms wrapped up and finally dispersed to form a disk containing ~ 3 lunar masses, whose silicate composition differed from that of the final planet by less than 1%. Because of the near symmetry of the collision, impactor and target material are distributed approximately proportionately throughout the final disk, so that the disk's δf_T value does not vary appreciably with distance from the planet.

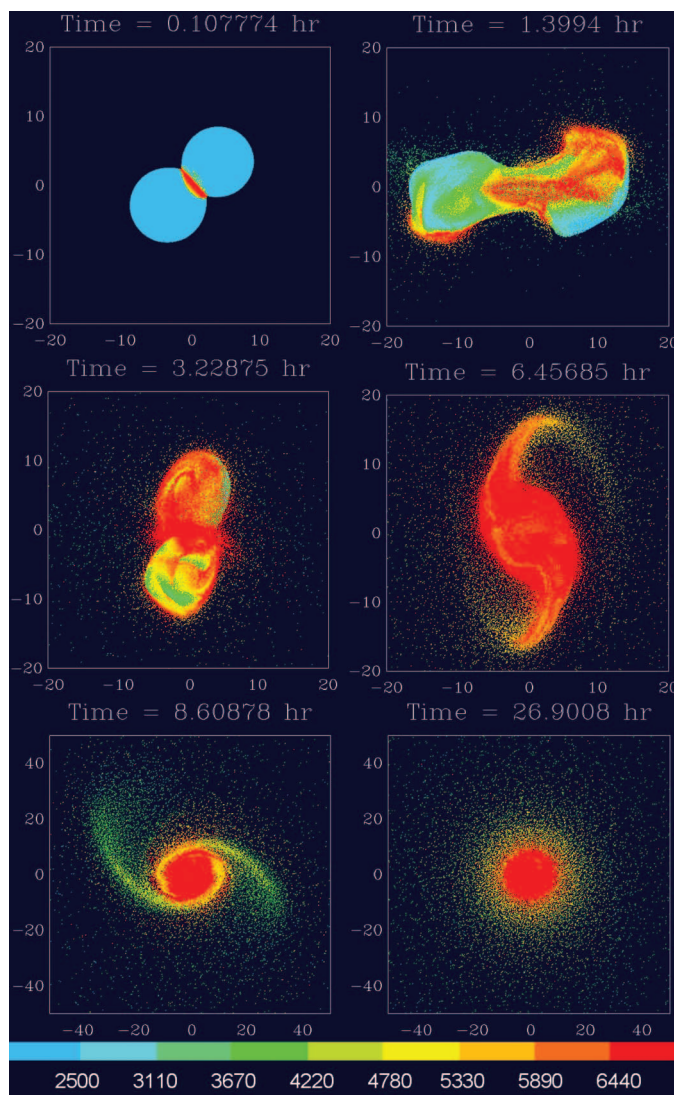
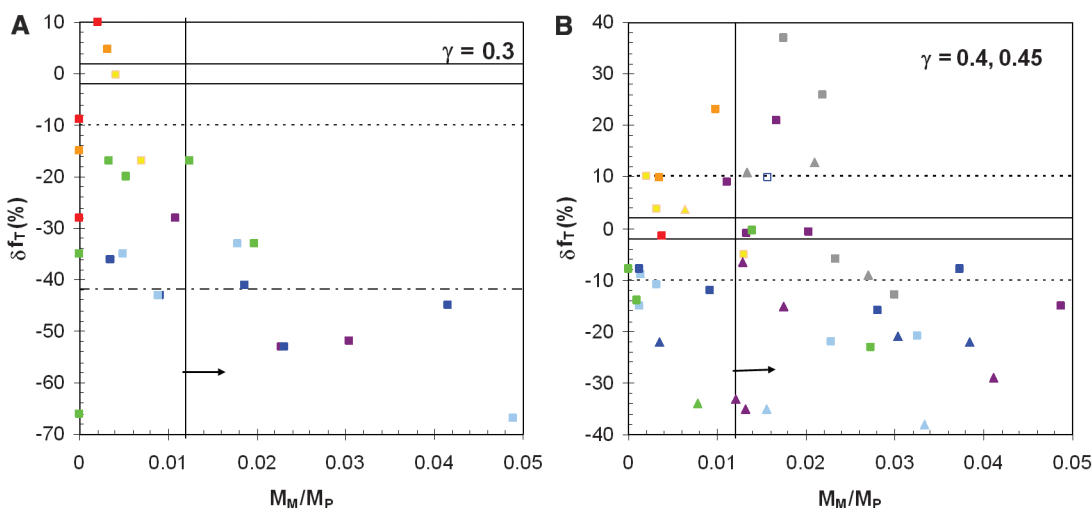


Fig. 2. Compositional difference between the disk and final planet (δf_T) (Eq. 2) produced by simulations with (A) $\gamma = 0.3$ and (B) $\gamma = 0.4$ (triangles) and 0.45 (squares) versus the predicted mass of the moon that would accrete from each disk (M_M) (Eq. 1) scaled to the final planet's mass (M_P). There is a change in y axis scales between the two plots. Gray, purple, dark blue, light blue, green, yellow, orange, and red points correspond to $v_{\text{imp}}/v_{\text{esc}} = 1.0, 1.1, 1.2, 1.3, 1.4, 1.6, 1.8,$ and 2.0 , respectively. The open square is run 60* from Table 1, which includes pre-impact rotation. Forming an appropriate-mass



Moon mass requires $M_M/M_P > 0.012$, the region to the right of the vertical solid line. Constraints on δf_T needed to satisfy Earth-Moon compositional similarities are shown by horizontal lines for oxygen (solid), titanium (dotted), and chromium (dot-dashed), assuming a Mars-composition impactor.

into a single moon at an orbital distance of about $3.8R_{\oplus}$, where R_{\oplus} is Earth's radius (19, 20),

$$\frac{M_M}{M_D} \approx 1.9 \left(\frac{L_D}{M_D \sqrt{2.9 G M_{\oplus} R_{\oplus}}} \right) - 1.1 - 1.9 \left(\frac{M_{\text{esc}}}{M_D} \right) \quad (1)$$

where M_{esc} is the mass that escapes from the disk as the Moon accretes. To estimate M_M , we used Eq. 1 and made the favorable assumption that $M_{\text{esc}} = 0$.

We tracked the origin (impactor versus target) of the particles in the final planet and the disk. To quantify the compositional difference between the silicate portions of the disk and planet, we define a deviation percentage

$$\delta f_T \equiv [F_{D,\text{tar}}/F_{P,\text{tar}} - 1] \times 100 \quad (2)$$

where $F_{D,\text{tar}}$ and $F_{P,\text{tar}}$ are the mass fractions of the silicate portions of the disk and of the planet derived from the target's mantle, respectively (21). Identical disk-planet compositions have $\delta f_T = 0$, whereas a disk that contains fractionally more impactor-derived silicate than the final planet has $\delta f_T < 0$, and a disk that contains fractionally less impactor-derived silicate than the final planet has $\delta f_T > 0$.

Prior impact simulations (1–3, 14, 15) that consider $\gamma \equiv M_{\text{imp}}/M_T \approx 0.1$ to 0.2 produce disks with $-90\% \leq \delta f_T \leq -35\%$ for cases with $M_M > M_L$, where M_L is the Moon's mass. Results with larger impactors having $\gamma = 0.3, 0.4$, and 0.45 are shown in Figs. 1 and 2 and Table 1. As the relative size of the impactor (γ) is increased, there is generally a closer compositional match between the final disk and the planet. For $\gamma \geq 0.4$, some disks have both sufficient mass and angular momentum to yield the Moon and nearly identical silicate compositions to that of the final

planet; others even contain proportionally more silicate from the target than from the impactor ($\delta f_T > 0$). We expect successful cases such as those shown in Fig. 1 and Table 1 could be identified across the $0.4 \leq \gamma \leq 0.5$ range.

One can roughly estimate how small $|\delta f_T|$ needs to be for consistency with observed geochemical similarities between the silicate Earth and the Moon. The impactor and target's original compositions are, of course, unknown. However, results of planet accretion simulations (10), in combination with the assumption that planetary embryo composition varied linearly with heliocentric distance, have been used to estimate that the average deviation of a large impactor's composition from that of the final planet was about half the observed compositional difference between Earth and Mars (9). We nominally adopt a "Mars-like" composition for our impactor and use a simple mass balance argument (15, 21) to estimate the required values for δf_T . The most restrictive constraint is from oxygen (4), which requires $|\delta f_T| < 2\%$ assuming a Mars-like impactor; accounting for the titanium (6) and chromium (5) similarities between Earth and the Moon requires $|\delta f_T| < 10\%$ and $|\delta f_T| < 42\%$, respectively. There is considerable uncertainty in these estimates because of both uncertainties in the compositional measurements and probable scatter in impactor compositions (15). For example, the relatively broad distribution of impactor compositions found by (9) implies that the impactor could have been substantially more similar compositionally to Earth than Mars, which would relax the oxygen constraint to $|\delta f_T|$ less than ~ 10 to 15% (15).

Impacts that produce an iron-poor moon of at least a lunar mass and $|\delta f_T| < 15\%$ are listed in Table 1 as our most promising candidates. Several disk-planet pairs are compositionally similar enough ($\delta f_T \sim 0\%$) to explain the Earth-Moon oxygen similarity even assuming a Mars-like impactor. The candidate impacts span a relatively broad range of impact parameters, with $0.35 \leq b \leq 0.7$ (where $b = \sin \xi$, ξ is the impact angle, and $b = 1$ is a grazing impact). For randomly oriented impacts (22), $\sim 40\%$ of all impacts would have b in this range. The impact velocity v_{imp} is a function of the mutual escape velocity of the colliding objects v_{esc} and their relative velocity at large separation v_{∞} , with $v_{\text{imp}}^2 = v_{\text{esc}}^2 + v_{\infty}^2$. The impacts listed in Table 1 have $1.0 \leq v_{\text{imp}}/v_{\text{esc}} \leq 1.6$, corresponding to $0 \leq v_{\infty} (\text{km s}^{-1}) \leq 11$. These v_{∞} values are in good agreement with terrestrial accretion simulations (23), which find $\langle v_{\infty} \rangle \approx 4$ to 5 km s^{-1} , with a typical range from 1 to 10 km s^{-1} for large impactors with $M_{\text{imp}} > 0.1 M_{\oplus}$. Similar models (15, 22) have found that the ratio of the mass of the largest impactor to collide with a planet (M_{lst}) to the final planet's mass (M_P) is $\langle M_{\text{lst}}/M_P \rangle \approx 0.3 \pm 0.08$ for planets with $M_P > 0.5 M_{\oplus}$, with $\sim 20\%$ of such planets experiencing a final collision with $\gamma \geq 0.4$.

Our impactors and targets are not rotating before collision. Planetary embryos would have been rotating with randomly oriented spin axes because of prior impacts (22). When the orientation of a pre-impact spin axis differs substantially from the angular momentum vector of the impact, the resulting disk mass and angular momentum are broadly similar to cases without

pre-impact rotation (3). However, it is also possible to find similar outcomes for the extreme case of perfect alignment between the pre-impact rotational axis and the impact angular momentum vector (such as Table 1, run 60*).

The impacts here differ greatly from the canonical Moon-forming impact that has $\gamma \sim 0.1$ to 0.15 (1–2). Here, the moon-forming collision involves two planetary embryos of comparable mass, which is similar in some respects to the collision invoked for the origin of Pluto-Charon (24). Compared with disks produced by the canonical impact, the disks here are hotter [those listed in Table 1 contain between 50 and 90% of their mass in vapor, versus 10 to 30% vapor in the canonical case (2)] and typically more massive. Recent work (25) suggests that Eq. 1 overestimates M_M for a given disk M_D and L_D , implying that more massive initial disks may be needed to form a lunar mass moon.

The impacts here can remove the need for an improbable compositional match between the impactor and target or for post-impact equilibration between the planet and disk (15). However, they all produce a planet-disk system whose angular momentum is substantially higher than that in the current Earth and Moon (L_{EM}). They thus require that the system angular momentum is decreased by about a factor of 2 to 2.5 after the moon forms because of capture into the evection resonance with the Sun, as proposed by (12, 13). Čuk and Stewart (13) find that reducing the system angular momentum to a value consistent with L_{EM} requires a specific (and relatively narrow) range for the ratio of the tidal parameters for the Moon, $(k_2/Q)_M$ (where k_2 is the degree 2 Love number and Q is the tidal quality factor), compared with those for Earth, $(k_2/Q)_{\oplus}$, at the time of the resonance. It is also possible that the duration of occupancy of the Moon in the evection resonance as the Moon's orbit contracts may vary with the specifics of the tidal model considered, which is a potential sensitivity that has not yet been assessed.

Table 1. Properties of candidate impacts. All cases had a total colliding mass $M_T = 1.04 M_{\oplus}$. Shown are the impactor-to-total mass ratio (γ), scaled impact parameter (b), impact velocity relative to the escape velocity ($v_{\text{imp}}/v_{\text{esc}}$), relative velocity at infinity (v_{∞}), disk mass in lunar masses (M_D/M_L), disk angular momentum in units of that of the current Earth-Moon system ($L_{\text{EM}} = 3.5 \times 10^{41} \text{ g cm}^2 \text{ s}^{-1}$), fraction of the disk mass in iron (M_{Fe}/M_D), final bound system angular momentum in units of L_{EM} , the post-impact rotational period of the planet in hours (T), the predicted mass of the Moon in lunar masses that would accrete from the disk (M_M/M_L), and the percent compositional deviation of the disk from the final planet (δf_T). Run 60* had a target with a 3-hour rotational day before the impact, with the pre-impact spin vector anti-aligned to the impact angular momentum vector. The values of T found here are consistent with successful evection models presented in (12), in which the resonance removes angular momentum from the Earth-Moon system until a value comparable with L_{EM} is achieved.

Run	γ	b	$v_{\text{imp}}/v_{\text{esc}}$	$v_{\infty} (\text{km s}^{-1})$	M_D/M_L	L_D/L_{EM}	M_{Fe}/M_D	L_F/L_{EM}	T (hours)	M_M/M_L	δf_T
1	0.40	0.60	1.0	0.0	2.94	0.51	0.01	2.32	2.2	2.17	−9%
3	0.40	0.55	1.0	0.0	1.74	0.29	0.02	2.18	2.2	1.10	11%
4	0.40	0.55	1.1	4.0	2.72	0.42	0.05	2.39	2.0	1.41	−15%
6	0.40	0.50	1.0	0.0	2.16	0.39	0.02	1.96	2.6	1.71	13%
7	0.40	0.50	1.1	4.0	1.93	0.30	0.05	2.17	2.2	1.05	−6.6%
11	0.45	0.35	1.6	10.9	2.30	0.31	0.06	1.89	2.0	0.96	−5%
14	0.45	0.40	1.1	4.0	1.87	0.30	0.03	1.77	2.7	1.09	−1%
17	0.45	0.40	1.4	8.6	2.88	0.39	0.03	2.22	2.0	1.09	−0.3%
31	0.45	0.55	1.1	4.0	3.03	0.47	0.02	2.45	2.0	1.64	−0.8%
32	0.45	0.55	1.2	5.8	5.06	0.78	0.03	2.52	2.1	2.89	−8%
35	0.45	0.60	1.0	0.0	2.84	0.47	0.01	2.37	2.1	1.88	−6%
39	0.45	0.65	1.0	0.0	3.63	0.60	0.00	2.61	2.0	2.40	−13%
40	0.45	0.65	1.1	4.0	5.46	0.90	0.01	2.63	2.1	3.75	−15%
43	0.45	0.70	1.0	0.0	5.58	0.97	0.00	2.71	2.2	4.39	−15%
60*	0.45	0.55	1.2	5.7	2.39	0.37	0.05	2.15	2.2	1.26	+10%

References and Notes

1. R. M. Canup, E. Asphaug, *Nature* **412**, 708 (2001).
2. R. M. Canup, *Icarus* **168**, 433 (2004).
3. R. M. Canup, *Icarus* **196**, 518 (2008).
4. U. Wiechert *et al.*, *Science* **294**, 345 (2001).
5. G. W. Lugmair, A. Shukolyukov, *Geochim. Cosmochim. Acta* **62**, 2863 (1998).
6. J. Zhang, N. Dauphas, A. M. Davis, I. Leya, A. Fedkin, *Nat. Geosci.* **5**, 251 (2012).
7. J. A. Wood, in *Origin of the Moon*, W. K. Hartmann, R. J. Phillips, G. J. Taylor, Eds. (LPI, Houston, 1984), pp. 17–55.
8. E. Belbruno, R. J. Gott III, *Astron. J.* **129**, 1724 (2005).
9. K. Pahlevan, D. J. Stevenson, *Earth Planet. Sci. Lett.* **262**, 438 (2007).
10. J. E. Chambers, *Icarus* **152**, 205 (2001).
11. H. J. Melosh, *Annual Meeting of the Meteoritical Society LXXII*, 5104 (2009).
12. M. Čuk, S. T. Stewart, *Early Solar System Impact Bombardment II*, Feb. 1 to 3, Houston, abstr. 4006 (2012).
13. M. Čuk, S. T. Stewart, *Science* **338**, 1047 (2012).
14. A. Reufer, M. M. Meier, W. Benz, R. Wieler, *Lunar Planet. Sci.* **XLII**, 1136 (2011).

15. Materials and methods are available as supplementary materials on Science Online.
16. W. Benz, A. G. W. Cameron, H. J. Melosh, *Icarus* **81**, 113 (1989).
17. S. L. Thompson, H. S. Lauson, *Technical Rep. SC-RR-710714*, Sandia Nat. Labs (1972).
18. H. J. Melosh, *Meteorit. Planet. Sci.* **42**, 2079 (2007).
19. S. Ida, R. M. Canup, G. R. Stewart, *Nature* **389**, 353 (1997).
20. E. Kokubo, J. Makino, S. Ida, *Icarus* **148**, 419 (2000).
21. M. M. Meier, A. Reufer, W. Benz, R. Wieler, *Annual Meeting of the Meteoritical Society LXXIV*, abstr. 5039 (2011).
22. C. B. Agnor, R. M. Canup, H. F. Levison, *Icarus* **142**, 219 (1999).
23. D. P. O'Brien, A. Morbidelli, H. F. Levison, *Icarus* **184**, 39 (2006).
24. R. M. Canup, *Science* **307**, 546 (2005).
25. J. J. Salmon, R. M. Canup, *Lunar Planet. Sci.* **XLIII**, 2540 (2012).

Acknowledgments: SPH simulation data are contained in tables S2 to S5 of the supplementary materials. Financial support for this project was provided by the NASA Lunar Science Institute and by NASA's LASER program.

Supplementary Materials

www.sciencemag.org/cgi/content/full/science.1226073/DC1

Materials and Methods

Figs. S1 and S2

Tables S1 to S5

References (26–36)

14 June 2012; accepted 1 October 2012

Published online 17 October 2012;

10.1126/science.1226073

How Does Plant Cell Wall Nanoscale Architecture Correlate with Enzymatic Digestibility?

Shi-You Ding,^{1*†} Yu-San Liu,^{1*} Yining Zeng,¹ Michael E. Himmel,¹ John O. Baker,¹ Edward A. Bayer²

Greater understanding of the mechanisms contributing to chemical and enzymatic solubilization of plant cell walls is critical for enabling cost-effective industrial conversion of cellulosic biomass to biofuels. Here, we report the use of correlative imaging in real time to assess the impact of pretreatment, as well as the resulting nanometer-scale changes in cell wall structure, upon subsequent digestion by two commercially relevant cellulase systems. We demonstrate that the small, noncomplexed fungal cellulases deconstruct cell walls using mechanisms that differ considerably from those of the larger, multienzyme complexes (cellulosomes). Furthermore, high-resolution measurement of the microfibrillar architecture of cell walls suggests that digestion is primarily facilitated by enabling enzyme access to the hydrophobic cellulose face. The data support the conclusion that ideal pretreatments should maximize lignin removal and minimize polysaccharide modification, thereby retaining the essentially native microfibrillar structure.

Modern biorefineries are being developed to produce transportation fuels from plant biomass using sustainable technologies that also benefit the environment by reducing greenhouse gas emissions (1). The major challenges facing this industry are the high cost of pretreatment and the low efficiency of enzymatic hydrolysis of plant cell wall polysaccharides to sugars. Further improvement of these processes is contingent on deeper understanding of biomass structure and chemistry, as well as improved understanding of the molecular mechanisms of biomass deconstruction (2).

Despite renewed interest in biomass degradation, there is little agreement about which plant cell wall features most affect digestibility by microbes and cellulytic enzymes. The activities of cellulytic enzymes are usually characterized by assay against purified or highly modified crystalline or amorphous celluloses, as well as soluble substrates (3). Actual plant cell walls, however, are complex nanocomposites containing networks of cellulose fibrils and complex "matrixing" poly-

mers. The overall performance of biomass saccharification may be attributed to the synergistic action of many complementary enzymes—including a variety of cellulases, hemicellulases, and accessory enzymes (4)—which makes it difficult to study one factor at a time. Traditional solution methods have suffered from the classical ensemble average limitation presented by analysis of these mixtures of complex biomass; therefore, the data gathered are sometimes inconclusive and, in part, contradictory. To overcome these problems, we visualized the action of these enzyme systems on untreated and delignified plant cell walls under controlled digestion conditions in real time with the use of a multimodal microscopy suite, including bright-field light microscopy, confocal laser scanning microscopy (CLSM), two-color stimulated Raman scattering (SRS) microscopy, and atomic force microscopy (AFM). The microscopes were custom-constructed to allow correlative imaging of the same biomass sample under near-physiological conditions and at high chemical (5, 6) and spatial (7, 8) resolutions at the tissue, cellular, and molecular levels. We examined two naturally existing enzyme systems of commercial relevance for saccharification of lignocellulosic biomass: (i) the secretome of the anaerobe *Clostridium thermocellum*, which is representative of multienzyme bacterial cellulosomes (9), and (ii) a commercially available blended enzyme mixture (Cellic CTec2, Novozymes, Bagsvaerd,

Denmark) derived from the fungus *Trichoderma reesei* (*Hypocrea jecorina*), which is representative of the fungal or "free" cellulases (10). We used green fluorescent protein (GFP)-tagged carbohydrate-binding modules (CBMs) to identify exposed cellulose surfaces and green dye (Alexa Fluor 488, Invitrogen, Carlsbad, CA)-labeled enzymes to examine overall cell wall accessibility to cellulases. *T. reesei* CBM1 derived from *T. reesei* cellobiohydrolase I (CBH I or Cel7A) (11) and *CtCBM3* derived from *C. thermocellum* cellosomal scaffoldin protein (CipA) (12) specifically recognize the planar face of crystalline cellulose (8, 13, 14) and play a critical role in the hydrolysis of crystalline cellulose (15, 16).

Naturally senescent, dried corn (*Zea mays* L.) stover stem internode sections served as an example of plant cell wall material. The transverse view of the untreated maize stem represents the typical tissue structure of monocotyledons with scattered vascular bundles (VBs) surrounded by parenchyma cells (fig. S1, A and B). In this context, cell walls in mature plants are generally classified as one of three types: (i) The primary walls (PWs) are thin (~100 nm) and expanded, but are neither elongated nor lignified. (ii) Parenchyma-type secondary walls (pSWs) are found in large parenchyma tissue between the VBs, which are elongated or expanded and partially lignified in the secondarily thickened wall (~1 to 2 μ m). (iii) Sclerenchyma-type SWs (sSWs) are elongated and fully lignified in the heavily thickened (~5 to 10 μ m) SW. The innermost side of a sSW is often covered by "warts," which mainly contain condensed lignin-like polyphenols (17). Note that the materials used in this study are from dead plants; cell walls in a living plant may be more structurally complex and diversified.

Using two-color SRS microscopy, where the Raman signal at 1600 cm^{-1} (aromatic-ring breathing modes) represents primarily lignin and the 2900 cm^{-1} (C-H stretch) band represents primarily polysaccharides (18), we found that the lignin and polysaccharide contents in sSWs were higher than those in pSWs (fig. S1, C to E) and that the polysaccharide content was generally higher in SWs than in PWs. These observations are in agreement with general plant anatomy.

The presence of lignins, a group of highly branched phenylpropanoid polymers found in terrestrial plants, is generally considered to be one of the most important limiting factors in

¹Biosciences Center, National Renewable Energy Laboratory, Golden, CO 80401, USA. ²Department of Biological Chemistry, The Weizmann Institute of Science, Rehovot 76100, Israel.

*These authors contributed equally to this work.

†To whom correspondence should be addressed. E-mail: shi.you.ding@nrel.gov

the enzymatic cell wall saccharification process (19). Whether lignins affect enzyme digestibility by physically impeding or nonspecifically absorbing enzymes remains open to debate. To address this question, we used acid chlorite to produce delignified cell walls. This delignification process has been widely used to produce holocellulose (20). At low temperature, acid chlorite oxidizes phenolic compounds (mainly lignins) in cell walls without altering cellulose and with minimum effect on associated hemicelluloses (5, 21).

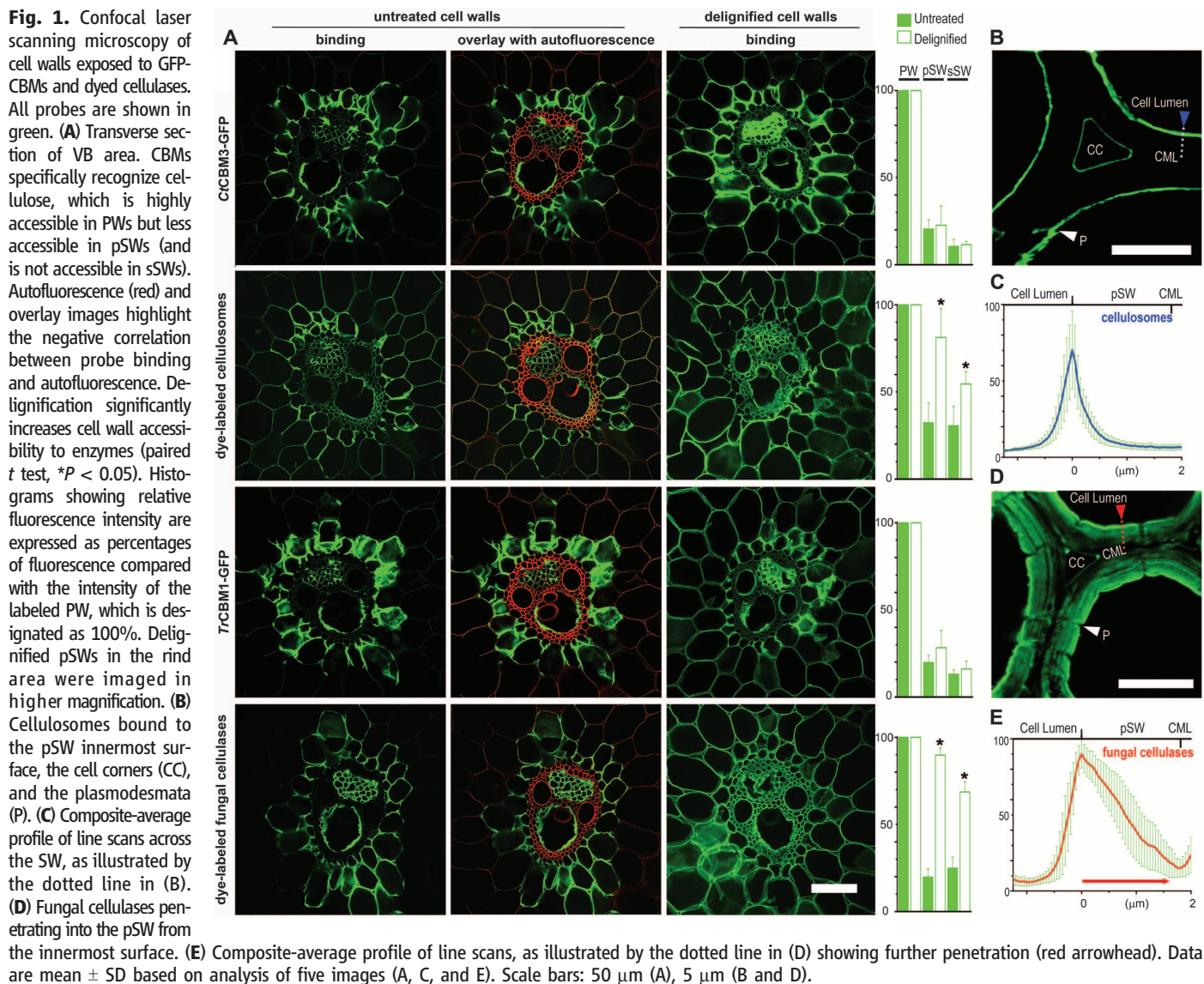
As anticipated, we confirmed that accessibility of untreated cell walls to CBMs and enzyme binding exhibits a strong negative correlation with their lignin content. All CBMs and enzymes bind strongly to nonlignified PWs and more weakly to pSWs. Binding to the condensed lignin “warty layer” in sSWs is negligible, indicating that nonspecific adsorption of processed lignin to enzyme reported previously (22) was not observed in the case of a native lignin examined in situ. Lignin removal enhanced overall binding of all probes to lignified walls (i.e., pSWs

and sSWs) (Fig. 1), following the trend: fungal cellulases (greatest enhancement), cellulosomes, *T*/CBM1, and then *C*/CBM3 (least enhancement). Accessibility of pSWs and sSWs to enzymes was more strongly enhanced than that to CBMs, which could generally be attributed to increased accessibility of hemicelluloses to enzymes after removal of blocking lignins. Further imaging of delignified pSWs by CLSM showed that cellulosomes primarily attached to the surface of the cell walls, the cell corners, and the plasmodesmata (Fig. 1, B and C, and fig. S2A). Fungal cellulases not only bound at these surfaces, but also penetrated inside the SW from its innermost side (Fig. 1, D and E, and fig. S2B), suggesting that delignification may render the cell wall more accessible to fungal cellulases.

After delignification, we found that the lignin signal at 1600 cm^{-1} was eliminated and the 2900-cm^{-1} signal was slightly reduced, suggesting that hemicelluloses are generally resistant to acid chlorite treatment at room temperature (Fig. 2, A to E).

The fungal cellulases and cellulosomes that we used in this study contain mixtures of enzymes specific for degradation of different polysaccharide components of cell walls. The digestion temperatures used here were optimal for the fungal (38°C) and cellulosomal (55°C) enzymes. In untreated cell walls, both enzyme systems readily digested PWs only (Fig. 2, F, G, J, and K), and SRS microscopy also revealed minor digestion of pSWs (Fig. 2E and fig. S3). Overall digestibility was strongly negatively correlated with lignin content. Complete degradation was not observed in naturally lignified walls (i.e., pSWs and sSWs), even with 100-fold greater concentrations of enzyme and extended periods of time (7 days).

After delignification, all cell walls were completely digested with the original level of cellulase protein loading (Fig. 2, H and L). Despite the difficulties of quantitatively determining enzyme digestion rates by microscopy alone, we discovered that fungal cellulases acted approximately five times faster than cellulosomes against either untreated or delignified cell walls, based on



the percentage loss of SRS signals at 2900 cm^{-1} . The time needed for complete digestion of the delignified walls apparently depends on wall mass concentration and not on wall types (Fig. 2, I and M). Thinner and less dense walls were digested rapidly, suggesting that the chemical features of the polysaccharides existing in different cell wall types may have less impact on overall digestibility than expected, at least in the case of acid chlorite-treated biomass, in which lignins have been selectively oxidized.

From experiments at room temperature, we made the qualitative observations that the cellulosomes first separated the walls from the compound middle lamella (CML) and then fragmented the walls into segments (Fig. 3A and movie S1), whereas fungal cellulases dissolved the entire wall in a uniform manner (Fig. 3B and movie S2). During the course of digestion by fungal cellulases, the CML remained mostly intact, suggesting that digestion occurred from the innermost side of the cell walls, thus supporting the binding data (Fig. 1D).

We used AFM for real-time imaging of pSW digestion at the microfibril level. In the untreated

cell wall, only a few surface microfibrils were degradable by either of the enzyme systems. After delignification, the cellulosomes appeared to peel off individual microfibrils from the cell wall surface (Fig. 3C and movie S3), whereas the fungal cellulases penetrated inside microfibril networks and made digestion holes or pits (Fig. 3D and movie S4). For quantitative analysis, the surface roughness was expressed by relative Z ranges of AFM images. In the case of cellulosomes, the roughness remained unchanged (Fig. 3E), whereas digestion by fungal cellulases increased the roughness dramatically (Fig. 3F). Individual microfibrils were digested within a few minutes by each of the enzyme systems. Because AFM movies were acquired within a $1\text{-}\mu\text{m}^2$ scan area, the length of the microfibrils is unknown; therefore, the digestion rate cannot be estimated unambiguously. The wall structure under buffer was similar to that in air with minor differences, consisting primarily of straightening and debundling surface fibrils (fig. S4).

Cellulose represents ~70% of the total cell wall polysaccharides, and its accessibility to enzymes determines the overall digestibility. We

have previously reported that CBH I binds to and hydrolyzes the hydrophobic planar faces of purified cellulose crystals (8). To further identify the cell wall architectural features that may contribute to differences in accessibility to and digestibility by cellulases, we used nanometer-scale AFM to image untreated and delignified cell walls.

As previously reported, we observed three types of fibrillar structures (7, 23): Ribbon-like macrofibrils, consisting of a number of cellulose elementary fibrils (CEFs), exist in PWs (fig. S5) and on the pSW surface (Fig. 4A and fig. S6). Microfibrils, which contain one CEF and associated hemicelluloses, are predominant in pSWs and sSWs (fig. S7). Although smaller CEFs, such as the 24-chain diamond-shaped model (24), have been proposed, we favor the 36-chain model, primarily based on microfibril size measured directly in the current study and on two primary assumptions: (i) that cell wall cellulose is mostly crystalline and (ii) that the CBM binding face recognizes the cellulose planar face involving three chains (14, 25). Therefore, packing of cellulose I β (26) would allow three chains on

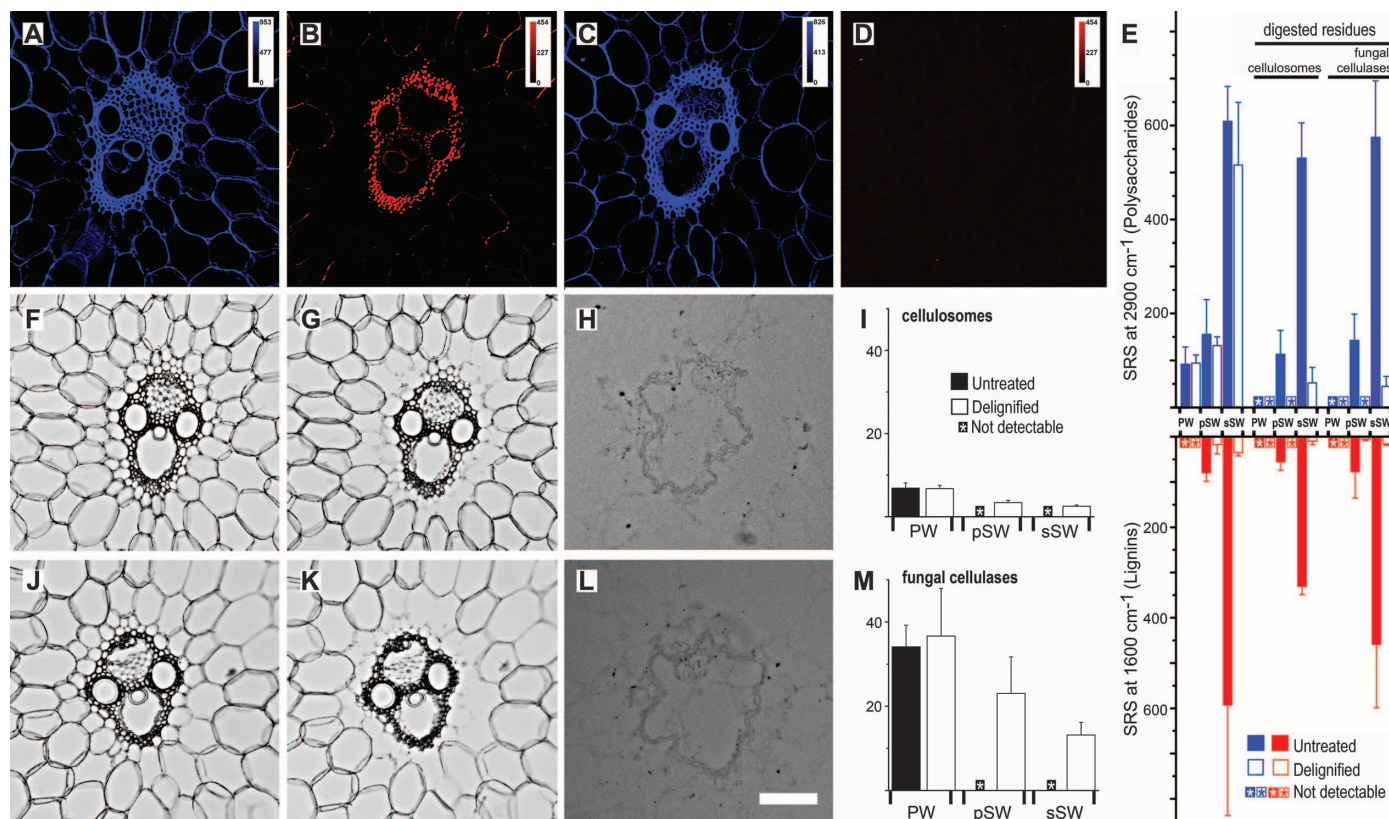


Fig. 2. Stimulated Raman scattering (SRS) microscopy of untreated cell walls showing (A) polysaccharides at 2900 cm^{-1} (blue) and (B) lignins at 1600 cm^{-1} (red). After delignification, (C) the signal at 2900 cm^{-1} is slightly reduced, and (D) the 1600 cm^{-1} signal is eliminated. (E) Histograms of SRS signals in untreated and delignified cell walls and enzyme-digested residues. Bright-field light images of untreated cell walls before (F) and after (G) digestion by cellulosomes for 15 hours at 55°C showing that only the PWs are completely digested. (H) Delignified walls digested by the cellulosomes for 17 hours at 55°C , showing that all cell walls are digested. (I) Relative digestion rates by

cellulosomes. (J and K) Untreated cell walls before (J) and after (K) digestion by fungal cellulases for 3 hours at 38°C , showing that only the PWs are digested. (L) Delignified cell walls are completely digested by fungal cellulases in 8 hours at 38°C . (M) Relative digestion rates by fungal cellulases. Color bars in (A) to (D) show the lock-in amplifier signals of SRS. Signals that are not detectable are indicated by asterisks in boxes in (E), (I), and (M). Relative digestion rates were calculated based on the percentage loss of SRS signal at 2900 cm^{-1} per hour (I and M). Data are mean \pm SD based on triplicate measurements (E, I, and M). Scale bar: $50\text{ }\mu\text{m}$ (A to L).

the planar faces (100 and -100), supporting the 36-chain model.

High-resolution AFM images also allowed precise measurement of the size of fibrillar structures. Isolated microfibrils (Fig. 4A) that appeared twisted were found occasionally on the dry cell wall surface. Note that this twisting effect was not found under aqueous conditions, suggesting that it may be caused by dehydration. In such cases, the AFM line-scan profiles of both vertical (Fig. 4B) and horizontal (Fig. 4C) orientations could be measured on the same CEF. Our measurement of a macrofibril containing two CEFs suggested that they are horizontally associated through their hydrophilic faces (Fig. 4, D and E). Individual microfibrils in pSWs were visualized as sharp edges with bridges partially covering the area between them (Fig. 4, A and D, and fig. S6E), in which the CEF appeared to be primarily vertically oriented. Macrofibril splitting and CEF rotation from horizontal to vertical may occur during cell elongation or expansion (fig. S8).

Quantitative analysis using AFM scan profiles of macrofibrils, microfibrils, and CEFs (Fig. 4F) showed that the widths are slightly larger [3.3 ± 0.5 nm (vertical) and 5.7 ± 0.9 nm (horizontal)] than those predicted from the 36-chain model (7) [i.e., 3.2 nm (vertical) by 5.3 nm (horizontal)], which may be caused by a combined effect of AFM tip broadening and CEF association with matrix polymers, especially in sSWs (fig. S7C). The microfibrils in the SW appeared to form parallel layers, observed in transverse sections (fig. S7E) and the broken surface in sSWs after delignification (fig. S7I). Cell wall porosity (open space) is measured by three distances between fibrils (5 to 20 nm), layers of microfibrils (10 to 20 nm) (7), and wall lamellae gaps (50 to 100 nm) appearing in the SWs (fig. S7B). Delignification did not substantially alter microfibril structure and arrangement, except for the reduction of matrix polymers of the sSW (fig. S7, G and H).

Schematic structures of the PW and the sandwich-like SW in pSWs and sSWs containing layers of microfibrils and lignin-polysaccharides are illustrated in Fig. 4G. Here, we combine the concepts suggested by the AFM and digestion data, which include the bundling of microfibrils into macrofibrils in PWs and the natural availability of cellulose planar faces in PWs.

These observations of cell wall architecture and microfibril structure are consistent with accessibility to (Fig. 1) and digestibility by (Fig. 2) enzymes, suggesting that the hydrophobic planar face of cellulose is the preferred binding face and thus is critical for enzyme access. In PWs, the CEF hydrophobic faces in macrofibrils are exposed to allow accessibility to cellulases, as confirmed by the strong binding of CBMs and complete digestibility by cellulases. In pSWs, the small surface macrofibrils and microfibrils are accessible, but microfibrils inside the wall are blocked by the lignin-polysaccharide complex

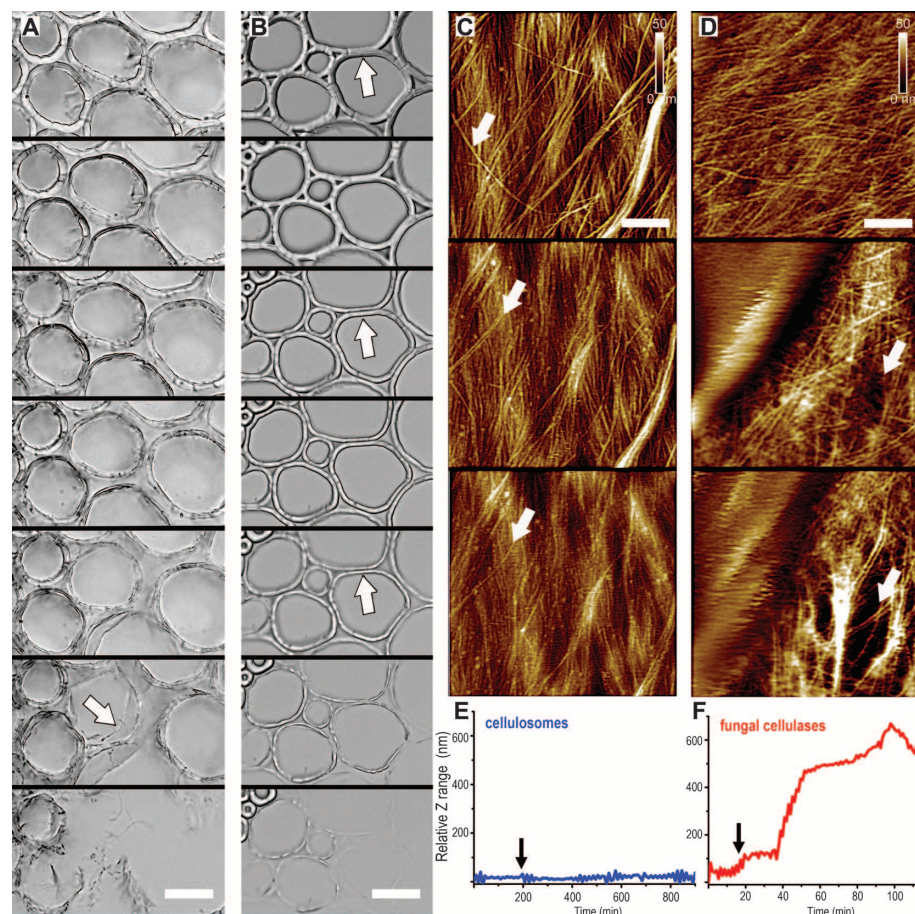


Fig. 3. Delignified pSWs imaged in real time during digestion at room temperature. Bright-field light microscopy of a transverse section digested (A) by cellulosomes for 7 days, showing wall fragmentation (white arrow), and (B) by fungal cellulases for 10 hours, showing wall dissolving. White arrows in (B) indicate the wall's innermost side. AFM imaging of a single pSW surface digested (C) by cellulosomes for 13 hours, showing peeling-off of individual microfibrils (white arrows), and (D) by fungal cellulases for 2 hours, showing penetration (white arrows). Images in (A) to (D) were taken from movies S1, S2, S3, and S4, respectively. Relative Z ranges of AFM images were recorded as changes of vertical distance during digestion by (E) cellulosomes (movie S3), showing conserved roughness, and by (F) fungal cellulases (movie S4), showing increasing roughness. Black arrows indicate the time points of enzyme addition. Color bars in (C) and (D) represent the scale of the AFM height images. Scale bars: 50 μ m (A and B), 200 nm (C and D).

between microfibril layers (Fig. 4G), resulting in diminished CBM binding and limited digestibility by enzymes. In sSWs, lignins form an additional barrier on the innermost side, the condensed lignin warty layer (17), that blocks accessibility of microfibrils to enzymes (Fig. 1), resulting in no digestibility of sSWs (Fig. 2). These observations are also supported by studies on cell wall development, which have indicated that SW thickening begins while the cell is still elongating (27). In later stages of elongation, SW deposition is accompanied by a lignification process that may cause a decrease and eventual cessation of cell elongation. pSWs are not lignified until cessation of vegetative growth in grassy plants; consequently, these walls are completely digestible if harvested during vegetative growth (28).

Acid chlorite treatment effectively removes lignins in the SW (Fig. 2 and fig. S7H) and the

warty layer in sSW (fig. S7F), thereby exposing microfibrils (fig. S7, G to I) to enzyme access, resulting in near-complete digestion of all cell walls. After lignin removal in the SWs, accessibility of the cellulose planar face is then determined by wall porosity. Under the conditions of this study, we observed enhanced digestibility by fungal cellulases due to their penetration into the pore structure of microfibril networks (Fig. 3D and movie S4). In contrast, the larger cellulosome complexes could only penetrate the larger wall lamella gaps (fig. S7B), resulting in fragmentation of walls (Fig. 3A and movie S1). The advantageous degradation properties exhibited by the fungal cellulases on cell walls may be compromised when digesting purified forms of crystalline cellulose, such as Avicel PH101 (Sigma, St. Louis, MO) (29), in which the porous architecture of the native cellulose microfibril network

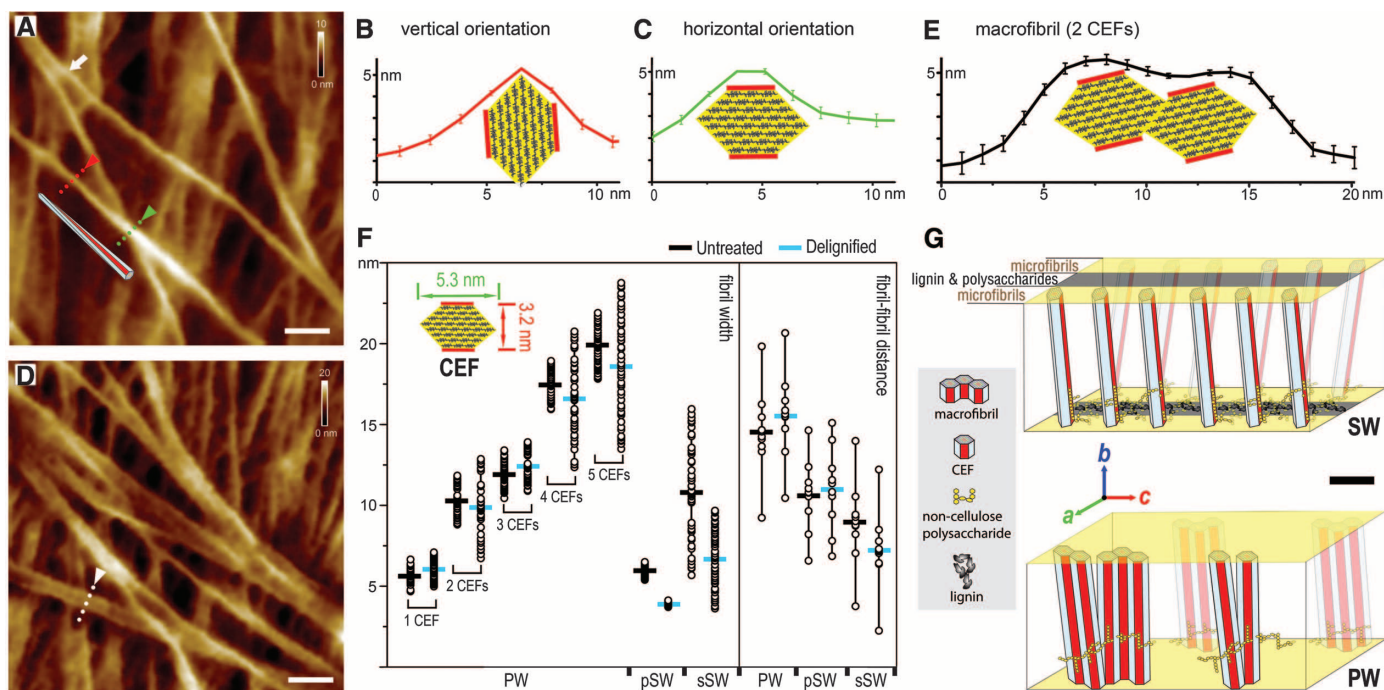


Fig. 4. Size, shape, and arrangement of the CEFs. (A) An individual twisted CEF shown in delignified pSW surfaces. Composite-average profile of line scans across the CEF appear in (B) vertical orientation [red dotted-line in (A)] and (C) horizontal orientation [green dotted-line in (A)]. (D) An untreated pSW showing macrofibrils and microfibrils. (E) Composite-average profile of line scans across macrofibrils [white dotted-line in (D)] containing two CEFs. Data are mean \pm SD based on measurements of five well-defined microfibrils (B and C) and macrofibrils (E). (F) Width measurements of 50 well-resolved fibrils (left) and average fibril-fibril distances measured in the entire image (right). Ten images were measured for untreated and delignified PWs, pSWs, and sSWs. Macrofibril widths containing two to five CEFs in a PW were determined directly by tracing fibril splitting. Horizontal bars denote mean values. (Inset) Dimensions of the 36-chain CEF model are 5.3 nm (horizontal, green arrow) by 3.2 nm

(vertical, red arrow). The hydrophobic CEF faces are indicated in red. Furthermore, one CEF in the PW is expected to display the horizontal orientation, which provides an apparent width of 5.3 nm based on cellulose structure. After delignification in pSWs, the vertical orientation is expected, which provides an apparent width of 3.2 nm. (G) Schematic illustration showing assembly of main cell wall components in the PW and the sandwich-like SW. Scale is based on the average fibril-fibril distance measured in (F). Cell wall orientations are indicated as: (a) transverse and (b) tangential relative to the cell lumen, and (c) cell long axis. Color bars in (A) and (D) represent the scale of the AFM height images; the white arrow in (A) indicates macrofibril splitting. Scale bar: 10 nm (A, D, and G). Additional images showing macrofibrils and microfibrils in untreated and delignified PWs, pSWs, and sSWs are presented in fig. S5 to S7, respectively. The proposed macrofibril splitting and rotating process is shown in fig. S8.

has been completely destroyed during its preparation process. Similarly, it has been reported that biomass digestibility was notably reduced upon near-complete removal of both lignin and hemicelluloses (21). In contrast, the activity of cellulosomes was reported to be higher than, or at least comparable to, that of the fungal cellulases on pure cellulose substrates (30).

Despite the different mechanisms of fungal cellulases and cellulosomes revealed in this study, cell wall materials are completely digestible by either when lignins are effectively removed. Thermochemical pretreatment strategies to enhance biomass digestibility by partial removal or redistribution of lignin have been developed (31), however, these mechanisms result in sugar degradation and loss at high severities (32). The challenge now is to effectively and economically modify lignins via strategies that maintain the integrity of fermentable sugars. Researchers have recently focused on genetically engineering plants for desirable lignin contents or compositions that are more amenable to classical pretreatment at low severities (33–35). In the foreseeable future, we expect that lignins in genetically modified energy plants will be extracted

under mild conditions and used as valuable chemicals; the remaining cell wall architecture could be left intact with minimum alteration of the polysaccharides. In this scenario, effective digestion by enzymes, especially fungal cellulases, could provide near-theoretical yields of fermentable sugars.

References and Notes

1. A. J. Ragauskas *et al.*, *Science* **311**, 484 (2006).
2. M. E. Himmel *et al.*, *Science* **315**, 804 (2007).
3. L. R. Lynd, P. J. Weimer, W. H. van Zyl, I. S. Pretorius, *Microbiol. Mol. Biol. Rev.* **66**, 506 (2002).
4. B. Henrissat, H. Driguez, C. Viet, M. Schülein, *Nat. Biotechnol.* **3**, 722 (1985).
5. B. G. Saar *et al.*, *Angew. Chem. Int. Ed.* **49**, 5476 (2010).
6. Y. N. Zeng *et al.*, *Bioenerg. Res.* **3**, 272 (2010).
7. S. Y. Ding, M. E. Himmel, *J. Agric. Food Chem.* **54**, 597 (2006).
8. Y. S. Liu *et al.*, *J. Biol. Chem.* **286**, 11195 (2011).
9. E. Morag, E. A. Bayer, R. Lamed, *Enzyme Microb. Technol.* **14**, 289 (1992).
10. L. E. Berghem, L. G. Pettersson, *Eur. J. Biochem.* **37**, 21 (1973).
11. D. J. Dagel *et al.*, *J. Phys. Chem. B* **115**, 635 (2011).
12. S. Y. Ding *et al.*, *Biotechniques* **41**, 435 (2006).
13. J. Lehtö *et al.*, *Proc. Natl. Acad. Sci. U.S.A.* **100**, 484 (2003).
14. J. Tormo *et al.*, *EMBO J.* **15**, 5739 (1996).
15. N. R. Gilkes, R. A. J. Warren, R. C. Miller Jr., D. G. Kilburn, *J. Biol. Chem.* **263**, 10401 (1988).
16. P. Tomme *et al.*, *Eur. J. Biochem.* **170**, 575 (1988).
17. S. Jansen, E. Smets, P. Baas, *IAWA J.* **19**, 347 (1998).
18. R. H. Atalla, U. P. Agarwal, *J. Raman Spectrosc.* **17**, 229 (1986).
19. R. Vanholme, B. Demedts, K. Morreel, J. Ralph, W. Boerjan, *Plant Physiol.* **153**, 895 (2010).
20. L. E. Wise, M. Murphy, A. A. D'Addieco, *Paper Trade J.* **122**, 35 (1946).
21. C. I. Ishizawa *et al.*, *Cellulose* **16**, 677 (2009).
22. H. Ooshima, D. S. Burns, A. O. Converse, *Biotechnol. Bioeng.* **36**, 446 (1990).
23. D. Harris, V. Bulone, S. Y. Ding, S. DeBolt, *Plant Physiol.* **153**, 420 (2010).
24. A. N. Fernandes *et al.*, *Proc. Natl. Acad. Sci. U.S.A.* **108**, E1195 (2011).
25. J. Kraulis *et al.*, *Biochemistry* **28**, 7241 (1989).
26. Y. Nishiyama, P. Langan, H. Chanzy, *J. Am. Chem. Soc.* **124**, 9074 (2002).
27. C. S. Gritsch, R. J. Murphy, *Ann. Bot. (London)* **95**, 619 (2005).
28. H. G. Jung, M. D. Casler, *Crop Sci.* **46**, 1801 (2006).
29. B. Yang, Z. Dai, S.-Y. Ding, C. E. Wyman, *Biofuels* **2**, 421 (2011).
30. E. A. Johnson, M. Sakajoh, G. Halliwell, A. Madia, A. L. Demain, *Appl. Environ. Microbiol.* **43**, 1125 (1982).
31. B. S. Donohoe *et al.*, *Biotechnol. Bioeng.* **103**, 480 (2009).

32. R. Kumar, C. E. Wyman, *Biotechnol. Bioeng.* **102**, 1544 (2009).
 33. C. X. Fu et al., *Proc. Natl. Acad. Sci. U.S.A.* **108**, 3803 (2011).
 34. F. Chen, R. A. Dixon, *Nat. Biotechnol.* **25**, 759 (2007).
 35. F. Chen, Y. Tobimatsu, D. Havkin-Frenkel, R. A. Dixon, J. Ralph, *Proc. Natl. Acad. Sci. U.S.A.* **109**, 1772 (2012).

Acknowledgments: We thank M. P. Tucker for the fungal cellulases; S. Xie for guidance regarding SRS microscopy; K. Ruckman for manuscript editing; and A. J. Ragauskas,

C. E. Wyman, M. F. Davis, D. J. Johnson, and R. H. Atalla for valuable discussion. This work was supported by the U.S. Department of Energy (DOE) under contract no. DE-AC36-08-GO28308 with the National Renewable Energy Laboratory. We acknowledge research support from the BioEnergy Science Center, a DOE Bioenergy Research Center, and the Genomic Science Program (ER65258), both supported by the Office of Biological and Environmental Research in the DOE Office of Science. S.-Y.D. conceptualized the project, conducted AFM, analyzed the data, and wrote the manuscript. Y.-S.L. conducted enzyme labeling, bright-field light microscopy, and CLSM. Y.Z. conducted SRS microscopy. E.A.B. purified the

cellulosomes. S.-Y.D., M.E.H., J.O.B., and E.A.B. revised the manuscript. We declare no competing financial interests.

Supplementary Materials

www.sciencemag.org/cgi/content/full/338/6110/1055/DC1
 Materials and Methods
 Figs. S1 to S8
 References (36–40)
 Movies S1 to S4

16 July 2012; accepted 21 September 2012
 10.1126/science.1227491

Quantum-State Resolved Bimolecular Collisions of Velocity-Controlled OH with NO Radicals

Moritz Kirste,^{1*} Xingan Wang,^{1*} H. Christian Schewe,¹ Gerard Meijer,¹ Kopin Liu,² Ad van der Avoird,³ Liesbeth M. C. Janssen,³ Koos B. Gubbels,³ Gerrit C. Groenenboom,^{3†} Sebastiaan Y. T. van de Meerakker^{3,1†}

Whereas atom-molecule collisions have been studied with complete quantum-state resolution, interactions between two state-selected molecules have proven much harder to probe. Here, we report the measurement of state-resolved inelastic scattering cross sections for collisions between two open-shell molecules that are both prepared in a single quantum state. Stark-decelerated hydroxyl (OH) radicals were scattered with hexapole-focused nitric oxide (NO) radicals in a crossed-beam configuration. Rotationally and spin-orbit inelastic scattering cross sections were measured on an absolute scale for collision energies between 70 and 300 cm⁻¹. These cross sections show fair agreement with quantum coupled-channels calculations using a set of coupled model potential energy surfaces based on ab initio calculations for the long-range nonadiabatic interactions and a simplistic short-range interaction. This comparison reveals the crucial role of electrostatic forces in complex molecular collision processes.

Rotationally inelastic scattering is one of the key processes underlying the exchange of energy between molecules (1, 2). In bulk systems, rotational energy transfer (RET) is responsible for the thermalization of state populations after a chemical reaction. In the dilute interstellar medium, inelastic collisions contribute to the formation of nonthermal population distributions that result in, for instance, interstellar masers (3). Accurate state-to-state inelastic scattering cross sections are essential ingredients for reliable models of chemical processes in combustion physics, atmospheric science, and astrochemistry.

In molecular beam collision experiments, the ability to prepare molecules in a single rotational (sub)level before the collision using electric, magnetic, or optical fields has been imperative to unravel the underlying mechanisms of molecular energy transfer. This has made scattering exper-

iments possible at the full state-to-state level and has resulted in the discovery of propensity rules for inelastic scattering (4), the stereodynamics of molecular collisions (5, 6), and quantum interference effects (7–9). The latest beam deceleration and acceleration methods (10, 11) allow for the precise variation of the collision energy, resulting in the observation of quantum threshold effects in the state-to-state cross sections (12, 13). This wealth of studies has contributed enormously to our present understanding of how intermolecular potentials govern molecular collision dynamics.

Thus far, these methods have mostly been used to study collisions of state-selected molecules with rare gas atoms. Yet, in most natural environments, molecule-molecule interactions play a major role. For instance, space telescope observations of cometary water may reveal the possible origin of water on Earth, but a conclusive interpretation requires accurate knowledge of RET in water-water collisions (14). Whereas atom-molecule scattering cross sections can now be calculated routinely in excellent agreement with experiment (13, 15), much less is known about RET in molecule-molecule collisions (16). As opposed to an atomic target, a molecular scattering partner possesses internal degrees of freedom of its own, adding a level of complexity that

can easily render ab initio quantum scattering calculations extremely challenging, if not impossible. This is particularly true for collisions involving radical species that are governed by multiple Born-Oppenheimer (BO) potential energy surfaces (PESs) with nonadiabatic couplings between them. Experimental data on bimolecular state-to-state cross sections is generally lacking, and kinetic models often use collision rate coefficients that are expected to be inaccurate (17).

The study of molecule-molecule collisions at the ultimate quantum level has been a quest in molecular beam physics since it was established in the 1950s (18). Major obstacles exist that have prevented studies of state-to-state bimolecular scattering (19). The main challenge is the need for reagent beams with sufficient quantum-state purity at the densities necessary to observe population transfer in one, or both, reagent beam(s). Thus far, experiments of this kind have only been possible using cryogenically cooled H₂ molecules as a target beam (20, 21).

Here, we report the successful measurement of state-resolved inelastic scattering between two state-selected molecular beams. We have chosen the OH ($X^2\Pi$) + NO ($X^2\Pi$) system (22) for this purpose, as both open-shell radical species are benchmark systems for the scattering of state-selected molecules with rare gas atoms that involve two BO PESs (23). Collisions between OH and NO involve eight interacting PESs, representing the full complexity of bimolecular inelastic collisions (24). The OH-NO system serves also as a prototypical example of radical-radical reactions of fundamental importance in gas-phase chemical kinetics (25). We used a Stark decelerator and a hexapole state selector in a crossed molecular beam configuration to produce reagent beams of OH and NO radicals with an almost perfect quantum-state purity. The collision energy was varied between 70 and 300 cm⁻¹ by tuning the velocity of the OH radicals before the collision using the Stark decelerator, revealing the quantum threshold behavior of the state-to-state inelastic scattering cross sections. The unusually well-defined distributions of reagent molecules allowed us to determine absolute scattering cross sections, which can normally be determined only on a relative scale in crossed-beam experiments. These cross sections showed fair agreement with a theoretical model for inelastic collisions between two ²Ti radical species, based solely on an accurate description of the full rotational and open-shell structure of both

¹Fritz-Haber-Institut der Max-Planck-Gesellschaft, Faradayweg 4-6, 14195 Berlin, Germany. ²Institute of Atomic and Molecular Sciences (IAMS), Academia Sinica, Taipei, Taiwan 10617. ³Radboud University Nijmegen, Institute for Molecules and Materials, Heijendaalseweg 135, 6525 AJ Nijmegen, The Netherlands.

*These authors contributed equally to this work.

†To whom correspondence should be addressed. E-mail: basvd@science.ru.nl (S.Y.T.v.d.M.), gerritg@theochem.ru.nl (G.C.G.)

radical species and their long-range nonadiabatic electrostatic interactions. This study revealed that inelastic scattering predominantly occurs at large intermolecular distances, even for the relatively high collision energies probed here.

The crossed molecular beam apparatus used to study inelastic collisions between OH and NO radicals is schematically shown in Fig. 1 (26). A packet of OH radicals [$X^2\Pi_{3/2}$, $v = 0$, $j = 3/2$, f (22), referred to hereafter as $F_1(3/2f)$] with a tunable velocity in the 200 to 750 m/s range was produced using a 2.6-m long Stark decelerator (27). The velocity of the OH radicals was tuned by applying a burst of high-voltage pulses to the electric field electrodes at the appropriate times. The state purity of the OH packets was such that less than 0.01% of the OH radicals populated a lower Λ -doublet component of any rotational level.

A beam of NO radicals with a fixed velocity was produced by seeding NO in a xenon carrier gas and was passed through a 30-cm-long electrostatic hexapole. NO radicals in the low-field-seeking $F_1(1/2f)$ state were focused into the collision region, whereas molecules in the high-field-seeking $F_1(1/2e)$ state were deflected from the beam axis. A 2-mm-diameter beamstop and diaphragm were installed in the center of the hexapole and 10 mm downstream from the hexapole, respectively, effectively filtering out the Xe atoms from the molecular beam pulse. The resulting state purity of the transmitted NO $F_1(1/2f)$ beam was better than 99.0%.

The reagent beams of OH and NO were detected state-selectively in the collision region by a

laser-induced fluorescence (LIF) detection scheme. From calibrated LIF measurements, the peak densities of the reagent packets were determined to be $(2 \pm 0.8) \times 10^8$ and $(9 \pm 3) \times 10^{10}$ molecules/cm³ for OH and NO, respectively. The collision-induced populations in the $F_1(3/2e)$, $F_1(5/2e)$, $F_1(7/2e)$, and $F_2(1/2e)$ levels of the OH radical were measured at the time when both beams maximally overlapped in the beam-crossing area. Depending on the inelastic channel, only a fraction of 10^{-4} to 10^{-6} of the OH radicals were inelastically scattered. Only final states of e symmetry were probed, as the Stark decelerator did not eliminate the initial population in the f states sufficiently. Detection of collision-induced population in the $F_1(3/2e)$ level was only possible by spectroscopically separating the magnetic dipole-allowed transitions that originated from the $F_1(3/2f)$ state (26). The insufficiently perfect state purity of the NO radical beam prevented the measurement of population transfer in NO.

The collision signals were measured as a function of the collision energy, from which the excitation functions of the state-to-state inelastic scattering cross sections (shown in Fig. 2) were determined (28). The extremely well-defined spatial distributions of the OH and NO packets allowed us to determine the scattering cross sections on an absolute scale. A cross section of 90 ± 38 Å² was determined for the $F_1(3/2e)$ channel at a collision energy of 220 cm⁻¹, from which the absolute cross sections for all scattering channels and all collision energies were derived (26). The experimental uncertainty was limited only by the

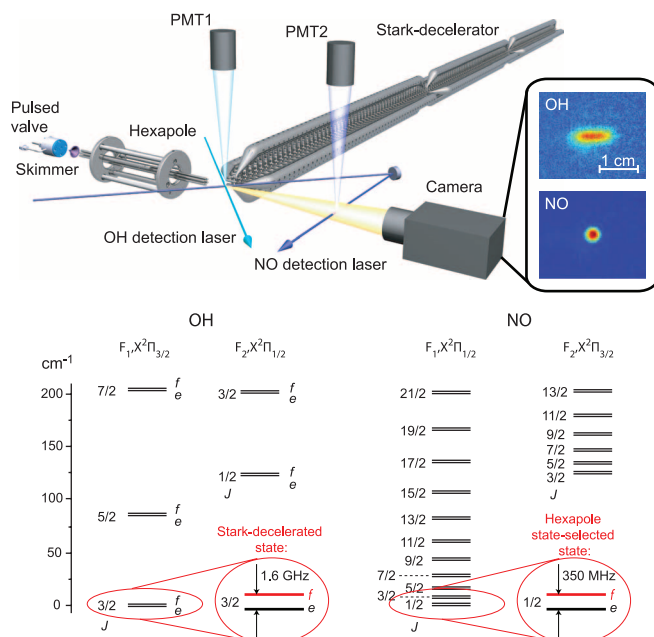
uncertainty in the measured value for the peak density of the NO packet.

We found that collisions that populate the $F_1(3/2e)$ level are most likely, and the cross section for this transition accounts for about 90% of the total inelastic scattering cross section. The cross sections to populate the $F_1(5/2e)$, the $F_1(7/2e)$, and the $F_2(1/2e)$ levels show a clear threshold behavior; the collision energies at which these channels become energetically possible are indicated by vertical arrows. These cross sections show large qualitative differences compared with the scattering of OH with atomic targets. The most striking difference is found in the relative contributions of the $F_1(3/2e)$ and $F_1(5/2e)$ channels to the total inelastic scattering cross section. The role of the $F_1(5/2e)$ channel, which dominates RET for OH-He and OH-Ne, gradually diminishes in favor of the $F_1(3/2e)$ channel in the series of targets He, Ne, Ar, Kr, and Xe (29). This behavior could be rationalized from the increasing well depth, anisotropy, and head-tail asymmetry of the two BO PESs (29, 30). The overwhelming dominance of the $F_1(3/2f) \rightarrow F_1(3/2e)$ quenching channel observed here for OH-NO reflects how a dipolar open-shell molecular scattering partner, rather than a spherical atomic partner, governs the collision dynamics.

To interpret our experimental results, we constructed a model for the scattering of two molecules in an open-shell ²Ti state. In contrast to scattering of OH or NO with rare gas atoms, ab initio calculations of multiple anisotropic PESs with their nonadiabatic couplings for OH-NO are beyond the capabilities of current theoretical methods. Coupling of the $S = 1/2$ electron spins gives rise to singlet ($S = 0$) and triplet ($S = 1$) potentials, which describe different short-range exchange interactions. There are four spatially distinct electronic states for each spin state, which are degenerate at long range and for linear geometries and which are coupled by nonadiabatic interactions. Nuclear derivative couplings with respect to all nuclear degrees of freedom exist between these states. Ab initio studies of the OH-NO complex (31) focused on the region where the chemical reaction $\text{OH} + \text{NO} \rightarrow \text{H} + \text{NO}_2$ takes place but considered only the lowest adiabatic potential for the singlet state. Even if we were able to compute all the relevant adiabatic PESs, there would be no simple recipe to take the nonadiabatic couplings between the PESs into account.

In our model, we exploit the hypothesis that the processes with the largest cross sections are governed by couplings that occur at relatively large OH-NO separations, beyond the HONO well region. As opposed to the short-range interactions, the long-range parts of the PESs can be calculated accurately by ab initio methods. We neglected the complicated short-range behavior of the PESs and replaced it with an isotropic repulsion term. However, we accurately calculated the long-range PESs that are governed by first-order electrostatic interactions between the dipole, quadrupole, and octupole moments of the

Fig. 1. Schematic representation of the experimental setup and the energy level schemes of the OH and NO radicals. A state-selected and velocity tunable beam of OH radicals produced using a 2.6-m-long Stark decelerator was crossed with a hexapole state-selected beam of NO radicals. Both radical species were detected state-selectively using LIF, with total fluorescence intensity measured using a photomultiplier tube (PMT), and the spatial distributions of both reagent molecular packets were imaged onto a charge-coupled device camera. Typical images of the OH and NO packets are shown in the upper and lower insets, respectively. The mean speed of the OH radical packet was precisely known from the settings of the Stark decelerator. The collision energy was calibrated from the NO beam speed measured by a second LIF detection zone located 30 cm downstream from the collision area. The $X^2\Pi$ electronic ground states of the OH and NO radicals are split into two rotational manifolds due to the spin-orbit interaction. The manifolds with lowest energy [$|Q| = 3/2$ for OH and $|Q| = 1/2$ for NO] are labeled F_1 . The energy splittings shown between the Λ -doublet components of each rotational level are greatly exaggerated for clarity.



collision partners (26). Moreover, we included isotropic dispersion and induction terms. The intermolecular Hamiltonian contained the usual radial and centrifugal kinetic energy operators and the full 4×4 matrix of diabatic interaction potentials (26, 32). Due to the noncylindrical symmetry of the $^2\Pi$ ground states of both the OH and NO radical, the off-diagonal elements of this matrix provided by the quadrupole and octupole moments of both radicals contain important couplings between the $^2\Pi_{3/2}$ and $^2\Pi_{1/2}$ states of both species.

The cross sections that were obtained from these model PESs by full coupled-channels cal-

culations are shown as solid lines in Fig. 2. Fair agreement between experiment and theory was obtained, in particular considering the simplistic approximations for the short-range PESs that were made. The absolute value for the cross section of the dominating $F_1(3/2e)$ channel, as well as the relative strengths of the inelastic channels, are reproduced well by the model calculations. The cross section for the spin-orbit-changing $F_2(1/2e)$ channel, as well as the cross section for the $F_1(3/2e)$ channel at low collision energies, are overestimated by the model.

We tested the sensitivity of the model calculations with respect to changes in the short-

range repulsion term (26). We observed that the cross section for the parity-changing $F_1(3/2e)$ channel is governed exclusively by the long-range electrostatic interaction; its value is converged to within a few percent. About half of this large quenching cross section originates from collisions with impact parameters exceeding $12 a_0$. The $F_1(5/2e)$ channel is also mainly determined by the long-range forces, although its cross section varies by 10 to 25% upon changes in the short-range model parameters (26). The weak $F_1(7/2e)$ and $F_2(1/2e)$ channels show larger variations, and more realistic short-range PESs are required to accurately predict their cross sections.

Our model also predicts the final states of the NO radical that are populated in coincidence with RET in the OH radical but that cannot be probed with the present experimental arrangement. The dominant $F_1(3/2e)$ quenching transition in OH is accompanied by the inelastic channels in NO as given in Table 1 for various collision energies. The general scattering behavior can be understood from the terms that lead to inversion parity changing or conserving collisions with respect to both collision partners. The OH-NO dipole-dipole interaction results in transitions that either change or conserve inversion parity in both OH and NO, whereas the dipole-quadrupole and quadrupole-dipole terms also allow for an inversion parity changing transition in OH or NO only. The largest cross sections that accompany the $F_1(3/2e)$ channel in OH are found for the dipole-dipole-dominated $F_1(3/2f)$ and $F_1(1/2e)$ channels of NO and for the dipole-quadrupole dominated $F_1(1/2f)$, $F_1(3/2e)$, and $F_1(5/2f)$ NO channels (33).

Our experiments show that the main mechanisms of RET in the reactive, chemically complex system studied here are captured using a model for the long-range interactions alone, provided that the full monomer Hamiltonians and all relevant long-range nonadiabatic couplings are taken into account. Even at relatively high collision energies, the inelastic scattering events with the largest cross sections predominantly occur at large intermolecular distances where the interaction potentials can be calculated accurately. The success attained here implies that reliable predictions for state-to-state scattering cross sections can now be made more generally for complex molecular systems involving radicals, helping to solve urgent scientific questions in, for instance, astrochemistry. Ultimately, new electronic structure methods that include the chemically reactive short-range potentials and nonadiabatic couplings are required to elucidate the exact mechanisms of radical-radical collisions.

References and Notes

1. R. D. Levine, R. B. Bernstein, *Molecular Reaction Dynamics and Chemical Reactivity* (Oxford University Press, New York, 1987).
2. D. W. Chandler, S. Stolte, in *Tutorials in Molecular Reaction Dynamics*, M. Brouard, C. Vallance, Eds. (Royal Society of Chemistry, Cambridge, 2010), chap. 5.
3. S. Weinreb, A. H. Barrett, M. L. Meeks, J. C. Henry, *Nature* **200**, 829 (1963).

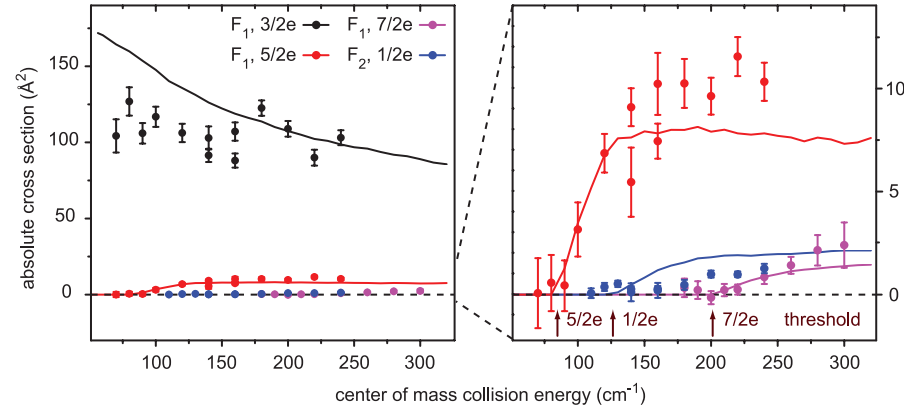


Fig. 2. Comparison of the collision-energy dependence of the measured (data points with error bars) and calculated (solid curves) state-to-state inelastic scattering cross sections of OH $F_1(3/2f)$ radicals in collision with NO $F_1(1/2f)$ radicals. The cross sections were first measured relatively with respect to each other, and the vertical error bars indicate combined estimates of both statistical and systematic errors (2 SD) (26). The vertical axis was then put on an absolute scale by a measurement of the absolute cross section for the $F_1(3/2e)$ channel at a collision energy of 220 cm^{-1} . The cross sections were computed on an energy grid of 10, 20, 30, 40, ..., 320 cm^{-1} . The cross section for the dominant $F_1(3/2e)$ channel converged to within a few percent; the cross sections for the weaker channels vary by 20 to 50% depending on changes in the short-range part of the theoretical model (26).

Table 1. Predicted state-to-state cross sections (\AA^2) for RET in NO [initial state $F_1(1/2f)$] that occurs in coincidence with the $F_1(3/2f) \rightarrow F_1(3/2e)$ transition in the OH radical at collision energies of 10, 20, 50, 100, 200, and 300 cm^{-1} . The inversion parity of the molecular levels is given. For comparison, the elastic cross section corresponding to the OH [$F_1(3/2f) \rightarrow F_1(3/2f)$] – NO [$F_1(1/2f) \rightarrow F_1(1/2f)$] channel is given in the last row of the table.

Final state (NO)	Inversion parity	10 cm^{-1}	20 cm^{-1}	50 cm^{-1}	100 cm^{-1}	200 cm^{-1}	300 cm^{-1}
$F_1(1/2e)$	+	152.3	106.6	54.5	33.5	20.0	15.3
$F_1(1/2f)$	–	45.1	37.0	25.8	13.9	6.3	4.2
$F_1(3/2e)$	–	19.1	17.6	21.4	17.5	12.1	10.0
$F_1(3/2f)$	+	18.0	19.5	46.9	54.3	38.8	29.7
$F_1(5/2e)$	+		6.5	8.5	9.0	6.3	5.0
$F_1(5/2f)$	–		6.6	7.1	8.7	11.8	13.4
$F_1(7/2e)$	–			5.3	5.4	4.4	3.8
$F_1(7/2f)$	+			4.7	5.2	5.6	5.6
$F_2(3/2e)$	–					0.5	0.4
$F_2(3/2f)$	+					0.5	0.4
$F_2(5/2e)$	+					0.4	0.3
$F_2(5/2f)$	–					0.4	0.4
$F_2(7/2e)$	–					0.3	0.3
$F_2(7/2f)$	+					0.3	0.3
Elastic		409.6	346.3	265.1	209.1	175.8	166.4

4. A. Schiffman, D. W. Chandler, *Int. Rev. Phys. Chem.* **14**, 371 (1995).
5. S. Stolte, *Nature* **353**, 391 (1991).
6. D. Watanabe, H. Ohoyama, T. Matsumura, T. Kasai, *Phys. Rev. Lett.* **99**, 043201 (2007).
7. K. T. Lorenz *et al.*, *Science* **293**, 2063 (2001).
8. C. J. Eyles *et al.*, *Nat. Chem.* **3**, 597 (2011).
9. H. Kohguchi, T. Suzuki, M. H. Alexander, *Science* **294**, 832 (2001).
10. S. Y. T. van de Meerakker, H. L. Bethlem, G. Meijer, *Nat. Phys.* **4**, 595 (2008).
11. S. Y. T. van de Meerakker, H. L. Bethlem, N. Vanhaecke, G. Meijer, *Chem. Rev.* **112**, 4828 (2012).
12. J. J. Gilijsse, S. Hoekstra, S. Y. T. van de Meerakker, G. C. Groenenboom, G. Meijer, *Science* **313**, 1617 (2006).
13. L. Scharfenberg *et al.*, *Phys. Chem. Chem. Phys.* **12**, 10660 (2010).
14. P. Hartogh *et al.*, *Nature* **478**, 218 (2011).
15. G. Paterson, M. L. Costen, K. G. McKendrick, *Int. Rev. Phys. Chem.* **31**, 69 (2012).
16. D. C. Clary, *Annu. Rev. Phys. Chem.* **41**, 61 (1990).
17. I. W. M. Smith, *Annu. Rev. Astron. Astrophys.* **49**, 29 (2011).
18. R. B. Bernstein, *Science* **144**, 141 (1964).
19. B. C. Sawyer *et al.*, *Phys. Chem. Chem. Phys.* **13**, 19059 (2011).
20. C. Berteloite *et al.*, *Phys. Rev. Lett.* **105**, 203201 (2010).
21. K. Schreel, J. J. ter Meulen, *J. Chem. Phys.* **105**, 4522 (1996).
22. The labels $\chi^2\Pi_{3/2}$, $\chi^2\Pi_{1/2}$, v , and j indicate the electronic states, the vibrational state, and the rotational state of both the OH and the NO radical, respectively. The spectroscopic symmetry labels e and f refer to the total parity of the electronic wave function, exclusive of rotation. The total inversion parity is indicated by the additional labels $+$ and $-$.
23. H. Kohguchi, T. Suzuki, *Annu. Rep. Prog. Chem. Sect. C* **98**, 421 (2002).
24. M. T. Vink, J. A. Bacon, C. F. Giese, W. R. Gentry, *J. Chem. Phys.* **106**, 1353 (1997).
25. P. Sharkey, I. R. Sims, I. W. M. Smith, P. Bocherel, B. R. Rowe, *J. Chem. Soc. Faraday Trans.* **90**, 3609 (1994).
26. Materials and methods are available as supplementary materials on Science Online.
27. L. Scharfenberg, H. Haak, G. Meijer, S. Y. T. van de Meerakker, *Phys. Rev. A* **79**, 023410 (2009).
28. It was verified that all scattered molecules are detected with equal probability, and no density-to-flux correction was needed to relate the measured scattering signals to relative inelastic cross sections. See supplementary materials for more information.
29. L. Scharfenberg *et al.*, *Eur. Phys. J. D* **65**, 189 (2011).
30. P. J. Dagdigian, M. H. Alexander, *J. Chem. Phys.* **130**, 094303 (2009).
31. M. T. Nguyen, R. Sumathi, D. Sengupta, J. Peeters, *Chem. Phys.* **230**, 1 (1998).
32. The OH-NO spin states with $S = 0$ and $S = 1$ are not distinguished in our model; the 4×4 matrices for each spin state are therefore identical.
33. Although the quadrupole moment vanishes in the $j = 1/2$ state of NO, the quadrupole moment in the molecular frame contributes to the collisions producing NO states with $j = 3/2$ and $5/2$ that yield important contributions to the measured cross sections.

Acknowledgments: S.Y.T.v.d.M. acknowledges support from the Netherlands Organisation for Scientific Research (NWO) via a VIDI grant. G.M. and K.B.G. acknowledge support from the ERC-2009-AdG under grant agreement 247142-MolChip. K.L. and A.v.d.A. acknowledge the Alexander von Humboldt Foundation (AvHF) for a Humboldt Research Award. X.W. acknowledges the AvHF for a research fellowship. We thank J. Blokland for her help setting up the narrowband laser system. We thank the referees for valuable and stimulating comments. The authors declare no competing financial interests.

Supplementary Materials
www.sciencemag.org/cgi/content/full/338/6110/1060/DC1
 Supplementary Text
 Figs. S1 to S3
 Tables S1 and S2
 References (34–49)

19 June 2012; accepted 10 October 2012
 10.1126/science.1229549

Body-Wave Imaging of Earth's Mantle Discontinuities from Ambient Seismic Noise

P. Poli,* M. Campillo, H. Pedersen, LAPNET Working Group

Ambient seismic noise correlations are widely used for high-resolution surface-wave imaging of Earth's lithosphere. Similar observations of the seismic body waves that propagate through the interior of Earth would provide a window into the deep Earth. We report the observation of the mantle transition zone through noise correlations of P waves as they are reflected by the discontinuities associated with the top [410 kilometers (km)] and the bottom (660 km) of this zone. Our data demonstrate that high-resolution mapping of the mantle transition zone is possible without using earthquake sources.

Earth's upper and lower mantle are separated by the transition zone, where the mantle mineralogy changes. At the top (~410 km depth) and bottom (~660 km depth) of the transition zone, phase changes introduce a rapid increase in seismic velocities over narrow depth intervals. This transition zone has a major role in Earth dynamics, particularly as it influences the convection within the mantle, slowing the subduction of slabs and the ascent of plumes (1, 2). Information from rock physics and the seismic character of the 410-km and 660-km discontinuities can constrain the mineralogy and temperatures of the mantle (3). However, mapping the depths and lateral variations of these discontinuities (4, 5) remains difficult. Seismic studies based

on the analysis of waves emitted by earthquakes are limited by the geographical distribution of the earthquakes and by the uncertainties in our knowledge of the location and the rupture processes.

Promising results from correlations of the coda of seismic waves (6) have led to the recent proposal that correlations of the continuous records of seismic ambient noise recorded at two distant points can provide an estimation of Earth's impulse response between these two points (7). This impulse response contains information on seismic wave speeds (7) and amplitude decays (8) without the need for the use of active sources or earthquakes. Because these seismic noise sources are located at Earth's surface, the noise correlations are dominated by surface waves, and the technique has become useful for seismic imaging at different scales (9–13). Seismic noise propagates continuously through Earth and is mainly created by oceanic swells and atmospheric disturbances (14–19).

Surface waves, however, are not sufficient to explore the deep structure of Earth, as they have limited depth resolution. Recent studies have detected high-frequency body waves within noise correlations at both the crustal scale (20–22) and at a very local scale (23). Here, we describe the use of seismic noise correlations to extract body-wave reflections from the 410-km and 660-km discontinuities of Earth's transition zone.

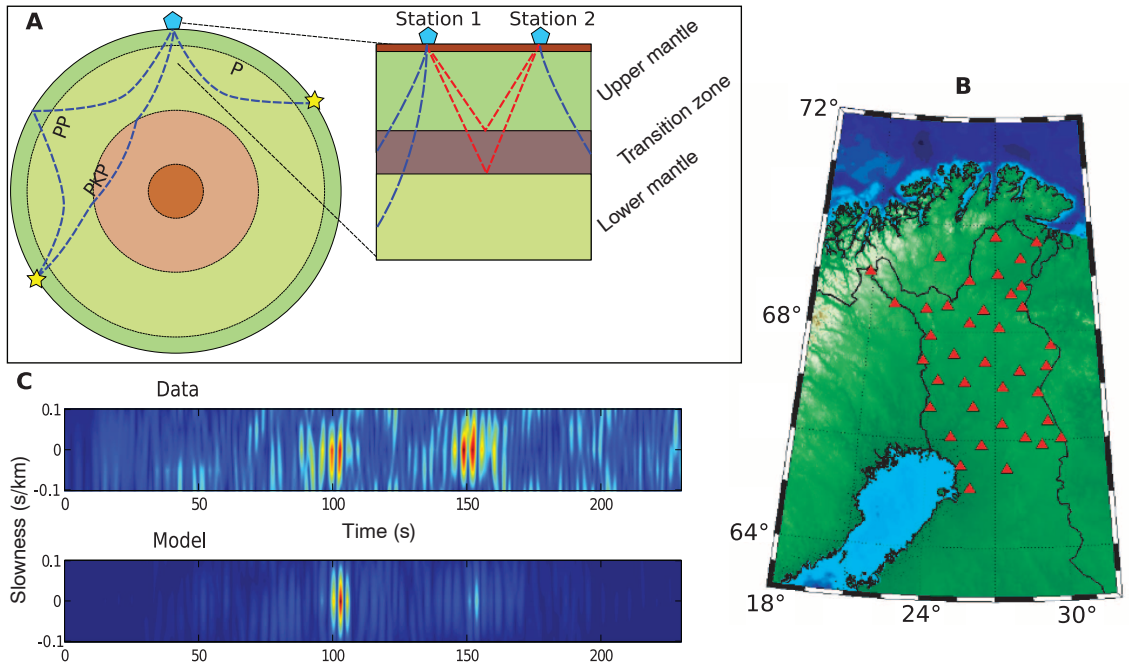
It is now known that seismic noise includes body waves that propagate through the whole planet (19, 24, 25), just as surface waves propagate through the upper layers of Earth (Fig. 1A). As for the surface-wave component of the wave field, we do not expect the noise field to be under the exact mathematical conditions for retrieval of the complete Earth impulse responses (26, 27). We show in the following that conditions are nonetheless favorable enough to extract deep body-wave phases by correlating ambient seismic noise. Because the signals we track have small amplitudes, we have applied specific processing techniques that are designed to improve the signal-to-noise ratio.

We used data from the temporary POLENET/LAPNET experiments in northern Finland (28) (Fig. 1B), complemented with data from permanent broadband stations. We previously extracted P waves and S waves (22) that are reflected on the Moho (the lower limit of Earth's crust). These data showed that the ancient crust in the study area (29, 30) is relatively transparent to seismic waves. Here, we used data from 42 stations that were continually operating from January to December 2008. For each of the 861 station pairs (fig. S1), we calculated the noise correlation of the vertical records in the frequency range 0.1 to 0.5 Hz, using the same processing as that implemented to extract Moho-reflected waves (22). We subsequently used the station pairs for which

Institut des Sciences de la Terre (ISTerre), Université de Grenoble I, CNRS, BP 53, F-38041 Grenoble Cedex 9, France.

*To whom correspondence should be addressed. E-mail: polip@ujf-grenoble.fr

Fig. 1. Reflected body waves from the mantle transition zone discontinuities beneath Finland. **(A)** Earth model in which noise is generated from oceanic sources (stars) and propagates partly as body waves (dashed blue lines) to the seismic sensors (pentagons). Correlation of the seismic noise recorded at the two sensors in theory yields the complete set of waves that would be recorded at one sensor if a seismic source had been active at the other sensor. The right panel shows the two body-wave reflections that are the focus of this report: *P* waves reflected on the 410-km and 660-km discontinuities (red dashed lines). **(B)** Map showing the stations of the seismic array (red triangles) in northern Finland. **(C)** Slowness-time stacks of the noise correlations (top) and the synthetic seismograms calculated using the AK135 standard Earth model (bottom). Note the wave arrivals at the same times as predicted by the AK135 model.



potential body waves reflected at the 410-km and 660-km interfaces did not arrive within the surface-wave train. For each of these traces, we folded the positive and negative time lags of the correlations and zeroed out the time window corresponding to the surface-wave arrivals.

To observe small-amplitude waves (fig. S2), we used stacking techniques that allow us to enhance the coherent body waves. Prior to the stacking, we aligned the traces along the predicted arrival times of the 410-km *P*-wave reflection using the AK135 standard Earth model (31) that was adapted to take into account the local crustal structure. Once aligned, the whole data set was stacked in the slowness-time domain.

The results of the slowness-time stack (Fig. 1C) show two peaks of energy at arrival times of approximately 100 and 150 s. Both peaks are located at zero slowness, which means that no further velocity correction is needed in addition to the initial alignment using the AK135 model, and that these are vertically propagating waves. We tentatively interpreted these two peaks as *P* waves reflected by the 410-km discontinuity (*P410P*) and the 660-km discontinuity (*P660P*).

To support this interpretation, we compared the two types of data by calculating the synthetic seismograms for each station pair and applying the same processing as that used for the field data. Prior to the stacking, we normalized the spectral amplitude of the synthetic seismograms and multiplied it by the average spectrum of the noise correlations. The comparison of the synthetics and the data stack confirms our interpretation that the observed peaks are the *P410P* and *P660P* reflections, despite slightly different waveforms

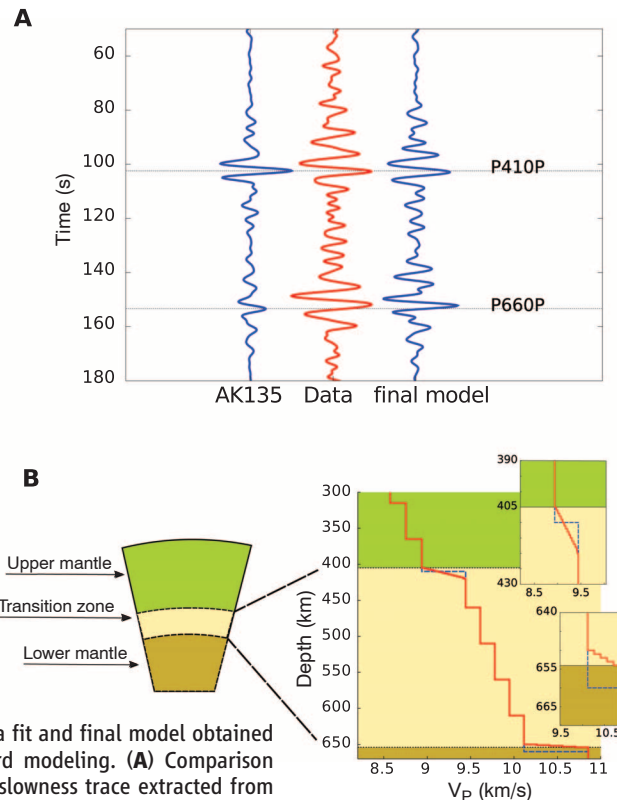


Fig. 2. Data fit and final model obtained from forward modeling. **(A)** Comparison of the zero-slowness trace extracted from the slowness-timestack of the noise correlations (red) and two zero-slowness traces of the synthetic seismogram stacks (as processed for the noise correlations): the AK135 standard Earth model (blue, left) and our final model (blue, right). The predicted vertical travel times for the *P410P* and *P660P* reflections in the AK135 model are shown (horizontal lines). The stack traces are normalized using the peak amplitude. **(B)** Final model (red line) for the mantle transition zone beneath northern Finland as compared to the AK135 model (dashed blue line). Insets show the detailed structure of the two discontinuities.

(Fig. 1C). The agreement of data and synthetic stacks is a good indication of the quality of the retrieved Green's function.

We attribute the minor differences between field data and synthetics to structural differences between the global reference model (31) and Earth's mantle beneath the study area. To test this hypothesis, we calculated the synthetic seismogram stacks for a series of models (table S1), and we qualitatively evaluated the fit between the stack of synthetic seismograms and the correlations (fig. S3). With the AK135 model as reference, we modified the depths of the two discontinuities and used gradients over narrow depth intervals, rather than first-order discontinuities. The stack of synthetics associated with the best model (Fig. 2A) is in good agreement with the data: The overall fit of the observations was drastically improved relative to that obtained using the AK135 model. With this refined model, the arrival times and the relative *P*410*P* and *P*660*P* amplitudes are similar.

The final model (Fig. 2B) of our study shows a “410-km discontinuity” that is 15 km thick and ranges from 405 to 420 km in depth. The “660-km discontinuity” is 4 km thick, at depths of 650 to 654 km. The depths of these two discontinuities are within the variations observed at a global scale (4, 5) and are in good agreement with a receiver function study in the same area (32). Our additional constraints on the fine structure of the discontinuities corresponded to those predicted by the thermodynamic modeling of the phase transitions (33, 34) and to constraints provided by seismological studies (35, 36).

We have shown that it is possible to identify and characterize deep body waves that propagate through Earth. Our study used a dense seismic network that is located above a relatively transparent Earth crust. Using seismic noise to image mantle discontinuities has several advantages. First, the correlation technique is independent of earthquake occurrence, and therefore independent of the uncertainties that are associated with source location, origin time, and detailed slip history. Second, the amount of noise correlation scales according to N^2 , where N is the number of stations, so it is relatively easy to obtain a large amount of data. Finally, the body waves that we have extracted are relatively high frequency (0.1 to 0.5 Hz) and they are sufficiently broadband to finely resolve the structure of the discontinuities.

References and Notes

- D. Zhao, *Phys. Earth Planet. Inter.* **146**, 3 (2004).
- C. Li, R. D. van der Hilst, E. R. Engdahl, S. Burdick, *Geochem. Geophys. Geosyst.* **9**, Q05018 (2008).
- Q. Cao, R. D. van der Hilst, M. V. de Hoop, S. H. Shim, *Science* **332**, 1068 (2011).
- Y. Gu, A. M. Dziewonski, C. B. Agee, *Earth Planet. Sci. Lett.* **157**, 57 (1998).
- P. Shearer, G. Masters, *Nature* **355**, 791 (1992).
- M. Campillo, A. Paul, *Science* **299**, 547 (2003).
- N. M. Shapiro, M. Campillo, *Geophys. Res. Lett.* **31**, L07614 (2004).
- G. A. Prieto, M. Denolle, J. F. Lawrence, G. C. Beroza, *C. R. Geosci.* **3**, 558 (2011).
- N. M. Shapiro, M. Campillo, L. Stehly, M. H. Ritzwoller, *Science* **307**, 1615 (2005).
- K. G. Sabra, P. Gerstoft, P. Roux, W. A. Kuperman, M. C. Fehler, *Geophys. Res. Lett.* **32**, L14311 (2005).
- H. Yao, R. D. van der Hilst, *Geophys. J. Int.* **179**, 1113 (2009).
- L. Stehly *et al.*, *Geophys. J. Int.* **178**, 338 (2009).
- F. C. Lin, M. H. Ritzwoller, R. Snieder, *Geophys. J. Int.* **177**, 1091 (2009).
- M. S. Longuet-Higgins, *Philos. Trans. R. Soc. London. Ser. A* **243**, 1 (1950).
- A. Friedrich, F. Krüger, K. Klinge, *J. Seismol.* **2**, 47 (1998).
- N. Kobayashi, K. Nishida, *Nature* **395**, 357 (1998).
- G. Ekström, *J. Geophys. Res.* **106**, 26483 (2001).
- J. Rhie, B. Romanowicz, *Nature* **431**, 552 (2004).
- G. Hillers *et al.*, *Geochem. Geophys. Geosyst.* **13**, Q01021 (2012).
- Z. Zhan, S. Ni, D. V. Helmberger, R. W. Clayton, *Geophys. J. Int.* **182**, 408 (2010).
- E. Ruigrok, X. Campman, K. Wapenaar, *C. R. Geosci.* **343**, 512 (2011).
- P. Poli, H. A. Pedersen, M. Campillo, POLNET/ LAPNET Working Group, *Geophys. J. Int.* **188**, 549 (2012).
- P. Roux, *Geophys. Res. Lett.* **32**, L19303 (2005).
- P. Gerstoft, P. M. Shearer, N. Harmon, J. Zhang, *Geophys. Res. Lett.* **35**, L23306 (2008).
- M. Landès, F. Hubans, N. M. Shapiro, A. Paul, M. Campillo, *J. Geophys. Res.* **115**, B05302 (2010).
- P. Gouédard *et al.*, *Geophys. Prospect.* **56**, 375 (2008).
- K. Wapenaar, E. Slob, R. Snieder, A. Curtis, *Geophysics* **75**, 75A211 (2010).
- E. Kozlovskaya, M. Poutanen, POLNET/ LAPNET Working Group, *Eos* **87** (fall meet. suppl.), abstr. S41A-1311 (2006).
- T. Janik, E. Kozlovskaya, J. Yliniemi, *J. Geophys. Res.* **112**, B04302 (2007).
- P. Poli, M. Campillo, H. A. Pedersen, “Seismic noise tomography in regions with small velocity contrasts and strong noise directivity: Application to the northern Baltic Shield”; available at <http://hal.archives-ouvertes.fr/hal-00721895>.
- B. L. N. Kennett, E. R. Engdahl, R. Buland, *Geophys. J. Int.* **122**, 108 (1995).
- A. Alinaghi, G. Bock, R. Kind, W. Hanka, K. Wylegalla, TOR, SVEKALAPKO, Working Groups, *Geophys. J. Int.* **155**, 641 (2003).
- E. Ohtani, T. Sakai, *Phys. Earth Planet. Inter.* **170**, 240 (2008).
- L. Stixrude, C. Lithgow-Bertelloni, *Geophys. J. Int.* **184**, 1180 (2011).
- T. Melbourne, D. Helmberger, *J. Geophys. Res.* **103**, 10091 (1998).
- J. Lawrence, P. Shearer, *Geochem. Geophys. Geosyst.* **7**, Q10012 (2006).

Acknowledgments: Supported by the QUEST Initial Training network funded within the European Union Marie Curie Programme, the Agence Nationale de la Recherche BegDy project, the Institut Paul Emil Victor, and European Research Council advanced grant “Whisper” 227507. Continuous data from the POLNET-LAPNET seismic experiment are available at the Réseau Sismologique et Géodésique Français (RESIF) Data Centre (www.resif.fr/portal) under network code XK. The POLNET/LAPNET project is a part of the International Polar Year 2007–2009 and a part of the POLNET consortium, and is supported by the Academy of Finland (grant 122762) and University of Oulu, International Lithosphere Programme task force VIII, grant IAA300120709 of the Grant Agency of the Czech Academy of Sciences, and the Russian Academy of Sciences (Programmes 5 and 9). The equipment for the temporary deployment was provided by RESIF–SisMob (France), EOST-IPG Strasbourg (France), Seismic Pool (MOBNET) of the Geophysical Institute of the Czech Academy of Sciences (Czech Republic), Sodankylä Geophysical Observatory (Finland), Institute of Geosphere Dynamics of RAS (Russia), Institute of Geophysics, ETH Zürich (Switzerland), Institute of Geodesy and Geophysics, Vienna University of Technology (Austria), and University of Leeds (UK). POLNET/ LAPNET data were prepared and distributed by the RESIF Data Centre. The POLNET/ LAPNET working group consists of E. Kozlovskaya, T. Jämsen, H. Silvennoinen, R. Hurskainen, H. Pedersen, C. Pequegnat, U. Achauer, J. Plomerova, E. Kissling, I. Sanina, R. Bodvarsson, I. Aleshin, E. Bourova, E. Brückl, T. Eken, R. Guiguet, H. Hausmann, P. Heikkinen, G. Houseman, P. Jedlicka, H. Johnsen, H. Kremenetskaya, K. Komminaho, H. Munzarova, R. Roberts, B. Ruzek, H. Shomali, J. Schweitzer, A. Shaumyan, L. Vecsey, and S. Volosov.

Supplementary Materials

www.sciencemag.org/cgi/content/full/338/6110/1063/DC1
Materials and Methods
Figs. S1 to S3
Table S1
Reference (37)

31 July 2012; accepted 12 October 2012
10.1126/science.1228194

Flows of Research Manuscripts Among Scientific Journals Reveal Hidden Submission Patterns

V. Calcagno,^{1,2,3*}† E. Demoinet,² K. Gollner,³ L. Guidi,⁴ D. Ruths,⁵ C. de Mazancourt³

The study of science-making is a growing discipline that builds largely on online publication and citation databases, while prepublication processes remain hidden. Here, we report on results from a large-scale survey of the submission process, covering 923 scientific journals from the biological sciences in years 2006 to 2008. Manuscript flows among journals revealed a modular submission network, with high-impact journals preferentially attracting submissions. However, about 75% of published articles were submitted first to the journal that would publish them, and high-impact journals published proportionally more articles that had been resubmitted from another journal. Submission history affected post-publication impact: Resubmissions from other journals received significantly more citations than first-intent submissions, and resubmissions between different journal communities received significantly fewer citations.

With the rise of Web technologies and online databases, knowledge is increasingly available regarding the process

of science-making itself (1). Gathering such “meta-knowledge” presents the opportunity to better understand, and optimize, the practice of research

(1, 2). Citation patterns have revealed research fronts (3), maps of science (4), and citation behavior (5, 6); coauthorship patterns have revealed

¹French National Institute for Agricultural Research, Institut Sophia Agrobiotech, Sophia-Antipolis, France. ²Department of Biology, McGill University, Montreal, Canada. ³Redpath Museum, McGill University, Montreal, Canada. ⁴Center for Microbial Oceanography, University of Hawaii, Honolulu HI, USA. ⁵Department of Computer Science, McGill University, Montreal, Canada.

*To whom correspondence should be addressed. E-mail: vincent.calcagno@sophia.inra.fr

†Present address: INRA, Sophia-Antipolis Research Center, Institut Sophia Agrobiotech, 400 Route des Chappes, BP 167, 06903 Sophia Antipolis Cedex, France.

collaboration networks (7); and even acknowledgments can help infer contributions to science-making (8). Yet all this research rests on the emerged part of science communication: publications. These represent only the outcome of a complex process that involves manuscript preparation, submission, peer review, and revision (9). Focusing on the final stage may give a very specific image of science (10, 11). Unfortunately, prepublication processes, which constitute a considerable amount of the time allocated to research, have remained a black box for which we lack systematic data (12–15).

To study prepublication history, we asked the corresponding author of virtually all research ar-

ticles published between 2006 and 2008 in 16 subject categories of biological sciences (923 journals) (table S1) whether the article was first submitted to the publishing journal and, if not, the name of the journal previously attempted (16). All evidence suggests that response bias was negligible (16). We thus retrieved the late submission history of 80,748 articles (37% of all enquiries), from which we could reconstruct the network of manuscript flows among scientific journals (Fig. 1 and fig. S2). In the network, an arrow from journal A to journal B represents a “resubmission link,” that is, an article that was submitted to and published by journal B after submission to journal

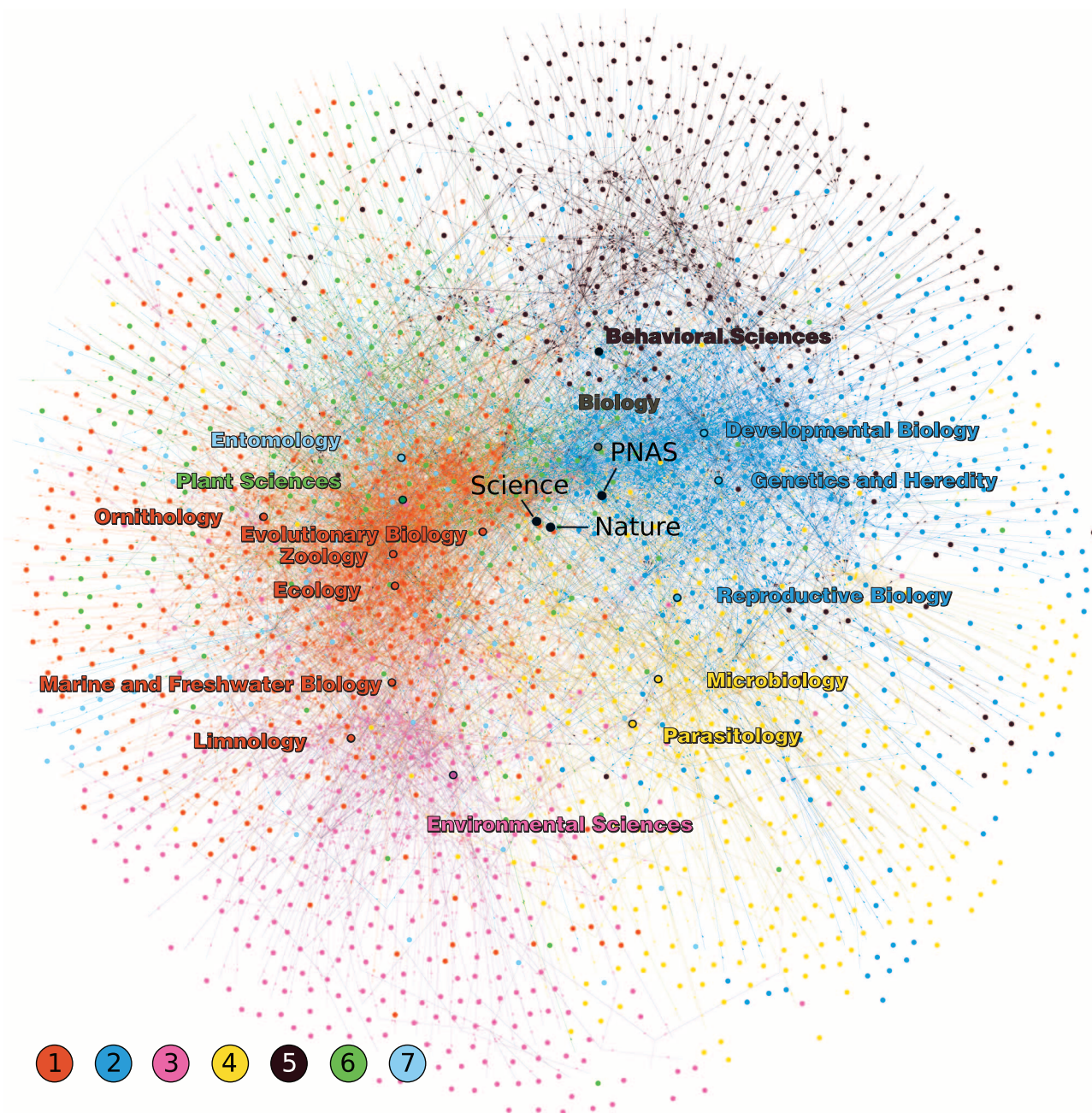


Fig. 1. The network of scientific journals as derived from manuscript submission flows. Nodes are journals, and the connections between them represent manuscript resubmissions (arrows not visible at this magnification level;

see fig. S2 for higher resolution). For clarity, only the seven largest communities detected ($N = 1841$ journals) are shown, each a different color. ISI subject categories are mapped on the graph as the centroid of their journals.

A. This network can be used to learn more about publication strategies and perceived journal importance than is available in citation networks alone (17, 18).

The submission network we obtained was densely connected (Fig. 1). Most journals are thus exchanging some manuscripts with at least one other journal (16 on average; first/third quartiles: 5/21). Resubmission flows were modular in that they occurred preferentially within subgroups of journals. Partitioning of the network with a modularity-maximizing algorithm (19) revealed seven principal communities (journal clusters). These were strongly consistent with subject categories as defined by the Institute for Scientific Information (ISI) (Fig. 1 and fig. S3), confirming the expectation that manuscript resubmissions should occur mainly within disciplines. The communities were less resolved than subject categories, though, and the resulting modularity value (0.5) was not extreme, indicating cross-community flow.

Journals more central in the resubmission network were also those with higher impact factor based on the ISI metric (Spearman correlation $\rho = 0.55$; $P < 0.001$) (fig. S4), especially the top three multidisciplinary journals included in our study (Fig. 1). Journal importance (20), here inferred from submission patterns, is thus associated with importance as inferred from citation patterns (17, 18). This could merely result from the fact that high-impact journals published more articles overall and so had more articles surveyed (fig. S4), which could increase centrality in itself.

We thus studied determinants of network centrality that are not affected by the number of articles published. The first quantity is the number

of times a journal was reported as an earlier choice for submission (the out-degree of a journal in the network). It increased sharply with impact factor (Fig. 2A) (Spearman rank correlation $\rho = 0.55$; $P < 0.001$), showing that high-impact-factor journals were more often earlier choices for submission. Furthermore, resubmission flows were highly nonreciprocal between pairs of journals (network reciprocity: 0.04) (16). This was explained to a large extent by journal impact factor: Resubmission flows were oriented downstream overall, as far as impact factor is concerned (Fig. 2B). If a journal's manuscript rejection rate increased with impact factor, a similar pattern could be created even in the absence of active preference by authors. Therefore, we built random graphs expected if resubmission behavior were independent of impact factor (16). The change in impact factor would have a very different distribution under this null scenario (Fig. 2B, dashed line), even considering the observed higher propensity of high-impact journals to be the source of resubmissions (Fig. 2A). The skew in the distribution cannot be accounted for without invoking an active tendency of authors to move from high impact factor to low impact factors (Fig. 2B, solid line). Despite that, extremely negative differences (left tail of the distribution) were less frequent than expected, which indicates that authors adopt a risk-limiting strategy and preferentially make small leaps in impact factor in the course of resubmissions.

The second quantity that could contribute to journal centrality is the percentage of published articles that are first-intents (i.e., that were initially targeted at the publishing journal). Overall, 75% of all published articles were first-intents,

with a range of 67 to 87% across subject categories (table S1). None of the journals we sampled was found to be purely recycling manuscripts rejected from other journals. Thus, most articles were initially targeted to the journal that would eventually publish them (this conclusion is robust to any reasonable nonresponse bias) (16). This indicates that authors were overall efficient at targeting their research and limiting the risk of rejection.

Our results so far (Fig. 2) suggest that high-impact journals would attract many initial submissions and could select among them. In contrast, journals with low impact factors would more often receive and publish manuscripts previously rejected by higher-impact journals. This would create a positive association between impact factor and the proportion of published articles that are first-intents. Unexpectedly, we found an opposite pattern (Fig. 3): The proportion of first-intents decreased across the range of impact factors (Spearman rank correlation $\rho = -0.21$; $P < 0.001$) for all except the three topmost journals in our sample (Fig. 3). Although there is a lot of scatter, qualitatively similar trends were observed within most subject categories taken individually (table S4). One explanation is that high-impact journals, albeit preferred by authors, also experience stronger competition for manuscripts: They have a denser competitive neighborhood (as revealed by their more central position in the submission network) (Fig. 1 and fig. S4) and, together with high rejection rates, this makes them more likely to receive (and publish) resubmissions. As an example, even *Nature* and *Science*, which are certainly preferred journals in many cases, are far from publishing 100% of first-intents (Fig. 3),

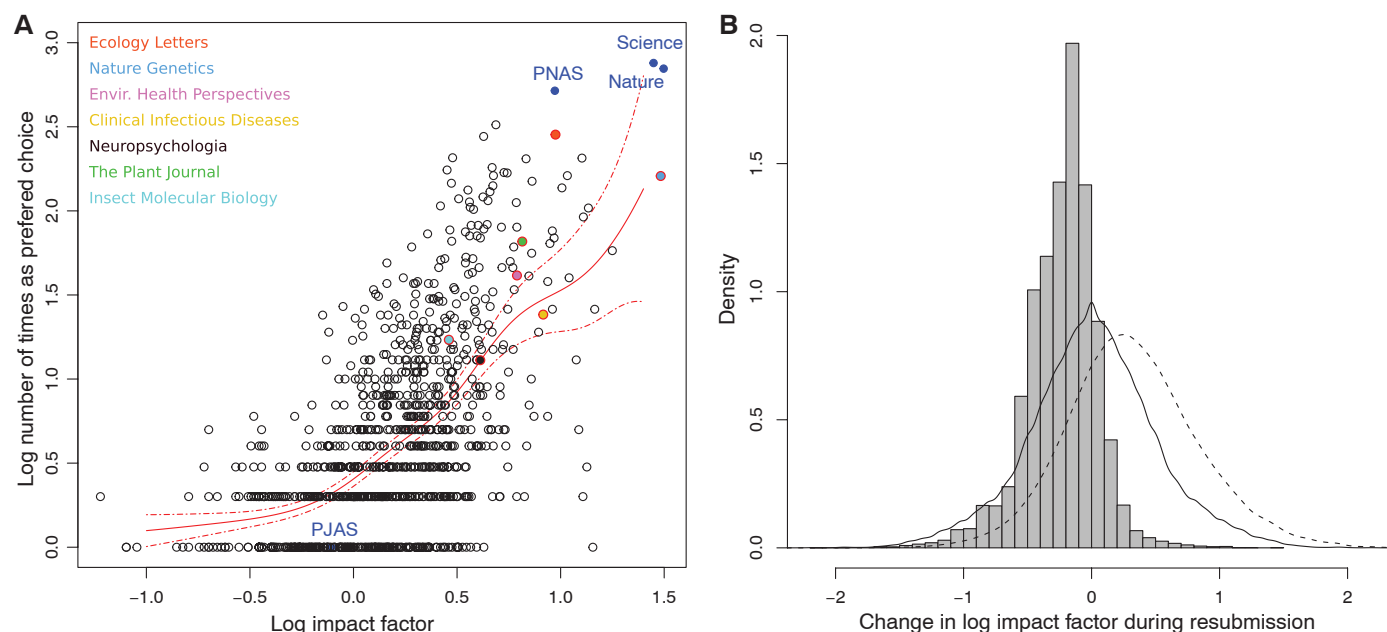


Fig. 2. Journal impact structures resubmission patterns. (A) The number of times a journal was first chosen for submission increases with impact factor. The average trend is shown as a red curve (± 2 SEM) (16). Multidisciplinary journals are highlighted in blue. One top journal per community is also highlighted (same color code as in Fig. 1). (B) The difference in impact factor

between the publishing journal and the one previously attempted is strongly skewed to negative values ($N = 18,078$). Mean difference in log impact factor: -0.23 , representing a 42% reduction on the natural scale. This differs from random graphs where the previously attempted journal was selected uniformly (dashed line) or in proportion to the values in (A) (solid line).

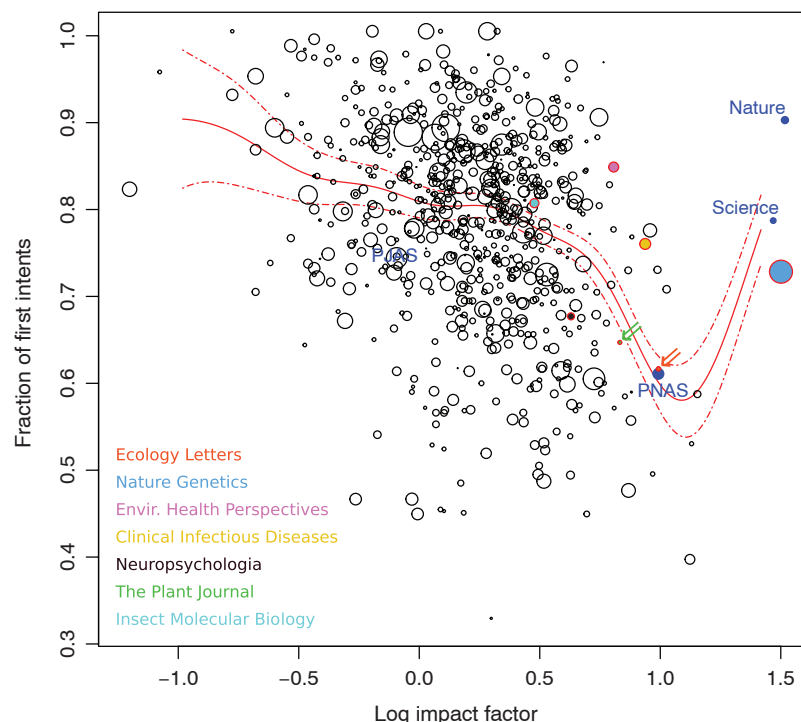


Fig. 3. High-impact journals publish proportionally fewer first-intent articles. Each circle is a journal (with area proportional to number of articles). The average trend is shown as a red curve (± 2 SEM) (16). For clarity, only journals with more than 20 articles are shown. Multidisciplinary journals are highlighted in blue. One top journal per community is also highlighted (same color code as in Fig. 1).

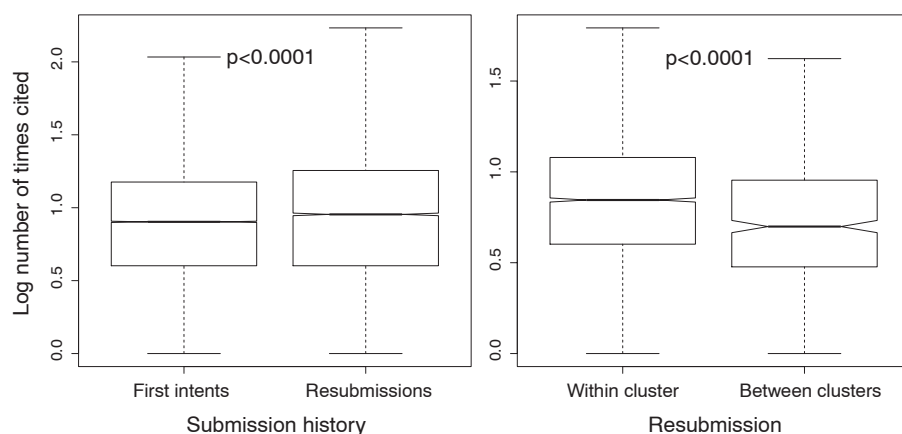


Fig. 4. Submission history affects citation counts. **(Left)** First-intent articles were less cited than resubmissions. **(Right)** Resubmissions were less cited if resubmitted between rather than within journal communities. Log-transformed citation counts are shown as box-whiskers plots (median/quartiles/range). *P* values are from permutation tests controlling for year and journal (16).

because each often publishes manuscripts rejected by the other. On the contrary, low-impact journals are more specialized, with a sparser competitive neighborhood and lower rejection rates in it. They receive proportionally fewer resubmissions from their neighbors.

Impact factor was here shown to affect the submission process, but does the submission process in turn affect citation counts and, thus, impact factor? Does submission history reflect the intrinsic “quality” or, in a more quantifiable way, the impact or utility of articles after publication?

We compared the number of times articles were cited (as of July 2011, i.e., 3 to 6 years after publication, from ISI Web of Science) depending on their being first-intents or resubmissions. We used methods robust to the skewed distribution of citation counts to ensure that a few highly cited articles were not driving the results (16). We controlled for year of publication, publishing journal (and thus impact factor), and their interaction (16). Resubmissions were significantly more cited than first-intents published the same year in the same journal (Fig. 4A).

This is challenging to explain because the submission history of articles is not public. With most resubmissions occurring from journals with higher impact (Fig. 2A), it could be that authors are able to assess the intrinsic quality of their research and its potential impact, so that manuscripts first submitted to high-impact journals, even when rejected, retained a higher propensity to be cited. However, this is unlikely because we found that resubmissions were more cited irrespective of their going up or down in impact factor (fig. S5). Several mechanisms could be involved, but perhaps the most likely explanation is that inputs from editors, reviewers, and the greater amount of time spent working on resubmissions significantly improve the citation impact of the final product. There are indications of the value of peer review from publication and editorial practice (15, 21). Our results suggest that it extends to citation impact. This validates the strategy of publishing groups that facilitate resubmission of declined manuscripts to other journals of the group (e.g., the Wiley Manuscript Transfer Program). Perhaps more important, these results should help authors endure the frustration associated with long resubmission processes and encourage them to take the challenge (14, 15).

An independent effect of manuscript submission history was that resubmissions occurring between two journals from the same journal community were significantly more cited than those between two different communities (Fig. 4B). This shows that, all else being equal, changing discipline during resubmission was a risky move, yielding lower-than-average impact after publication. Hence, the boundaries self-defined by author submission behavior (the journal clusters in Fig. 1) are reasonable in that transgressing them comes at a cost in terms of impact.

The network we have built from submission links (16) revealed that despite the prevalent fear of manuscript rejection (14, 22, 23), most published articles were initially targeted at the journal that would publish them and resubmission eventually paid off in terms of citation impact. Further aspects of the submission process could be investigated with this network, and it will be insightful to formally compare it to other social networks (4, 24). Adapting existing analytical methods for submission flow data could form the basis of journal impact metrics closer to author perceptions (25, 26). Surveying a broader range of disciplines to compare their standards (9) would be feasible but quite time-consuming. Just as for citation analysis, a great step forward could come from concerted efforts at recording the meta-knowledge contained in manuscript flows.

References and Notes

1. J. A. Evans, J. G. Foster, *Science* **331**, 721 (2011).
2. E. Garfield, *Int. J. Epidemiol.* **35**, 1127 (2006).
3. D. J. de Solla Price, *Science* **149**, 510 (1965).
4. K. W. Boyack, R. Klavans, K. Börner, *Scientometrics* **64**, 351 (2005).
5. X. Shi, J. Leskovec, D. A. McFarland, *Proceedings of the ACM International Conference on Digital Libraries* **2010**, 58 (2010).

6. J. A. Evans, *Science* **321**, 395 (2008).
7. M. E. J. Newman, *Proc. Natl. Acad. Sci. U.S.A.* **101**, (suppl. 1), 5200 (2004).
8. C. L. Giles, I. G. Councill, *Proc. Natl. Acad. Sci. U.S.A.* **101**, 17599 (2004).
9. H. Zuckerman, R. K. Merton, *Minerva* **9**, 66 (1971).
10. J. Bollen, H. Van de Sompel, *Scientometrics* **69**, 227 (2006).
11. J. Bollen, H. Van de Sompel, J. A. Smith, R. Luce, *Inf. Process. Manage.* **41**, 1419 (2005).
12. F. Rowland, *Learn. Publ.* **15**, 247 (2002).
13. R. Smith, *BMJ* **309**, 143 (1994).
14. E. J. Weber, P. P. Katz, J. F. Waeckerle, M. L. Callahan, *JAMA* **287**, 2790 (2002).
15. P. Clapham, *Bioscience* **55**, 390 (2005).
16. Materials and methods are available as supplementary materials on Science Online.
17. E. Garfield, *Science* **178**, 471 (1972).
18. S. Saha, S. Saint, D. A. Christakis, *J. Med. Libr. Assoc.* **91**, 42 (2003).
19. S. Fortunato, *Phys. Rep.* **486**, 75 (2010).
20. S. P. Borgatti, *Soc. Networks* **27**, 55 (2005).
21. V. Bakanic, C. McPhail, R. J. Simon, *Am. Sociol. Rev.* **52**, 631 (1987).
22. L. W. Aarssen *et al.*, *The Open Ecology Journal* **1**, 14 (2008).
23. P. Cassey, T. M. Blackburn, *Trends Ecol. Evol.* **18**, 375 (2003).
24. J. Bollen *et al.*, *PLoS ONE* **4**, e4803 (2009).
25. *Nature* **465**, 870 (2010).
26. C. Bergstrom, *Coll. Res. Libr. News* **68**, 314 (2007).

Acknowledgments: We thank all participants of the survey. M. Fromont-Racine and D. Pike provided decisive input. V.C. received funding from the Centre for Applied Mathematics in Bioscience and Medicine of McGill University, an INRA startup grant, and a Natural Sciences and Engineering

Research Council of Canada discovery grant to C.d.M. This research was approved by the Research Ethics Board of McGill. V.C. conceived the project, performed the survey, and processed the data. V.C. analyzed the data with inputs from E.D., K.G., D.R., and C.d.M. and wrote the manuscript with all authors.

Supplementary Materials

www.sciencemag.org/cgi/content/full/science.1227833/DC1

Materials and Methods

Figs. S1 to S5

Tables S1 to S3

Databases S1 and S2

References (27–30)

19 July 2012; accepted 28 September 2012

Published online 11 October 2012;

10.1126/science.1227833

SAICAR Stimulates Pyruvate Kinase Isoform M2 and Promotes Cancer Cell Survival in Glucose-Limited Conditions

Kirstie E. Keller,¹ Irene S. Tan,² Young-Sam Lee^{1*}

Pyruvate kinase isoform M2 (PKM2) plays an important role in the growth and metabolic reprogramming of cancer cells in stress conditions. Here, we report that SAICAR (succinylaminoimidazolecarboxamide ribose-5'-phosphate, an intermediate of the de novo purine nucleotide synthesis pathway) specifically stimulates PKM2. Upon glucose starvation, cellular SAICAR concentration increased in an oscillatory manner and stimulated PKM2 activity in cancer cells. Changes in SAICAR amounts in cancer cells altered cellular energy level, glucose uptake, and lactate production. The SAICAR-PKM2 interaction also promoted cancer cell survival in glucose-limited conditions. SAICAR accumulation was not observed in normal adult epithelial cells or lung fibroblasts, regardless of glucose conditions. This allosteric regulation may explain how cancer cells coordinate different metabolic pathways to optimize their growth in the nutrient-limited conditions commonly observed in the tumor microenvironment.

An emerging hallmark of cancer cells is metabolic reprogramming, which includes elevated glucose uptake and oxygen-independent lactate fermentation called the Warburg effect (1–3). This reprogramming is necessary for the growth and survival of tumors (4) in stress conditions and in xenografts. However, the molecular basis for this event and its role in cancer growth have remained unclear.

Several proteins, including pyruvate kinase isoform M2 (PKM2), play important roles in the metabolic reprogramming and growth of cancer cells (4–6). PKM2 is one of four pyruvate kinases (PKs) found in mammals (7). It is highly expressed in fetal cells and cancer cells, whereas the other isoforms (PKM1, PKR, and PKL) are expressed in normal somatic tissues. Replacement of PKM2 in cancer cells with any other PK isoform drastically reduces cancer cell survival in stress conditions [hypoxia (4) or glucose depletion (8)] and suppresses tumorigenicity (4). This suggests that subtle differences between this tumor-

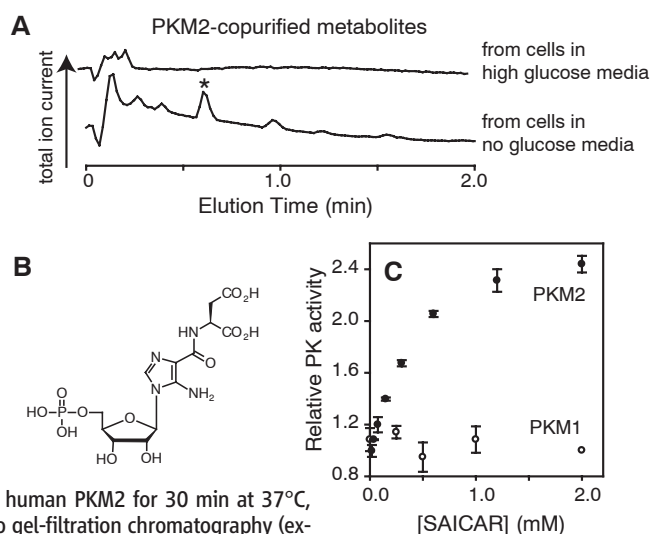
specific isoform and its normal cell counterparts are essential for tumor growth (4).

Biochemically, PKM2 is less active than its splice variant PKM1 owing to its higher Michaelis-

Fig. 1. Identification of SAICAR as a regulator of PKM2.

(A) LC-MS total ion current chromatographs of PKM2-copurified metabolites from glucose-rich (top) and glucose-free cells (bottom). A metabolite further characterized (fig. S1) is noted with an asterisk (*). A549 cells were incubated in fresh Dulbecco's modified Eagle's medium (10% dialyzed fetal bovine serum) containing either 25 mM or no glucose for 30 min, and used for metabolite extraction as described in materials and methods. Extracted metabolites

were mixed with recombinant human PKM2 for 30 min at 37°C, cooled on ice, and subjected to gel-filtration chromatography (exclusion limit: 10 kD) at 4°C. Metabolites that copurified with PKM2 were subjected to LC-MS analysis (C_{18} , electrospray ionization, positive mode). (B) Structure of SAICAR. (C) Effect of enzymatically synthesized SAICAR (fig. S2) on PK activities of (●) PKM2 and (○) PKM1. Data are means \pm SD ($n = 3$ independent experiments).



¹Department of Biology, Johns Hopkins University, 3400 North Charles Street, Baltimore, MD 21218, USA. ²National Institutes of Health—Johns Hopkins University Graduate Partnerships Program, Baltimore, MD 21218, USA.

*To whom correspondence should be addressed. E-mail: ylee99@jhu.edu

PKR) also activated by FBP cannot replace PKM2 for cancer cell growth in stress conditions (4, 7).

To identify other metabolites that interact with PKM2 in a glucose-dependent manner, we extracted cellular metabolites from A549 human lung cancer cells treated with high (~25 mM) or no glucose media (for 0.5 hours). Metabolites that bound to recombinant PKM2 were then identified as described in the supplementary materials by liquid chromatography–mass spectrometry (LC-MS, Fig. 1A). When metabolite extracts from cells grown in glucose-rich conditions were used, peaks corresponding to known PKM2-binding metabolites (FBP and pyruvate) could be identified. When metabolites from glucose-depleted cells were used, a metabolite peak (mass-to-charge ratio in positive ion mode: 455.0817) was found (Fig. 1A, asterisk). This compound was identified as SAICAR (succinylaminoimidazolecarboxamide ribose-5'-phosphate, Fig. 1B), an intermediate in the biosynthesis of purine nucleotide, on the basis of its mass (calculated exact mass, $[M-H]^+$: 455.0815) and its fragmentation pattern (fig. S1). There were several peaks other than that of SAICAR, but none were specific to PKM2, as they also coeluted with PKM1.

To determine whether SAICAR affects PKM2's function, we synthesized SAICAR (11)

(fig. S2) and tested its effect on PKM2 using a lactate dehydrogenase (LDH)–coupled method. SAICAR activates PKM2 with a half-maximal effective concentration (EC_{50}) of 0.3 ± 0.1 mM (Fig. 1D). Increasing the incubation time (to 3 hours) did not alter the EC_{50} . SAICAR did not affect other PKs tested (Fig. 1 and fig. S3). Binding of SAICAR increased the catalytic turnover number (k_{cat}) of PKM2 by a factor of 2 to 3 while reducing the K_m for PEP from ~2 to ~0.1 mM. SAICAR did not affect the K_m for adenosine 5'-diphosphate (ADP). Overall, the binding of SAICAR rendered PKM2's pyruvate kinase activity similar to that of PKM1.

When effects of other compounds related to SAICAR were tested (fig. S4), succinyl-adenosine 5'-monophosphate (S-AMP) stimulated PKM2 with an EC_{50} value (1.5 ± 0.4 mM) several times that of SAICAR. None of the other tested compounds affected PKM2 activity at physiologically relevant concentrations. SAICAR did not affect LDH activity (fig. S5). The stimulation of PKM2 by SAICAR and by FBP was not additive (fig. S6). Although this could be consistent with a competitive binding between FBP and SAICAR for an identical binding site, the study of mutant PKM2 proteins (discussed below) argues against this possibility.

To assess the physiological importance of this interaction, we measured SAICAR concentrations in several cell lines by LC-MS. In all human cancer cells tested (HeLa cervical cancer, A549, U87 glioblastoma, and H1299 non-small cell lung cancer cells), cellular concentrations of SAICAR were elevated upon glucose starvation from 20 to 100 μ M to ~0.3 to 0.7 mM (Fig. 2, A to C). The concentration of SAICAR is similar to that measured in glucose-rich leukemia cells [~40 μ M (12)]. The increase in cellular SAICAR level is oscillatory in HeLa (Fig. 2A) and H1299 cells (fig. S7). Pyruvate, lactate, and the adenosine 5'-triphosphate (ATP)/ADP ratio also changed in a manner similar to the oscillation of SAICAR levels (Fig. 2A and fig. S7). Accumulation of SAICAR in HeLa cells could be observed even after a 12-hour incubation in glucose-free media. At a fixed time point (30 min), cellular SAICAR levels in HeLa cells increased as extracellular glucose concentration decreased [Fig. 2B; physiological blood glucose concentration in healthy patients: 4 to 7 mM (13)]. In NIH 3T3 mouse embryonic fibroblast cells, an increase in SAICAR level was observed only when extracellular glucose concentrations were far below the physiological range. In normal human mammary epithelial (HuMEC) and in adult lung fibroblast

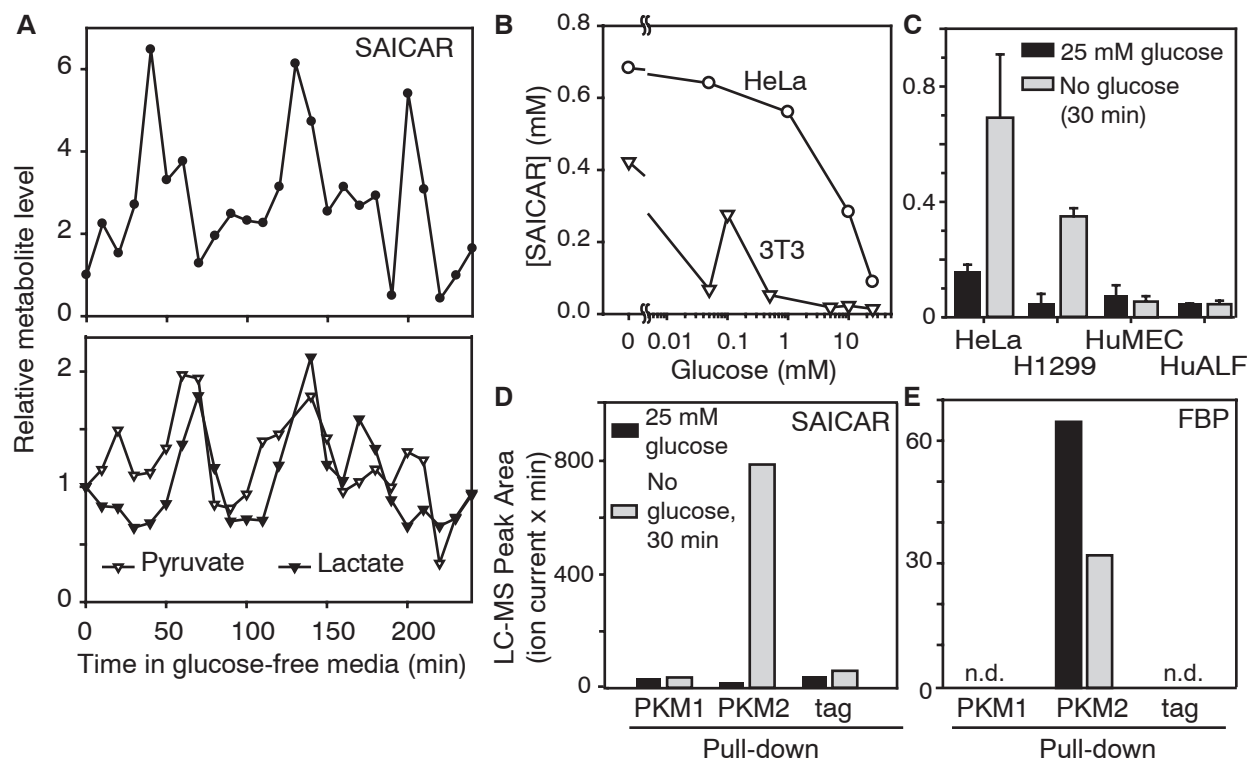


Fig. 2. SAICAR binds to PKM2 in glucose-depleted cancer cells. (A) Top: Cellular concentration of SAICAR in HeLa cells in response to glucose depletion. HeLa cells were incubated in glucose-free media, and the time-course changes in SAICAR concentration were measured by LC-MS as described in materials and methods. Bottom: Pyruvate and lactate concentration changes are also noted. (B) Effect of extracellular glucose concentration on cellular SAICAR amount. Cellular concentration of SAICAR was measured in (○) HeLa and in (▽) NIH 3T3 cells 30 min after incubation in media with various glucose concentrations. (C)

Effect of cell type. HeLa, H1299, HuMEC, and HuALF were incubated in 25 mM (filled bars) or in no glucose media (gray bars) for 30 min and used for the analysis of SAICAR level. Data are means \pm SD ($n = 3$). Other cancer cell lines tested (A549 and U87) also showed glucose-depletion–dependent increase of cellular SAICAR level. (D) LC-MS peak area of SAICAR copurified with PKM1, PKM2, or StreptII tag from H1299 cells incubated for 30 min in fresh 25 mM or no glucose media. (E) Amount of FBP that copurified with the protein of interest analyzed as in (D). n.d., not detectable.

(HuALF) cells, SAICAR accumulation was not observed even in glucose-free media (Fig. 2C). In all cells tested, FBP levels were gradually decreased upon glucose depletion (fig. S8). These results suggest that the cellular concentration of SAICAR increases to a level sufficient to stimulate PKM2 in glucose-deprived cancer cells. It also suggests that SAICAR accumulation in glucose-depleted conditions may be limited to highly proliferating cells, perhaps because these cells use the de novo nucleotide synthesis pathway more than normal cells. However, other pro-

liferating normal cells expressing PKM2 may also use this regulatory mechanism.

To determine if the PKM2-SAICAR interaction also occurs in cancer cells, we used an approach similar to the global metabolite-protein interaction mapping in yeast (14). HeLa cells were transfected with plasmids coding StrepII-tagged PKM2 or PKM1. These proteins were affinity purified. Metabolites copurified with these proteins were then analyzed by LC-MS (Fig. 2D). Copurification of SAICAR with PKM2 was observed when PKM2 was purified from glucose-

depleted cells. SAICAR was not enriched with PKM1 (Fig. 2E). FBP copurified with PKM2 from glucose-rich cells, as expected. These results suggest that the isozyme-specific PKM2-SAICAR interaction occurs in cells.

We then examined the effect of SAICAR on the pyruvate kinase activity of PKM2 in cancer cells. We prepared HeLa and H1299 cells stably transfected with short hairpin RNA (shRNA) vectors targeting expression of the SAICAR synthase PAICS and the SAICAR cleavage enzyme adenylosuccinate lyase (ADSL, Fig. 3A). In cells where PAICS is knocked down (*paics-kd*), cellular SAICAR could not be induced whereas *adsl-kd* cells have constitutively elevated SAICAR levels (Fig. 3B). Depletion of glucose for 30 min further increased cellular levels of SAICAR in *adsl-kd* cells. Prolonged (>12 hours) glucose depletion eventually led to a decrease in cellular SAICAR levels in *adsl-kd* cells (fig. S9). In *paics-kd adsl-kd* double-knockdown cells, no increase in SAICAR levels was observed. When PK activity in cell extracts was measured, the PK activity was higher in *adsl-kd* cells (fig. S10). Addition of SAICAR to the cell extract elevated pyruvate kinase activity of control-kd (cells transfected with scrambled shRNA) and *paics-kd* cell extracts, and only slightly in *adsl-kd* cell extracts (fig. S10). These results support our hypothesis that elevated cellular level of SAICAR stimulates PKM2.

Next, we measured whether SAICAR affects cancer metabolism. The glucose consumption rate of *paics-kd* cells was reduced compared with control-kd and *adsl-kd* cells (Fig. 3C). The lactate fermentation rate of *adsl-kd* cells was increased compared with control-kd and *paics-kd* cells (Fig. 3D). Similar results were obtained with LC-MS analysis of cellular metabolites (fig. S11). Both *adsl-kd* and *paics-kd* cells showed increased glutamine consumption (fig. S12). These results show that commonly observed metabolic phenotypes of cancer cells are either directly or indirectly affected by SAICAR levels. In addition, in a glucose-limited condition (30 min), *adsl-kd* cells had more ATP than the control-kd or *paics-kd* cells (figs. S13 and S14), suggesting that the cellular metabolism of these SAICAR-overproducing cells is adjusted in glucose-limiting conditions.

Because metabolic flux and cellular energy balance were altered by the changes in SAICAR concentration, we investigated whether SAICAR affected cancer cell survival in a glucose-dependent manner (Fig. 3E). In glucose-limited conditions, cells with higher SAICAR concentrations (*adsl-kd* cells or cells overexpressing PAICS, fig. S15) survived longer whereas *paics-kd* cells died earlier than control-kd cells (Fig. 3E). Double knockdown of PAICS and ADSL (*paics-kd adsl-kd*) had an effect similar to that of the PAICS knockdown alone. These results indicate that SAICAR promotes cancer cell survival in glucose-limited conditions.

To confirm the necessity of the PKM2-SAICAR interaction for increased cell survival in glucose-limited conditions, we searched for a PKM2 mutant that is insensitive to SAICAR while

Fig. 3. SAICAR level affects glucose metabolism, cancer cell survival, and proliferation. (A) A schematic diagram showing the synthesis and metabolism of SAICAR. (B) Cellular levels of SAICAR in HeLa control-kd (black bars), *adsl-kd* (open bars), and *paics-kd* (gray bars) before and after 30 min of incubation in glucose-free media. Data are the means \pm SD ($n = 3$). (C and D) Effect of SAICAR on (C) glucose uptake and (D) lactate fermentation. The amount of glucose and lactate in the media was measured by enzymatic assays and LC-MS analysis, respectively (normalized with total cellular protein concentration). Bars denote means \pm SD, respectively. (E) Survivals of HeLa control-kd (control; cells transfected with random shRNA vector), *adsl-kd*, *paics-kd*, and *paics-kd adsl-kd* cells in glucose-free media were measured by a Trypan blue exclusion method. Data are means \pm SD ($n = 3$, where >50 cells were counted to calculate the percentage of live cells in each measurement).

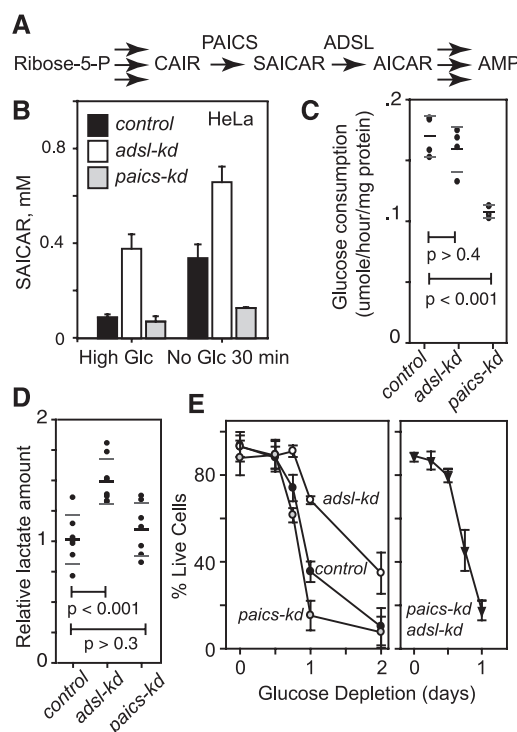
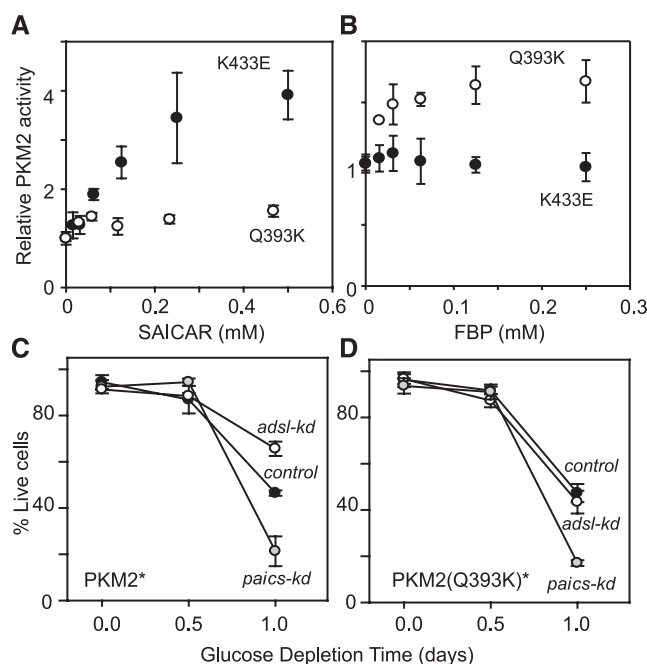


Fig. 4. SAICAR-PKM2 interaction is responsible for the promotion of cancer cell survival. (A and B) Identification of a PKM2 mutant insensitive to SAICAR. Effect of (A) SAICAR and (B) FBP on pyruvate kinase activities of PKM2 Q393K (Gln³⁹³→Lys) (○) and PKM2 K433E (Lys⁴³³→Glu) (●) mutants are shown. Data are means \pm SD ($n = 3$). (C and D) Cell viability in glucose-depletion conditions was measured as in Fig. 3E in HeLa cells expressing (C) PKM2* and (D) PKM2* Q393K mutant while endogenous PKM2 expression is knocked down. Data are means \pm SD ($n = 3$, >50 cells were counted for each measurement). Control: cells transfected with scrambled shRNA vectors.



retaining its other properties. Because PKM1 (only 22 amino acids different from PKM2) is insensitive to SAICAR (Fig. 1), we prepared several PKM2 mutants in which PKM2-specific residues were mutated to those of their corresponding PKM1 counterparts. The Q393K mutant was SAICAR-insensitive (Fig. 4A) and retained wild-type basal activity (fig. S16). This Q393K mutant was also stimulated by FBP (Fig. 4B). In contrast, the phosphotyrosine-insensitive mutant K433E [(15); K433 is also the residue contacting FBP (Protein Data Bank ID 3ME3)] continued to be stimulated by SAICAR (Fig. 4A).

We used the Q393K mutant to test whether the effect of cancer cell survival in *adsl-kd* cells is due to the PKM2-SAICAR interaction. By a previously described method (4), endogenous PKM2 was knocked down and rescued with plasmid-coded PKM2 or PKM2 Q393K (M2-rescue and Q393K-rescue cells, respectively). Western blot analysis showed that more than 90% of endogenous PKM2 expression was knocked down without detectable effects on plasmid-coded PK expression. The PK activity of the Q393K-rescue cells was similar to the level observed in *paics-kd* cells, but the activity was not stimulated by SAICAR (fig. S16B). The PKM2-rescue cells behaved similarly to the cells with endogenous PKM2 in both glucose-rich and glucose-limited conditions (Fig. 4C). The expression level of PKM2 was similar in untransfected and in Q393K-rescue cells. Q393K-rescue cells behaved nearly identically to cells with endogenous PKM2 in glucose-rich conditions. However, knockdown of ADSL in Q393K-rescue cells no longer promoted cell survival in glucose-limited conditions (Fig. 4D), indicating that the effect of SAICAR on cell

survival in this condition is due to the SAICAR-PKM2 interaction.

On the basis of these results, we conclude that at least some aspects of PKM2's role in tumor biology can be explained by SAICAR-mediated allosteric stimulation. This feature of PKM2 may allow cells to adjust their energy generation in response to nutritional and metabolic demands. When sufficient amounts of glucose are provided, diverting glycolytic intermediates to biosynthetic processes like the pentose phosphate pathway can promote cell growth. However, in energy-depleting conditions such as nutrient limitation, continued diversion of glycolytic intermediates to biosynthetic processes can hamper cells by depleting cellular energy below the minimal level required. The SAICAR-PKM2 interaction described here can be a molecular mechanism for achieving this delicate balance. Ribose-5-phosphate, the starting material of nucleotide biosynthesis, is produced from the pentose phosphate pathway, which diverts glycolytic intermediates away from energy production (16). Connecting PKM2's PK activity with an intermediate of the de novo purine nucleotide biosynthesis pathway could enable cells to fine-tune control of their metabolism in demanding conditions. SAICAR is produced from L-aspartate, a by-product of glutaminolysis, which is important in cancer cell metabolism (17), and the cleavage of SAICAR yields fumarate, which contributes to the citric acid cycle in mitochondria (18). SAICAR is therefore positioned to convey cellular metabolic demands to PKM2.

References and Notes

1. D. Hanahan, R. A. Weinberg, *Cell* **144**, 646 (2011).
2. P. P. Hsu, D. M. Sabatini, *Cell* **134**, 703 (2008).

3. W. H. Koppenol, P. L. Bounds, C. V. Dang, *Nat. Rev. Cancer* **11**, 325 (2011).
4. H. R. Christofk *et al.*, *Nature* **452**, 230 (2008).
5. A. Le *et al.*, *Proc. Natl. Acad. Sci. U.S.A.* **107**, 2037 (2010).
6. A. Wolf *et al.*, *J. Exp. Med.* **208**, 313 (2011).
7. S. Mazurek, *Int. J. Biochem. Cell Biol.* **43**, 969 (2011).
8. G. A. Spoden *et al.*, *Exp. Cell Res.* **315**, 2765 (2009).
9. M. G. Vander Heiden, L. C. Cantley, C. B. Thompson, *Science* **324**, 1029 (2009).
10. A. N. Macintyre, J. C. Rathmell, *Mol. Cell* **42**, 713 (2011).
11. P. Lee, R. F. Colman, *Protein Expr. Purif.* **51**, 227 (2007).
12. M. E. Sant, S. D. Lyons, L. Phillips, R. I. Christopherson, *J. Biol. Chem.* **267**, 11038 (1992).
13. American Diabetes Association, *Diabetes Care* **29** (suppl. 1), S4 (2006).
14. X. Li, T. A. Gianoulis, K. Y. Yip, M. Gerstein, M. Snyder, *Cell* **143**, 639 (2010).
15. H. R. Christofk, M. G. Vander Heiden, N. Wu, J. M. Asara, L. C. Cantley, *Nature* **452**, 181 (2008).
16. X. Tong, F. Zhao, C. B. Thompson, *Curr. Opin. Genet. Dev.* **19**, 32 (2009).
17. C. V. Dang, *Cell Cycle* **9**, 3884 (2010).
18. N. Raimundo, B. E. Baysal, G. S. Shadel, *Trends Mol. Med.* **17**, 641 (2011).

Acknowledgments: We thank T. Coupet, D. Meyer, and E. Pryce for technical assistance; R. Coleman, Y. Wang, C. Arrowsmith, and members of our department for sharing their equipment and materials; and A. Le, E. O'Shea, and members of our department for comments on the manuscript. Supported by Johns Hopkins University Krieger School of Arts and Sciences startup fund to Y.-S.L. The authors declare no conflict of interest.

Supplementary Materials

www.sciencemag.org/cgi/content/full/science.1224409/DC1
Materials and Methods
Figs. S1 to S16
References (19–24)

8 May 2012; accepted 20 September 2012

Published online 18 October 2012;

10.1126/science.1224409

The *Legionella* Effector RavZ Inhibits Host Autophagy Through Irreversible Atg8 Deconjugation

Augustine Choy,¹ Julia Dancourt,² Brian Mugo,² Tamara J. O'Connor,³ Ralph R. Isberg,³ Thomas J. Melia,^{2*} Craig R. Roy^{1*}

Eukaryotic cells can use the autophagy pathway to defend against microbes that gain access to the cytosol or reside in pathogen-modified vacuoles. It remains unclear if pathogens have evolved specific mechanisms to manipulate autophagy. Here, we found that the intracellular pathogen *Legionella pneumophila* could interfere with autophagy by using the bacterial effector protein RavZ to directly uncouple Atg8 proteins attached to phosphatidylethanolamine on autophagosome membranes. RavZ hydrolyzed the amide bond between the carboxyl-terminal glycine residue and an adjacent aromatic residue in Atg8 proteins, producing an Atg8 protein that could not be reconstituted by Atg7 and Atg3. Thus, intracellular pathogens can inhibit autophagy by irreversibly inactivating Atg8 proteins during infection.

Legionella pneumophila is an intracellular pathogen that manipulates evolutionarily conserved membrane transport pathways to create a specialized vacuole that supports bacterial replication in host cells (1). *Legionella* requires a type IV secretion system called Dot/Icm to replicate intracellularly (2, 3). Effector proteins

that modulate membrane transport are translocated into host cells by the Dot/Icm system (1, 4).

The autophagy pathway is used by eukaryotic cells to sequester cytosolic proteins and organelles into a membrane-bound compartment called an autophagosome (AP), which fuses with lysosomes to promote cargo degradation (5). Autophagy

can be used by plant and animal cells to target intracellular pathogens for degradation in lysosomes (6, 7). An essential step in the autophagy pathway is the coupling of an Atg8 homolog to the lipid phosphatidylethanolamine (PE) on early AP structures (8). The most widely studied Atg8 protein in mammalian cells is the microtubule-associated protein light chain 3 (LC3) (9). Unconjugated LC3 (LC3-I) runs more slowly by SDS-polyacrylamide gel electrophoresis (SDS-PAGE) than the lipidated form of LC3 (LC3-II), which means that measuring LC3-II levels by immunoblot analysis provides an indication of autophagy activity in a cell (10).

Here, we measured LC3-II levels during infection of host cells by *Legionella* to determine if this pathogen modulates autophagy (see supplementary materials and methods). LC3-II levels

¹Department of Microbial Pathogenesis, Yale University School of Medicine, New Haven, CT, USA. ²Department of Cell Biology, Yale University School of Medicine, New Haven, CT, USA. ³Howard Hughes Medical Institute and Department of Molecular Biology and Microbiology, Tufts University School of Medicine, Boston, MA, USA.

*To whom correspondence should be addressed. E-mail: thomas.melia@yale.edu (T.J.M.); craig.roy@yale.edu (C.R.R.)

were reduced in human embryonic kidney (HEK) 293 cells infected with a virulent strain of *Legionella pneumophila* Philadelphia-1 when compared with uninfected cells (Fig. 1A). The block in LC3-II generation was more apparent when degradation of LC3-II was prevented upon treatment of cells with bafilomycin A1 to neutralize lysosomal pH. LC3-II levels were not affected when cells were infected with an isogenic *Legionella dotA* mutant (11), which has a nonfunctional Dot/Icm system (Fig. 1A). Uninfected cells and cells infected with the *dotA* mutant contained punctate LC3-positive APs resulting from basal levels of autophagy, whereas punctate LC3-positive APs were absent in most cells infected with virulent *Legionella* (Fig. 1, B and C). Additionally, LC3-II levels were low in primary macrophages that had been injected by the Dot/Icm system (Fig. 1D and fig. S1), and LC3 puncta were absent

in these infected macrophages (Fig. 1, E and F). Thus, *Legionella* has a Dot/Icm-dependent mechanism to inhibit the autophagy pathway.

Isogenic *Legionella* strains with large chromosomal deletions were used to determine the genetic basis for autophagy inhibition (12). Autophagy inhibition was not observed after infection with a “pentuple” mutant with five large chromosomal deletions that eliminate 71 putative effectors (Fig. 2A). Autophagy inhibition was also lost in the $\Delta 3$ mutant, which is missing only 10 of the effectors deleted in the pentuple mutant (Fig. 2A). When these 10 effectors were produced individually as green fluorescent protein (GFP)–effector fusions in HEK293 cells, only cells producing the GFP-RavZ fusion protein displayed low LC3-II levels (Fig. 2B). GFP-RavZ also prevented the formation of LC3 puncta in transfected HEK293 cells (fig. S2) and interfered with autophagy-dependent

degradation of the long-lived protein substrates (Fig. 2C). Thus, RavZ can block autophagy.

An in-frame deletion of the *ravZ* gene was constructed in a *Legionella* strain that contained all other effectors. The $\Delta ravZ$ mutant and the *dotA* mutant were equally defective for autophagy inhibition, as measured by LC3-II levels (Fig. 2D) and the presence of LC3 puncta in the infected cells (Fig. 2E). Complementation in both assays was achieved using a plasmid-encoded *ravZ* allele (Fig. 2, D and E). Likewise, introducing *ravZ* on a plasmid into the $\Delta 3$ strain restored autophagy inhibition during infection, whereas the other nine presumed effectors encoded in the $\Delta 3$ region could not (fig. S3). Thus, RavZ is necessary to block autophagy during *Legionella* infection.

Although AP formation was restored in cells infected with a RavZ-deficient strain of *Legionella*, LC3-positive membranes were not recruited to

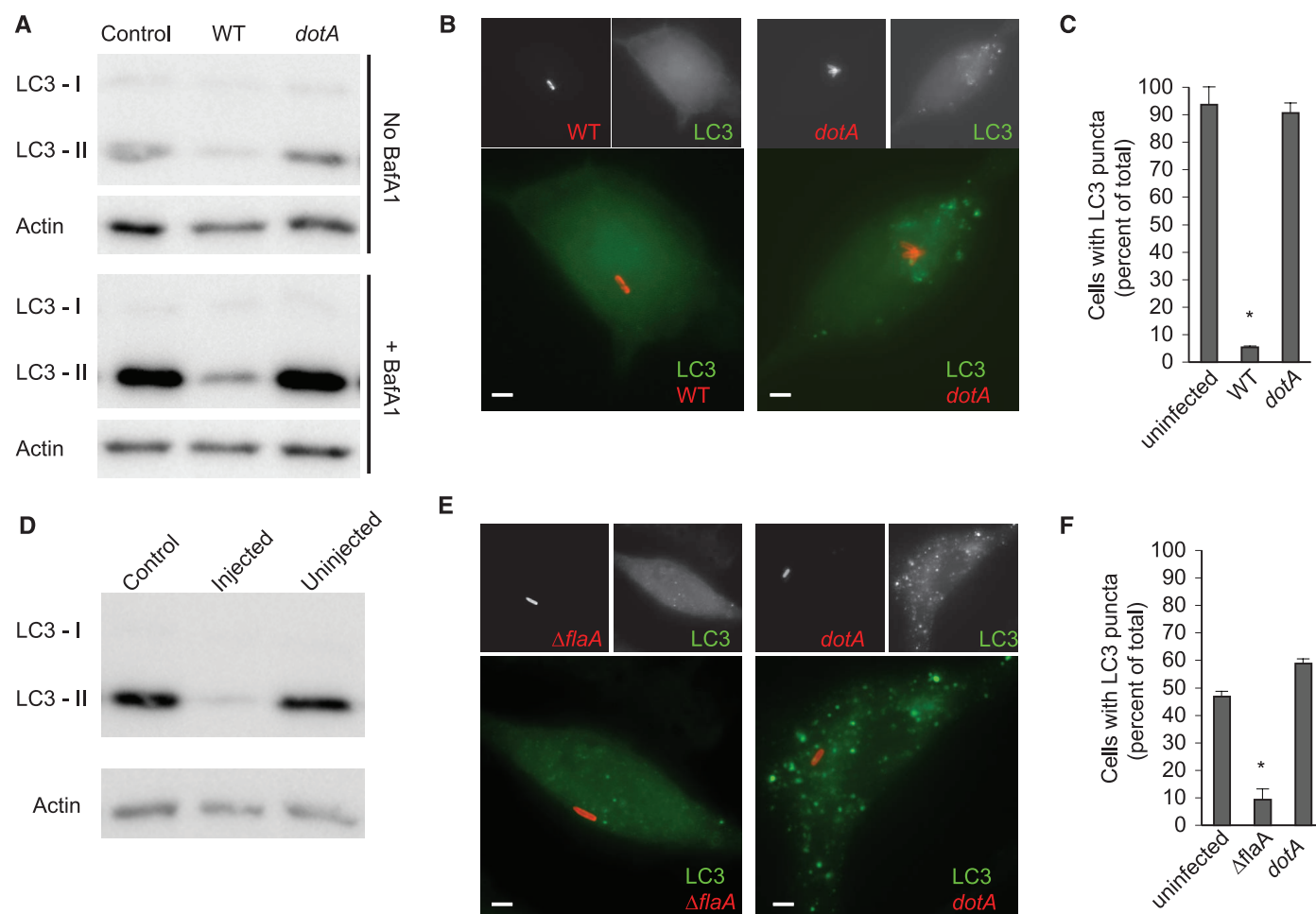


Fig. 1. *Legionella* inhibits autophagy by a Dot/Icm-dependent mechanism. (A) Immunoblot analysis of LC3-I and LC3-II levels in uninfected cells (control) and cells infected for 2 hours with either wild-type (WT) *Legionella* or a *dotA* mutant. Treatment of cells with bafilomycin A1 is indicated. (B) Images show LC3 (green) distribution in HEK293 cells infected with the indicated *Legionella* strains (red) for 2 hours. Scale bars, 1 μ m. (C) Percent of cells containing LC3-puncta calculated from three independent assays, where a total of 100 cells were scored in each assay. Data represent the average \pm SD (error bars); * P < 0.0001 compared to the uninfected control. (D) Mouse bone marrow–derived macrophages were infected for 2 hours with a *Legionella* $\Delta flaA$ strain produc-

ing a BlaM-RalF fusion protein. Immunoblot analysis was used to detect LC3-I and LC3-II levels in injected and uninfected cells (fig. S1). (E) Representative images of bone marrow–derived macrophages from GFP-LC3 transgenic mice infected with the indicated *Legionella* strains (red) for 2 hours. Cells were stained using an antibody specific for GFP (green). Scale bars, 1 μ m. (F) GFP-LC3 puncta staining for uninfected and infected mouse bone marrow–derived macrophages. The percent of cells containing GFP-LC3 puncta was calculated from three independent assays where a total of 100 cells were scored in each assay. Data represent the average \pm SD; * P < 0.0001 compared to the uninfected control.

vacuoles containing a *ΔravZ* mutant (fig. S4). The isogenic *ΔravZ* mutant grew equally well in control macrophages and autophagy-deficient macrophages lacking Atg5 when compared to the parental strain (fig. S4). Thus, vacuoles containing the *ΔravZ* mutant evade a functional autophagy system, which suggests that *Legionella* encodes additional effectors capable of disrupting recognition of the vacuole containing *Legionella* by the autophagy system.

To better understand how RavZ interferes with autophagy, purified RavZ was added to an in vitro assay that reconstitutes conjugation of Atg8 proteins to PE (13). A recombinant human Atg8 homolog called GABARAP-L1 (GR) was conjugated to PE on synthetic liposomes by a reaction requiring adenosine triphosphate and purified Atg7 and Atg3 (Fig. 3A). GR lipidation was strongly inhibited when RavZ was added to this reaction (Fig. 3A). RavZ inhibited GR lipidation when added at concentrations that were more than 1000-fold lower than Atg7 and Atg3 (Fig. 3B), indicating that RavZ functions catalytically to interfere with GR lipidation. Thus, RavZ can inhibit autophagy by acting directly in the Atg8 lipidation pathway.

The addition of RavZ to isolated liposomes (fig. S5) drove the complete conversion of lipidated GR-PE back to an apparently unmodified form of GR (Fig. 3C). Likewise, direct addition of RavZ to finished in vitro conjugation reactions also resulted in deconjugation of GR-PE (fig. S6). RavZ delipidated all Atg8 family members that we tested (fig. S6). Thus, RavZ is a deconjugating enzyme that targets Atg8 proteins covalently attached to PE.

Atg8 proteins are synthesized as inactive pro-forms that contain additional amino acid residues after the conserved reactive glycine located near the C terminus (5). Atg4 is a cysteine protease that regulates autophagy by cleaving the C terminus of pro-Atg8 after the conserved glycine, which is required for the glycine to participate in the PE conjugation reaction (5). The protease activity of Atg4 can also release Atg8 proteins from vesicles by reversing the amide bond linking the C-terminal glycine to PE (14). Based on their similar ability to deconjugate Atg8 proteins bound to PE, we asked whether RavZ was functioning as an Atg4 mimic.

The addition of *N*-ethylmaleimide (NEM) to the GR-PE deconjugation reaction, which inhibits its cysteine proteases by covalently modifying

reactive cysteine residues, interfered with RavZ-mediated deconjugation of GR in vitro (Fig. 3D). Thus, RavZ appears to use a catalytic mechanism similar to Atg4. We used anisotropy to measure the kinetics of deconjugation of fluorescently labeled GR attached to PE on liposome membranes. RavZ deconjugated GR-PE rapidly and Atg4B deconjugation occurred more slowly (Fig. 3E). RavZ deconjugated the entire pool of GR-PE within 1 min, whereas a measureable amount of GR-PE was still detected 60 min after the addition of Atg4B (fig. S7). RavZ did not cleave a recombinant GR protein with yellow fluorescent protein (YFP) fused to the native C terminus (Fig. 3F) or LC3 proteins with extended C-terminal regions (fig. S8), which were all cleaved efficiently by Atg4B in solution. Thus, RavZ and Atg4 have different substrate preferences, with RavZ being highly active on lipid-conjugated Atg8 proteins and having no detectable protease activity toward Atg8 proteins in solution.

We used liquid chromatography–tandem mass spectrometry (LC-MS/MS) to analyze Atg8 reaction products after RavZ treatment. The C-terminal peptide [DESVYG (D, Asp; E, Glu; S, Ser; V, Val;

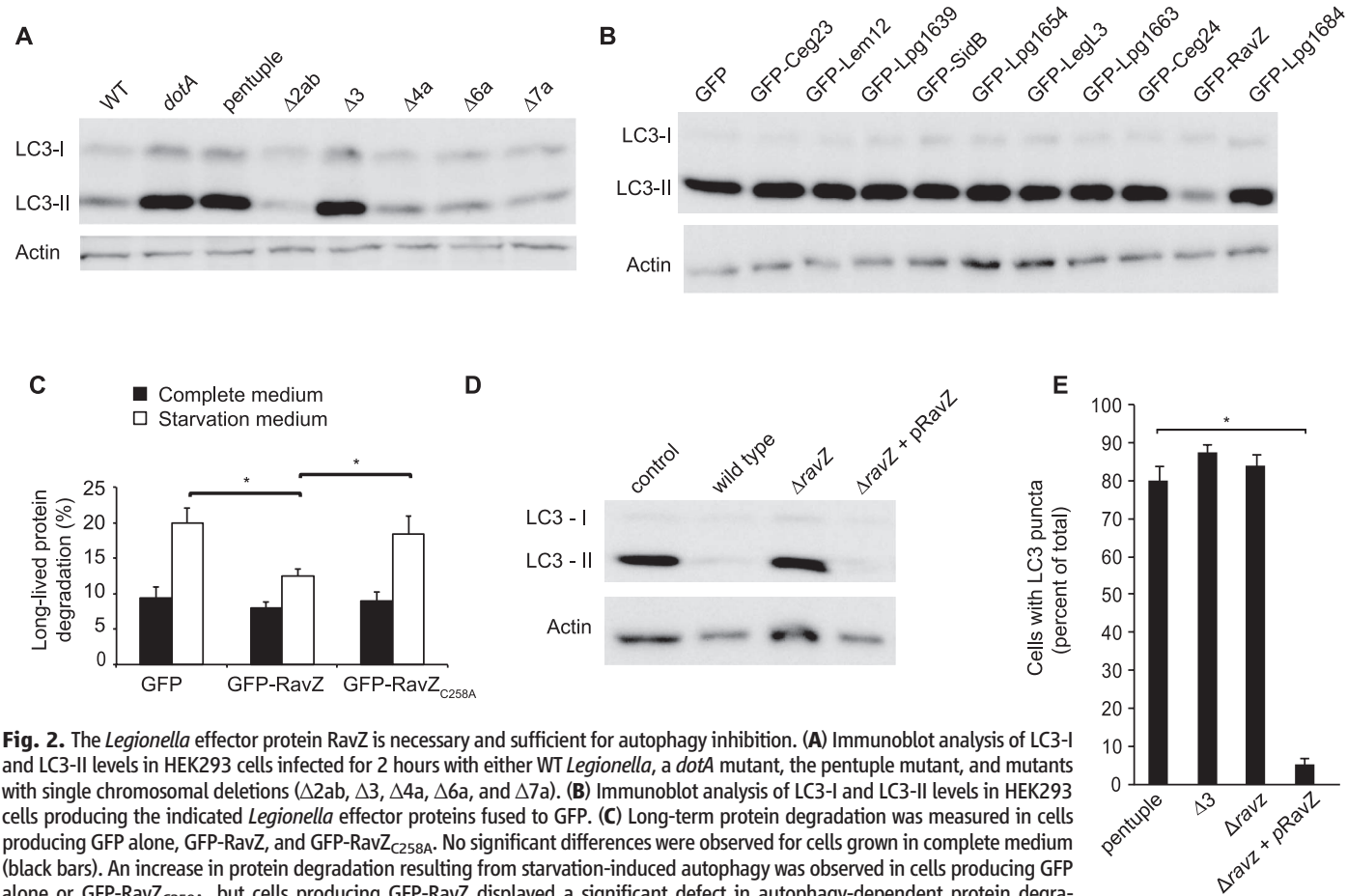


Fig. 2. The *Legionella* effector protein RavZ is necessary and sufficient for autophagy inhibition. **(A)** Immunoblot analysis of LC3-I and LC3-II levels in HEK293 cells infected for 2 hours with either WT *Legionella*, a *dotA* mutant, the pentuple mutant, and mutants with single chromosomal deletions ($\Delta 2ab$, $\Delta 3$, $\Delta 4a$, $\Delta 6a$, and $\Delta 7a$). **(B)** Immunoblot analysis of LC3-I and LC3-II levels in HEK293 cells producing the indicated *Legionella* effector proteins fused to GFP. **(C)** Long-term protein degradation was measured in cells producing GFP alone, GFP-RavZ, and GFP-RavZ_{C258A}. No significant differences were observed for cells grown in complete medium (black bars). An increase in protein degradation resulting from starvation-induced autophagy was observed in cells producing GFP alone or GFP-RavZ_{C258A} but cells producing GFP-RavZ displayed a significant defect in autophagy-dependent protein degradation. Data represent average \pm SD (error bars) from three independent triplicates; $*P < 0.001$. **(D)** Immunoblot analysis of LC3-I and LC3-II levels in HEK293 cells infected for 2 hours with WT *Legionella*, a *dotA* mutant, a $\Delta ravZ$ mutant, or the complemented RavZ-deficient strain ($\Delta ravZ$ + pRavZ). **(E)** HEK293 cells infected for 2 hours with the indicated strains of *Legionella* were fixed and stained for LC3. Infected cells were scored for the presence of LC3-positive puncta. The graph shows the percent of cells containing LC3-puncta calculated from three independent assays, in which a total of 100 cells were scored in each assay. Data represent the average \pm SD; $*P < 0.0001$ compared to the pentuple mutant control.

Y, Tyr; G, Gly)] in GR was detected in untreated samples and also in reactions where GR in solution was incubated with RavZ (Fig. 3G). When GR was isolated after being deconjugated from PE by RavZ *in vitro*, the C-terminal glycine residue had been removed from the peptide (DESVY) (Fig. 3G, bottom graph). Thus, RavZ targeted the amide bond between the tyrosine and the PE-conjugated glycine residue, unlike Atg4, which targets the amide bond linking glycine to PE (fig. S9). Thus, RavZ is a deconjugating enzyme that produces an Atg8 product that would be resistant to re-conjugation by the host machinery due to the absence of the reactive C-terminal glycine.

The otubain family of deubiquitinating enzymes are proteases with a reactive cysteine res-

idue presented in a conserved DGNC (N, Asn; C, Cys) sequence (15), which closely matched the cysteine residue at amino acid position 258 in RavZ that is presented in the context of an EGNC motif. RavZ_{C258A} derivatives were inactive in the *in vitro* assays that measure GR-PE deconjugation (Fig. 3D), the *in vivo* assays that measure LC3-II conversion and AP formation by staining LC3 puncta (fig. S10), and the starvation-mediated long-lived protein degradation assay (Fig. 2D). GFP-RavZ localized to structures that were Atg16-positive and LC3-negative, whereas GFP-RavZ_{C258A} localized to structures that were Atg16-negative and LC3-positive (fig. S11). Thus, RavZ can bind early AP membranes, and RavZ_{C258A} represents a noncatalytic substrate-trapping mutant that

remains associated with Atg8-PE on mature AP membranes.

We have found that the *Legionella* RavZ protein inhibits host autophagy by functioning as a cysteine protease that specifically targets lipid-conjugated Atg8 proteins and generates a deconjugated Atg8 product that lacks the essential C-terminal glycine required for re-conjugation. RavZ can both prevent Atg8 from accumulating on the membranes of phagophores that mature into AP structures and also inactivate the Atg8 protein during the deconjugation reaction. Thus, *Legionella* has evolved a specific mechanism to interfere with host autophagy by directly targeting the Atg8 proteins involved in AP formation.

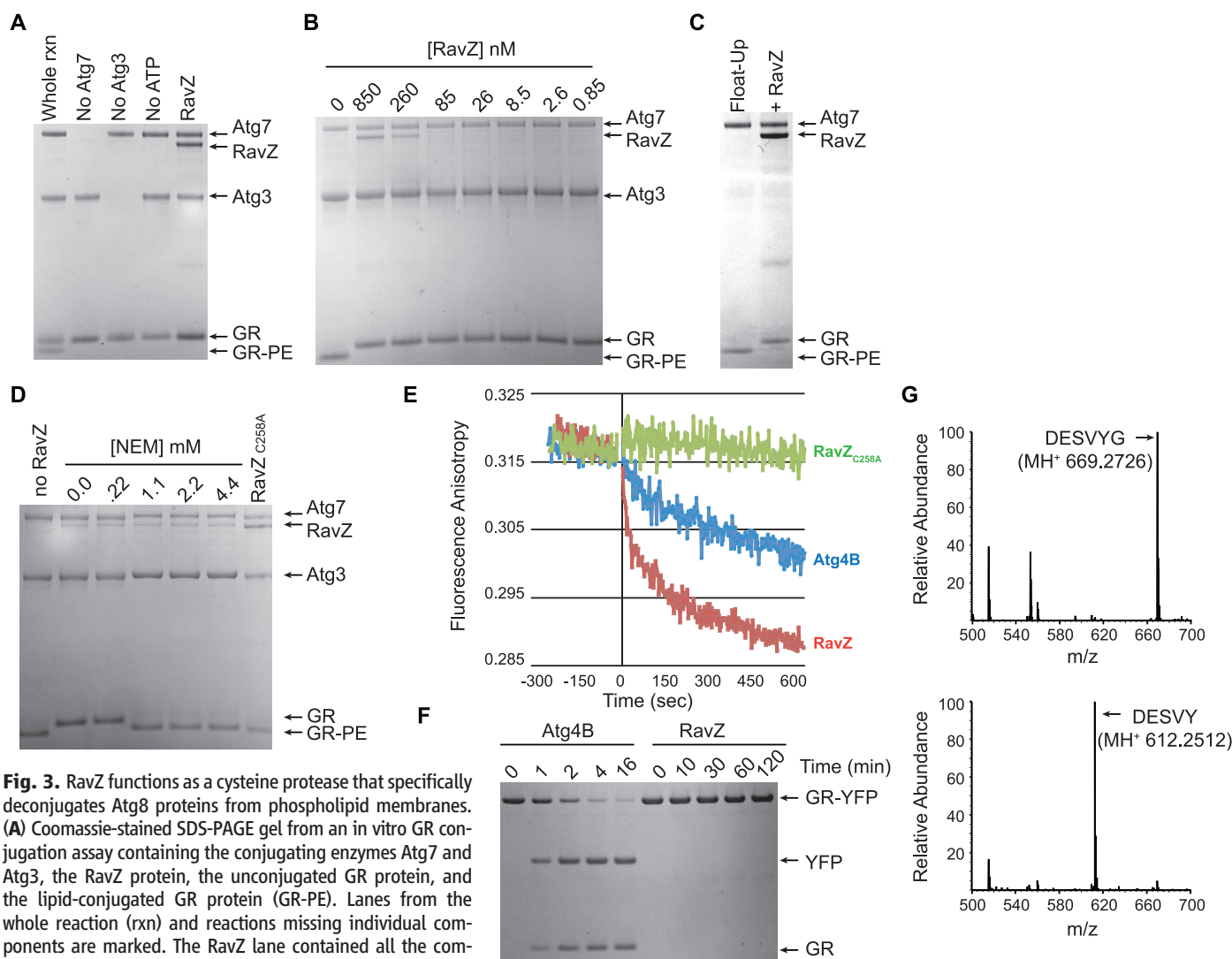


Fig. 3. RavZ functions as a cysteine protease that specifically deconjugates Atg8 proteins from phospholipid membranes. **(A)** Coomassie-stained SDS-PAGE gel from an *in vitro* GR conjugation assay containing the conjugating enzymes Atg7 and Atg3, the RavZ protein, the unconjugated GR protein, and the lipid-conjugated GR protein (GR-PE). Lanes from the whole reaction (rxn) and reactions missing individual components are marked. The RavZ lane contained all the components of the whole reaction plus purified RavZ protein. ATP, adenosine triphosphate. **(B)** Indicated above each lane are the concentrations of purified RavZ added to a conjugation assay containing GR at a concentration of 12 μ M. **(C)** Liposomes containing GR conjugated to PE were isolated on a flotation gradient (Float-Up lane) and treated with RavZ (+RavZ lane). **(D)** Liposomes containing GR-PE were treated with RavZ, in the presence of the indicated concentrations of NEM, or with the RavZ_{C258A} protein. **(E)** Fluorescence anisotropy was used to analyze the release kinetics of Texas Red-labeled GR from liposomes *in vitro* upon treatment with RavZ (red), Atg4B

(blue), and RavZ_{C258A} (green). **(F)** Stained SDS-PAGE gels show that GR-YFP was rapidly cleaved by Atg4B to generate the products GR and YFP. No cleavage of GR-YFP was observed by RavZ after a 120-min reaction. **(G)** LC-MS/MS chromatograms from samples containing purified GR (top) and GR that was isolated after RavZ-mediated deconjugation from PE-containing liposomes (bottom). Arrows indicate that the native C-terminal peptide in GR (DESVYG) was abundant in the untreated sample and that RavZ-mediated deconjugation resulted in a loss of the C-terminal glycine (DESVY). m/z, mass/charge ratio.

References and Notes

1. A. Hubber, C. R. Roy, *Annu. Rev. Cell Dev. Biol.* **26**, 261 (2010).
2. G. Segal, M. Purcell, H. A. Shuman, *Proc. Natl. Acad. Sci. U.S.A.* **95**, 1669 (1998).
3. J. P. Vogel, H. L. Andrews, S. K. Wong, R. R. Isberg, *Science* **279**, 873 (1998).
4. A. W. Ensminger, R. R. Isberg, *Curr. Opin. Microbiol.* **12**, 67 (2009).
5. Z. Xie, D. J. Klionsky, *Nat. Cell Biol.* **9**, 1102 (2007).
6. A. P. Hayward, S. P. Dinesh-Kumar, *Annu. Rev. Phytopathol.* **49**, 557 (2011).
7. P. Kuballa, W. M. Nolte, A. B. Castoreno, R. J. Xavier, *Annu. Rev. Immunol.* **30**, 611 (2012).
8. Y. Ichimura *et al.*, *Nature* **408**, 488 (2000).
9. Y. Kabeya *et al.*, *EMBO J.* **19**, 5720 (2000).
10. D. J. Klionsky *et al.*, *Autophagy* **4**, 151 (2008).
11. H. Nagai, J. C. Kagan, X. Zhu, R. A. Kahn, C. R. Roy, *Science* **295**, 679 (2002).
12. T. J. O'Connor, Y. Adepoju, D. Boyd, R. R. Isberg, *Proc. Natl. Acad. Sci. U.S.A.* **108**, 14733 (2011).
13. A. Jotwani, D. N. Richerson, I. Motta, O. Julca-Zevallos, T. J. Melia, *Methods Cell Biol.* **108**, 93 (2012).
14. T. Kirisako *et al.*, *J. Cell Biol.* **151**, 263 (2000).
15. M. Y. Balakirev, S. O. Tcherniuk, M. Jaquinod, J. Chroboczek, *EMBO Rep.* **4**, 517 (2003).

Acknowledgments: We thank N. Mizushima and A. Iwasaki for providing GFP-LC3 and Atg5-deficient mice and S. Shin for providing the plasmid encoding BlaM-RaIF. Support for this research came from the Science, Technology and Research Scholars Program at Yale University (B.M.); the

Howard Hughes Medical Institute (T.J.O. and R.R.I.); and NIH Awards AI007019 (A.C.), NS063973 (T.J.M.), AI041699, and AI048770 (C.R.R.). The data presented in this manuscript are tabulated in the main paper and in the supplementary materials.

Supplementary Materials

www.sciencemag.org/cgi/content/full/science.1227026/DC1
Materials and Methods
Figs. S1 to S11
References (16–25)

5 July 2012; accepted 12 October 2012
Published online 25 October 2012;
10.1126/science.1227026

Structural Basis of Transcription Initiation

Yu Zhang,¹ Yu Feng,¹ Sujoy Chatterjee,¹ Steve Tuske,² Mary X. Ho,² Eddy Arnold,² Richard H. Ebright^{1*}

During transcription initiation, RNA polymerase (RNAP) binds and unwinds promoter DNA to form an RNAP-promoter open complex. We have determined crystal structures at 2.9 and 3.0 Å resolution of functional transcription initiation complexes comprising *Thermus thermophilus* RNA polymerase, σ^A , and a promoter DNA fragment corresponding to the transcription bubble and downstream double-stranded DNA of the RNAP-promoter open complex. The structures show that σ recognizes the –10 element and discriminator element through interactions that include the unstacking and insertion into pockets of three DNA bases and that RNAP recognizes the –4/+2 region through interactions that include the unstacking and insertion into a pocket of the +2 base. The structures further show that interactions between σ and template-strand single-stranded DNA (ssDNA) preorganize template-strand ssDNA to engage the RNAP active center.

In transcription initiation, RNA polymerase (RNAP), together with at least one transcription initiation factor, binds to promoter DNA to yield an RNAP-promoter closed complex (RPc) and then unwinds ~12 base pairs of promoter DNA to form a “transcription bubble” and yield an RNAP-promoter open complex (RPO) (*1*). RPO is the critical, catalytically competent, intermediate in transcription initiation, and modulation of the formation, stability, and activity of RPO is an important means of regulation of gene expression (*1*). Structural models of RPO have been generated based on information from electron microscopy, fluorescence-resonance-energy-transfer measurements, and protein-DNA crosslinking (*2–9*). However, no high-resolution structural information for a functional, promoter-dependent, initiation-factor-dependent RPO previously has been reported.

Here, we report crystal structures of a bacterial RPO and a bacterial RPO in complex with a ribodinucleotide primer at 2.9 and 3.0 Å resolution, respectively. The results define the inter-

actions of RNAP and the transcription initiation factor σ with the nontemplate and template strands of the transcription bubble in RPO, the interactions of RNAP with downstream double-stranded DNA (dsDNA) in RPO, and the RNAP clamp conformation in RPO.

To obtain a structure of RPO, we used a synthetic nucleic-acid scaffold corresponding to the transcription bubble and downstream dsDNA of RPO (*10*) (fig. S1). The top strand comprised a 14-nucleotide (nt) single-stranded DNA (ssDNA) tail containing a consensus promoter –10 element (*11*) and consensus discriminator element (*12, 13*), followed by a 13-nt duplex-forming segment. The bottom strand comprised a noncomplementary 6-nt ssDNA tail, followed by a 13-nt duplex-forming segment. The scaffold was functional in RNAP-DNA complex formation (fig. S1E) and in de novo transcription initiation with position +1 as the transcription start site (fig. S1F). Published work indicates that scaffolds of this form recapitulate all functional properties of the transcription bubble and downstream dsDNA of RPO (*14*).

We prepared complexes of the scaffold with *Thermus thermophilus* RNAP holoenzyme containing σ^A , identified crystallization conditions by use of robotic crystallization trials, grew crystals, collected data at a synchrotron, solved the struc-

ture by molecular replacement, and refined the structure, yielding a structure of RPO with a resolution of 2.9 Å and free R factor (R_{free}) of 0.226 (fig. S1). Electron-density maps showed unambiguous density for nontemplate-strand nucleotides –12 to +12, template-strand nucleotides –4 to +12, 3139 RNAP residues, and 346 σ residues, and showed density for template-strand nucleotides +1 and +2 in the RNAP active-center “i” and “i + 1” sites. Analysis of crystals obtained using a derivative of the scaffold containing 5-bromouracil (5-BrU) in place of T at template-strand position +1 showed a single peak of Br anomalous difference density at the expected position, confirming that RNAP interacts with the scaffold in the crystals in a single translocational register and confirming that the translocational register places template-strand nucleotides +1 and +2 in the RNAP active-center “i site” and “i + 1 site” (fig. S2).

To obtain a structure of RPO in complex with a ribodinucleotide primer, we used an analogous nucleic-acid scaffold containing GpA, a ribodinucleotide complementary to template-strand positions –1 and +1 (Fig. 1A and fig. S3). Biochemical experiments verified that this scaffold is functional in primer-dependent transcription initiation (fig. S3, E and F). Crystals were prepared, and data were collected and processed as above, yielding a structure of RPO-GpA with a resolution of 3.0 Å and R_{free} of 0.247 (Fig. 1, A and B, and fig. S3). Protein-DNA interactions were essentially identical in the structures of RPO and RPO-GpA (fig. S4).

The structures show that RNAP and σ recognize promoter elements through sequence-specific interactions with transcription-bubble nontemplate-strand ssDNA (Figs. 1 to 3). σ makes sequence-specific interactions with the upstream part of the transcription-bubble nontemplate strand (positions –12 to –4) (Fig. 1, A to C, and Fig. 2), and RNAP makes sequence-specific interactions with the downstream part of the transcription-bubble nontemplate strand (positions –4 to +2) (Fig. 1, A to C, and Fig. 3).

σ interacts with the promoter –10-element nontemplate strand through a deep, L-shaped groove that runs across σ region 2 (σ R2) and part of σ region 1.2 (σ R1.2) (Fig. 1, A to C, and

¹Howard Hughes Medical Institute, Waksman Institute, and Department of Chemistry and Chemical Biology, Rutgers University, Piscataway, NJ 08854, USA. ²Center for Advanced Biotechnology and Medicine and Department of Chemistry and Chemical Biology, Rutgers University, Piscataway, NJ 08854, USA.

*To whom correspondence should be addressed. E-mail: ebright@waksman.rutgers.edu

Fig. 2A). σ interacts with all six nucleotides of the -10 element and potentially interacts with bases of five nucleotides of the -10 element (positions -12 , -11 , -9 , -8 , and -7) (Fig. 1, A to C, Fig. 2A, and figs. S5 and S6). The interactions

with bases involve σ residues L110, E116, N383, R385, L386, K418, F419, E420, R423, Y425, S428, T429, Y430, T432, W433, and R436 (residues numbered throughout as in *Escherichia coli* RNAP and σ^{70}). Alanine substitutions of

these residues result in defects in transcription, indicating that these residues are functionally important (Fig. 2B). Model building indicates that σ residues Q437 and T440 could contact a nucleotide base-paired to nontemplate-strand position -12 , providing a structural explanation for results indicating that these residues are important for sequence recognition at position -12 (15, 16) (Fig. 2A and fig. S5). The interactions between σ and the -10 element in RPo and RPo-GpA are essentially identical to those observed in a crystal structure of a σ R2 fragment bound to a -10 element ssDNA oligonucleotide (17, 18).

σ interacts with the promoter discriminator-element nontemplate strand through a shallow groove that runs across the face of σ R1.2 (Figs. 1A and 2C). σ interacts with bases of three nucleotides of the discriminator element (positions -6 through -4) (Figs. 1A and 2C, and fig. S7). The interactions involve σ residues D96, V98, R99, M102, R103, M105, G106, and R385. Alanine substitutions of these residues result in defects in transcription (Fig. 2D). σ residue M102 makes direct van-der-Waals contact with the base at nontemplate-strand position -5 , providing a structural explanation for the observation that σ M102 can be crosslinked to this base (19) (Figs. 1A and 2C, and fig. S7B).

A striking feature of the interactions between σ and the -10 and discriminator elements is that σ unstacks three DNA bases, flips them out of base stacks, and inserts them into pockets formed by residues of σ (Figs. 1 and 2, and figs. S6, A and C, and S7A). σ R2 unstacks, flips, and inserts into a deep pocket the adenine base at the second position of the -10 element (A-11) (Fig. 2, A and E, and fig. S6A). Within this deep pocket, A-11 makes stacking interactions with one aromatic amino acid (σ Y430), makes edge-edge interactions with two aromatic amino acids (σ Y419 F419 and Y425), and makes H bonds between base Watson-Crick atoms and two amino-acid backbone atoms (σ K418 and Y419 E420), enabling unambiguous sequence read-out (fig. S6A). In an analogous manner, σ R2 unstacks, flips, and inserts into a deep pocket the thymine base at the sixth position of the -10 element (T-7) (Fig. 2, A, C, and F, and fig. S6C), and σ R1.2 unstacks, flips, and inserts into a deep pocket the guanine base at the first position of the discriminator element (G-6) (Fig. 2, C and F, and fig. S7A). The insertion of flipped-out bases into pockets provides an effective means to read sequence, because it enables contacts with essentially all atoms of the bases. This mode of interaction accounts for the fact that A-11 and T-7 are the most important positions of the -10 element (17). The insertion of flipped-out bases into pockets also provides an effective means to use binding energy to drive DNA unwinding, because this mode of interaction can occur only when DNA is unwound. This mode of interaction accounts for the ability of σ to facilitate promoter unwinding.

RNAP core enzyme interacts with transcription-bubble nontemplate-strand positions -4 to $+2$,

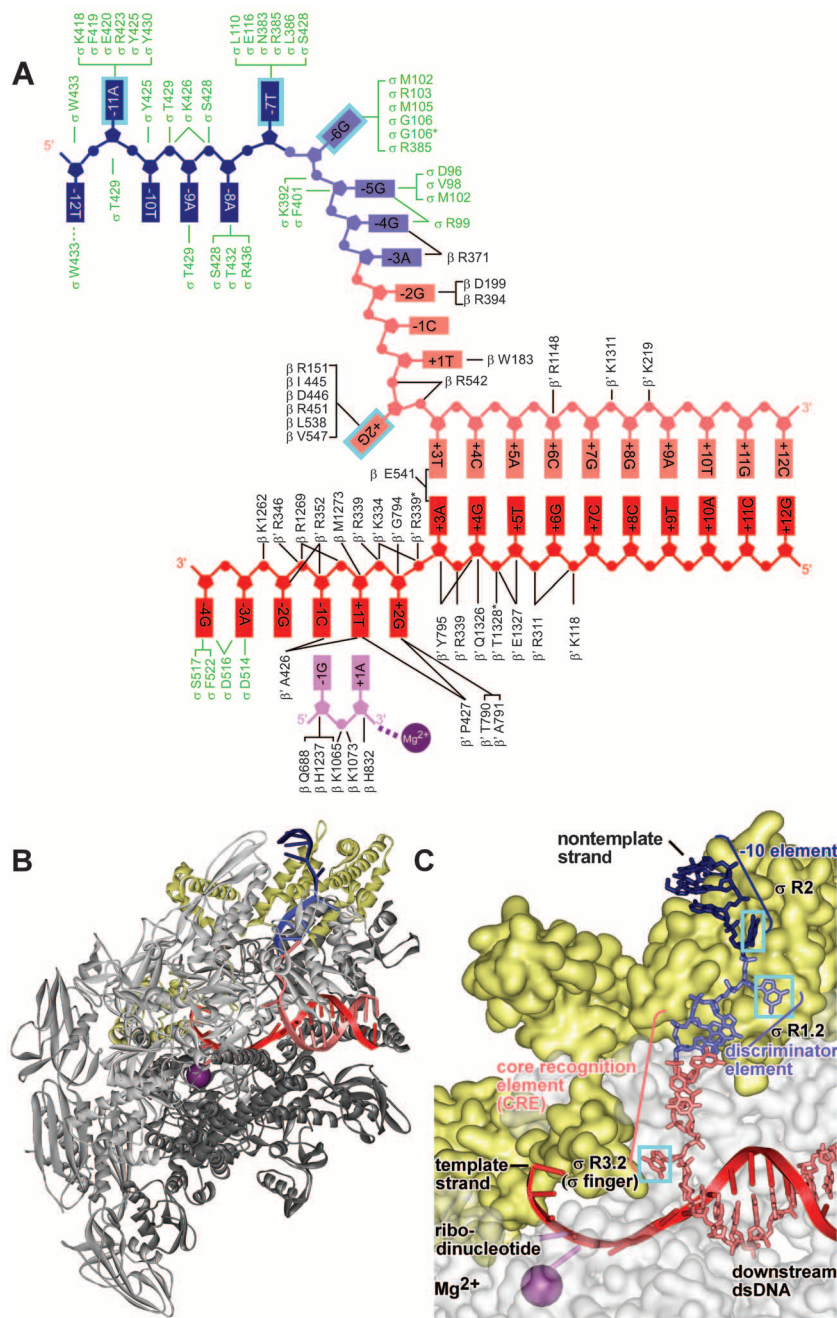


Fig. 1. Structure of RPo-GpA. (A) Summary of protein–nucleic-acid interactions. Black residue numbers and lines, interactions by RNAP; green residue numbers and lines, interactions by σ ; blue, -10 element of DNA nontemplate strand; light blue, discriminator element of DNA nontemplate strand; pink, rest of DNA nontemplate strand; red, DNA template strand; magenta, GpA; violet, active-center Mg²⁺; asterisks, water-mediated interactions; cyan boxes, bases unstacked and inserted into pockets. Residues are numbered as in *E. coli* RNAP and σ^{70} . (B) Overall structure (RNAP β' nonconserved domain omitted for clarity). RNAP, gray; σ , yellow. Other colors as in (A). (C) Interactions of RNAP and σ with transcription-bubble nontemplate strand, transcription-bubble template strand, and downstream dsDNA (RNAP β subunit and β' nonconserved domain omitted for clarity). Colors as in (B). Single-letter abbreviations for the amino acid residues are as follows: A, Ala; C, Cys; D, Asp; E, Glu; F, Phe; G, Gly; H, His; I, Ile; K, Lys; L, Leu; M, Met; N, Asn; P, Pro; Q, Gln; R, Arg; S, Ser; T, Thr; V, Val; W, Trp; and Y, Tyr.

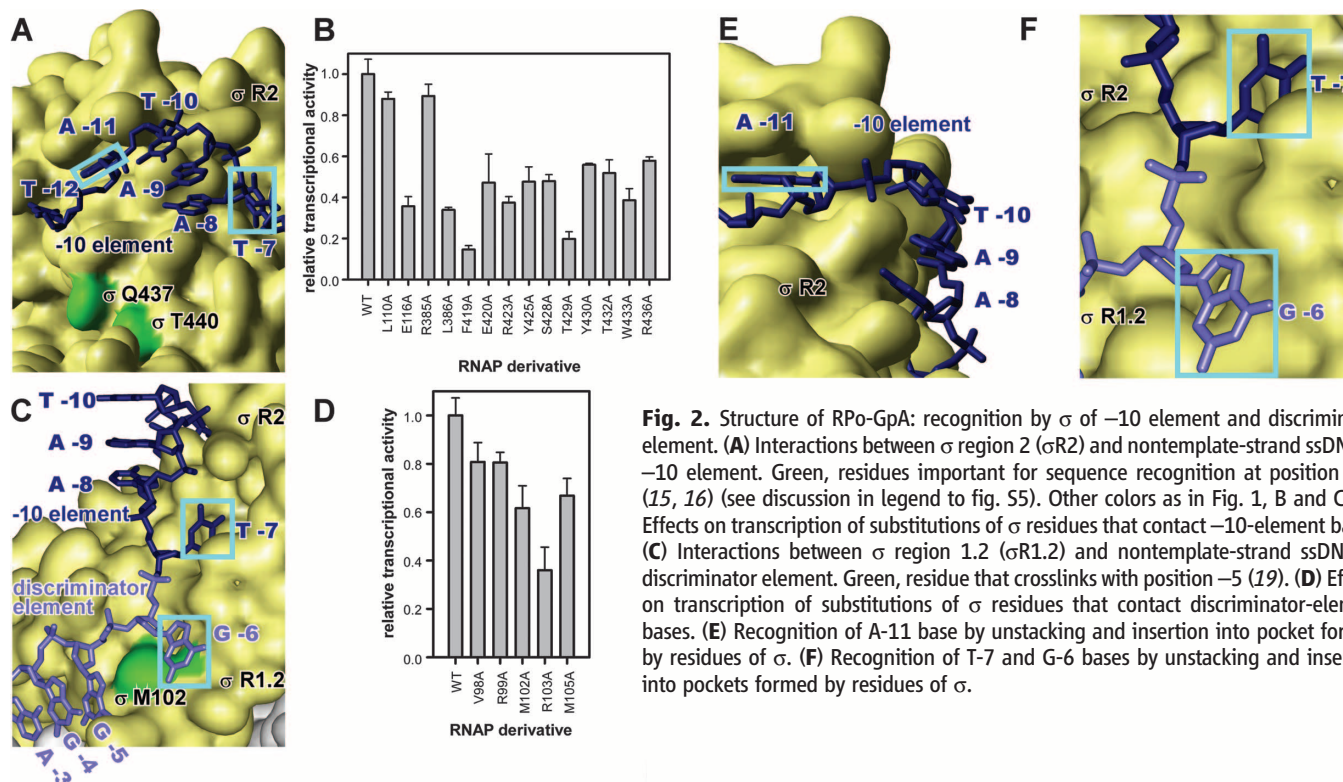
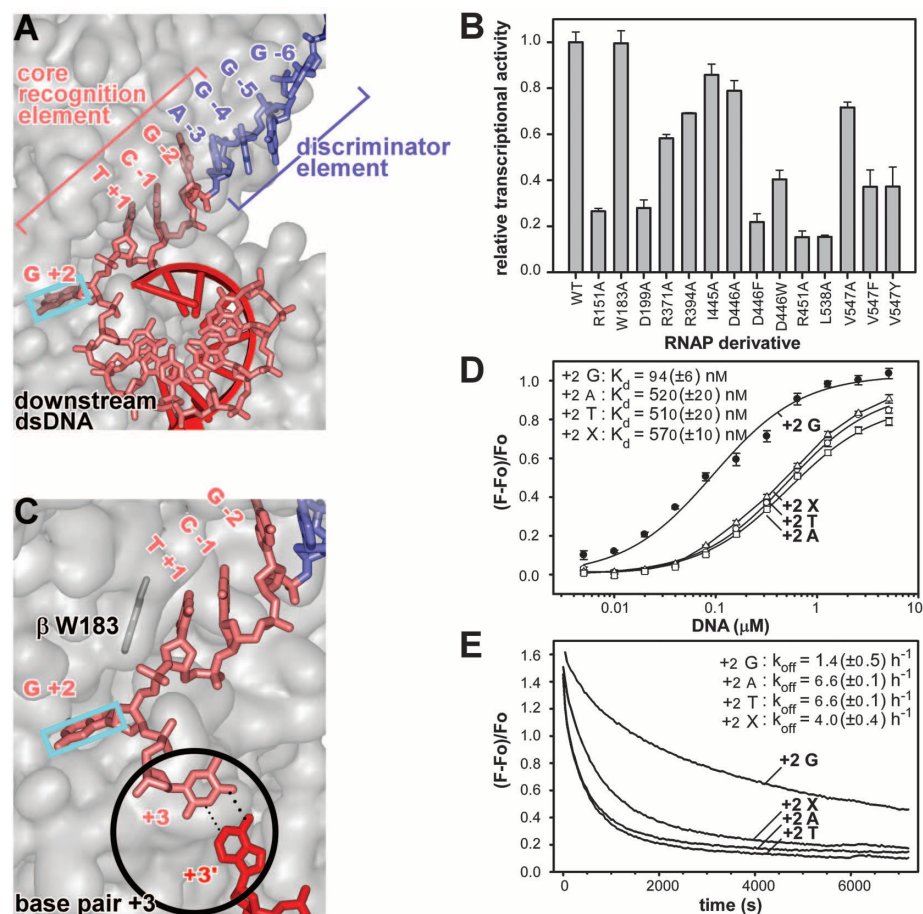


Fig. 3. Structure of RPo-GpA: recognition by RNAP of CRE. (A) Interactions between RNAP β subunit and nontemplate-strand ssDNA of CRE (positions -4 through +2). RNAP β' subunit and σ omitted for clarity. Downstream dsDNA helix viewed end-on. Colors as in Fig. 1, B and C. (B) Effects on transcription of substitutions of RNAP β -subunit residues that contact CRE bases. (C) Recognition of G+2 base by unstacking and insertion into pocket formed by residues of RNAP β subunit, and stacking of T+1 base on RNAP β -subunit residue W183. (D and E) Effects on RNAP-DNA interaction of substitutions of G+2 base by A, T, or abasic site (X). (D) shows fluorescence-detected equilibrium binding. (E) shows fluorescence-detected high-salt-induced dissociation.



which we term the “core recognition element” (CRE) (Fig. 1, A and C, and Fig. 3), and which we show to be a sequence-specific promoter element (see below). RNAP core enzyme interacts with bases of five of six nucleotides of the CRE (positions -4 , -3 , -2 , $+1$, and $+2$) (Figs. 1A and 3A, and fig. S8). The interactions involve RNAP β -subunit residues R151, W183, D199, R371, R394, I445, D446, R451, L538, and V547. Alanine substitutions of all except one of these residues result in defects in transcription (Fig. 3B). The interactions account for the previously observed crosslinking of nontemplate-strand positions -4 through $+2$ to β residues 84 to 642 (2).

The interactions between RNAP and the most-downstream nucleotide of the transcription-bubble nontemplate strand, G+2, are especially noteworthy. RNAP unstacks the G+2 base, flips it out of the base stacks, and inserts it into a deep pocket formed by RNAP β subunit (“ β pocket”), in a manner analogous to the manner in which σ interacts with A-11, T-7, and G-6 (Fig. 3, A and C, and fig. S8C). Six residues of the β pocket make van-der-Waals interactions with the G+2 base (β R151, I445, D446, R451, L538, and V547), and two residues of the β pocket make H bonds with Watson-Crick atoms of the G+2 base (β D446 and R451) (fig. S8C). The structures suggest that the interactions between RNAP and G+2 are sequence-specific (fig. S8C), and equilibrium-binding and kinetic experiments confirm that the interactions between RNAP and G+2 are

sequence-specific (Fig. 3, D and E, and fig. S9). RNAP exhibits an equilibrium dissociation constant lower by a factor of 5, and an off-rate lower by a factor of 5, for a promoter derivative having G at nontemplate-strand position $+2$ than for promoter derivatives having A, T, C, or an abasic site at nontemplate-strand position $+2$ (Fig. 3, D and E, and fig. S9). In principle, the sequence-specific interactions between RNAP and nontemplate-strand G+2 shown here to occur in transcription initiation complexes may occur also in transcription elongation complexes. More than 30 crystal structures of elongation complexes have been determined to date (fig. S10). However, only one includes nontemplate-strand position $+2$: namely, PDB 3PO2, a structure of a yeast RNAPII backtracked and arrested elongation complex (20). Strikingly, in this structure, although not noted in the publication on this structure, the nontemplate-strand position $+2$ base is inserted into a pocket formed by RNAPII residues equivalent to β R151, β I445, β D446, β R451, β L538, and β V547, adopting a conformation similar to, and making interactions similar to, G+2 in the structures of RPo and RPo-GpA (fig. S10). This observation, together with other observations (21), suggests that the RNAP-DNA interactions that mediate recognition of G+2 in initiation complexes may occur also in elongation complexes, where they may influence sequence-dependent translational bias (22) and sequence-dependent pausing (23). This observation further suggests that these RNAP-

DNA interactions may be made not only by bacterial RNAP but also by eukaryotic RNAPII.

The interaction between RNAP and the adjacent nucleotide of the transcription-bubble nontemplate strand, T+1, also is noteworthy. RNAP β -subunit residue W183 makes an aromatic-amino-acid/base stacking interaction with T+1 (Fig. 3C and fig. S8B). This interaction forces the unstacking of T+1 and G+2—making G+2 available to interact with the β pocket—and also likely nucleates or stabilizes the stacking of nucleotides at nontemplate-strand positions -5 through $+1$ (Fig. 3C).

Although it has been established that RNAP-CRE interactions involving position $+2$ are sequence-specific (Fig. 3, D and E, and fig. S9), it remains to be determined whether RNAP-CRE interactions involving positions -4 through $+1$ are sequence-specific. We conclude that RNAP-CRE interactions contribute to sequence-specific promoter recognition, and we propose that RNAP-CRE interactions also contribute to the formation and maintenance of the transcription bubble. It seems likely that RNAP-CRE interactions enable RNAP to assist σ in promoter unwinding during σ -dependent initiation and enable RNAP to perform promoter unwinding during σ -independent initiation.

The structures also show that RNAP and σ “preorganize” the transcription-bubble template strand and downstream dsDNA (Fig. 4, A and B). The transcription-bubble template strand in the structures adopts the same A-form helical

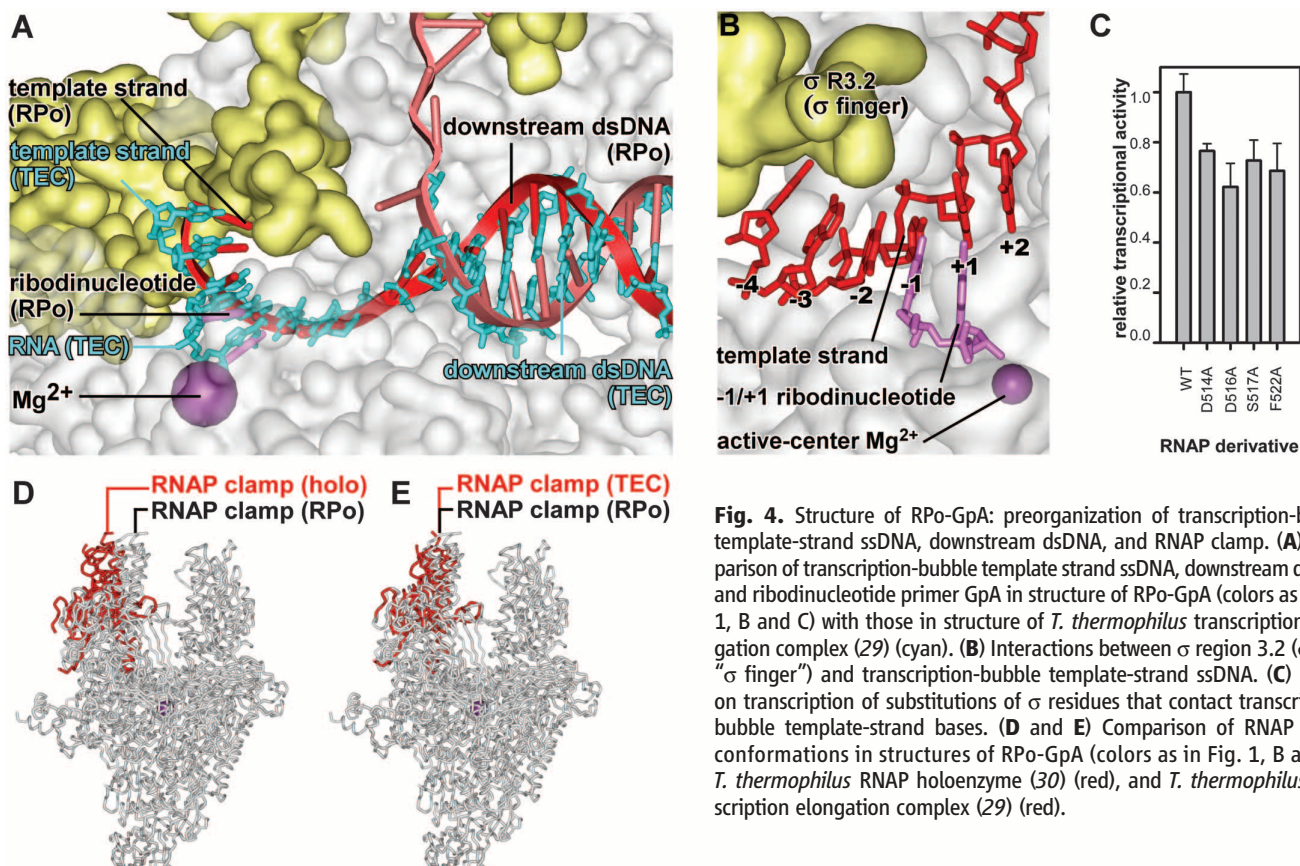


Fig. 4. Structure of RPo-GpA: preorganization of transcription-bubble template-strand ssDNA, downstream dsDNA, and RNAP clamp. (A) Comparison of transcription-bubble template strand ssDNA, downstream dsDNA, and ribodinucleotide primer GpA in structure of RPo-GpA (colors as in Fig. 1, B and C) with those in structure of *T. thermophilus* transcription elongation complex (29) (cyan). (B) Interactions between σ region 3.2 (σ finger) and transcription-bubble template-strand ssDNA. (C) Effects on transcription of substitutions of σ residues that contact transcription-bubble template-strand bases. (D and E) Comparison of RNAP clamp conformations in structures of RPo-GpA (colors as in Fig. 1, B and C), *T. thermophilus* RNAP holoenzyme (30) (red), and *T. thermophilus* transcription elongation complex (29) (red).

conformation, and makes the same interactions with the RNAP active-center “i” and “i + 1” sites, as in an elongation complex (Fig. 4A). The downstream dsDNA and the ribonucleotide primer GpA in the structures also exhibit the same conformations and interactions as the downstream dsDNA and the 3' ribonucleotides of the RNA product in an elongation complex (Fig. 4A). We conclude that a promoter-dependent, initiation-factor-dependent transcription initiation complex is preorganized to proceed to transcription elongation without major changes in the conformation or interactions of the transcription-bubble template strand, downstream dsDNA, and RNA. The preorganization of the template strand in the promoter-dependent, initiation-factor-dependent initiation complex is in contrast to the situation in promoter-independent, initiation-factor-independent initiation complexes, in which template-strand ssDNA is disordered (24), or all but 5 nt of template-strand ssDNA is disordered (25), except in the presence of ≥ 4 nt of RNA. The presence of the initiation factor appears to account for the difference. The initiation factor σ makes direct interactions with the template strand that preorganize the template strand. The segment of σ region 3.2 (σ R3.2) comprising σ residues 510 to 522—the “ σ finger”—penetrates the RNAP active-center cleft, occupies part of the region occupied by RNA in a transcription elongation complex, makes an aromatic-amino-acid/base edge-edge interaction with the template-strand base at position –4, and makes four H bonds with Watson-Crick atoms of the template-strand bases at positions –4 and –3 (Fig. 4B and fig. S11). The interactions with DNA bases at template-strand positions –4 and –3 involve σ residues D514, D516, D517, and F522. Alanine substitutions of these residues result in defects in transcription (Fig. 4C). The interactions between the σ finger and the template strand constrain the template strand to adopt an A-form helical conformation and buttress the template strand to engage the RNAP active center in a manner compatible with binding of initiating NTPs. These interactions provide a structural explanation for the ability of the σ finger to facilitate the binding of initiating NTPs (26, 27). The interactions between the σ finger and the template strand must be disrupted, and the σ finger must be displaced, to synthesize >4 nt of RNA. The need to disrupt these interactions and displace the σ finger provides a structural explanation for effects of the σ finger on abortive initiation (26, 27).

The structures also define the conformational state of the RNAP clamp—the movable wall of the RNAP active-center cleft (28)—in the transcription initiation complex (Fig. 4, D and E). The clamp is closed by $\sim 11^\circ$ relative to the crystal structure of RNAP holoenzyme (Fig. 4D) and exhibits the same conformation as in the crystal structure of the elongation complex (Fig. 4E), consistent with fluorescence-resonance-energy-transfer results indicating that the clamp closes upon formation of RPo and remains closed

during elongation (28). The finding that clamp conformations are the same in the initiation complex and the elongation complex provides further evidence that the initiation complex is preorganized to proceed to elongation.

The structures of RPo and RPo-GpA determined in this work reveal how RNAP and σ interact with the transcription-bubble nontemplate strand to accomplish promoter recognition and promoter unwinding and reveal how RNAP and σ interact with the transcription-bubble template strand and downstream dsDNA to preorganize the transcription initiation complex for subsequent reactions. The structures provide a foundation for understanding transcription initiation and transcriptional regulation.

References and Notes

1. R. M. Saecker, M. T. Record Jr., P. L. Dehaseth, *J. Mol. Biol.* **412**, 754 (2011).
2. N. Naryshkin, A. Revyakin, Y. Kim, V. Mekler, R. H. Ebricht, *Cell* **101**, 601 (2000).
3. V. Mekler *et al.*, *Cell* **108**, 599 (2002).
4. B. P. Hudson *et al.*, *Proc. Natl. Acad. Sci. U.S.A.* **106**, 19830 (2009).
5. K. S. Murakami, S. Masuda, E. A. Campbell, O. Muzzini, S. A. Darst, *Science* **296**, 1285 (2002).
6. X. Liu, D. A. Bushnell, D. Wang, G. Calero, R. D. Kornberg, *Science* **327**, 206 (2010).
7. D. Kostrewa *et al.*, *Nature* **462**, 323 (2009).
8. B. Treutlein *et al.*, *Mol. Cell* **46**, 136 (2012).
9. S. Grünberg, L. Warfield, S. Hahn, *Nat. Struct. Mol. Biol.* **19**, 788 (2012).
10. Materials and methods are available as supplementary materials on Science Online.
11. R. Shultzaberger, Z. Chen, K. Lewis, T. Schneider, *Nucleic Acids Res.* **35**, 771 (2007).
12. A. Feklistov *et al.*, *Mol. Cell* **23**, 97 (2006).
13. S. P. Haugen *et al.*, *Cell* **125**, 1069 (2006).
14. V. Mekler, L. Minakhin, K. Severinov, *J. Biol. Chem.* **286**, 22600 (2011).

15. D. A. Siegele, J. C. Hu, W. A. Walter, C. A. Gross, *J. Mol. Biol.* **206**, 591 (1989).
16. C. Waldburger, T. Gardella, R. Wong, M. M. Susskind, *J. Mol. Biol.* **215**, 267 (1990).
17. A. Feklistov, S. A. Darst, *Cell* **147**, 1257 (2011).
18. X. Liu, D. A. Bushnell, R. D. Kornberg, *Cell* **147**, 1218 (2011).
19. S. P. Haugen, W. Ross, M. Manrique, R. L. Gourse, *Proc. Natl. Acad. Sci. U.S.A.* **105**, 3292 (2008).
20. A. C. Cheung, P. Cramer, *Nature* **471**, 249 (2011).
21. M. L. Kireeva, C. Domecq, B. Coulombe, Z. F. Burton, M. Kashlev, *J. Biol. Chem.* **286**, 30898 (2011).
22. P. P. Hein, M. Palangat, R. Landick, *Biochemistry* **50**, 7002 (2011).
23. R. Landick, *Proc. Natl. Acad. Sci. U.S.A.* **106**, 8797 (2009).
24. X. Liu, D. A. Bushnell, D. A. Silva, X. Huang, R. D. Kornberg, *Science* **333**, 633 (2011).
25. A. C. Cheung, S. Sainsbury, P. Cramer, *EMBO J.* **30**, 4755 (2011).
26. K. S. Murakami, S. Masuda, S. A. Darst, *Science* **296**, 1280 (2002).
27. A. Kulbachinskiy, A. Mustaev, *J. Biol. Chem.* **281**, 18273 (2006).
28. A. Chakraborty *et al.*, *Science* **337**, 591 (2012).
29. D. G. Vassilyev, M. N. Vassilyeva, A. Perederina, T. H. Tahir, I. Artsimovitch, *Nature* **448**, 157 (2007).
30. D. G. Vassilyev *et al.*, *Nature* **417**, 712 (2002).

Acknowledgments: We thank the Brookhaven National Synchrotron Light Source and Cornell High Energy Synchrotron Source for beamline access; the Argonne Photon Source CCP4 School for training; and S. Borukhov, P. deHaseth, K. Kuznedelov, L. Minakhin, K. Severinov, and D. Temiakov for plasmids and discussion. This work was funded by NIH grants GM41376 and AI072766 and a Howard Hughes Medical Institute Investigatorship to R.H.E. PDB accession codes are 4G7H, 4G7Z, and 4G7O.

Supplementary Materials

www.sciencemag.org/cgi/content/full/science.1227786/DC1
Materials and Methods
Figs. S1 to S11
References (31–48)

23 July 2012; accepted 26 September 2012
Published online 18 October 2012;
10.1126/science.1227786

Dedifferentiation of Neurons and Astrocytes by Oncogenes Can Induce Gliomas in Mice

Dinorah Friedmann-Morvinski,¹ Eric A. Bushong,² Eugene Ke,^{1,3} Yasushi Soda,¹ Tomotoshi Marumoto,^{1,4} Oded Singer,¹ Mark H. Ellisman,² Inder M. Verma^{1*}

Glioblastoma multiforme (GBM) is the most common and aggressive malignant primary brain tumor in humans. Here we show that gliomas can originate from differentiated cells in the central nervous system (CNS), including cortical neurons. Transduction by oncogenic lentiviral vectors of neural stem cells (NSCs), astrocytes, or even mature neurons in the brains of mice can give rise to malignant gliomas. All the tumors, irrespective of the site of lentiviral vector injection (the initiating population), shared common features of high expression of stem or progenitor markers and low expression of differentiation markers. Microarray analysis revealed that tumors of astrocytic and neuronal origin match the mesenchymal GBM subtype. We propose that most differentiated cells in the CNS upon defined genetic alterations undergo dedifferentiation to generate a NSC or progenitor state to initiate and maintain the tumor progression, as well as to give rise to the heterogeneous populations observed in malignant gliomas.

Despite progress in the genetic analysis and classification of gliomas based on pathology and genomics, the prognosis

for patients with brain tumors continues to be very poor (1). One of the reasons for the lack of clinical advances in the treatment of glioblastoma

multiforme (GBM) for decades has been the insufficient understanding of the underlying mechanisms of progression and recurrence of gliomagenesis.

We recently used Cre-inducible lentiviral vectors to generate a novel mouse glioma model (2). Here we have expanded the utility of our lentiviral system by generating a new construct that carries two short hairpin RNAs (shRNAs): one targeting the gene encoding neurofibromatosis type I (NF1, mutated in 18% of GBMs) and the other targeting p53 (mutated in over 35% of GBMs) (Fig. 1, A and B). It has previously been shown that the combined loss of both NF1 and p53 results in high-grade glioma formation (3, 4). The loss of NF1 leads to increased Ras mitogenic signaling and augments cell proliferation, whereas the loss of functional p53 induces genomic instability, two important events relevant for tumorigenesis that were part of our rationale for using H-RasV12 and the inactivation of p53 in the initial pTomo lentivector (2).

¹Laboratory of Genetics, The Salk Institute for Biological Studies, La Jolla, CA 92037, USA. ²Center for Research in Biological Systems, National Center for Microscopy and Imaging Research, University of California San Diego, La Jolla, CA 92093, USA. ³Graduate Program in Bioinformatics, University of California San Diego, La Jolla, CA 92093, USA. ⁴Division of Molecular and Clinical Genetics, Department of Molecular Genetics, Medical Institute of Bioregulation, Kyushu University, Higashi-ku, Fukuoka 812-8582, Japan.

*To whom correspondence should be addressed. E-mail: verma@salk.edu

As shown in Fig. 1C and fig. S1, stereotaxic injection of oncogenic lentivector containing either shNF1-shp53 or H-RasV12-shp53 in the hippocampus (HP) of glial fibrillary acidic protein (GFAP)-Cre mice gives rise to gliomas with similar histological and morphological characteristics. Glial cells (5, 6), oligodendrocyte precursor cells (7, 8), and neural stem cells (NSCs) (4, 9) have been suggested to be good candidates for the cell of origin of gliomas. Here we show that neurons can also be the target of transformation and generate malignant gliomas. Injections of shNF1-shp53 virus in the cortex (CTX) of Synapsin I-Cre transgenic mice (SynI-Cre; 8 to 16 weeks old), which express Cre specifically in neurons but not in glial cells (10), induced the formation of gliomas (Fig. 2A). Because the shRNAs targeting genes encoding either NF1 or p53 are not regulated by Cre (Fig. 1A), the tumors that we obtained were a mixture of green fluorescent protein-positive and red fluorescent protein-negative (GFP⁺/RFP⁻) or GFP⁺/RFP⁺ (due to leakiness from the internal ribosome entry site; see arrows in Fig. 2B). Only tumor cells that are GFP⁺/RFP⁻ are considered to be of neuronal origin, because they are expressing Cre to delete RFP. We extended these results by transducing H-RasV12-p53 vector in the CTX of SynI-Cre mice. Neurons transduced with this oncogenic vector expressed only GFP, because the expression of Ras is regulated by Cre (fig. S2) (10).

Analysis of brain sections 5 days after the injection of the lentivirus revealed GFP⁺/RFP⁻

expression specifically in NeuN⁺ and Tuj1⁺ cells (see representative images in Fig. 2C and quantification of staining in table S1), and the same specificity was observed when SynI-Cre mice were crossed with a LacZ reporter line (fig. S3A), both results showing that Cre is specifically expressed in terminally differentiated neurons (10). To provide further evidence that mature neurons can be transformed by these oncogene/tumor suppressor genes as observed *in vivo*, we isolated primary cortical neurons from SynI-Cre mice and transduced them *in vitro* with shNF1-shp53 virus. The isolated neurons were Map2-positive (a marker of mature neurons), GFAP-negative, doublecortin-negative (a neuronal progenitor marker), and Ki67-negative (a marker for cell proliferation) (figs. S4A and S5). The transduced neurons were transplanted into NOD-SCID mice, and the resulting tumors (fig. S4B) exhibited the same histopathology features as those observed with the direct *in vivo* stereotaxic transductions. These tumors also expressed high levels of the progenitor markers Nestin and Sox2 (fig. S4C).

To determine the frequency of the tumor-initiating cells in tumors obtained by shNF1-shp53 injections in the CTX of SynI-Cre mice, we dissociated the tumors in single-cell suspension and sorted them into two different populations: GFP⁺/RFP⁻ and GFP⁺/RFP⁺ cells. After limiting dilution analysis, we transplanted these cells back into new mice and obtained in both cases and with similar frequencies high-grade

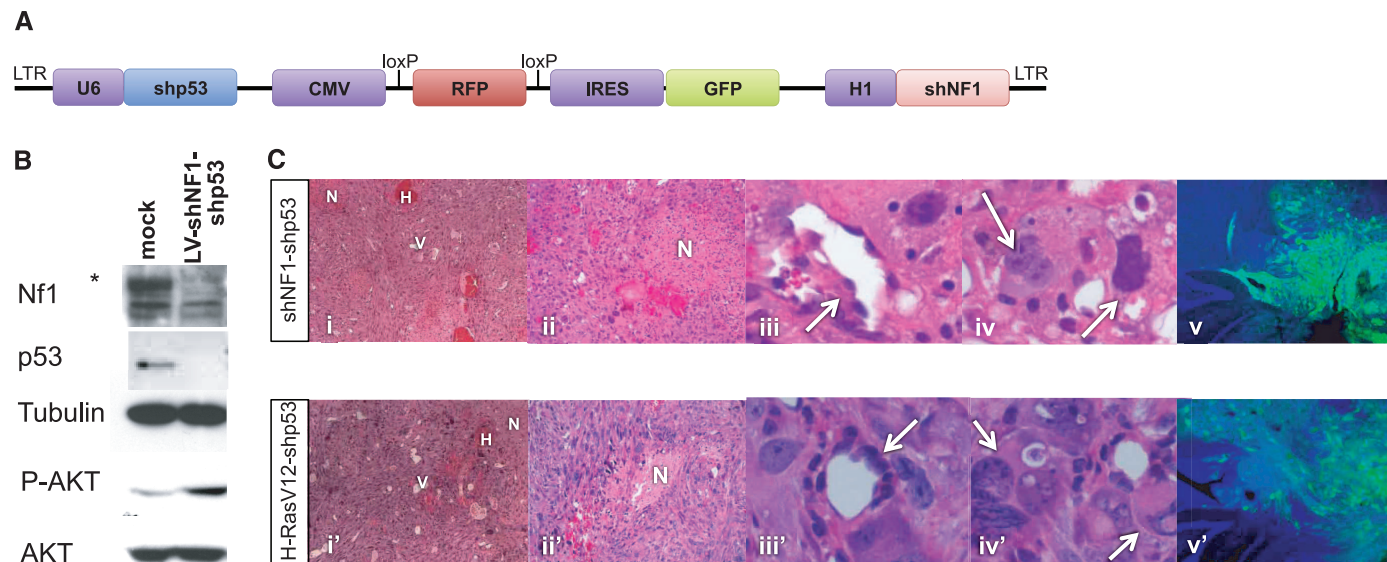


Fig. 1. Glioblastomas induced by a single lentiviral vector. **(A)** Schematic representation of the lentivector. In the shNF1-shp53 vector, the hairpin targeting NF1 was cloned under the H1 promoter at the 3' untranslated region, and the hairpin targeting p53 was cloned 5' to the cytomegalovirus promoter and under the U6 promoter. LTR, long terminal repeat. **(B)** Western blot (WB) showing silencing of both NF1 and p53. NF1 loss resulted in increased phosphorylation of Akt (P-Akt); total Akt expression was used as a control. MEF/ikr2^{-/-} cells were infected with the indicated lentivectors. The cell lysate was collected and analyzed by WB. Tubulin detection was used as a loading control. **(C)** Hematoxylin and eosin (H&E) histology and immuno-

fluorescence of sections from either shNF1-shp53- or H-RasV12-shp53-induced glioblastomas in GFAP-Cre mice (HP injected). (i) and (i') show images of the tumors (magnification $\times 20$), in which increased cellularity, vascularity (V), hemorrhage (H), and necrotic areas (N) can be observed. The rest of the panels show all the classical GBM features: necrotic areas [N, (ii) and (ii')]; $\times 40$, perivascular infiltration [indicated by arrows in (iii) and (iii')]; $\times 40$ plus two electrical zoom], and multinucleated giant cells [arrows in (iv) and (iv')]; $\times 40$ plus two electrical zoom]. (v) and (v') show, by immunofluorescence staining, the infiltrative characteristic of the tumor, crossing the midline and migrating to the other hemisphere (blue, DAPI; green, GFP; $\times 5$).

gliomas (fig. S4D). In culture, these cells present all the characteristics of tumor-initiating cells (fig. S6).

We also used a second transgenic model, CamK2a-Cre mice (11), to target mature neurons with our oncogenic lentivectors (figs. S3 and S7). Even though both SynI-Cre and CamK2a-Cre mice were injected using the same virus titer (1×10^9 infectious units), the latter developed tumors with a much longer latency. These results can be explained by the different subtypes of neurons that were targeted when the CamK2a-Cre mice were used, mostly excitatory neurons, which may be more refractory to transformation, in addition to being less numerous in the CTX (11).

In the central nervous system (CNS) of adult mice, constitutive neurogenesis is observed mainly in two regions: the subventricular zone (SVZ) and the subgranular zone (SGZ) of the HP (1, 12). Glial-lineage progenitors have been found in areas outside the classic neurogenic regions, including the optic nerve, striatum, hypothalamus, and subcortical white matter, but in these areas the majority of cells expressing GFAP are mostly differentiated astrocytes (13). For the next series of injections, we elected to use the oncogenic vector H-RasV12-shp53, in which the oncogene is Cre-inducible (limitation with the shNF1-shp53 vector). Furthermore, at the gross histological and transcriptional level, the two oncogenic vectors exhibit similar characteristics (Fig. 1). All transduced GFAP-Cre mice developed tumors when injected either in the HP, SVZ, striatum, or CTX (table S2). When Nestin-Cre mice were injected, tumors were obtained only when the virus was injected in the HP (SGZ) and SVZ but not in the CTX or striatum, because Nestin-expressing neural progenitor/stem cells are infrequent in these locations (4). Similar results were obtained when Sox2-Cre mice were injected in the same locations (table S2). Taking advantage of the GFP reporter in our oncogenic vector, we decided to follow the kinetics of expression of some of these markers during tumor development. Five days after injection of the vector in the CTX of 8-week-old GFAP-Cre mice (Fig. 3A, approximately 60 cells were infected), GFP⁺/RFP⁻ cells were negative for NeuN, Ki67, Nestin, Olig2, and Rip markers but positive for GFAP, suggesting that glial cells were transduced. Using high-resolution large-scale mosaic images (14), we analyzed the expression of GFAP and Nestin markers at 2, 4, and 8 weeks after injection of the oncogenic vector either in the CTX (Fig. 3B) or the HP (fig. S8, A and B) of GFAP-Cre mice. Already at the early stages of cell proliferation (tumor initiation), most of the GFP⁺ cells tended to lose GFAP expression, and as tumor growth progressed, the GFAP expression was progressively diminished (Fig. 3B). On the other hand, Nestin expression that was hardly detectable in the transduced cells 5 days after injection (Fig. 3A) increased significantly as tumors developed (Fig. 3B). Most of the cells that expressed Nestin by 8 weeks after injection also expressed Sox2, another progenitor marker (fig. S8C).

Using qRT-PCR, we observed an increase of more progenitor/stem cell markers (15) as the tumor progressed and the mice succumbed to the disease, as well as diminished expression of differentiation state markers (16) (fig. S9). We

suggest that the mature/differentiated cell initially infected, in the process of transformation, acquires the capacity to dedifferentiate to a cell that has the attributes of a neuroprogenitor cell, which can then not only maintain its pluripotency

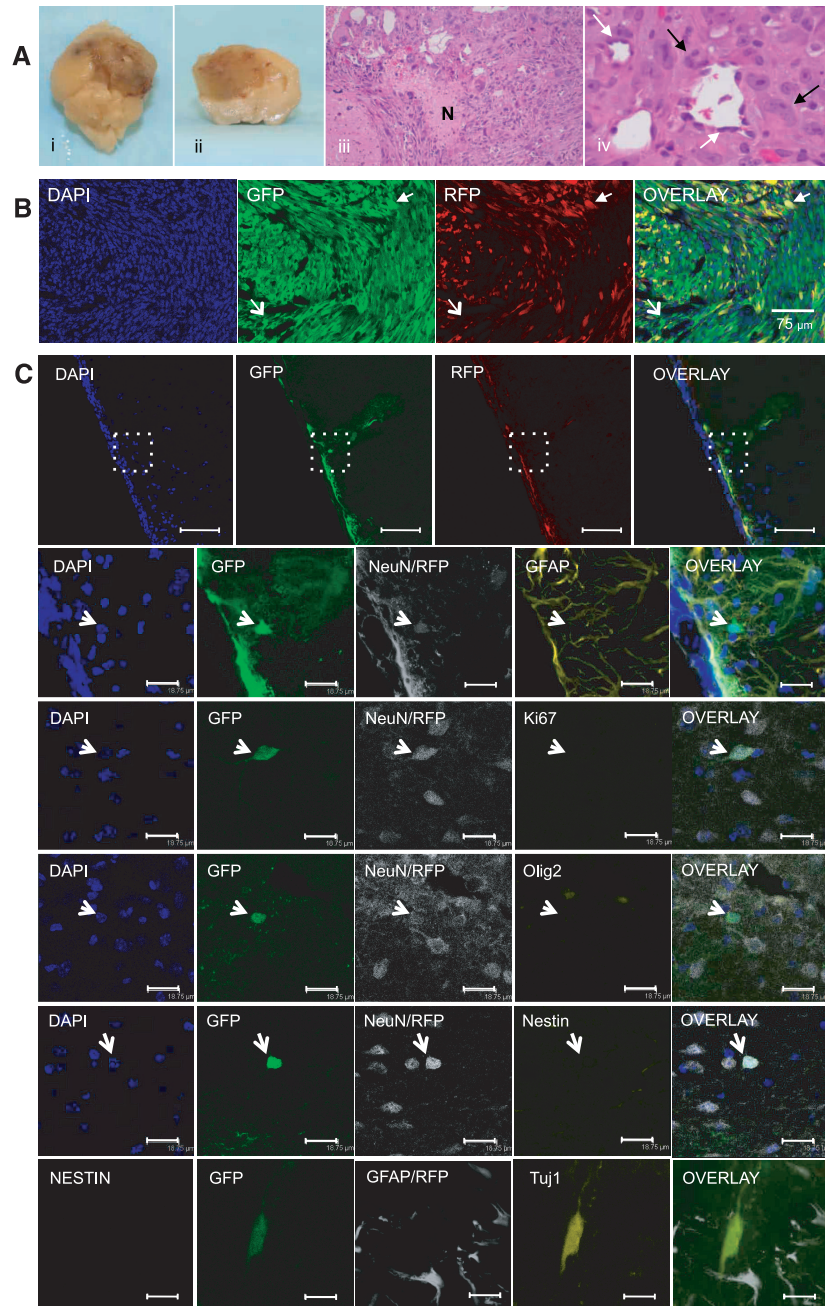


Fig. 2. Induction of gliomas by shNF1-shp53 lentiviral transduction of neurons. (A) Photographs (i) and (ii) showing the massive lesion in the brain and H&E staining of shNF1-shp53-induced tumors in the CTX of SynI-Cre mice [(iii), magnification $\times 40$; (iv), magnification $\times 40$ plus two electrical zoom, showing perivascular infiltration (white arrows) and a multinucleated giant cell (black arrows)]. (B) Confocal images showing the presence of both GFP⁺/RFP⁻ (open arrowhead) and GFP⁺/RFP⁺ cells (solid arrowhead) in the tumor. (C) Confocal images showing oncogene/tumor suppressor expression specifically in NeuN⁺ and Tuj1⁺ cells. Five days after injection of the virus in the CTX of SynI-Cre transgenic mice, brains were collected and fixed. Sections of the brain were stained with the indicated antibodies. The upper panels show representative confocal images of GFP/RFP before antibody staining (scale bar, 75 μ m). The lower panels show representative (arrows) colabeling using the antibodies/markers indicated in each panel. When possible, DAPI staining was also assessed (in blue). Scale bars, 18.75 μ m; N, necrosis.

but also give rise to the heterogeneous cell populations observed in malignant gliomas (2).

To further confirm this hypothesis and support our *in vivo* observations, we established primary cortical astrocytes cultures from GFAP-Cre P11 (postnatal day 11) mice. These cells were characterized by immunofluorescent staining, expressed only bona fide markers of astrocytes (S-100 β , GFAP-positive; Fig. 4A, panels ii to iv), and were Nestin and Sox2-negative (Fig. 4A, panel v). Early-passage GFAP⁺ primary astrocytes (that expressed Cre as shown in Fig. 4A, panel vi, and were Ki67-negative as shown in fig. S5) were transduced *in vitro* with either shNF1-shp53 or H-RasV12-shp53 virus (fig. S10A, see expression of GFP; the efficiency of transduction was usually more than 90%) and transplanted into the brains of NOD-SCID mice (3×10^5 cells per injection). All the transplanted mice developed tumors with clinical and histopathological features (Fig. 4B) that were similar to those observed in the tumors obtained in the lentivirus-induced model (Fig. 1). Confocal microscopy analysis of these tumors revealed that the vast majority of the tumor cells (GFP⁺) express progenitor markers Nestin and Sox2 (fig. S10B), and a few cells express Tuj1 (a neuronal marker) (see arrows in Fig. 4B). These findings further support the idea that terminally differentiated astrocytes can give rise to tumors that are composed of some differentiated neurons, thus providing evidence that these astrocytes

underwent dedifferentiation (or possibly transdifferentiation) during tumorigenesis.

To mimic this dedifferentiation process *in vitro*, we took the shNF1-shp53- or H-RasV12-shp53-infected cortical astrocytes that were generated in media containing serum (under this condition, the cells maintained their astrocyte identity; Fig. 4C, panel i) and transferred them to stem cell media devoid of serum and supplemented with FGF-2. Under these new conditions, the cells started to change morphology, from a more elongated shape to a contracted cytoplasm, and in a time period of approximately 1 week, in the center of each aggregate of cells a small neurosphere-like structure formed and detached from the dish (Fig. 4C, panels ii to iv). These neurospheres, when collected from the supernatant, treated with low-grade trypsin (TrypLE), and cultured back in new dishes, continued to proliferate. These neurospheres showed expression of Nestin and Sox2 (Fig. 4D). Under the same tissue culture conditions, uninfected primary cortical astrocytes never changed their morphology and continued to retain the immunofluorescent markers of fully differentiated astrocytes (fig. S11, A and B). Primary astrocytes infected with a lentivirus containing only the shRNA targeting p53 or expressing only H-RasV12 (fig. S11, C and D) remained astrocytes. Our data support the notion that the co-operation between p53 deficiency and the receptor tyrosine kinase signaling pathway (through Ras activation) are both required for the dedifferen-

tiation of astrocytes during tumorigenesis. Similarly, transduced mature neurons *in vitro*, when switched to NSC media supplemented with FGF-2, followed the same dedifferentiation changes as observed in the experiments described above using astrocytes and also formed neurosphere-like structures (fig. S12).

We performed qRT-PCR analysis to show that the dedifferentiated GFP⁺ NSCs acquired the expression of NSC-specific genes and largely lost the astrocyte-specific genes (fig. S13). These GFP⁺ NSCs also expressed CD133, a marker previously associated with brain cancer stem cells (17) (fig. S14A). These cells also expressed CD15, better known as SSEA1, a glycoprotein usually expressed in embryonic stem cells and commonly used for induced pluripotent stem (iPS) cell characterization (18) (fig. S14A). This was not the only common feature that we found our dedifferentiated GFP⁺ NSCs share with reprogramming of normal iPS cells; the GFP⁺ NSCs also express the transcription factors Sox2, c-myc, and Nanog and have an open, more relaxed chromatin structure (fig. S14, B and C).

Finally, the human relevance of our findings was supported by microarray analysis, which revealed that tumors derived from GFAP-Cre mice injected either in the CTX, HP, or SVZ, as well as tumors derived from SynI-Cre mice injected in the CTX, exhibit a very strong mesenchymal molecular subtype signature, whereas most of the Nestin Cre-derived tumors display a neural

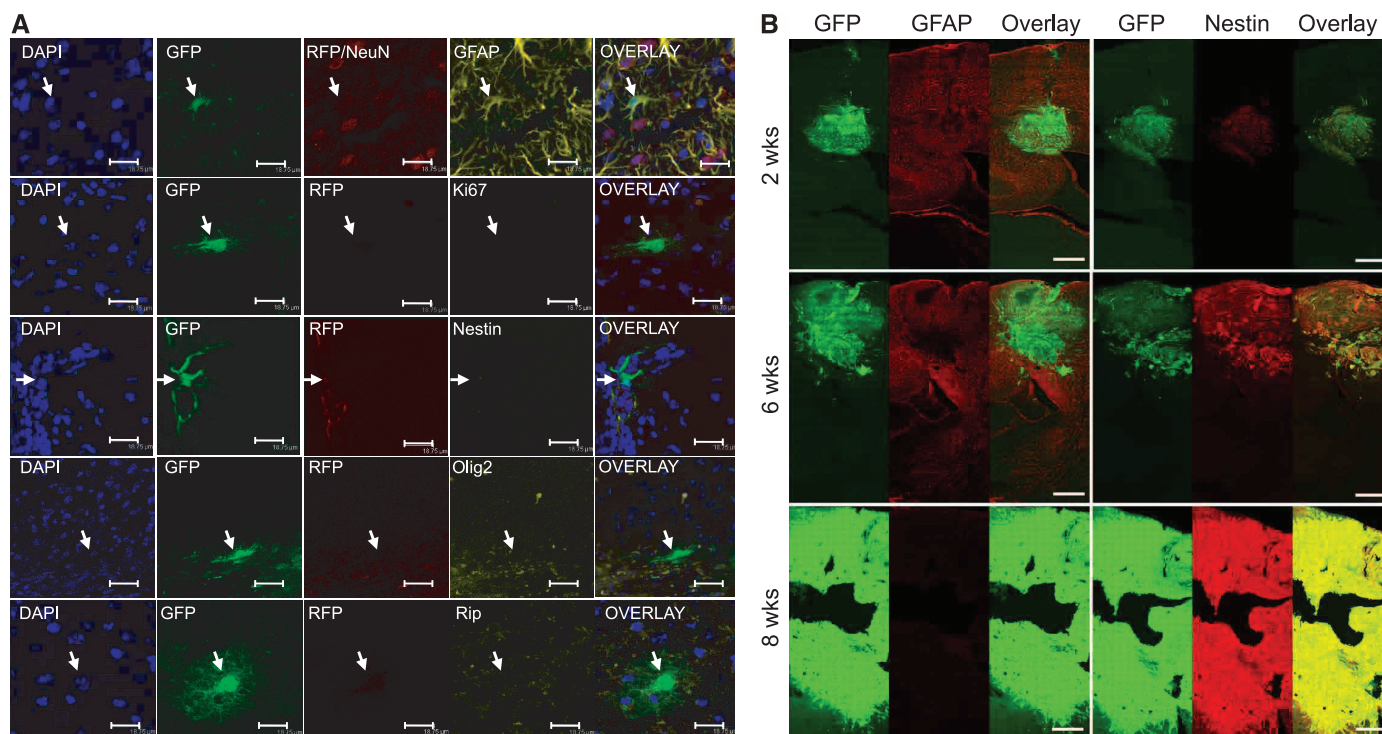


Fig. 3. Tumorigenesis in the CTX. **(A)** Confocal microscopy analysis of brain sections 5 days after injection of H-RasV12-shp53 virus in the CTX of GFAP-Cre mouse. Panels show representative (arrows) colabeling with the markers indicated in each of the images. Scale bars, 18.75 μ m. **(B)** Maximum-intensity

projections of large-scale mosaic volumes. Immunolabeling for GFAP and Nestin in tumors at 2, 6, and 8 weeks after the injection of lentivirus in the CTX is shown. GFAP staining intensity is seen to decrease with tumor progression, whereas Nestin labeling increases. Scale bars, 500 μ m.

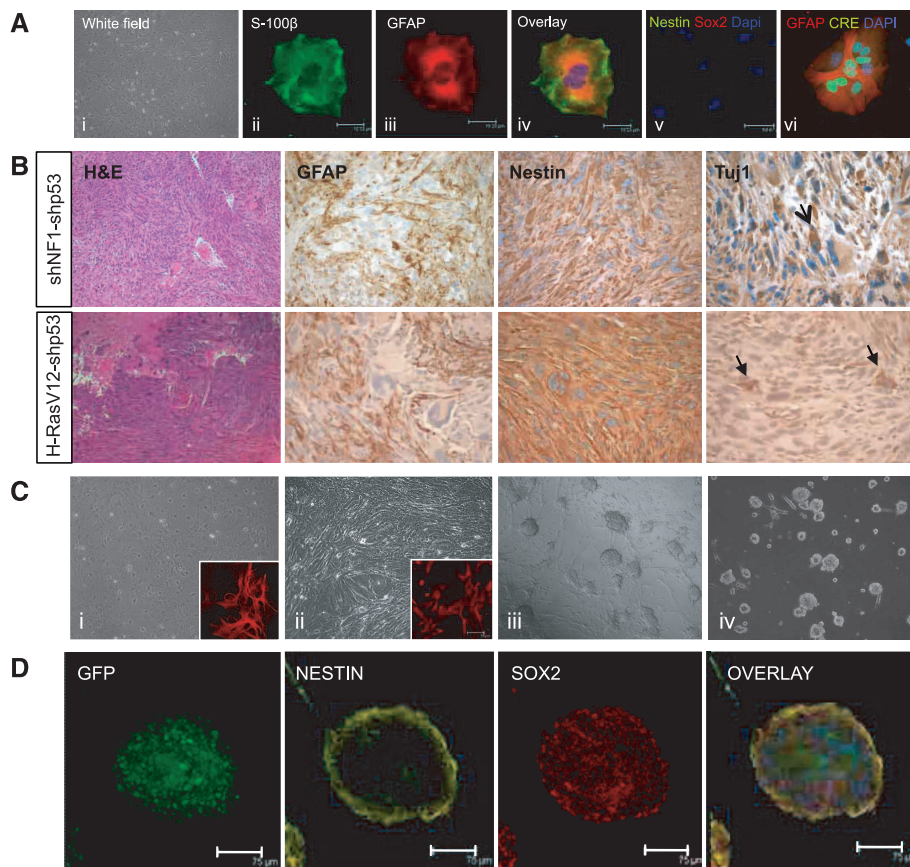


Fig. 4. Mature astrocytes transduced with either shNF1-shp53 or H-RasV12-shp53 virus dedifferentiate to a neural progenitor/stem cell-like state. **(A)** Morphology and staining of cortical astrocytes obtained from GFAP-Cre mice. Confocal microscopy analysis shows double staining for S-100β and GFAP (ii) to (iv), lack of expression of the stem/progenitor markers Nestin and Sox2 (v), and expression of Cre in all GFAP⁺ astrocytes [(vi): red, GFAP; green, Cre; blue, DAPI]. **(B)** Tumors derived from either shNF1-shp53- or H-RasV12-shp53-transduced astrocytes orthotopically transplanted into the HP of NOD-SCID mice; H&E histology and immunohistochemistry. Arrows point to representative Tuj1-positive cells. **(C)** (i) Astrocytes before transduction maintained in media plus serum express GFAP (inset red, GFAP; scale bar, 75 μm). (ii) Transduced astrocytes in media plus serum (inset red, GFAP). (iii) and (iv) Transduced astrocytes transferred to serum-free media supplemented with FGF-2. Light microscopy magnification, ×20. **(D)** Confocal microscopy analysis of the neurospheres described in (C), (iv) [green, GFP (vector); yellow, Nestin; red, Sox2; scale bar, 75 μm].

subclass (fig. S15, A and B, and database S1). These results support our observations that both astrocytic- and neuronal-derived tumors not only have overlapping histopathological features but also share the same molecular signature. Our mouse model of GBM resembles the mesenchymal subtype, which is of high interest to the field, because patients having this classification exhibit worse survival and are more resistant to treatment than the other groups (19–21). The mesenchymal subtype is reminiscent of a transition that has been linked to dedifferentiated and transdifferentiated tumors (22), whereas the neural subtype is most similar to normal brain tissue, and its signature reflects a tendency to the differentiation phenotype (23). Finally, the The Cancer Genome Atlas study has revealed that both mesenchymal and neural subtypes harbor deletions and/or mutations in the NF1 and p53 genes (23), further

supporting our findings that H-RasV12-shp53 tumors are representatives of the shNF1-shp53 tumors. Similar results were obtained when our microarray data were compared to the molecular signature identified by Phillips *et al.* (20) (fig. S15C).

We have shown that both NSCs residing either in the SVZ or HP (e.g., in Nestin-Cre- and Sox2-Cre-injected mice) and mature neurons and astrocytes can be targets of genetic alterations that can lead to gliomagenesis. Although we have not formally shown this using our lentiviral vectors system, it has already been reported that oligodendrocyte progenitor cells can also act as cells of origin for glioma (7, 8). We propose that the genetically altered differentiated cell acquires the capacity to dedifferentiate to a more progenitor (stem cell) state, and that tumor progression probably requires a permissive microenvironment

composed of cell types and molecular signals that can sustain both differentiation of tumor cells and the maintenance of tumor stem-like cells. Our results offer an explanation for the recurrence of gliomas after treatment, because any tumor cell that is not eradicated can continue to proliferate and induce tumor formation, thereby perpetuating the cycle of continuous cell replication to form malignant gliomas.

References and Notes

1. N. Sanai, A. Alvarez-Buylla, M. S. Berger, *N. Engl. J. Med.* **353**, 811 (2005).
2. T. Marumoto *et al.*, *Nat. Med.* **15**, 110 (2009).
3. K. M. Reilly, D. A. Loisel, R. T. Bronson, M. E. McLaughlin, T. Jacks, *Nat. Genet.* **26**, 109 (2000).
4. S. Alcantara Llaguno *et al.*, *Cancer Cell* **15**, 45 (2009).
5. H. Zhu *et al.*, *Proc. Natl. Acad. Sci. U.S.A.* **106**, 2712 (2009).
6. L. M. Chow *et al.*, *Cancer Cell* **19**, 305 (2011).
7. N. Lindberg, M. Kastemar, T. Olofsson, A. Smits, L. Uhrbom, *Oncogene* **28**, 2266 (2009).
8. C. Liu *et al.*, *Cell* **146**, 209 (2011).
9. Y. Zhu *et al.*, *Cancer Cell* **8**, 119 (2005).
10. Y. Zhu *et al.*, *Genes Dev.* **15**, 859 (2001).
11. J. Z. Tsien *et al.*, *Cell* **87**, 1317 (1996).
12. F. H. Gage, *Science* **287**, 1433 (2000).
13. J. Jiao, D. F. Chen, *Stem Cells* **26**, 1221 (2008).
14. D. L. Price *et al.*, *Neuroinformatics* **4**, 65 (2006).
15. T. Hide *et al.*, *Stem Cells* **29**, 590 (2011).
16. J. D. Cahoy *et al.*, *J. Neurosci.* **28**, 264 (2008).
17. A. L. Vescovi, R. Galli, B. A. Reynolds, *Nat. Rev. Cancer* **6**, 425 (2006).
18. T. Brambrink *et al.*, *Cell Stem Cell* **2**, 151 (2008).
19. C. E. Pellowski *et al.*, *Clin. Cancer Res.* **11**, 3326 (2005).
20. H. S. Phillips *et al.*, *Cancer Cell* **9**, 157 (2006).
21. H. Colman *et al.*, *Neuro-oncol.* **12**, 49 (2010).
22. J. P. Thiery, *Nat. Rev. Cancer* **2**, 442 (2002).
23. R. G. Verhaak *et al.*; Cancer Genome Atlas Research Network, *Cancer Cell* **17**, 98 (2010).

Acknowledgments: We thank G. Estepa for her technical help, F. H. Gage and S. Subramaniam for useful discussions, and N. Varki and S. Kesari for pathological analysis. I.M.V. is an American Cancer Society Professor of Molecular Biology and holds the Irwin and Joan Jacobs Chair in Exemplary Life Sciences. D.F.-M. was supported by a fellowship from the European Molecular Biology Organization. This work was supported in part by grants from the National Institutes of Health (NIH) (HL053670), a Cancer Center Core Grant (P30 CA014195-38), Ipsen/Biomeasure, Sanofi Aventis, the H. N. and Frances C. Berger Foundation, and National Center for Research Resources grant 5P41RR004050 to M.H.E. The content is solely the responsibility of the authors and does not necessarily represent the official views of the National Institute of Allergy and Infectious Diseases or NIH. Microarray data have been deposited in the Gene Expression Omnibus (GEO) database (accession no. GSE35917). The authors (T.M., I.M.V., and Y.S.) and the Salk Institute have filed a patent application relating to mouse tumor models created with lentiviral vectors.

Supplementary Materials

www.sciencemag.org/cgi/content/full/science.1226929/DC1
Materials and Methods
Figs. S1 to S15
Tables S1 to S4
References (24–34)
Database S1

20 April 2012; accepted 21 September 2012
Published online 18 October 2012;
10.1126/science.1226929

A Global Pattern of Thermal Adaptation in Marine Phytoplankton

Mridul K. Thomas,^{1,2*†} Colin T. Kremer,^{1,3†} Christopher A. Klausmeier,^{1,3} Elena Litchman^{1,2}

Rising ocean temperatures will alter the productivity and composition of marine phytoplankton communities, thereby affecting global biogeochemical cycles. Predicting the effects of future ocean warming on biogeochemical cycles depends critically on understanding how existing global temperature variation affects phytoplankton. Here we show that variation in phytoplankton temperature optima over 150 degrees of latitude is well explained by a gradient in mean ocean temperature. An eco-evolutionary model predicts a similar relationship, suggesting that this pattern is the result of evolutionary adaptation. Using mechanistic species distribution models, we find that rising temperatures this century will cause poleward shifts in species' thermal niches and a sharp decline in tropical phytoplankton diversity in the absence of an evolutionary response.

Marine phytoplankton are responsible for nearly half of global primary productivity (1). They play essential roles in food webs and global cycles of carbon, nitrogen, phosphorus, and other elements (2, 3). Empirical studies have shown that recent ocean warming has driven changes in productivity (4), population size (5), phenology (6), and community composition (7). Global ocean circulation models predict further temperature-driven reductions in phytoplankton productivity this century, with consequent decreases in marine carbon sequestration (8, 9). The main mechanism that these studies have identified is indirect: Rising temperatures drive an increase in ocean stratification, which in turn leads to a decrease in nutrient supply to surface waters. However, most models do not consider the direct effects of rising temperatures on individual phytoplankton species, which experience sharp declines in growth rate above their optimum temperatures for growth. They may, therefore, underestimate the effects of warming on ecosystems.

To understand how ocean warming will directly affect marine and estuarine phytoplankton, we examined growth responses to temperature in 194 strains belonging to more than 130 species from the major phytoplankton groups (10). Temperature-related traits, such as the optimum temperature for growth and the thermal niche width (the temperature range over which growth rate is positive), are among the most important in ectothermic species, especially given predictions of global warming (11). We estimated these traits from >5000 growth rate measurements, synthesized from 81 papers published between 1935 and 2011. The strains were isolated from 76°N to 75°S, giving us exceptionally broad cover-

age of the latitudinal and temperature gradients (fig. S1).

Growth responses to changes in temperature are characterized by thermal tolerance curves (reaction norms). Two features of these curves are common to all ectotherms: unimodality and negative skewness (i.e., a sharper decline in fitness above the optimum temperature than below) (fig. S2) (11, 12). The latter condition makes ectotherms living at their optimum temperature more sensitive to warming than cooling, with important consequences for their performance in the environment (13). Furthermore, there is an exponential increase in the maximum growth rate attainable with increasing temperature (across species). These curves may be described using three principal traits: maximum growth rate, optimum temperature for growth, and thermal niche width. We estimated these traits for each strain by fitting a thermal tolerance function to the data (14) and examined their relationships with environmental and taxonomic covariates (10).

Our analysis revealed large-scale patterns in thermal traits. First, strains exhibited a clear

latitudinal trend in the optimum temperature for growth [Fig. 1, coefficient of determination (R^2) = 0.55, $P < 0.0001$], demonstrating the existence of a global pattern in a key microbial trait. Second, optimum temperature was even more strongly related to mean annual temperature at the isolation location (Fig. 2A, $R^2 = 0.69$, $P < 0.0001$), suggesting that temperature is a major selective agent and that adaptation to local environmental conditions occurs in marine microbes despite the potential for long-distance dispersal through ocean currents. In contrast, the width of the thermal niche was unrelated to temperature regimes. Third, strains from polar and temperate waters had optimum temperatures that were considerably higher than their mean annual temperatures, whereas tropical strains had optima closer to or lower than the mean temperatures (Fig. 2A). Finally, variation in optimum temperature and niche width was not explained by taxonomic differences above the level of genus, indicating that thermal adaptation is not highly phylogenetically constrained in this group (tables S1 and S2).

This strong trait-environment relationship suggests that microbes are adapted to the temperatures that they experience locally. However, this pattern could also occur through a correlated response to selection on other traits. To test whether the observed pattern arose as an adaptive response to variable thermal regimes, we used an eco-evolutionary model (15, 16) to predict the optimum temperatures that maximize fitness at each isolation location. The model allows us to study the effects of thermal adaptation alone by forcing all other aspects of strains to be identical. Purely theoretical applications of such eco-evolutionary models have been extensive, but they have rarely been compared to quantitative field data (17).

In the model, strains differ only in their thermal tolerance curves (characterized by their optimum temperature) while competing for a single

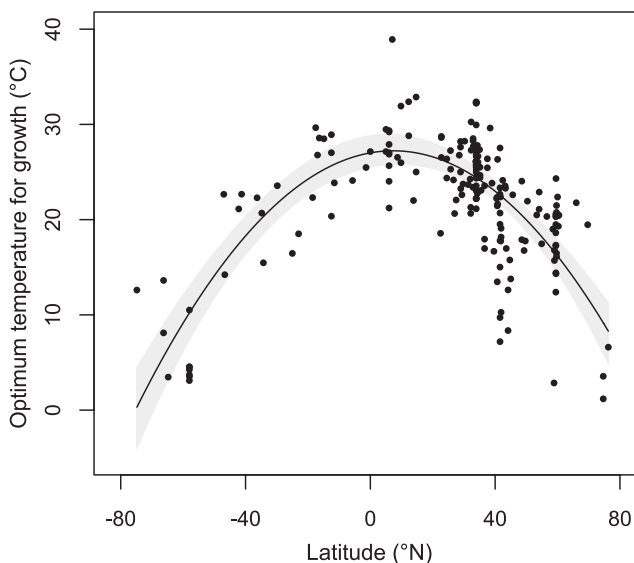


Fig. 1. Latitudinal gradient in the optimum temperature for growth of marine and estuarine phytoplankton strains ($n = 194$ strains, $R^2 = 0.55$, $P < 0.0001$). Each point represents the optimum temperature for growth of a single strain, estimated by fitting a thermal tolerance function (14) to the data. The regression line (black) is shown, along with 95% confidence bands (gray). Confidence bands account for asymmetric uncertainty in trait estimates using a bootstrapping algorithm (10, see also fig. S9).

¹W. K. Kellogg Biological Station, Michigan State University, Hickory Corners, MI 49060, USA. ²Department of Zoology, Michigan State University, East Lansing, MI 48824, USA. ³Department of Plant Biology, Michigan State University, East Lansing, MI 48824, USA.

*To whom correspondence should be addressed. E-mail: thomasmr@msu.edu

†These authors contributed equally to this work.

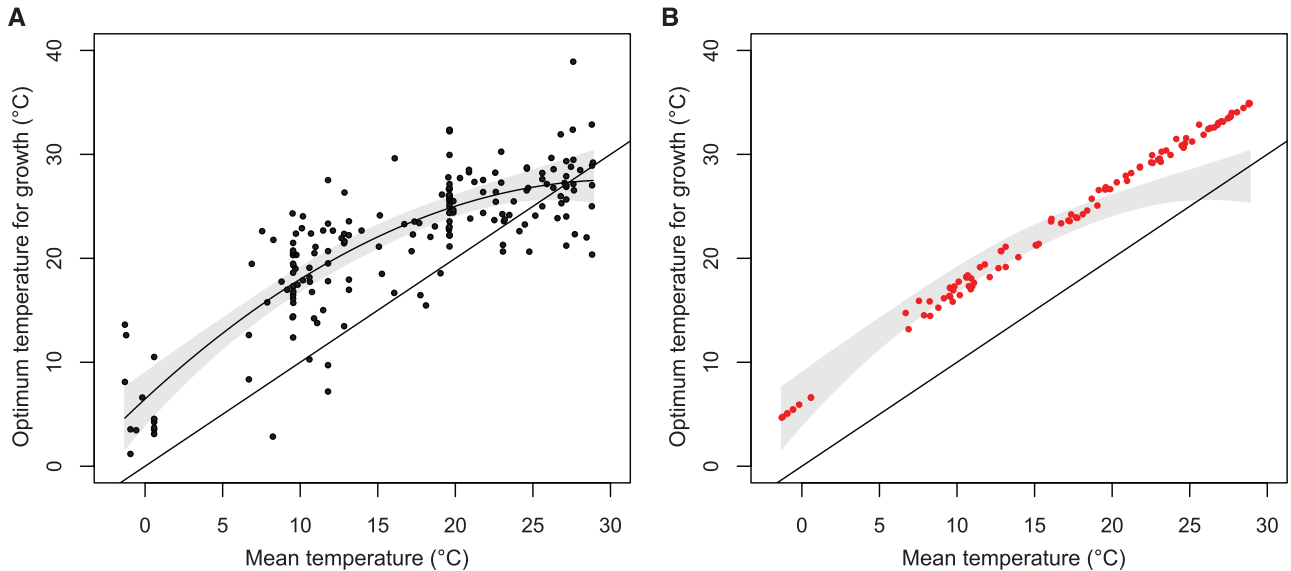


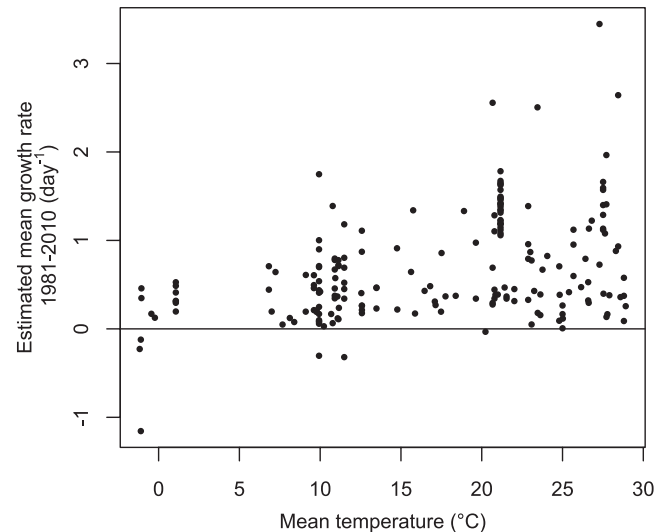
Fig. 2. Optimum temperatures for growth across a gradient of ocean temperature. **(A)** The optimum temperature of phytoplankton strains is well explained by variation in the mean annual temperature at their isolation locations ($n = 194$, $R^2 = 0.69$, $P < 0.0001$), indicating adaptation to local environmental conditions. The 1:1 line (black, straight), regression line (black, curved) and 95% confidence bands (gray) from bootstrapping are shown (10). The regression line shown is for

the best model (table S4), which posits a quadratic relationship between mean temperature and optimum temperatures. **(B)** The eco-evolutionary model predicts evolutionarily stable optimum temperatures (red points) for each isolation location that are several degrees higher than the mean environmental temperatures (i.e., above the black line) and agree well with the data, except in the warmest waters. The confidence band from (A) is shown in gray for comparison.

nutrient. The growth rates of all strains are bounded by an exponential function that increases with temperature, an empirical relationship known as the Eppley curve (12). We require that each individual strain's thermal tolerance curve touch the Eppley curve at a single point, forcing maximum growth rate to become a function of optimum temperature. Niche widths are held constant across strains, because we found no significant relationship in our data set between niche width and environmental or taxonomic covariates (tables S1 and S2). Given these constraints, we allow optimum temperatures of a set of strains to evolve in response to deterministic temperature regimes. These regimes were based on model fits to a 30-year sea surface temperature time series at every isolation location (10, 18). For each environment, we used an evolutionary algorithm based on quantitative genetics to identify evolutionarily stable states (ESSs) (10, 16). At an ESS, the strains that persist (defined by their traits) cannot be invaded by any other strain. These temperature optima serve as a theoretical prediction of the best strategy (or strategies) at each isolation location, which we can then compare to our data as a test of thermal adaptation.

Our eco-evolutionary model predicts that optimum temperatures should increase with mean temperature and exceed it by several degrees (Fig. 2B and fig. S3). This is in agreement with the observed pattern (Fig. 2A) and bolsters the case that this relationship arises from adaptation to mean temperature. However, in regions with the highest mean temperatures (the tropics), the model predicts optima that are significantly higher than those observed. Although

Fig. 3. Estimated mean daily growth rates of all strains at their isolation locations, between 1980 and 2010. These estimates were based on monthly temperature records (19) and each strain's thermal tolerance curve, and depend on the assumption that growth is limited solely by temperature. Even warm-water strains have mean growth rates exceeding zero (the horizontal line), indicating that they are capable of persisting in their environment, although their optima are below what our model predicts to be most adaptive.



this discrepancy suggests that tropical strains may be less well-adapted to their environmental temperatures, we estimated that these strains are capable of persistence under the temperature regimes they experience (Figs. 2B and 3) (19). The difference may be a result of interactions between temperature and other factors, constraints on thermal adaptation at high temperatures, or adaptation to laboratory temperatures before measurement. Examining model predictions across a range of assumed niche widths reveals that wider niches lead to larger differences between predicted optima and the mean annual temperatures and to a decrease in the number of coexisting strains (fig. S3). These re-

sults illustrate that temperature variation can support species coexistence, although it cannot fully explain the levels of trait diversity observed in the data.

Phytoplankton strains may be adapted to their current conditions, but could be negatively affected by warming oceans. Moving from the eco-evolutionary model to purely physiological mechanistic species distribution models (SDMs), we then examined whether changing environmental temperatures could alter species ranges and global diversity patterns. These models use physiological trait measurements to predict species abundances across environmental gradients (20) but do not account for species interactions or

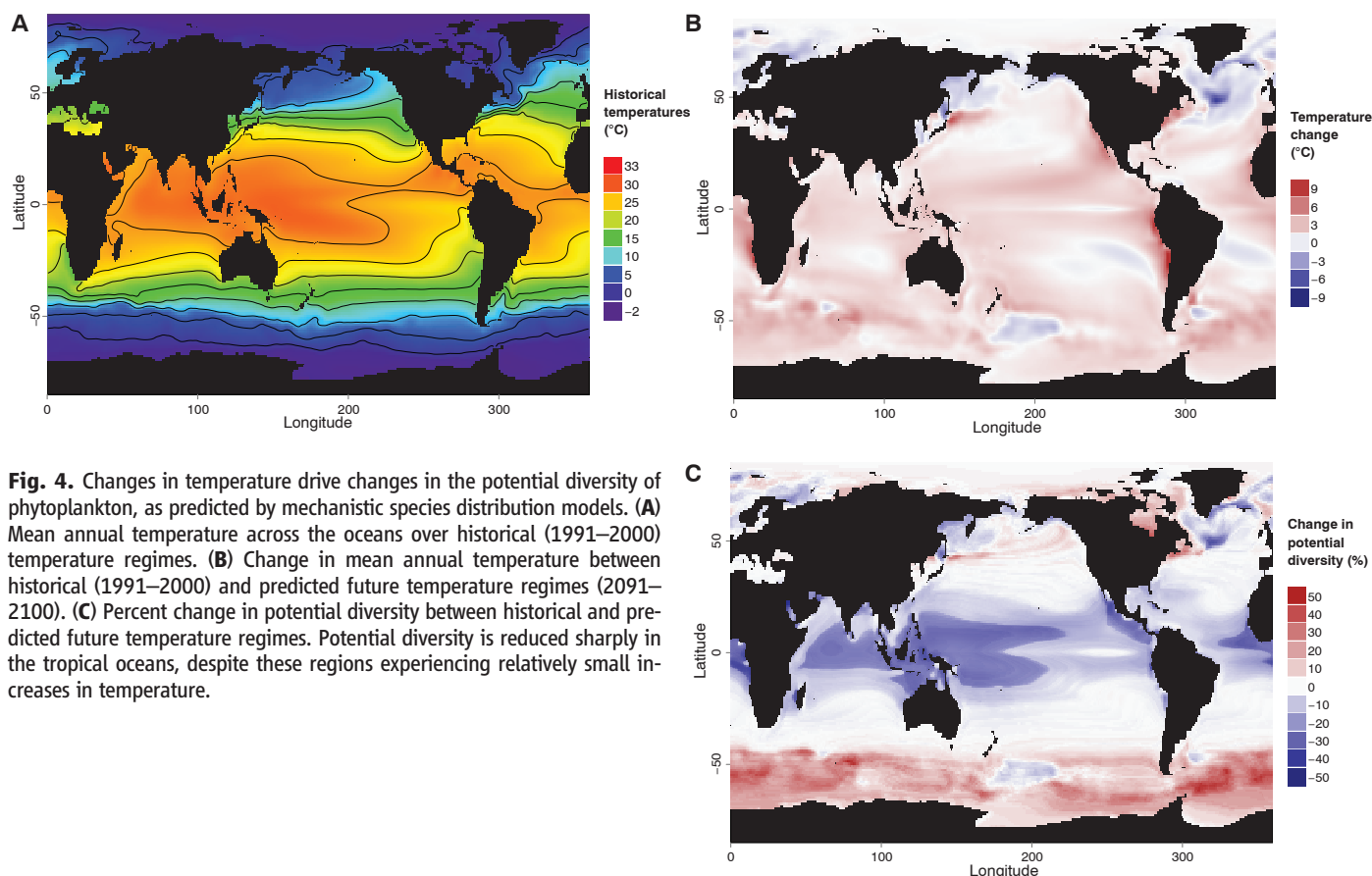


Fig. 4. Changes in temperature drive changes in the potential diversity of phytoplankton, as predicted by mechanistic species distribution models. (A) Mean annual temperature across the oceans over historical (1991–2000) temperature regimes. (B) Change in mean annual temperature between historical (1991–2000) and predicted future temperature regimes (2091–2100). (C) Percent change in potential diversity between historical and predicted future temperature regimes. Potential diversity is reduced sharply in the tropical oceans, despite these regions experiencing relatively small increases in temperature.

evolution. We generated growth rate predictions across the ocean for each strain represented in our data set, based on their thermal tolerance curves and a 10-year temperature time series (10). If the 10-year mean growth rate of a strain was positive at a location, the location was deemed to fall within its range. We repeated this using both historical (1991–2000) and future (2091–2100) temperature regimes, the latter having been predicted by a global climate model (10, 19, 21–23). These estimates indicate that ocean warming is likely to drive poleward shifts in strains' equatorial boundaries, although polar range boundaries remain approximately constant (fig. S4). Consequently, many strains are predicted to experience a reduction in range size (figs. S5, S6, and S12), potentially increasing extinction probabilities. Our SDMs assume that growth rates are limited solely by temperature, but other factors, such as nutrient availability, could also be incorporated if relevant trait data were available.

When the range shifts of all strains are considered in the aggregate, they can be used to predict global patterns of phytoplankton diversity change as a result of ocean warming (Fig. 4) (24). In order to do this, we calculated "potential diversity," defined as the number of phytoplankton strains (out of the 194 in our data set) theoretically capable of growing at a location, assuming that temperature is the sole limiting factor (figs. S7 and S8). A comparison of potential diversity

patterns under both historical and future temperature regimes shows that temperature change may drive a large reduction in tropical phytoplankton diversity over the course of this century. Approximately one-third of contemporary tropical strains are unlikely to persist there in 2100 (Fig. 4C), despite a change in mean temperature of only $\sim 2^\circ\text{C}$ (Fig. 4, A and B). High latitudes may experience small increases in potential diversity, as a result of poleward shifts in strain ranges. Rising temperatures have the strongest effect on tropical strains, because tropical optima are close to current mean temperatures (Fig. 2A) and thermal tolerance curves are negatively skewed. Small increases in temperature can therefore lead to sharp declines in growth rate. A decrease in diversity is likely to have a strong impact on tropical ecosystems, because biodiversity loss is a major cause of ecosystem change (25). One possible consequence is a decrease in tropical primary productivity, which could occur through two distinct mechanisms: the loss of highly productive species or a decrease in complementarity (26, 27).

Our findings lend support to the hypothesis that tropical communities are most vulnerable to increases in temperature (28). However, the existence of high genetic diversity within species, as has been noted in some cases (29), may prevent the loss of entire species. Adaptation to changing temperatures may mitigate some of the predicted

losses in diversity, particularly in rapidly reproducing taxa such as phytoplankton. The evolution of thermal tolerance has been examined in a few taxa, including phytoplankton (30–32), but we currently lack the information necessary to accurately model the consequences of evolutionary change on ecosystem processes (33, 34). In the case of phytoplankton, we need estimates of rates of adaptation to high temperature stress in a variety of taxa, as well as an examination of the evolutionary constraints and trade-offs that may be associated with this. Characterizing these constraints will allow us to make improved forecasts of species survival and may prove critical for understanding the fate of tropical communities and oceanic ecosystems.

References and Notes

1. C. B. Field, M. J. Behrenfeld, J. T. Randerson, P. G. Falkowski, *Science* **281**, 237 (1998).
2. A. C. Redfield, *Am. Sci.* **46**, 205 (1958).
3. P. G. Falkowski, R. T. Barber, V. Smetacek, *Science* **281**, 200 (1998).
4. M. J. Behrenfeld *et al.*, *Nature* **444**, 752 (2006).
5. D. G. Boyce, M. R. Lewis, B. Worm, *Nature* **466**, 591 (2010).
6. M. Edwards, A. J. Richardson, *Nature* **430**, 881 (2004).
7. X. A. G. Morán, Á. López-Urrutia, A. Calvo-Díaz, W. K. W. Li, *Glob. Change Biol.* **16**, 1137 (2010).
8. L. Bopp *et al.*, *Global Biogeochem. Cycles* **15**, 81 (2001).
9. M. Steinacher *et al.*, *Biogeosciences* **7**, 979 (2010).
10. Materials and methods are available as supplementary materials on Science Online.

11. J. G. Kingsolver, *Am. Nat.* **174**, 755 (2009).
12. R. W. Eppley, *Fish Bull.* **70**, 1063 (1972).
13. T. L. Martin, R. B. Huey, *Am. Nat.* **171**, E102 (2008).
14. J. Norberg, *Limnol. Oceanogr.* **49**, 1269 (2004).
15. S. A. H. Geritz, É. Kisdi, G. Meszéna, J. A. J. Metz, *Evol. Ecol.* **12**, 35 (1997).
16. P. A. Abrams, *Ecol. Lett.* **4**, 166 (2001).
17. J. C. Stegen, R. Ferriere, B. J. Enquist, *Proc. Biol. Sci.* **279**, 1051 (2011).
18. R. W. Reynolds *et al.*, *J. Clim.* **20**, 5473 (2007).
19. R. W. Reynolds, N. A. Rayner, T. M. Smith, D. C. Stokes, W. Wang, *J. Clim.* **15**, 1609 (2002).
20. M. R. Kearney, W. Porter, *Ecol. Lett.* **12**, 334 (2009).
21. Intergovernmental Panel on Climate Change (IPCC), *Climate Change 2007: The Physical Science Basis. Contribution of Working Group I to the Fourth Assessment Report of the Intergovernmental Panel on Climate Change*, S. Solomon *et al.*, Eds. (Cambridge Univ. Press, Cambridge, 2007).
22. N. Nakicenović *et al.*, *Special Report on Emissions Scenarios: A Special Report of Working Group III of the Intergovernmental Panel on Climate Change*, N. Nakicenović, R. Swart, Eds. (Cambridge Univ. Press, Cambridge, 2000); www.osti.gov/energycitations/product.biblio.jsp?osti_id=15009867.
23. T. Delworth *et al.*, *J. Clim.* **19**, 643 (2006).
24. D. W. McKenney, J. H. Pedlar, K. Lawrence, K. Campbell, M. F. Hutchinson, *Bioscience* **57**, 939 (2007).
25. D. U. Hooper *et al.*, *Nature* **486**, 105 (2012).
26. D. Tilman, D. Wedin, J. Knops, *Nature* **379**, 718 (1996).
27. P. B. Reich *et al.*, *Science* **336**, 589 (2012).
28. C. A. Deutsch *et al.*, *Proc. Natl. Acad. Sci. U.S.A.* **105**, 6668 (2008).
29. K. Hårnström, M. Ellegaard, T. J. Andersen, A. Godhe, *Proc. Natl. Acad. Sci. U.S.A.* **108**, 4252 (2011).
30. A. F. Bennett, R. E. Lenski, in *In the Light of Evolution. Volume 1. Adaptation and Complex Design*, J. C. Avise, F. J. Ayala, Eds. (National Academies Press, Washington, DC, 2007), pp. 225–238.
31. J. L. Knies, R. Izem, K. L. Supler, J. G. Kingsolver, C. L. Burch, *PLoS Biol.* **4**, e201 (2006).
32. I. E. Huertas, M. Rouco, V. López-Rodas, E. Costas, *Proc. Biol. Sci.* **278**, 3534 (2011).
33. S. L. Chown *et al.*, *Clim. Res.* **43**, 3 (2010).
34. M. J. Angilletta Jr., R. S. Wilson, C. A. Navas, R. S. James, *Trends Ecol. Evol.* **18**, 234 (2003).

Acknowledgments: This research was supported by NSF (grants DEB-0845932, DEB-0845825, and OCE-0928819), including the BEACON Center for the Study of Evolution in Action (grant DBI-0939454) and a Graduate Research

Fellowship to C.T.K., as well as a grant from the James S. McDonnell Foundation. K. Edwards and N. Swenson provided statistical advice, and J. Lennon, G. Mittelbach, and E. Miller provided comments on the manuscript. The trait data presented are shown in table S5, and the collated growth rate data are in table S6. Also thanks to NOAA/OAR/ESRL PSD, Boulder, CO, USA, for NOAA_OI_SST_V2 data provided at their Web site, www.esrl.noaa.gov/psd/. This is W. K. Kellogg Biological Station contribution number 1694. E.L. and M.K.T. conceived the original idea; M.K.T. collected the growth-temperature data; M.K.T. and C.T.K. analyzed the data; C.T.K. and C.A.K. developed and C.T.K. analyzed the eco-evolutionary model; M.K.T. and C.T.K. ran the mechanistic species distribution models; and M.K.T., C.T.K., and E.L. wrote and C.A.K. commented on the manuscript.

Supplementary Materials

www.sciencemag.org/cgi/content/full/science.1224836/DC1

Materials and Methods

Figs. S1 to S12

Tables S1 to S6

References (35–135)

17 May 2012; accepted 10 October 2012

Published online 25 October 2012;

10.1126/science.1224836

Decoding Human Cytomegalovirus

Noam Stern-Ginossar,¹ Ben Weisburd,¹ Annette Michalski,^{2*} Vu Thuy Khanh Le,³ Marco Y. Hein,² Sheng-Xiong Huang,⁴ Ming Ma,⁴ Ben Shen,^{4,5,6} Shu-Bing Qian,⁷ Hartmut Hengel,³ Matthias Mann,² Nicholas T. Ingolia,^{1†} Jonathan S. Weissman^{1*}

The human cytomegalovirus (HCMV) genome was sequenced 20 years ago. However, like those of other complex viruses, our understanding of its protein coding potential is far from complete. We used ribosome profiling and transcript analysis to experimentally define the HCMV translation products and follow their temporal expression. We identified hundreds of previously unidentified open reading frames and confirmed a fraction by means of mass spectrometry. We found that regulated use of alternative transcript start sites plays a broad role in enabling tight temporal control of HCMV protein expression and allowing multiple distinct polypeptides to be generated from a single genomic locus. Our results reveal an unanticipated complexity to the HCMV coding capacity and illustrate the role of regulated changes in transcript start sites in generating this complexity.

The herpesvirus human cytomegalovirus (HCMV) infects the majority of humanity, leading to severe disease in newborns and immunocompromised adults (1). The HCMV genome is ~240 kb with estimates of between 165 and 252 open reading frames (ORFs) (2, 3). These annotations likely do not capture the complexity of the HCMV proteome (4) because HCMV

has a complex transcriptome (5, 6), and genomic regions studied in detail reveal noncanonical translational events, including regulatory (7) and overlapping ORFs (8–11). Defining the full set of translation products—both stable and unstable, the latter with potential regulatory/antigenic function (12)—is critical for understanding HCMV.

To identify the range of HCMV-translated ORFs and monitor their temporal expression, we infected human foreskin fibroblasts (HFFs) with the clinical HCMV strain Merlin and harvested cells at 5, 24, and 72 hours after infection using four approaches to generate libraries of ribosome-protected mRNA fragments (Fig. 1A and table S1). The first two measured the overall in vivo distribution of ribosomes on a given message; infected cells were either pretreated with the translation elongation inhibitor cycloheximide or, to exclude drug artifacts, lysed without drug pretreatment (no-drug). Additionally, cells were pretreated with harringtonine or lactimidomycin (LTM), two drugs with distinct mechanisms, which lead to strong accumulation of ribosomes at translation initiation sites and depletion of ribosomes over the body of the message (Fig. 1A) (13–15). A modi-

fied RNA sequencing protocol allowed quantification of RNA levels as well as identification of 5' transcript ends by generating a strong overrepresentation of fragments that start at the 5' end of messages (fig. S1) (16).

The ability of these approaches to provide a comprehensive view of gene organization is illustrated for the UL25 ORF: A single transcript start site is found upstream of the ORF (Fig. 1A, mRNA panel). Harringtonine and LTM mark a single translation initiation site at the first AUG downstream of the transcript start (Fig. 1A, Harr and LTM). Ribosome density accumulates over the ORF body ending at the first in-frame stop codon (Fig. 1A, CHX and no-drug). In the no-drug sample, excess ribosome density accumulates at the stop codon (Fig. 1A, no-drug) (14).

Examination of the full range of HCMV translation products, as reflected by the ribosome footprints, revealed many putative previously unidentified ORFs: internal ORFs lying within existing ORFs either in-frame, resulting in N-terminally truncated translation products (Fig. 1B), or out of frame, resulting in entirely previously unknown polypeptides (Fig. 1C); short uORFs (upstream ORFs) lying upstream of canonical ORFs (Fig. 2A); ORFs within transcripts antisense to canonical ORFs (Fig. 2B); and previously unidentified short ORFs encoded by distinct transcripts (Fig. 2C). For all of these categories, we also observed ORFs starting at near-cognate codons (codons differing from AUG by one nucleotide), especially CUG (Fig. 2D).

HCMV expresses several long RNAs lacking canonical ORFs, including $\beta 2.7$, an abundant RNA, which inhibits apoptosis (17). In agreement with $\beta 2.7$'s observed polysome association (18), multiple short ORFs are translated from this RNA (Fig. 2E and fig. S2), and the corresponding proteins for two of these ORFs were detected by means of high-resolution MS (Fig. 2E). Although the translation efficiency

¹Department of Cellular and Molecular Pharmacology, Howard Hughes Medical Institute, University of California, San Francisco, San Francisco, CA 94158, USA. ²Department of Proteomics and Signal Transduction, Max Planck Institute of Biochemistry, Martinsried D-82152, Germany. ³Institut für Virologie, Heinrich-Heine-Universität Düsseldorf, 40225 Düsseldorf, Germany. ⁴Department of Chemistry, Scripps Research Institute, 130 Scripps Way #3A2, Jupiter, FL 33458, USA. ⁵Department of Molecular Therapeutics, Scripps Research Institute, 130 Scripps Way #3A2, Jupiter, FL 33458, USA. ⁶Natural Products Library Initiative at The Scripps Research Institute, Scripps Research Institute, 130 Scripps Way #3A2, Jupiter, FL 33458, USA. ⁷Division of Nutritional Sciences, Cornell University, Ithaca, NY 14853, USA.

*To whom correspondence should be addressed. E-mail: michalsk@biochem.mpg.de (A.M.); weissman@cmp.ucsf.edu (J.S.W.)

†Present address: Department of Embryology, Carnegie Institute for Science, Baltimore, MD 21218, USA.

of these ORFs is low, four of them are highly conserved across HCMV strains (table S2). We found three similar polycistronic coding RNAs (including RNA1.2 and RNA4.9), and two short proteins encoded by these RNAs were confirmed with MS (fig. S3).

To define systematically the HCMV-translated ORFs using the ribosome profiling data, we first annotated HCMV splice junctions, identifying 88 splice sites (table S3). We then exploited the harringtonine-induced accumulation of ribosomes at translation start sites so as to identify ORFs using a support vector machine (SVM)-based machine learning strategy (14, 19). We observed a strong enrichment for AUG (33-fold) and near cognate codons in the translation initiation sites identified with this analysis (Fig. 3A). Visual inspection of the ribosome profiling data

confirmed the SVM-identified ORFs and suggested an additional 53 putative ORFs (table S4). The large majority (86%) of the SVM-identified ORFs, and all of the manually identified ones, were identified by means of SVM analysis of an independent biological replicate (table S5 and fig. S4). The observed initiation sites were not caused by harringtonine because LTM treatment also induced ribosome accumulation at the vast majority (>98%) of these positions (Fig. 3B).

In total, we identified 751 translated ORFs that were supported by both the LTM and harringtonine data (tables S5 and S6 and file S1). The footprint density measurements for these ORFs were reproducible between biological replicates (figs. S5 and S6). Of these ORFs, 147 were previously suggested to be coding (Fig. 3C). We did not find strong evidence of translation for 24

previously annotated ORFs (table S7), although these proteins may well be expressed under different conditions.

Many newly identified ORFs are very short (245 ORFs ≤ 20 codons) (Fig. 3C) and are found upstream of longer ORFs. We also identified 239 short ORFs (21 to 80 codons) (Fig. 3D). Last, we identified 120 ORFs that are longer than 80 amino acids. These are primarily ORFs that contain splice junctions or alternative 5' ends of previous annotations.

Several lines of evidence support the validity of the ORFs we identified. First, as seen for the previously annotated ORFs, newly identified ORFs showed a significant [$P < 10^{-70}$; Kolmogorov-Smirnov (K-S) test] excess of ribosome footprints at the predicted stop codon (Fig. 1A and fig. S7). Because our ORF predictions

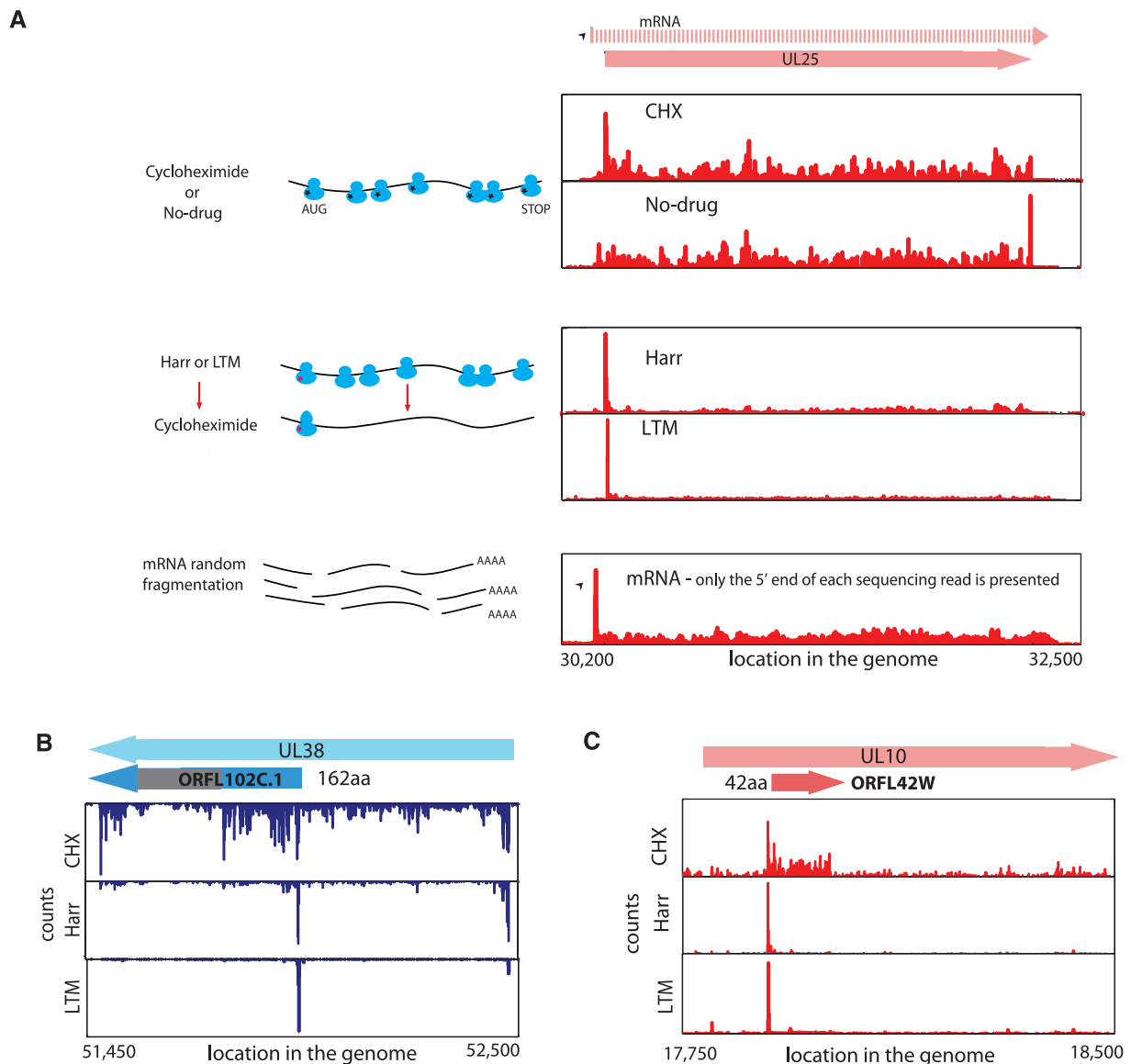


Fig. 1. Ribosome profiling of HCMV-infected cells. **(A)** Ribosome occupancies after various treatments (illustrated to left); cycloheximide (CHX), no-drug, harringtonine (Harr), and LTM together with mRNA profiles of the UL25 gene

at 72 hours after infection. An arrow marks the mRNA start. **(B and C)** Ribosome occupancy profiles for **(B)** UL38 and **(C)** UL10 genes that contain internal initiations. The gray area symbolizes a low-complexity region.

were based on translation initiation sites found in the harringtonine and LTM samples, the observation that these accurately predicted downstream stop codons in an untreated sample provides independent support for our approach. Second, ribosome-protected footprints displayed a 3-nucleotide (nt) periodicity that was in phase with the predicted start site both globally (Fig. 3E) and in specific ORFs that contain internal

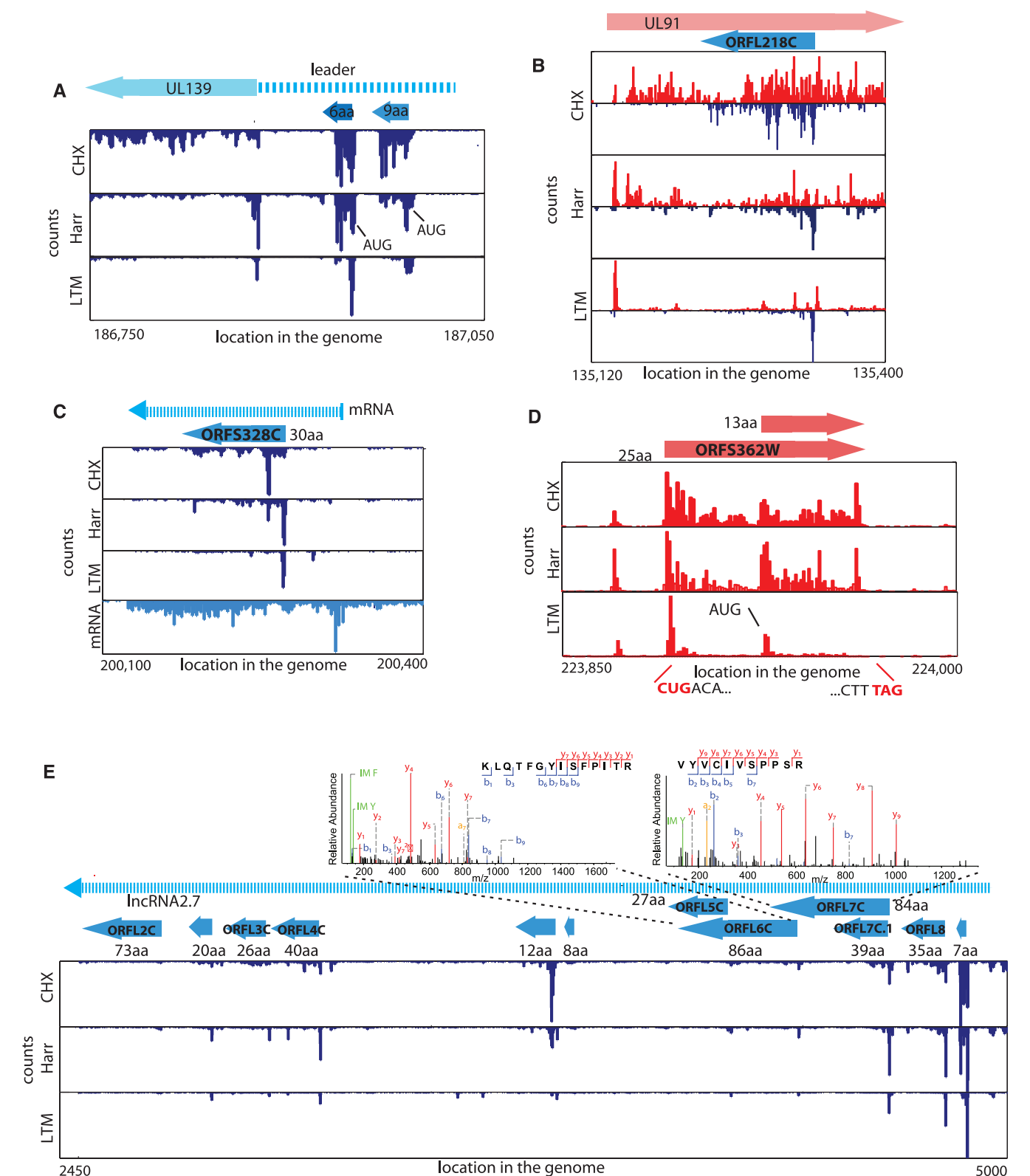


Fig. 2. Many ribosome footprints do not correspond to previously annotated ORFs. (A) Ribosome occupancy profiles for the leader region of UL139 gene. (B) Ribosome occupancy profiles of plus and minus strands (red and blue, respectively) for the UL91 gene. (C) mRNA and ribosome occupancy profiles for a previously unidentified short ORF. (D) Ribosome occupancies around a short ORF that initiates at a CUG codon. (E) Ribosome occupancy profiles for RNA β2.7. (Top) The annotated MS/MS spectra of two distinct peptides originating from ORF6C and ORF7C.

out-of-frame ORFs (fig. S8). Third, brief inhibition of translation initiation using an eIF4A inhibitor Pateamine A (20) led to depletion of ribosome density from the body of the large majority of the predicted ORFs (fig. S9), indicating that the ribosomes were engaged in active elongation. The newly identified ORFs also exhibited a distribution of expression levels similar to that of previously annotated canonical ORFs (fig. S10). Last, many of the newly identified ORFs are conserved in other HCMV strains (table S2).

High-resolution tandem mass spectrometric measurements on virally infected cells by using stringent criteria and manual validation (files S2 and S3) (16, 21) unambiguously detected 53 previously unidentified proteins out of the 96 genomic loci that are not overlapping with annotated ORFs and contain at least one specific previously unidentified protein that is longer than 55 amino acids (table S8). For classes of new ORFs that were difficult to monitor with MS (truncated forms of longer proteins or short proteins), we used a tagging approach. For two N-terminally truncated proteins (derived from UL16 and UL38), we confirmed the appearance of alternative shorter transcripts and detected the expected full length and truncated tagged protein products (fig. S11).

The truncated protein derived from UL16 was also observed in the context of the native virus (fig. S12), and we confirmed a splice variant of UL138 by using an antibody (fig. S12). For five short ORFs (including two initiated at near cognate start sites), we fused the ORFs in frame to a green fluorescent protein (GFP)-coding region in their otherwise native transcript context. We identified protein products of the expected sizes and confirmed that we correctly identified the translation start sites (fig. S13). We also showed that one of these short proteins (US33A-57aa), which was not identified with MS but was recently predicted by means of transcript analysis to be coding (6), is expressed in the context of the native virus (Fig. 3F and fig. S12). Additionally, we focused on the very short, near cognate driven uORFs that lie directly upstream of UL119 and US9, whose inclusion changes during infection as a result of changes in the 5' end of the transcripts. We found that these uORFs modulated the translation efficiency of a downstream reporter gene (fig. S14).

Last, we examined the subcellular localization for 18 newly identified ORFs (11 of which were detected by means of mass spectrometry) (table S9) using transient expression of GFP-

tagged proteins. We detected 15 proteins, 10 of which showed specific subcellular localization patterns: six in mitochondria, three in the endoplasmic reticulum (ER), and one in the nucleus (Fig. 3G and fig. S15). Immunoprecipitation and MS experiments on two of these GFP-tagged proteins, ORF359W (ER localized) and US33A (mitochondrially localized), identified a few specific interacting proteins. Western blot analysis confirmed the interactions with TAP1 (ORF359W) and the mitochondrial inner membrane transport TIM machinery (US33A) (fig. S16).

HCMV genes are expressed in a temporally regulated cascade. Our data provides an opportunity to monitor viral protein translation throughout infection. Most of the viral genes, including newly identified ORFs, showed tight temporal regulation of protein synthesis levels; 82% of ORFs varied by at least fivefold. Hierarchical clustering of viral coding regions by their footprint densities during infection (a measure of the relative translation rates) revealed several distinct temporal expression patterns (fig. S17).

As was seen previously for a limited number of genomic loci (8–11, 22), examination of viral transcripts during infection revealed a pervasive use of alternative 5' ends that is critical to the

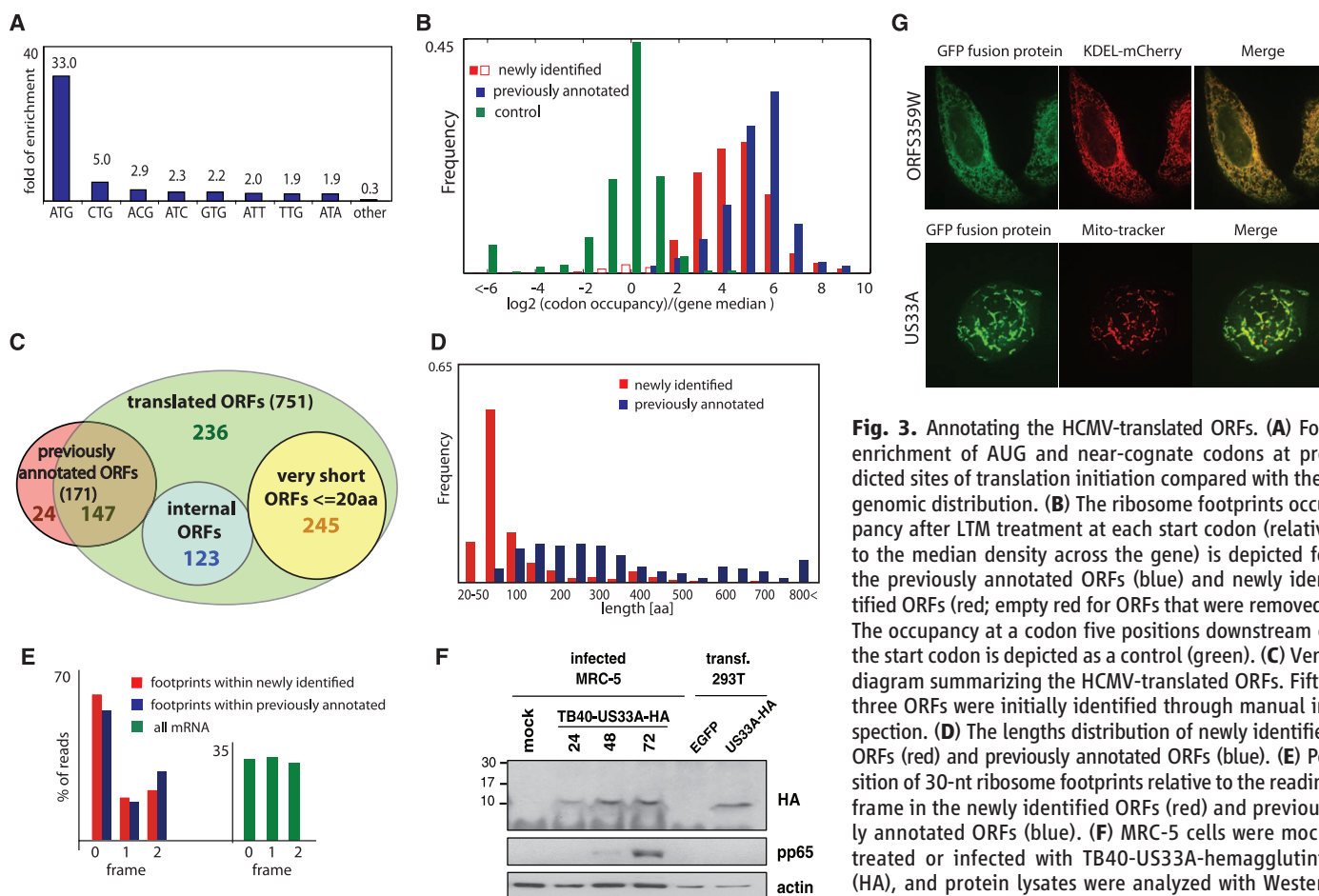


Fig. 3. Annotating the HCMV-translated ORFs. **(A)** Fold enrichment of AUG and near-cognate codons at predicted sites of translation initiation compared with their genomic distribution. **(B)** The ribosome footprints occupancy after LTM treatment at each start codon (relative to the median density across the gene) is depicted for the previously annotated ORFs (blue) and newly identified ORFs (red); empty red for ORFs that were removed. The occupancy at a codon five positions downstream of the start codon is depicted as a control (green). **(C)** Venn diagram summarizing the HCMV-translated ORFs. Fifty-three ORFs were initially identified through manual inspection. **(D)** The lengths distribution of newly identified ORFs (red) and previously annotated ORFs (blue). **(E)** Position of 30-nt ribosome footprints relative to the reading frame in the newly identified ORFs (red) and previously annotated ORFs (blue). **(F)** MRC-5 cells were mock-treated or infected with TB40-US33A-hemagglutinin (HA), and protein lysates were analyzed with Western blotting with indicated antibodies. **(G)** HeLa cells were

transfected with GFP fusion proteins together with an ER marker (KDEL-mCherry) or stained with MitoTracker Red (Invitrogen, Grand Island) and imaged by means of confocal microscopy.

tight temporal regulation of viral genes expression and production of alternate protein products during infection. For example, at the US18-US20 locus, 5 hours after infection there is one main transcript starting just upstream of US20 enabling US20 translation. At 24 hours after infection, a shorter version of the transcript is detected starting immediately upstream of US18, enabling its translation. A third previously unknown transcript isoform starting within the US18 coding sequence emerges at 72 hours after infection, resulting in translation of a truncated version of US18 (ORFS346C.1) at this time point (Fig. 4, A and B). Another example is detailed in fig. S18, and we identified reproducible temporal regulation of

5' ends in 61 viral loci (encompassing ~350 ORFs) (figs. S19 and S20 and table S10), six of which we confirmed with Northern blot analysis (Fig. 4B and figs. S11 and S21). Thus, our studies reveal a pervasive mode of viral gene regulation in which dynamic changes in 5' ends of transcripts control protein expression from overlapping coding regions. Just as alternative splicing (a process in which a single gene codes for multiple proteins) expands protein diversity, alternative transcript start sites may provide a broadly used mechanism for generating complex proteomes.

The genomic era began with the sequencing of the bacterial DNA virus, phi X, in 1977 (23) and the mammalian DNA virus, Simian virus 40

(24), the following year. Since then, extraordinary advances in sequencing technology have enabled the determination of a vast array of viral genomes. Deciphering their protein coding potential, however, remains challenging. Here, we present an experimentally based analysis of translation of a complex DNA virus, HCMV, by using both next-generation sequencing and high-resolution proteomics. It is possible that many of the short ORFs we have identified are rapidly degraded and do not act as functional polypeptides. Nonetheless, these could still have regulatory function or be an important part of the immunological repertoire of the virus as major histocompatibility complex (MHC) class I bound peptides are

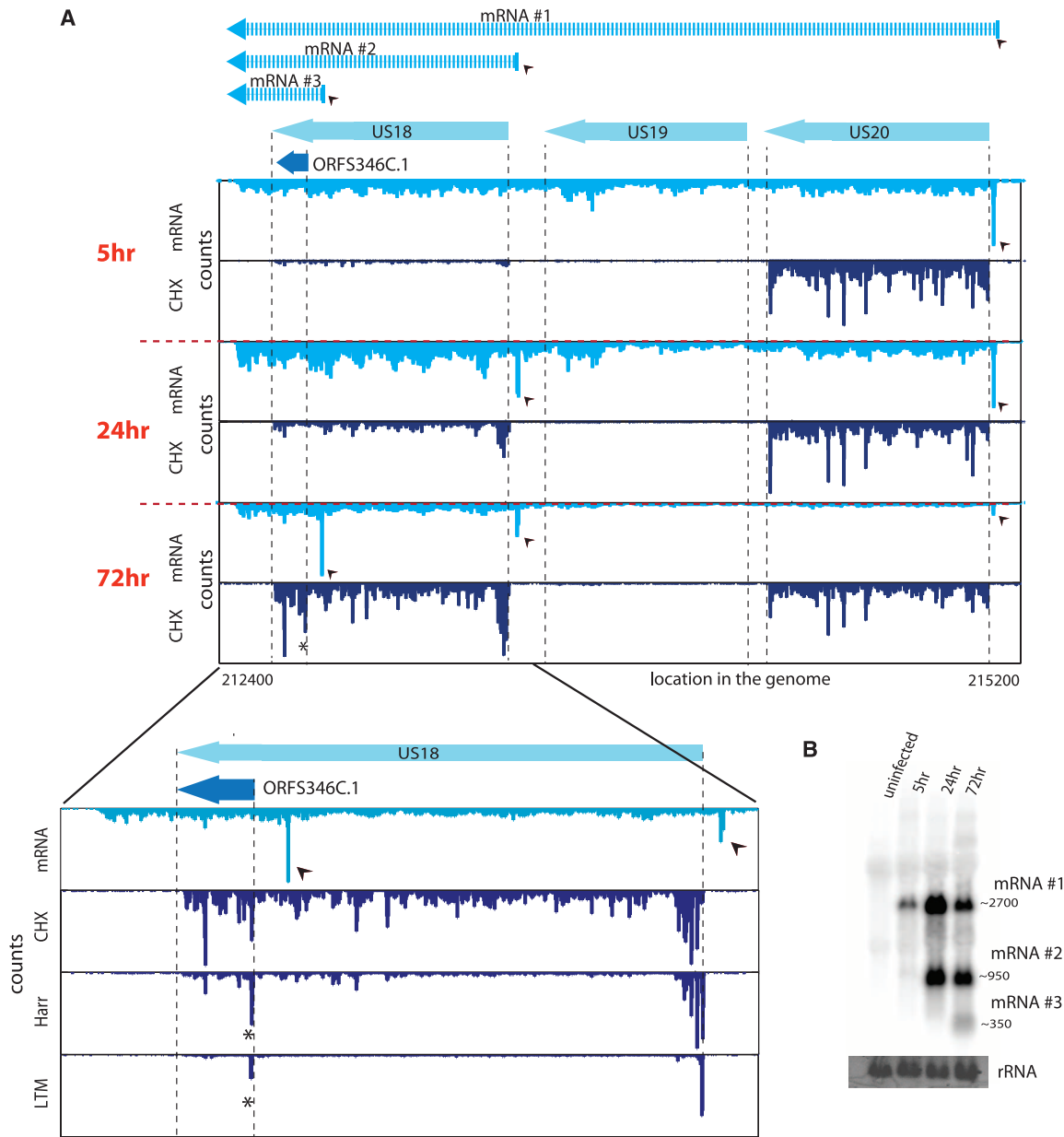


Fig. 4. A major source of ORFs' diversity during infection originates from alternative transcripts starts. **(A)** The mRNA and ribosome occupancy profiles around US18 to US20 loci at different infection times (marked left). Small arrows denote the different mRNA starts, and (top) the corresponding mRNAs

are illustrated. (Bottom) An expanded view of the US18 locus at 72 hours after infection and includes the harringtonine and LTM profiles (asterisks indicate the internal initiation). **(B)** Total RNA extracted at different time points during infection was subjected to Northern blotting for ORFS346C.1.

generated at higher efficiency from rapidly degraded polypeptides (25). Our work yields a framework for studying HCMV by establishing the viral proteome and its temporal regulation, providing a context for mutational studies and revealing the full range of HCMV functional and antigenic potential.

References and Notes

1. E. S. Mocarski, T. Shenk, R. F. Pass, in *Fields Virology*, B. N. Fields, D. M. Knipe, P. M. Howley, Eds. (Lippincott, Williams & Wilkins, Philadelphia, PA, 2007), pp. 2701–2772.
2. A. J. Davison *et al.*, *J. Gen. Virol.* **84**, 17 (2003).
3. E. Murphy, I. Rigoutsos, T. Shibuya, T. E. Shenk, *Proc. Natl. Acad. Sci. U.S.A.* **100**, 13585 (2003).
4. E. Murphy, T. Shenk, *Curr. Top. Microbiol. Immunol.* **325**, 1 (2008).
5. G. J. Zhang *et al.*, *J. Virol.* **81**, 11267 (2007).
6. D. Gatherer *et al.*, *Proc. Natl. Acad. Sci. U.S.A.* **108**, 19755 (2011).
7. J. Cao, A. P. Geballe, *Mol. Cell. Biol.* **16**, 7109 (1996).
8. T. Stamminger *et al.*, *J. Virol.* **76**, 4836 (2002).
9. B. J. Biegalka, E. Lester, A. Branda, R. Rana, *J. Virol.* **78**, 9579 (2004).
10. Z. Qian, B. Xuan, T. T. Hong, D. Yu, *J. Virol.* **82**, 3452 (2008).
11. L. Grainger *et al.*, *J. Virol.* **84**, 9472 (2010).
12. S. R. Starck *et al.*, *Science* **336**, 1719 (2012).
13. F. Robert *et al.*, *PLoS ONE* **4**, e5428 (2009).
14. N. T. Ingolia, L. F. Lareau, J. S. Weissman, *Cell* **147**, 789 (2011).
15. S. Lee *et al.*, *Proc. Natl. Acad. Sci. U.S.A.* **109**, 2424 (2012).
16. Materials and methods are available as supplementary materials on Science Online.
17. M. B. Reeves, A. A. Davies, B. P. McSharry, G. W. Wilkinson, J. H. Sinclair, *Science* **316**, 1345 (2007).
18. P. C. Lord, C. B. Rothschild, R. T. DeRose, B. A. Kilpatrick, *J. Gen. Virol.* **70**, 2383 (1989).
19. T. Joachim, in *Making Large Scale SVM Learning Practical*, B. Schölkopf, C. J. C. Burges, A. J. Smola, Eds. (MIT Press, Cambridge, MA, 1998), pp. 169–184.
20. M. E. Bordeleau *et al.*, *Chem. Biol.* **13**, 1287 (2006).
21. J. Cox *et al.*, *J. Proteome Res.* **10**, 1794 (2011).
22. F. S. Leach, E. S. Mocarski, *J. Virol.* **63**, 1783 (1989).
23. F. Sanger, S. Nicklen, A. R. Coulson, *Proc. Natl. Acad. Sci. U.S.A.* **74**, 5463 (1977).
24. W. Fiers *et al.*, *Nature* **273**, 113 (1978).
25. J. W. Yewdell, *Curr. Opin. Immunol.* **19**, 79 (2007).

Acknowledgments: We thank O. Mandelboim, D. Wolf, M. Trilling, A. Laurant, S. Karniely, and Weissman lab members for critical reading of the manuscript; C. Chu for assistance with sequencing; and J. Pelletier for providing Pateamine A. N.S.-G. is supported by a human frontier science program postdoctoral fellowship. This work was supported by the Howard Hughes Medical Institute (J.S.W.) and the Max Planck Society (M.M.). The Gene Expression Omnibus accession number for the data is GSE41605.

Supplementary Materials

www.sciencemag.org/cgi/content/full/338/6110/1088/DC1
Materials and Methods
Figs. S1 to S22
Tables S1 to S10
Files S1 to S3

25 July 2012; accepted 12 October 2012
10.1126/science.1227919

Egg Cell–Secreted EC1 Triggers Sperm Cell Activation During Double Fertilization

Stefanie Sprunck,^{1*} Svenja Rademacher,^{1†} Frank Vogler,¹ Jacqueline Gheyselinck,^{2‡} Ueli Grossniklaus,² Thomas Dresselhaus¹

Double fertilization is the defining characteristic of flowering plants. However, the molecular mechanisms regulating the fusion of one sperm with the egg and the second sperm with the central cell are largely unknown. We show that gamete interactions in *Arabidopsis* depend on small cysteine-rich EC1 (EGG CELL 1) proteins accumulating in storage vesicles of the egg cell. Upon sperm arrival, EC1-containing vesicles are exocytosed. The sperm endomembrane system responds to exogenously applied EC1 peptides by redistributing the potential gamete fusogen HAP2/GCS1 (HAPLESS 2/GENERATIVE CELL SPECIFIC 1) to the cell surface. Furthermore, fertilization studies with *ec1* quintuple mutants show that successful male-female gamete interactions are necessary to prevent multiple-sperm cell delivery. Our findings provide evidence that mutual gamete activation, regulated exocytosis, and sperm plasma membrane modifications govern flowering plant gamete interactions.

Sexual reproduction depends on the successful union of two gametes of opposite sex at fertilization. In flowering plants such as *Arabidopsis thaliana*, sexual reproduction is distinct in that two gamete fusion events take place in a coordinated manner, a phenomenon termed “double fertilization” (1). Two nonmotile sperm cells are delivered by a

pollen tube into the female gametophyte (embryo sac) that harbors two dimorphic female gametes (Fig. 1A). One sperm fuses with the egg cell, giving rise to the embryo, whereas the second sperm cell fuses with the central cell to develop the triploid endosperm. Although this distinct mode of reproduction was discovered more than a century ago (2, 3) and recent live-cell imaging has shed some light on the behavior of *Arabidopsis* sperm nuclei during double fertilization (4), almost nothing is known about the molecules mediating gamete interactions. To date, the evolutionary conserved HAP2 (HAPLESS 2)/GCS1 (GENERATIVE CELL SPECIFIC 1) is the only sperm protein known to be essential at a late step in gamete interactions (5, 6), and its role as a fusogen is strongly supported by the observation that HAP2-deficient gametes of *Chlamydomonas* and *Plasmodium berghei* are able to adhere but fail to fuse (7).

Based on a transcriptomics approach that uses isolated egg cells of wheat (8), we discovered a family of *Arabidopsis* genes with sequence similarity to the largest wheat egg cell-specific transcript cluster, termed EC-1 (Egg Cell 1) (see supplementary materials and methods). We found transcripts of the five *Arabidopsis* EC1-like genes (*EC1.1*, *EC1.2*, *EC1.3*, *EC1.4*, and *EC1.5*) only in female reproductive tissues (Fig. 1B). Egg cell-specificity of EC1 was shown by expressing the β -glucuronidase (GUS) reporter under control of individual EC1 promoters (Fig. 1, C and D) and by in situ hybridization to tissue sections. Transcripts of EC1 genes are specifically present in the egg cell (Fig. 1, E to G) but are not detectable early after fertilization (Fig. 1H and fig. S1B), whereas GUS remains active in zygotes and early embryos (fig. S1, D to F).

EC1 proteins belong to the large and unexplored group of ECA1 (Early Culture Abundant 1) gametogenesis-related cysteine-rich proteins characterized by their conserved cysteine-spacing signature (9). Within 118 ECA1 proteins of *Arabidopsis*, the EC1 family forms a distinct subclade (fig. S2A). Notably, we identified EC1-like genes or transcripts only in flowering plant species, including the basal angiosperm *Amborella trichopoda*, and not in gymnosperms, ferns (*Adiantum* sp.), Bryophytes (*Physcomitrella patens*), or green algae (*Volvox* sp.; *Chlamydomonas* sp.). Protein-sequence analyses revealed common features of EC1 proteins, such as a predicted N-terminal signal peptide for secretion and a similar predicted intramolecular disulfide bond arrangement (Fig. 2A). Two conserved signature sequences, termed S1 and S2, were identified by multiple sequence alignments with representatives from monocots, dicots, and basal angiosperms (fig. S2B).

To investigate the subcellular localization of EC1, we stably expressed a translational fusion of EC1.1 and the green fluorescent protein (GFP) under control of the *EC1.1* promoter. The

¹Cell Biology and Plant Biochemistry, Biochemie-Zentrum Regensburg, University of Regensburg, Universitätsstrasse 31, D-93053 Regensburg, Germany. ²Institute of Plant Biology and Zürich-Basel Plant Science Center, University of Zürich, Zollikerstrasse 107, CH-8008 Zürich, Switzerland.

*To whom correspondence should be addressed. E-mail: stefanie.sprunck@biologie.uni-regensburg.de

†Present address: Plant Breeding Center of Life and Food Sciences Weihenstephan, Technische Universität München, Emil-Ramann-Strasse 4, D-85354 Freising, Germany.

‡Present address: Département de Biologie Moléculaire Végétale, Université de Lausanne, Biophore 4403, CH-1015 Lausanne, Switzerland.

calculated molecular mass of the EC1.1-GFP fusion, excluding the leader peptide, corresponds to its size in anti-GFP Western blots (Fig. 2B),

arguing against posttranslational proteolytic processing of EC1. We found EC1-GFP to accumulate in spherical vesicle-like structures within the

unfertilized egg cell, but never as extracellular signal (Fig. 2, C to E, and fig. S3). To study EC1-GFP localization during the short-lived event of double

Fig. 1. The *EC1* gene family is specifically expressed in the egg cell. (A) Schematic of an *Arabidopsis* ovule harboring the haploid generation, termed “female gametophyte” (dashed line), which comprises two female gametes (egg cell and central cell) and two accessory cell types (synergids and antipodal cells). (B) Reverse transcription polymerase chain reaction (RT-PCR) detects *EC1* transcripts only in female reproductive tissues. (C and D) Egg cell-specific β -glucuronidase (GUS) reporter activity, driven by the *EC1.1* (C) and *EC1.2* (D) promoters. (E to H) Expression pattern of *EC1* as detected by in situ hybridization on ovules. *EC1* transcripts are present only in egg cells (E to G) but not in zygotes (H). ap, antipodal cells; as, antisense RNA; cc, central cell; ec, egg cell; fert., fertilized; fg, female gametophyte; syn, synergid cell; zyg, zygote; -, water control; +, genomic DNA. Scale bars, 20 μ m.

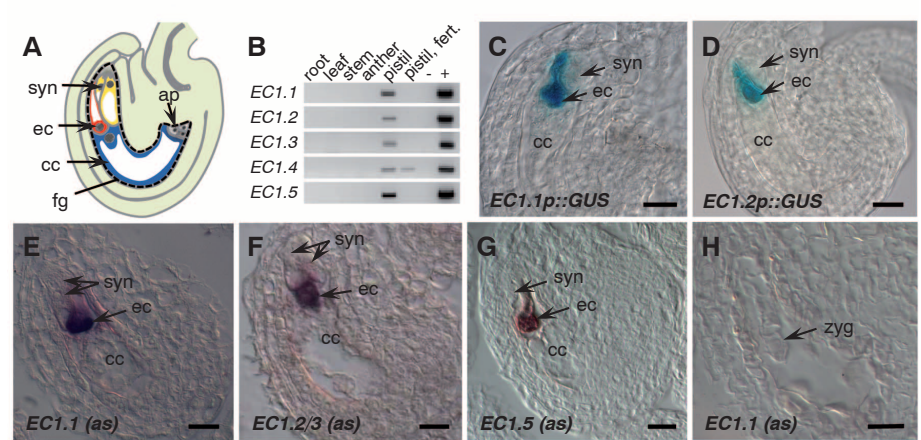
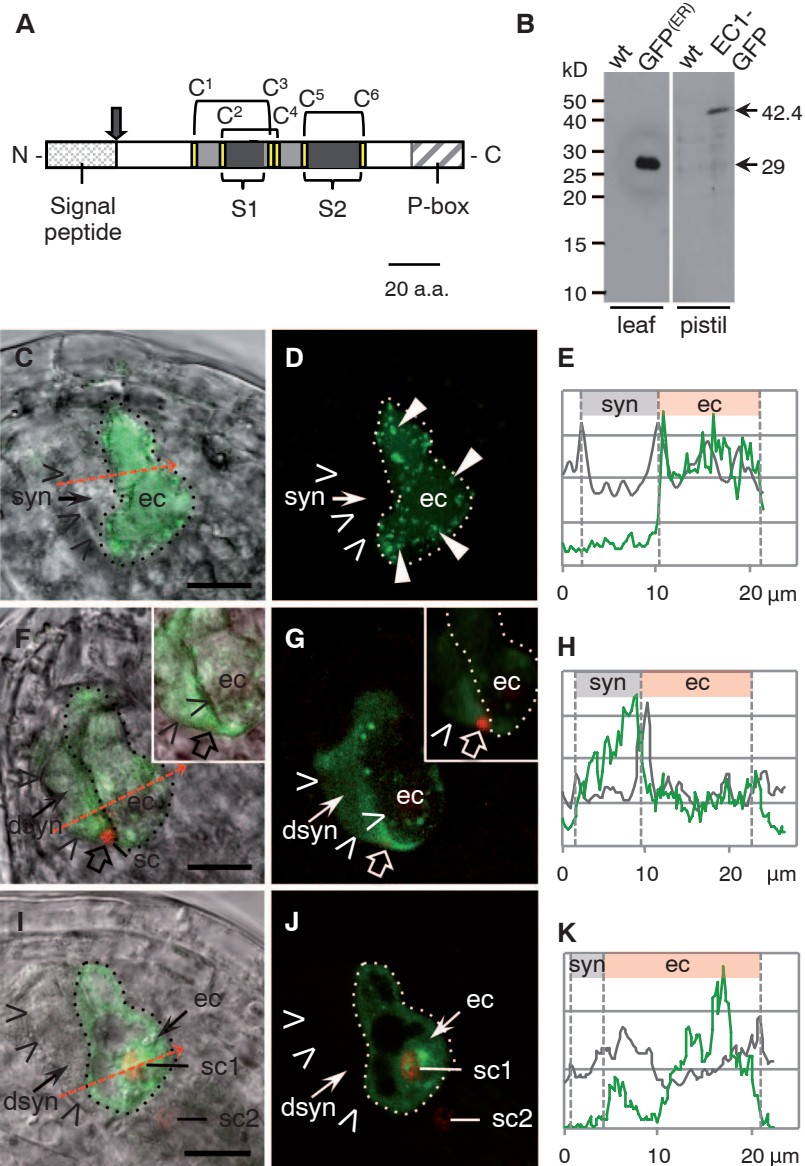


Fig. 2. Triggered secretion of small cysteine-rich EC1 proteins. (A) Schematic of EC1 precursor protein. Predicted N-terminal signal peptide cleavage site (arrow). Prolines at the C terminus (P-box), two signature motifs (S1 and S2), and a conserved cysteine-spacing signature (C¹ to C⁶) forming three predicted disulfide bonds (black lines) are shown. (B) Western blot showing the 42.4-kD EC1-GFP fusion in a pistil protein extract, compared with endoplasmic reticulum-localized GFP (29 kD) from leaves. (C to H) EC1-GFP is secreted upon sperm cell arrival. Merged bright-field and fluorescence images at a single z plane (C, F, and I) and corresponding fluorescence images (D, G, and J) are shown together with plot profiles of relative signal intensities (E, H, and K) detected along a line drawn across one synergid cell and the egg cell (red arrows in C, F, and I). *x* axis, distances (in micrometers) along the drawn line; *y* axis, relative signal intensities of GFP (green) and reciprocal grayscale values [1/bright field; gray]. Dashed lines denote the position of cell borders. (C to E) EC1-GFP signals are visible as vesicle-like structures (solid arrowheads) in the cytoplasm of unfertilized egg cells but not outside the egg cell. (F to H) EC1-GFP is detected extracellularly when the sperm cells (red nuclei) reach the gamete fusion sites (open arrows). Insets in (F) and (G) represent different focal planes. One sperm nucleus is out of focus. (I to K) Control. Egg cell-expressed cytoplasmic ARO1-GFP is not detected extracellularly during gamete interactions. dsyn, degenerating synergid; sc, sperm cell. Dotted lines delimit egg cell borders; open arrowheads point at synergid cell borders. Scale bars, 10 μ m. See figs. S3 and S4 and movies S1 and S2 for additional data.



fertilization, we used a red fluorescent marker for sperm nuclei (10). Upon sperm cell arrival in the female gametophyte and during double fertilization, EC1-GFP signals are detected extracellularly, especially in the apical region of the degenerating synergid cell (Fig. 2G), which is where gamete fusions will take place (4, 11). Quantification of GFP fluorescence in the egg cell and the flanking synergid cell during gamete interaction and fusion revealed that signal intensities are gradually increasing toward the egg cell membrane (Fig. 2H and fig. S4), indicating regulated exocytosis of EC1-GFP by the egg cell during gamete interactions. By contrast, extracellular GFP signals were never observed in control egg cells expressing a GFP fusion of ARO1 (ARMADILLO REPEAT-ONLY 1) (Fig. 2K and fig. S4), a cytoplasmic and endomembrane-associated gametophyte-specific Armadillo repeat protein found to be essential for polar pollen tube growth (12).

Recent live-cell imaging revealed that the sperm cells remain in the boundary region between the egg and the central cell for only 7.4 ± 3.3 min before they fuse (4). We therefore proposed the narrow time slot of EC1 secretion to be associated with sperm-egg recognition or adhesion, with egg cell signaling, or with a polyspermy block on the egg cell. However, the five *EC1* genes appear to be functionally redundant, as we did not find negative effects on fertility in single, double, or triple knockout mutants (fig. S5). *EC1.2* and *EC1.3* are tandemly arranged on chromosome 2 and, thus, are not suitable to generate double mutants. We used the strong *EC1.1* promoter for simultaneous knockdown of *EC1.2* and *EC1.3* expression in the egg cell via RNA interference (RNAi), but we did not find any effect on fertility (fig. S5). We only observed reduced seed set when we down-regulated *EC1.2/3* in egg cells of the triple knockout *ec1.1/4/5* (Fig.

3B and fig. S5; referred to as *ec1-RNAi*). Reciprocal backcrosses and segregation ratios of self-fertilized *ec1-RNAi* lines revealed the expected female gametophytic effect on transfer DNA transmission, resulting in only heterozygous or wild-type (WT) offspring (tables S1 and S2). Despite the lower transcript abundance of *EC1.2* and *EC1.3* in heterozygous *ec1-RNAi* pistils (fig. S6), both embryo sac development (fig. S7) and pollen tube reception (fig. S8) were comparable to the same processes in WT ovules.

To study the *EC1* knockdown phenotype in more detail, we pollinated pistils of the wild type and four independent *ec1-RNAi* lines with the sperm marker HTR10-mRFP1 (10). The evaluation of ovules at 30 to 40 hours after pollination (hap) revealed that *ec1-RNAi* ovules allow sperm release but block gamete fusion (table S3). We found that 43.5 to 46.7% of *ec1-RNAi* embryo sacs had two, or even four, unfused sperm cells (Fig. 3, D to F), whereas in the wild type, both sperm cell delivery and fusion are completed within 6 to 10 hap (Fig. 3C) (13). Notably, multiple-sperm cell delivery in *ec1-RNAi* ovules involves both synergids (fig. S9). We conclude that, due to failed gamete fusion, the second synergid of an *ec1-RNAi* ovule continues to secrete pollen tube attractants, even after the first pollen tube has successfully discharged its sperm pair into the receptive synergid cell. This suggests a gamete fusion–based molecular mechanism preventing multiple-pollen tube attraction and is in accordance with recent observations of mutants with defective sperm cells that fail to fuse (14, 15).

It is vital to ensure that both gamete fusion events take place in a timely and efficient manner, because typically only one pair of sperm cells is delivered into the embryo sac, and both female gametes need to be fertilized for reproductive success. The two sperm cells of flowering plants are known to be physically associated (arrowhead in Fig. 4A) (16), and this connection may ensure the simultaneous delivery of both sperm cells to the gamete fusion sites. To address the question of whether EC1 secretion serves as a precisely timed signal for sperm cell separation, we generated transgenes expressing a GFP-labeled membrane protein (TET9-GFP) in sperm cells to visualize the sperm membranes during double fertilization. Both the intercellular sperm connection and the cytoplasmic projection that is known to connect the front sperm (sc1) with the vegetative nucleus (16) are visible (Fig. 4, A and B). Notably, the physical link between the two sperm cells appears to be membrane-enriched (arrowhead in Fig. 4B). This membranous link remains between the unfused sperm cells in *ec1-RNAi* ovules (Fig. 4, C and D). However, we also detect the physical association at the time point of sperm-egg fusion in WT embryo sacs (Fig. 4, E and F), arguing against a role for EC1 in sperm separation. After plasmogamy, remnants of the membranous link are visible at the apical edge of the degenerating synergid (Fig. 4, G and H),

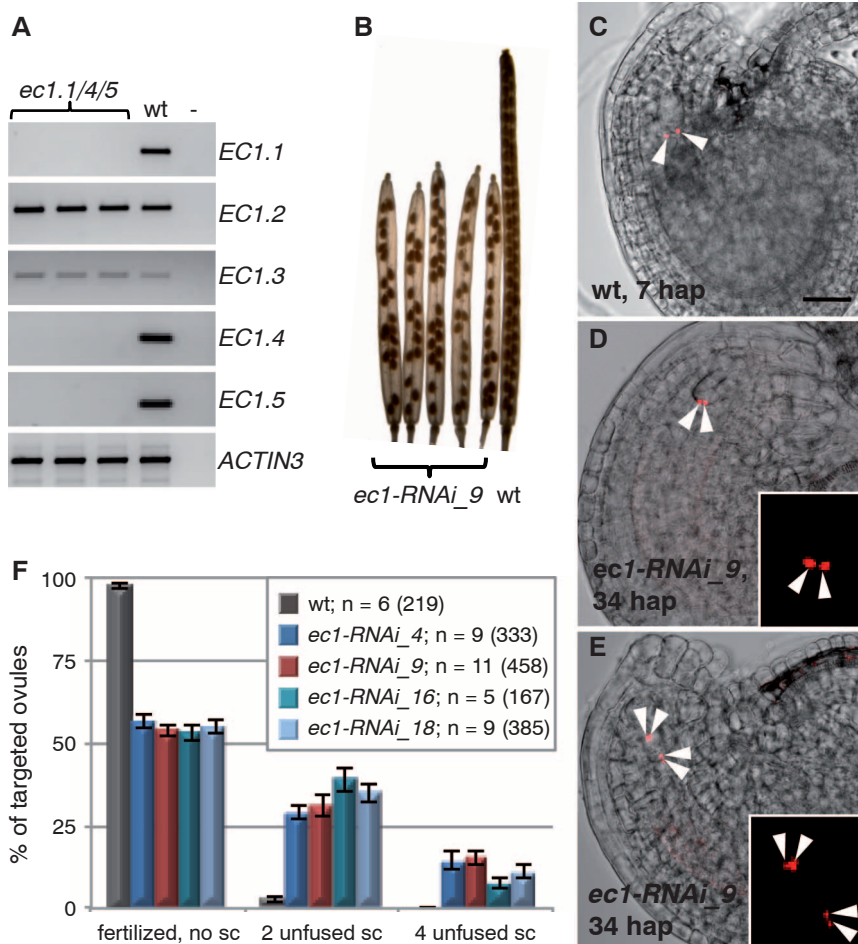


Fig. 3. The *EC1* gene family is essential for gamete fusion and for blocking supernumerary sperm cell delivery. (A) *ec1.1/4/5* is a triple knockout, shown by RT-PCR. (B) The reduced seed set was observed only in siliques of the quintuple knockdown *ec1-RNAi*. (C to E) Confocal images of sperm nuclei (red) in the wild type and in *ec1-RNAi* ovules. (C) Sperm cells (arrowheads) fusing with WT female gametes at 7 hap. (D and E) *ec1-RNAi* ovules with two (D) or four (E) unfused sperm cells (arrowheads). (F) Quantitative assessment of *ec1-RNAi* phenotypes at 30 to 40 hap. Phenotypes of ovules targeted by a pollen tube were classified as indicated. Mean values \pm SEM (error bars) are shown [n = numbers of siliques counted (number of ovules)]. Scale bar in (C), 20 μ m.

where they stay attached, even when the synergid collapses. At that stage, we also find traces of GFP-labeled sperm membranes at the surface of the fertilized egg cell, most likely representing the sperm-egg fusion site (fig. S10).

Gamete-interaction studies in other organisms revealed that gamete adhesion and/or binding initiates a signaling cascade that leads to the activation of the male gamete and to the exposure of fusogenic membrane regions (17–21). So far, the only known flowering plant candidate gamete fusogen is HAP2/GCS1, a sperm-expressed single-pass transmembrane domain protein (5, 6). Notably, fluorescent signals of HAP2–yellow fluorescent protein (YFP) in sperm cells of semi-in vivo grown *Arabidopsis* pollen tubes are endomembrane-associated and not located at the sperm surface (Fig. 4, I and J) (22), implying the need for membrane remodeling to acquire full fertilization competence when the sperm cells reach their fusion sites. However, the weak fluorescence of HAP2–YFP prevented us from detecting any redistribution of HAP2/GCS1 within the ovule. To investigate the effect of exogenously applied EC1 on HAP2–YFP localization, we developed a bioassay with sperm cells freshly released from semi-in vivo grown pollen tubes. Because all attempts to express recombinant EC1 or to generate synthetic EC1 proteins failed, we tested the effect of two synthetic EC1.1 peptides, comprising the signature motifs S1 and S2 (Fig. 2A). Neither peptide alone showed an obvious effect on sperm cells, but when we treated the sperm cells with an equimolar peptide mixture [EC1(pep)], the HAP2–YFP signal significantly shifted toward the sperm plasma membrane, compared with controls treated with a mixture of two randomized peptides based on the same amino acids or a peptide-free solution (Fig. 4, K to Q).

Taken together, our results strongly suggest that EC1 is a protein factor controlling *Arabidopsis* gamete fusion by mediating sperm activation. We propose that the regulated secretion of EC1 by the egg cell upon sperm-egg interaction ensures the appropriate localization of the cell-fusion machinery in distinct sperm membrane domains to accomplish gamete fusion. Although both sperm cells stay close together after being delivered at the site where the two fusion events take place, we show that they remain spatially separated from one another, which may be a strategy to avoid polyspermy and to guarantee reliable and efficient double fertilization after achieving full fertilization competence. The observed mutual gamete activation furthermore suggests a complex mode of intercellular communication between the flowering plant egg and sperm cell before fusion. This may include the on-time delivery of other, yet undiscovered fertilization molecules to the gamete surfaces.

Although the reproductive strategy of flowering plants is considerably different from those of other sexual reproducing organisms, we report here on some essential common processes and

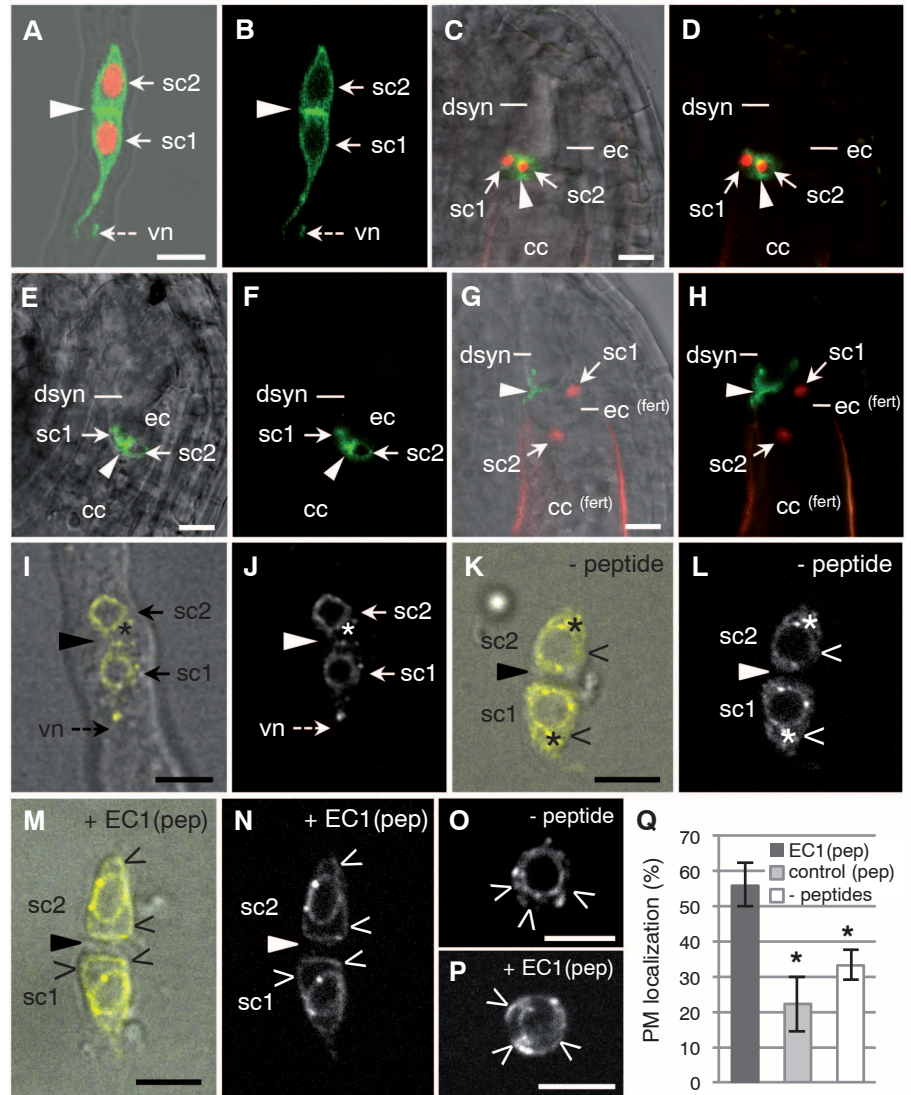


Fig. 4. EC1 peptides activate the sperm endomembrane system. (A and B) Confocal images of sperm cell marker line simultaneously labeling sperm nuclei (red) and sperm membranes (green). Note the membranous connection between the sperm cells (solid arrowheads) and the cytoplasmic projection associated with the vegetative nucleus (dashed arrows). (C to F) Sperm membranes stay physically connected (solid arrowheads) during gamete interaction, in both *ec1-RNAi* (C and D) and WT ovules (E and F). (G and H) After plasmogamy, the membranous connection (solid arrowheads) is visible at the apical edge of the degenerating synergid. (I to P) Spinning disc images of sperm cells expressing HAP2–YFP. (I and J) HAP2–YFP localization in the endomembrane system of sperm cells within a semi-in vivo growing pollen tube. Solid arrowheads point at the position of the membranous intercellular connection. (K and L) Sperm cell pair released in peptide-free control solution, showing endomembrane-associated HAP2–YFP (asterisks). (M and N) HAP2–YFP localization at the plasma membrane (arrowheads) of sperm cells treated with EC1.1 peptide mix [EC1(pep)]. (O) Single sperm cell in a peptide-free control solution. (P) HAP2–YFP at the plasma membrane (arrowheads) of EC1(pep)-treated single sperm cell. (Q) Quantitative assessment of HAP2–YFP localization at plasma membranes of EC1(pep)-treated sperm cells, compared with randomized control peptides and a peptide-free solution. Mean values (\pm SEM) of at least three independent experiments with ≥ 20 sperm cells each are shown. Asterisks indicate statistically significant difference from the controls ($*P < 0.05$), according to Student's *t* test. vn, vegetative nucleus. Scale bars, 5 μ m.

principles. Our results indicate that, like the male gametes of other species, *Arabidopsis* sperm cells must be activated to acquire fertilization competence. However, animal sperm become activated after interacting with the outer vestment of the egg, whereas the egg responds by undergoing the cortical reaction only after fusion (17–19, 23).

Thus, the mutual activation of *Arabidopsis* gametes before fusion points to an evolutionary link between flowering plant fertilization and fertilization in unicellular sexual reproducing organisms such as yeast and *Chlamydomonas* (20, 21), where both mating-type gametes become activated before fusion.

References and Notes

1. F. Berger, Y. Hamamura, M. Ingouff, T. Higashiyama, *Trends Plant Sci.* **13**, 437 (2008).
2. S. G. Nawashin, *Bull. Acad. Imp. Sci. St Petersburg* **9**, 377 (1898).
3. M. L. Guignard, *Rev. Gén. Bot.* **11**, 129 (1899).
4. Y. Hamamura *et al.*, *Curr. Biol.* **21**, 497 (2011).
5. T. Mori, H. Kuroiwa, T. Higashiyama, T. Kuroiwa, *Nat. Cell Biol.* **8**, 64 (2006).
6. K. von Besser, A. C. Frank, M. A. Johnson, D. Preuss, *Development* **133**, 4761 (2006).
7. Y. Liu *et al.*, *Genes Dev.* **22**, 1051 (2008).
8. S. Sprunck, U. Baumann, K. Edwards, P. Langridge, T. Dresselhaus, *Plant J.* **41**, 660 (2005).
9. K. A. Silverstein *et al.*, *Plant J.* **51**, 262 (2007).
10. M. Ingouff, Y. Hamamura, M. Gourgues, T. Higashiyama, F. Berger, *Curr. Biol.* **17**, 1032 (2007).
11. S. Sprunck, *Biochem. Soc. Trans.* **38**, 635 (2010).
12. M. Gebert, T. Dresselhaus, S. Sprunck, *Plant Cell* **20**, 2798 (2008).
13. J. E. Faure, N. Rotman, P. Fortuné, C. Dumas, *Plant J.* **30**, 481 (2002).
14. K. M. Beale, A. R. Leydon, M. A. Johnson, *Curr. Biol.* **22**, 1090 (2012).
15. R. D. Kasahara *et al.*, *Curr. Biol.* **22**, 1084 (2012).
16. A. D. McCue, M. Cresti, J. A. Feijó, R. K. Slotkin, *J. Exp. Bot.* **62**, 1621 (2011).
17. N. Hirohashi *et al.*, *Dev. Growth Differ.* **50**, S221 (2008).
18. N. Inoue, M. Ikawa, M. Okabe, *Asian J. Androl.* **13**, 81 (2011).
19. A. T. Neill, V. D. Vacquier, *Reproduction* **127**, 141 (2004).
20. E. Grote, *J. Cell Sci.* **123**, 1902 (2010).
21. J. Pan, W. J. Snell, *Curr. Opin. Microbiol.* **3**, 596 (2000).
22. J. L. Wong, M. A. Johnson, *Trends Cell Biol.* **20**, 134 (2010).
23. J. Parrington, L. C. Davis, A. Galione, G. Wessel, *Dev. Dyn.* **236**, 2027 (2007).

Acknowledgments: Seeds were kindly provided by M. Johnson (HAP2p:HAP2-YFP) and F. Berger (HTR10p:HTR10-mRFP1). We thank M. Gebert for her help in *in situ* hybridization, M. Gahrtz for providing plasmids, M. Kammerer and

B. Bellmann for technical assistance, and F. Sprenger for his support in spinning disc microscopy. This work was supported by the Deutsche Forschungsgemeinschaft (grants SP 686/1-2 and SFB924 to S.S. and DR 334/5 to T.D.), by a graduate scholarship of Universität Bayern e.V. (to S.R.), and, in part, by the Australian Grains Research Development Corporation (to T.D.) and the Swiss National Science Foundation (grant 3100AO-112489 to U.G.). S.S. and T.D. are inventors on a patent (WO 2007/092992) related to the *EC1* promoter sequences. Accession numbers and author contributions are listed in the supplementary materials.

Supplementary Materials

www.sciencemag.org/cgi/content/full/338/6110/1093/DC1

Materials and Methods

Supplementary Text

Figs. S1 to S10

Tables S1 to S3

References (24–46)

Movies S1 and S2

27 April 2012; accepted 4 October 2012

10.1126/science.1223944

Content-Specific Fronto-Parietal Synchronization During Visual Working Memory

R. F. Salazar,¹ N. M. Dotson,¹ S. L. Bressler,² C. M. Gray^{1*}

Lateral prefrontal and posterior parietal cortical areas exhibit task-dependent activation during working memory tasks in humans and monkeys. Neurons in these regions become synchronized during attention-demanding tasks, but the contribution of these interactions to working memory is largely unknown. Using simultaneous recordings of neural activity from multiple areas in both regions, we find widespread, task-dependent, and content-specific synchronization of activity across the fronto-parietal network during visual working memory. The patterns of synchronization are prevalent among stimulus-selective neurons and are governed by influences arising in parietal cortex. These results indicate that short-term memories are represented by large-scale patterns of synchronized activity across the fronto-parietal network.

Working memory enables the short-term representation and utilization of behaviorally relevant information when that information is no longer available from the environment. How are such representations maintained in the brain? Extensive evidence demonstrates sustained activation in frontal and parietal areas during memory delay periods (1–4). Although the specific role of these activity patterns is not fully understood, theoretical, anatomical, and electrophysiological studies suggest that synchronous interactions among these cortical regions support working memory processes (5–11). While task-specific synchronization has been observed between prefrontal and parietal areas (12, 13), its contribution to working memory is largely unknown. We tested the hypothesis that neuronal synchronization across the fronto-

parietal network carries content-specific information that contributes directly to visual working memory. The pattern of fronto-parietal synchronization should thus vary as a function of the object held in memory.

We performed multi-electrode recordings of broadband neuronal activity [separated into unit activity and local field potentials (LFPs)] in prefrontal (PFC) and posterior parietal (PPC) cortices in two macaque monkeys (A and B) while they performed an oculomotor, delayed match-to-sample task (Fig. 1, A and B) (14). This task required the monkeys to match the identity of the sample object. Figure S1 shows the recording locations and sample sizes relative to the cortical sulci in both monkeys. We simultaneously sampled activity from up to six PPC and six PFC areas (see fig. S2 for an example), yielding a total of 30 fronto-parietal, interareal comparisons. The resulting data set, consisting of LFPs and unit activity recorded over 27 and 47 days in monkeys A and B, respectively, is given in table S1.

We first determined the time course of fronto-parietal synchronization by computing the time-

frequency coherence spectrum on correct trials for fronto-parietal LFP pairs from all sessions (14). These calculations revealed a common temporal pattern of synchronization that correlated with the events of the task (Fig. 1C). In this example, coherence in the 15- to 25-Hz band peaked during the presample period, transiently declined following the sample stimulus onset, and increased again during the delay (15), reaching a maximum before the match. The relative phase between the signals in this frequency range also varied over the course of the trial (Fig. 1D). During the presample and sample periods, PFC showed a phase lead near 25° that increased during the delay period to ~40°.

To determine how synchronization varies with the sample stimulus held in memory, we first identified pairs having significant coherence (Table 1) and then applied mutual information analysis to the LFP coherence spectra from those pairs at all time-frequency bins (14). [Since the analysis of mutual information is applied to coherence spectra, rather than individual trials, we refer to the resulting metric as the coherence selectivity index (CSI).] Because the sample stimuli differed in their location and identity, we assessed the identity selectivity at each stimulus location and the location selectivity for each identity (16). Figure 2A shows a fronto-parietal pair displaying identity-specific coherence during the delay period. A band of elevated coherence (centered at ~20 Hz) during the delay period differs in magnitude and time course with the object held in memory. Figure 2B quantifies this effect, revealing a significant increase in CSI during the late delay period.

To assess the stimulus selectivity across the entire sample, we first identified pairs with significant CSI (Table 1) and then pooled the data separately for identity and location for those pairs having significant CSI during the delay. If a pair showed selectivity for multiple locations and/or objects, the stimulus condition with the highest coherence was chosen. The median CSI value, as a function of time and frequency

¹Cell Biology and Neuroscience, Montana State University, Bozeman, MT 59717, USA. ²Center for Complex Systems and Brain Sciences, Florida Atlantic University, Boca Raton, FL 33431, USA.

*To whom correspondence should be addressed. E-mail cmgray@cns.montana.edu

$CSI(t, f)$], from the selected pairs is shown in Fig. 2C. [The $CSI(t, f)$ distributions for identity are shown separately for each monkey in fig. S3A.] Several effects are notable. First, location specificity, and to a lesser extent identity specificity, appear during the sample period at frequencies less than 15 Hz. This likely reflects the spatial and identity selectivity of neuronal populations in fronto-parietal networks (17–20). Second, on average, an increase in CSI occurs throughout the delay period with a peak frequency at ~15 Hz. Third, we found no significant differences in the CSI values between the pairs tuned for location and identity, in the frequency range of 12 to 22 Hz, at any time bin throughout the trial [minimum $P = 0.6$; Kolmogorov-Smirnov (KS) test, Bonferroni correction]. Consistent with delay-period selectivity observed at the cellular level (16, 19–21), these findings demonstrate both identity and location specificity of fronto-parietal synchronization during the memory period.

The content specificity of delay-period coherence observed in the CSI raised the question of how coherence magnitude and phase vary as a function of time and stimuli. Because a major objective of this study was to characterize identity-specific activity, using the identity matching-rule, we focused all subsequent analysis on identity specificity. For each identity-selective pair, we rank ordered the mean delay-period coherence in the 12- to 22-Hz range for the three identities (maximum, intermediate, and minimum). Figure 2D shows the time course of the ranked mean coherence (\pm SEM) for each category. The coherence values for the three objects maintain a clear difference throughout the delay. (Distributions of the maximum coherence for each monkey are shown in fig. S3B.) The mean relative phase ranged from 15° to 40° throughout the trial (at the center frequency of 17 Hz, these relative phase values correspond to time lags of 2.45 and 6.53 ms, respectively), showing a consistent prefrontal phase lead that gradually increased over time, but showed no apparent difference with respect to the stimuli (fig. S4). (A small percentage of phase values ranged between 140° and 180°, indicating a near antiphase relationship.) To further identify the source of the coherence differences, we analyzed the mean and variance of the relative phase and power across the distributions in the 12- to 22-Hz range. The phase variance showed a significant difference across the population in the interval between 1.15 and 1.70 s [$P < 0.05$, Kruskal-Wallis (KW) test, Bonferroni corrected], indicating an inverse relation between coherence magnitude and phase variance in the identity-selective pairs (Fig. 2E). We found no difference in the power in the same frequency range for any of the three stimuli in either PPC or PFC (KW test; $P > 0.05$, Bonferroni corrected) (fig. S5), suggesting that the differences in coherence were due primarily to differences in phase consistency.

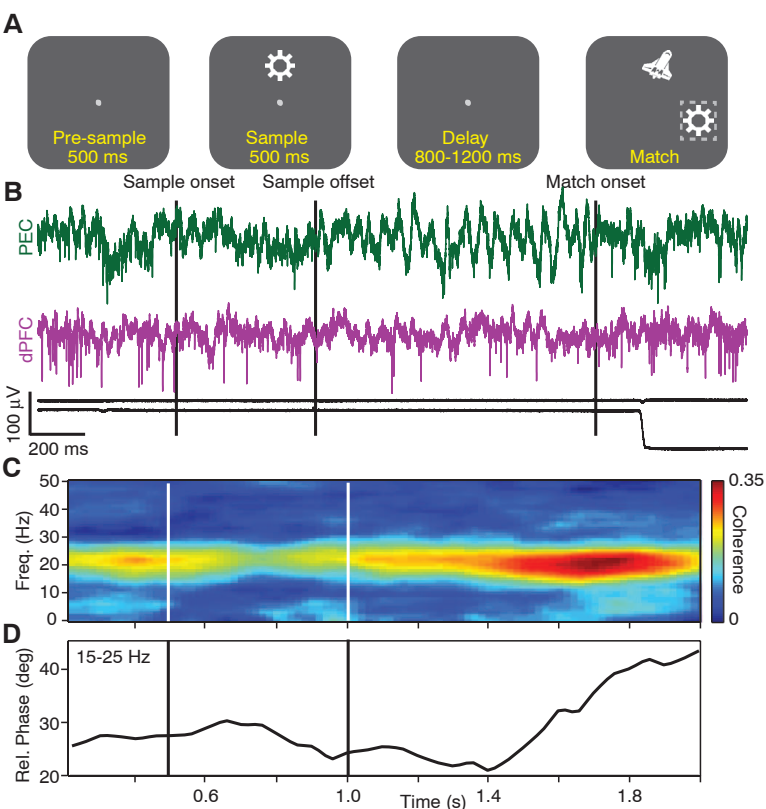


Fig. 1. Task dependence of fronto-parietal coherence. **(A)** Timeline of the identity-matching task. During visual fixation, a sample stimulus, consisting of one out of three possible objects positioned at one out of three possible locations, was presented for 500 ms, followed by a random delay of 800 to 1200 ms. At the end of the delay, a match stimulus was presented, consisting of the previous sample object (target) and a distracter object positioned at two out of three possible locations. A saccadic eye movement to the target was rewarded with juice (14). **(B)** Example of the signals recorded on a single trial in monkey A. Top two traces: broadband signals from area PEC of the parietal cortex (PEC, green) and dorsolateral prefrontal cortex (dPFC, purple). Bottom two traces: horizontal and vertical eye position. **(C and D)** Time-frequency coherence spectrum (C) and average relative phase between 15 and 25 Hz (D) locked to the sample presentation (all stimuli, correct trials, 400-ms window, 50-ms step). In (B) to (D) and all subsequent figures, the vertical lines show the onset and offset of the sample. Time-frequency distributions in this and subsequent figures are interpolated at 1-Hz and 2-ms resolution.

Table 1. Number of fronto-parietal pairs with significant coherence and CSI between 10 and 42 Hz. Abbreviations: PRE, presample period; SA, sample period; DE1, early delay period; DE2, late delay period; DE, the whole delay consisting of either DE1 or DE2, or both. The timing of these periods is shown in parentheses.

<i>N</i> = 2191		PRE (0.1–0.4 s)	SA (0.6–0.9 s)	DE1 (1.1–1.4 s)	DE2 (1.4–1.7 s)	DE (DE1 and/or DE2)
Identity	Sig. Coh	1349	1216	1369	1599	1662
	Sig. CSI	51	199	244	290	438
		3.8%	16.4%	17.8%	18.1%	26.4%
Location	Sig. Coh	1286	1160	1274	1488	1550
	Sig. CSI	41	194	223	263	409
		3.2%	16.7%	17.5%	17.7%	26.4%

To determine which cortical areas engage in the synchronous memory-related activity, we sorted the fronto-parietal pairs showing significant delay-period CSI according to their respective cortical areas. The results reveal several notable findings (fig. S6). First, although our

sample distribution was nonuniform, we found content-specific, fronto-parietal coherence among all sampled cortical areas. Second, the incidence of significant coherence selectivity varied widely (ranging from 4 to 50%) and occurred more often than expected from a uniform distribution

Fig. 2. Content-specific fronto-parietal synchronization during working memory. **(A)** Time-frequency coherence spectra for an LFP pair for the three sample objects presented at one location. **(B)** Coherence selectivity index as a function of time and frequency [CSI(t, f)] for the same pair showing significant selectivity (significance threshold at $P < 0.02$ indicated by white contours) during the delay period. **(C)** Median value of CSI(t, f) for LFP pairs showing selectivity for the sample identity (upper) and location (lower) during the delay. **(D)** Mean rank-ordered coherence (\pm SEM) in the 12- to 22-Hz band for the same identity-selective pairs as in the upper plot of (C). **(E)** Mean standard deviation of the relative phase (\pm SEM) in the 12- to 22-Hz band for the same identity-selective pairs as in the upper plot of (C). In plots (D), (E), and Fig. 3A, the two SEMs were calculated with the number of pairs or sessions as the degree of freedom.

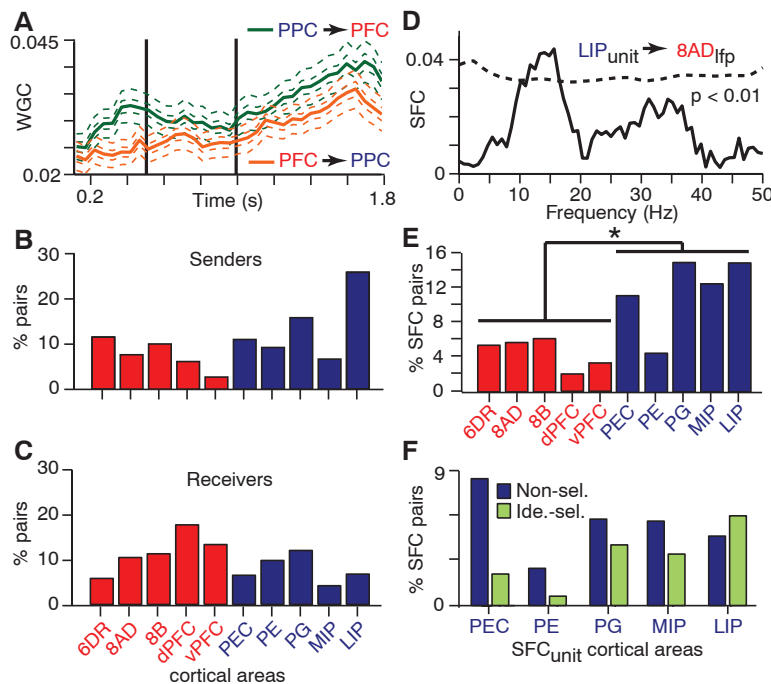
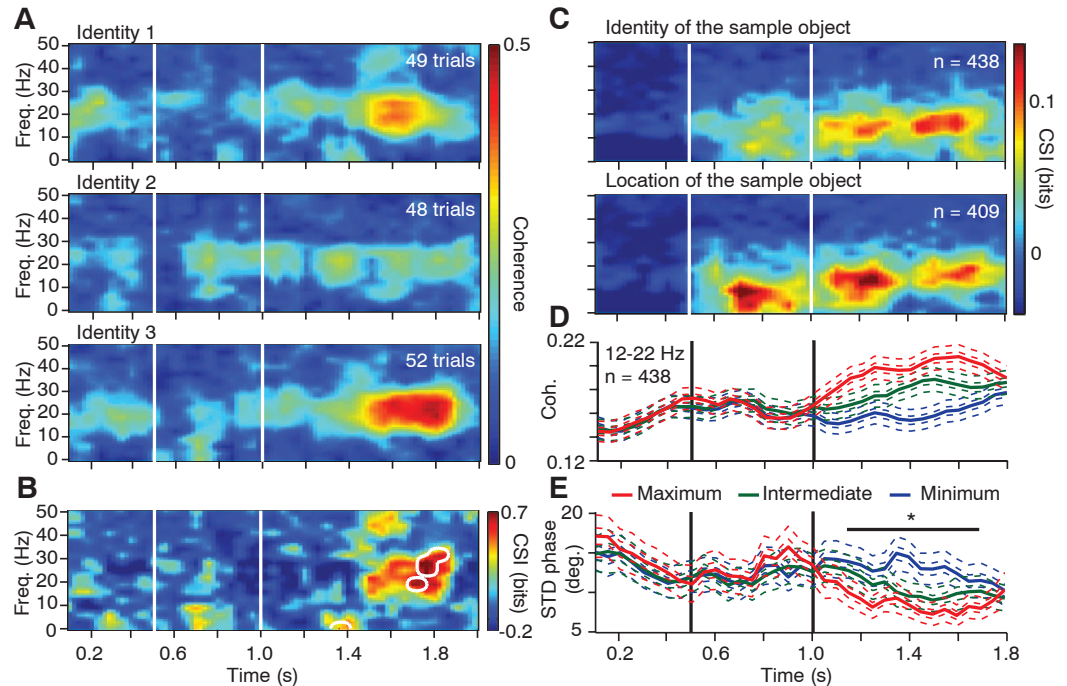


Fig. 3. Fronto-parietal interactions are dominated by parietal-to-frontal influences. **(A)** Time course of WGC in the 12- to 22-Hz frequency range for all identity-selective pairs (mean \pm SEM; $n = 438$). **(B)** and **(C)** Bar charts of the incidence of significant WGC directional differences with respect to cortical area for all the signal pairs in (A). **(D)** Example of the SFC for a LIP unit and the field recorded in area 8AD. Dashed line indicates confidence limit ($P < 0.01$, randomized surrogate). **(E)** Percentage of fronto-parietal pairs with significant SFC between 12 and 22 Hz. The unit activity was recorded in the labeled areas. See tables S1 and S3 for abbreviations and sample sizes. **(F)** Percentage of significant PPC_{unit}–PFC_{unit} pairs with respect to the parietal area in which the unit activity was recorded and split according to the stimulus selectivity of the cellular responses.

($P < 0.05$; randomization test) for both identity and location only among pairs involving the lateral bank of the intraparietal sulcus (i.e., areas PG

and LIP). Thus, memory-related, fronto-parietal synchronization is a widespread process distributed across multiple cortical regions (15, 22, 23).

Having demonstrated content-specific synchronization during the delay period, we sought evidence for which cortical areas exert influences that might control or modulate this activity. Using Wiener-Granger causality (WGC) in the time-frequency domain, we estimated the two directions of predictive influence within each fronto-parietal pair for the object yielding the maximum delay-period coherence (14). Figure 3A shows the time course of the mean (\pm SEM) WGC for the two directions in the 12- to 22-Hz band. On average, the influence is greater from PPC to PFC, and both directions of influence increase during the delay period ($P < 0.001$ for time and causation; two-way analysis of variance). Because taking the average obscures the heterogeneity of causal influences across the population, we implemented a method to detect significant differences between the two directions of influence for each pair (14) (fig. S7). We applied this method to the 400 ms of data preceding match onset to avoid potential nonstationarities due to the sample stimulus offset. For each pair with significant directional difference in WGC, the source of the larger value (PFC or PPC) was considered the sender and that of the smaller value the receiver. We then parsed the data according to cortical area in PFC and PPC regions, and plotted the incidence of senders and receivers of each area in the 12- to 22-Hz band with respect to all areas in the other cortical region (Fig. 3, B and C; areas PGM and 9L were excluded because of small sample sizes). All cortical areas displayed directional influences as senders and receivers, but the incidence of senders was greater in PPC (13.6%) than PFC (7.5%), and some PPC areas did not receive causal influence at all from some

PFC areas. The area with the highest incidence of senders was LIP (25.7%) and that with the highest incidence of receivers was dPFC (17.5%).

Our WGC analysis suggests that fronto-parietal synchronization is governed by synaptic influences in PFC that arise in PPC. We used interareal spike-field coherence (SFC) measurements to evaluate this prediction (14), reasoning that this measure is indicative of directed synaptic influences (13). For each fronto-parietal pair, we calculated the SFC between spikes in one region and the LFP in the other during the delay period (1.0 to 1.8 s) and detected significant SFC as a function of frequency ($P < 0.01$). This revealed significant spectral peaks at frequencies between 10 and 30 Hz (see Fig. 3D for an example). We then calculated the mean incidence of significant SFC in the 12- to 22-Hz range for each cortical area in which the unit activity was recorded (see table S2 for sample distribution). The results support the WGC finding of a dominant PPC to PFC influence by demonstrating that significant SFC occurred more often in PPC_{unit}–PFC_{lfp} pairs than PFC_{unit}–PPC_{lfp} pairs (Fig. 3E, $P < 0.05$, KS test). The agreement between the WGC and SFC results, supporting a dominant PPC to PFC influence, as opposed to the relative phase results showing a PFC phase lead, supports previous findings that relative phase is not a reliable index of neural influence (24).

To further evaluate the contribution of unit response selectivity, we calculated the mutual information for firing rate as a function of time (fig. S8) and, consistent with previous reports (19, 20, 25), found widespread selectivity during the sample and/or delay across both PFC and PPC areas (table S3). We then subdivided the SFCs according to the identity selectivity of the cellular responses. The results for the PPC_{unit}–PFC_{lfp} pairs show that significant SFC with PFC involves both selective and nonselective parietal neurons (Fig. 3F). (PFC_{unit}–PPC_{lfp} pairs were not included because of small sample sizes.) However, the majority of spike-field interactions involving identity-selective units come from cells recorded in areas LIP, PG, and to a lesser extent, MIP.

Our findings demonstrate that fronto-parietal synchronization during visual working memory is widespread, task-dependent, and content-specific during the delay period. The patterns of synchronization are governed by influences arising in PPC (26) and are prevalent among parietal neurons that display identity selectivity (19). These findings are consistent with other reports on the relationship between synchronization and performance in working memory tasks (15, 22, 27), the presence of fronto-parietal synchronization during memory-related search (12), and the spatial attention modulation of interareal coherence (28). Thus, although other cognitive processes—such as attention, anticipation, and motor planning—are likely to contribute to these effects, our findings demonstrate that short-term memories are represented as stimulus-specific patterns of synchronized activity that are widely distributed throughout the fronto-parietal network (29). This raises the question of how these patterns, their directional influences, spectral dynamics, and spatial distribution are modified by other working memory processes, such as retrieval, resistance to distraction, load, manipulation, and object-based attention. Other frequency bands have been associated with working memory (22, 30–32), and abundant evidence indicates that other cortical areas contribute to these representations. A major challenge will be to elucidate the neuronal mechanisms underlying memory-related, fronto-parietal interactions and their relationship to different frequency bands and other cortical areas.

References and Notes

1. J. M. Fuster, G. E. Alexander, *Science* **173**, 652 (1971).
2. J. W. Gnadt, R. A. Andersen, *Exp. Brain Res.* **70**, 216 (1988).
3. M. V. Chafee, P. S. Goldman-Rakic, *J. Neurophysiol.* **79**, 2919 (1998).
4. C. Rottschy et al., *Neuroimage* **60**, 830 (2012).
5. D. O. Hebb, *The Organization of Behavior* (Wiley, New York, 1949).
6. S. L. Bressler, *Brain Res. Brain Res. Rev.* **20**, 288 (1995).
7. J. Fell, N. Axmacher, *Nat. Rev. Neurosci.* **12**, 105 (2011).
8. L. D. Selemon, P. S. Goldman-Rakic, *J. Neurosci.* **8**, 4049 (1988).
9. C. Cavada, P. S. Goldman-Rakic, *J. Comp. Neurol.* **287**, 422 (1989).
10. M. V. Chafee, P. S. Goldman-Rakic, *J. Neurophysiol.* **83**, 1550 (2000).
11. J. Quintana, J. M. Fuster, J. Yajeya, *Brain Res.* **503**, 100 (1989).
12. T. J. Buschman, E. K. Miller, *Science* **315**, 1860 (2007).
13. B. Pesaran, M. J. Nelson, R. A. Andersen, *Nature* **453**, 406 (2008).
14. See supplementary materials on Science Online.
15. C. Tallon-Baudry, O. Bertrand, C. Fischer, *J. Neurosci.* **21**, RC177 (2001).
16. S. C. Rao, G. Rainer, E. K. Miller, *Science* **276**, 821 (1997).
17. R. A. Andersen, G. K. Essick, R. M. Siegel, *Science* **230**, 456 (1985).
18. S. Funahashi, C. J. Bruce, P. S. Goldman-Rakic, *J. Neurophysiol.* **61**, 331 (1989).
19. A. B. Sereno, J. H. Maunsell, *Nature* **395**, 500 (1998).
20. F. A. Wilson, S. P. Scalaidhe, P. S. Goldman-Rakic, *Science* **260**, 1955 (1993).
21. G. Rainer, W. F. Asaad, E. K. Miller, *Proc. Natl. Acad. Sci. U.S.A.* **95**, 15008 (1998).
22. S. Liebe, G. M. Hoerzer, N. K. Logothetis, G. Rainer, *Nat. Neurosci.* **15**, 456, (2012).
23. Y. B. Saalmann, I. N. Pigarev, T. R. Vidyasagar, *Science* **316**, 1612 (2007).
24. A. Brovelli et al., *Proc. Natl. Acad. Sci. U.S.A.* **101**, 9849 (2004).
25. E. K. Miller, C. A. Erickson, R. Desimone, *J. Neurosci.* **16**, 5154 (1996).
26. B. E. Verhoeve, R. Vogels, P. Janssen, *J. Neurophysiol.* **105**, 2030 (2011).
27. M. P. Deiber et al., *J. Cogn. Neurosci.* **19**, 158 (2007).
28. G. G. Gregoriou, S. J. Gotts, H. Zhou, R. Desimone, *Science* **324**, 1207 (2009).
29. B. R. Postle, *Neuroscience* **139**, 23 (2006).
30. M. W. Howard et al., *Cereb. Cortex* **13**, 1369 (2003).
31. H. Lee, G. V. Simpson, N. K. Logothetis, G. Rainer, *Neuron* **45**, 147 (2005).
32. M. Siegel, M. R. Warden, E. K. Miller, *Proc. Natl. Acad. Sci. U.S.A.* **106**, 21341 (2009).

Acknowledgments: This work was supported by grants from the National Institute of Mental Health (MH069374, MH081162), the National Institute of Neurological Disorders and Stroke (NS059312), and the Swiss National Science Foundation. We thank B. Goodell for the design and development of the microdrive systems used in this study and U. Köster for technical support in the computational procedures. We also thank two anonymous reviewers for helpful comments on an earlier version of the manuscript.

Supplementary Materials

www.sciencemag.org/cgi/content/full/science.1224000/DC1
Materials and Methods
Figs. S1 to S9
Tables S1 to S3
References

30 April 2012; accepted 3 October 2012
Published online 1 November 2012;
10.1126/science.1224000

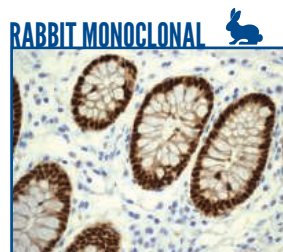


THE RABBIT **MONOCLONAL** ADVANTAGE

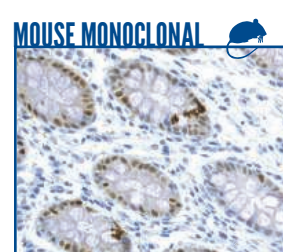
- More diverse epitope recognition
- High specificity and affinity
- Improved response to mouse antigens
- Highly validated - every antibody tested in WB, IHC, ICC, Flow Cytometry, and IP

Rabbit Monoclonal Antibodies (RabMAbs®) provide the combined benefits of superior antigen recognition of the rabbit immune system with the specificity and consistency of a monoclonal antibody, bringing you the highest quality antibody possible.

Over **4000 RabMAbs®** online, visit
www.epitomics.com



CDX2 RabMAb



CDX2 Mouse MAb

Paraffin-embedded human colon tissue stained with Epitomics' CDX2 RabMAb (Cat.# 2475-1) and Vendor A's CDX2 Mouse Monoclonal under optimal conditions

Find out more @ www.epitomics.com/advantage



Antibody Satisfaction Guarantee

www.epitomics.com

US & Canada | 1-877-772-2622
Outside NA | 650-583-6688

THE SECOND MOST NECESSARY EQUIPMENT IN THE LAB?



You never go into the lab without your goggles, so why would you start your project without SciFinder®? Used by top researchers, SciFinder is the only tool that provides access to the most comprehensive and trustworthy chemistry-related content. And that's why SciFinder is the choice for chemistry research.™

Find out more at www.cas.org.

 **SciFinder®**
The choice for chemistry research.™

There's only one

DR. SHIRLEY MALCOM



To Dr. Shirley Malcom, born and raised in the segregated South more than 65 years ago, a career based on her studies in science seemed even less likely than the launch of the Soviet's Sputnik. But with Sputnik's success, the Space Race officially started and, in an instant, brought a laser-like focus to science education and ways to deliver a proper response. Not long after, Dr. Malcom entered the picture.

Although black schools at the time received fewer dollars per student and did not have sufficient resources to maintain their labs at a level equivalent to the white schools, Dr. Malcom found her way to the University of Washington where she succeeded in obtaining a B.S. in spite of the difficulties of being an African American woman in the field of science. From there she went on to earn a Ph.D. in ecology from Penn State and held a faculty position at the University of North Carolina, Wilmington.

Dr. Malcom has served at the AAAS in multiple capacities, and is presently Head of the Directorate for Education and Human Resources Programs. Nominated by President Clinton to the National Science Board, she also held a position on his Committee of Advisors on Science and Technology. She is currently a member of the Caltech Board of Trustees, a Regent of Morgan State University, and co-chair of the Gender Advisory Board of the UN Commission on Science and Technology for Development. She has held numerous other positions of distinction and is the principal author of *The Double Bind: The Price of Being a Minority Woman in Science*.

Of her active career in science, Dr. Malcom says, "I guess I have become a poster child for taking one's science background and using that in many other ways: we ask questions; we try to understand what we find; we consider what evidence we would need to confirm or refute hypotheses. And that happens in whatever setting one finds oneself."

At *Science* we are here to help you in your own scientific career with expert career advice, forums, job postings, and more — all for free. Visit *Science* today at ScienceCareers.org.



For your career in science, there's only one **Science**

ScienceCareers.org

New Products

ELECTRIC CAPPER

Designed to work with all sample storage 96-format tube and rack combinations, without use of adapters, the Univo Electric Capper CP480 sets a new benchmark for ease of use, versatility, and speed of operation. Operating as a stand-alone benchtop unit the compact Univo Electric Capper is able to uniformly cap a complete rack of 96 sample storage tubes in only four to nine seconds—less than half the time of competitive systems. The versatile Univo Electric Capper can cap all Micronic plug style caps: capmats, capbands, and capclusters made of TPE, EVA, or other materials on 96-format Micronic tubes and racks. The capper is also compatible with most other brands of tubes and caps. The Univo Electric Capper is extremely easy-to-use. For capping, simply place the rack filled with tubes in the sample holder and place a capmat, capband, or capcluster on the tubes.

Micronic

For info: +31-320-277070 | www.micronic.com

**AUTOMATED COMPOUND QUALITY CONTROL**

The Brooks Plate Auditor is a fast, accurate, and noninvasive tool for identification of precipitate and empty wells in compound and screening plates. The new Plate Auditor is the result of a successful collaboration with the Scripps Research Institute. The new Plate Auditor is designed to evaluate the quality of microplate-based compound samples for precipitation and liquid volume prior to use in compound management and high throughput screening activities. The system rapidly analyzes plates to automatically verify sample integrity thus eliminating the need for extensive manual quality control. The ability of the instrument to provide sample color information makes the Plate Auditor a unique option for monitoring sample quality over time, and identifying wells with artifacts which may interfere with or invalidate screening results.

Brooks Life Science Systems

For info: 978-262-2400 | www.brooks.com

ELECTROCOMPETENT CELLS

CloneCatcher Gold DH5G Electrocompetent *E. coli* cells exhibit extremely high electroporation efficiencies that approach the theoretical maximum of 3.4×10^{11} cfu/ μ g pUC19 DNA. Transferring exogenous DNA into *E. coli* is a standard laboratory method for cloning genes and constructing cDNA, genomic, and epitope libraries. The limiting factor in many library-screening efforts or multiple fragment ligations is the efficiency by which DNA can be introduced into *E. coli*. Electroporation is one method to efficiently introduce DNA into *E. coli*. CloneCatcher Gold cells meet the needs of scientists that are seeking to find rare clones or are building complex or metagenomic libraries. CloneCatcher Gold significantly outperforms all other commercially available Electrocompetent Cells when introducing ligated DNA. When the amount of input DNA is limited, CloneCatcher Gold enhances your likelihood of success. CloneCatcher Gold requires less topoisomerase-loaded vector and therefore can reduce the overall operating costs.

AMS Biotechnology

For info: +44-(0)-1235-828200 | www.amsbio.com

HPLC COLUMN

A new 5 μ m particle has been added to the Kinetex core-shell product line. As the largest diameter particle in the family, Kinetex 5 μ m core-shell columns deliver better performance than 3 μ m or 5 μ m fully porous offerings, with no increase in backpressure. In fact, the new 5 μ m media provides 90% higher average efficiencies compared to the same size fully porous columns and little to no method development is required to achieve improved performance on standard high-performance liquid chromatography (HPLC) systems. Chromatographers can simply substitute these columns into reversed phase HPLC methods that use traditional fully porous columns. Kinetex 5 μ m delivers increased resolution and higher efficiencies and extends the scalability and portability of the product line. With the current range of available particle sizes, including 1.3 μ m, 1.7 μ m, and 2.6 μ m, the same method can be easily transferred from UHPLC to HPLC to Preparative LC with Kinetex Core-Shell Technology.

Phenomenex

For info: 310-212-0555 | www.phenomenex.com

THERMAL TEST ENCLOSURES

A line of thermal test enclosures for the ThermoJet ES precision temperature cycling system is now available. The thermal enclosures provide highly accurate testing and processing of temperature sensitive electronic products. Available in either clamshell or hood configurations, the thermal test enclosures may be used to isolate a device under test (DUT) at a precise temperature insulated from external conditions, thereby providing the optimal conditions for highly accurate testing. Maintaining a uniform stable temperature with real-time thermal measurements on a DUT, the new thermal enclosures deliver unmatched test accuracy and precision. The thermal enclosures allow temperature testing of a variety of device sizes into almost any test setup, enabling characterization, qualification, and fault isolation on components or production level testing. All thermal test enclosures are electrostatic discharge-free and/or electromagnetic interference shielded.

SP Scientific

For info: 845-255-5000 | www.spscientific.com

Electronically submit your new product description or product literature information! Go to www.sciencemag.org/products/newproducts.dtl for more information.

Newly offered instrumentation, apparatus, and laboratory materials of interest to researchers in all disciplines in academic, industrial, and governmental organizations are featured in this space. Emphasis is given to purpose, chief characteristics, and availability of products and materials. Endorsement by *Science* or AAAS of any products or materials mentioned is not implied. Additional information may be obtained from the manufacturer or supplier.

Announcing our new partnership with NASA Federal Credit Union

Dear Member:

AAAS is committed to offering you member benefits that fit your needs and make your membership more valuable.

With that in mind AAAS is embarking on a new partnership with NASA Federal Credit Union that will provide you with access to a wide range of financial tools and products. Like AAAS, NASA Federal Credit Union is dedicated to serving the scientific community. This shared perspective is just one of the many reasons that we are embarking on this partnership.

As you may know, we have recently ended our banking relationship with Bank of America, but we're confident that our new partnership with NASA FCU will provide you with a superior banking experience. NASA FCU offers members better ways to save and smarter ways to borrow with friendly, professional service – along with anytime, anywhere account access.

Moreover, unlike other financial institutions that have public stockholders, NASA FCU is a not-for-profit financial cooperative where being a member means being an owner, too. And as a member/owner, you will enjoy unique benefits like: better loan rates, higher dividends and state-of-the-art products and services.

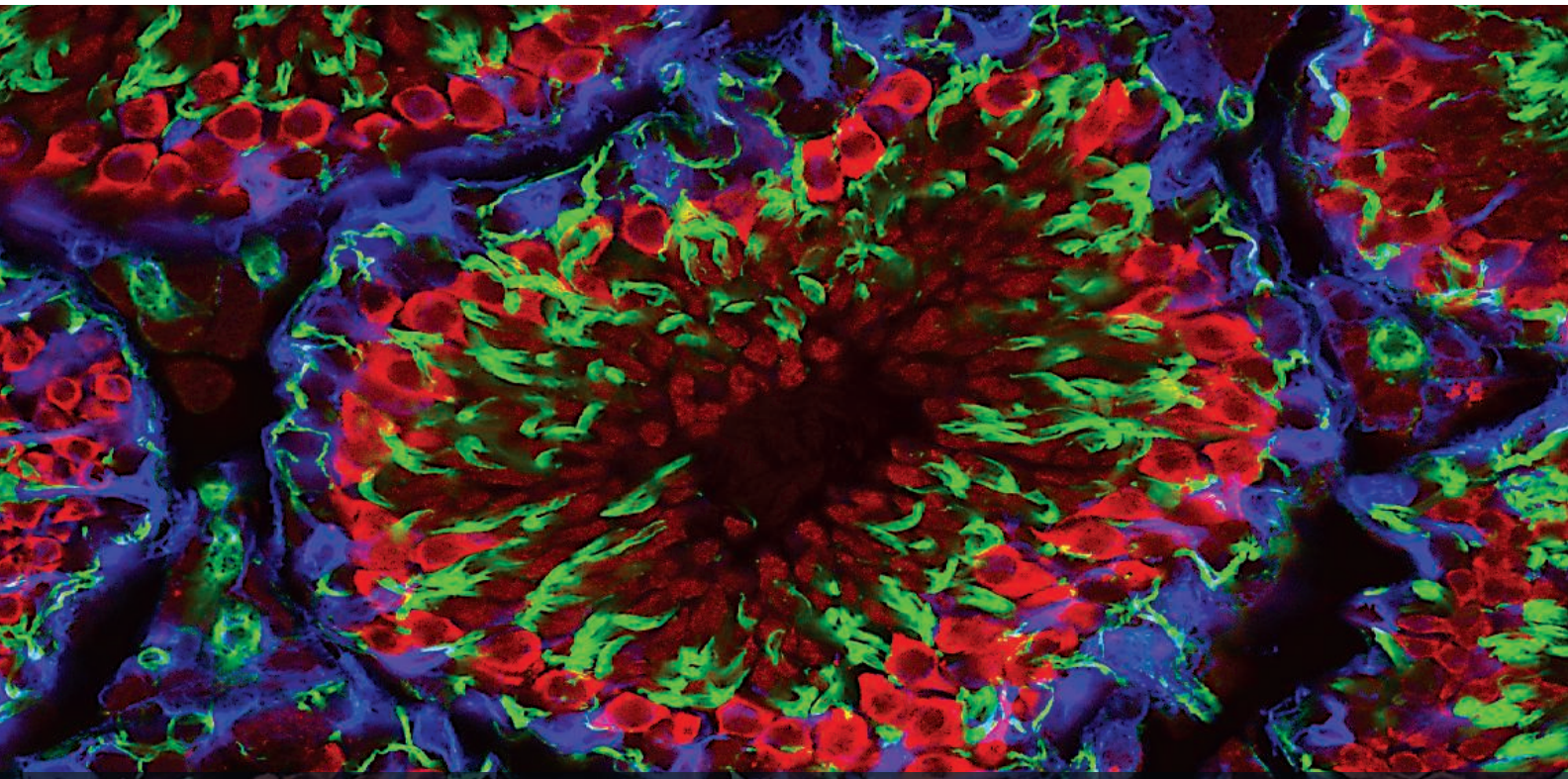
We'll be sending you more information about this great new benefit over the coming months. In the meantime, be sure to visit nasafcu.com/AAASpackage to apply for the new AAAS Platinum Advantage Rewards or Platinum Cash Rewards credit cards. You can also take a sneak peek at the AAAS Check Card and Checks coming soon.

Sincerely,

A handwritten signature in blue ink, appearing to read 'Ian King'.

Ian King
Director of Marketing and Membership, AAAS





XP[®] Monoclonal Antibodies, *one antibody, multiple applications*

**Unparalleled product quality, validation,
and technical support.**

XP[®] monoclonal antibodies are a line of high quality rabbit monoclonal antibodies exclusively available from Cell Signaling Technology. Any product labeled with XP has been carefully selected based on superior performance in the most relevant applications.

XP monoclonal antibodies are generated using XMT[®] technology, a proprietary monoclonal method developed at Cell Signaling Technology. This technology provides access to a broad range of antibody-producing B cells unattainable with traditional monoclonal technologies, allowing more comprehensive screening and the identification of XP monoclonal antibodies.

eXceptional specificity

As with all of our antibodies, the antibody is specific to your target of interest, saving you valuable time and resources.

+eXceptional sensitivity

The antibody will provide a stronger signal for your target protein in cells and tissues, allowing you to monitor expression of low levels of endogenous proteins, saving you valuable materials.

+eXceptional stability and reproducibility

XMT technology combined with our stringent quality control ensures maximum lot-to-lot consistency and the most reproducible results.

=eXceptional Performance[™]

XMT technology coupled with our extensive antibody validation and stringent quality control delivers XP monoclonal antibodies with eXceptional Performance in the widest range of applications.

Above: Confocal IF analysis of rat testis using Miwi (D92B7) XP[®] Rabbit mAb #6915 (red pseudocolor) and Vimentin (D21H3) XP[®] Rabbit mAb (Alexa Fluor[®] 647 Conjugate) #9856 (blue pseudocolor). Actin filaments were labeled with DY-554 phalloidin (green pseudocolor).



For experimental details, additional information, and a complete list of available XP[®] monoclonal antibodies visit...

www.cellsignal.com



Cell Signaling

TECHNOLOGY[®]



There's only one

Science

Science Careers Advertising

For full advertising details, go to ScienceCareers.org and click For Employers, or call one of our representatives.

Tracy Holmes
Worldwide Associate Director
Science Careers
Phone: +44 (0) 1223 326525

THE AMERICAS
E-mail: advertise@sciencecareers.org
Fax: 202-289-6742

Tina Burks
East Coast/West Coast/South America
Phone: 202-326-6577

Allyson Rosen
Midwest/Canada/Corporate
Phone: 202-326-6578

Marci Gallun
Sales Administrator
Phone: 202-326-6582

Online Job Posting Questions
Phone: 202-312-6375

EUROPE & REST OF WORLD
E-mail: ads@science-int.co.uk
Fax: +44 (0) 1223 326532

Ben Asfaha
Phone: +44 (0)1223 326529

Lucy Nelson
Phone: +44 (0)1223 326527

Kelly Grace
Phone: +44 (0) 1223 326528

JAPAN
Yuri Kobayashi
Phone: +81-50-3696-5100
E-mail: ykobayas@aaas.org

CHINA & TAIWAN
Ruolei Wu
Phone: +86-1367-1015-294
E-mail: rwu@aaas.org

All ads submitted for publication must comply with applicable U.S. and non-U.S. laws. Science reserves the right to refuse any advertisement at its sole discretion for any reason, including without limitation for offensive language or inappropriate content, and all advertising is subject to publisher approval. Science encourages our readers to alert us to any ads that they feel may be discriminatory or offensive.

Science Careers
From the journal *Science* AAAS

POSITIONS OPEN



FACULTY POSITION Eukaryotic Genetics and Genomics University of Connecticut-Storrs

The Department of Molecular and Cell Biology in the College of Liberal Arts and Sciences at the University of Connecticut seeks to fill two nine-month faculty positions: one at the tenure-track **ASSISTANT PROFESSOR** level, and one at **OPEN RANK**, in Eukaryotic Genetics and Genomics, starting August 23, 2013 (Search #2013194). We are interested in candidates who study aspects of eukaryotic genetics, genomics, and/or genome biology. For details on the position, qualifications, and application instructions please visit **website: <http://www.jobs.uconn.edu>**. The University of Connecticut is an Equal Employment Opportunity/Affirmative Action Employer.

FACULTY POSITION Assistant/Associate/Full Professor Center for NeuroGenetics University of Florida College of Medicine

The Center for NeuroGenetics at the University of Florida (UF) College of Medicine invites applications for a tenure-track position at the **ASSISTANT, ASSOCIATE, or FULL PROFESSOR** level. We seek an outstanding investigator in the areas of gene discovery and/or genetic, computational, or pathophysiological models of neurological disease. The Center has active research programs in human, mouse, and *Drosophila* genetics, as well as computational biology, and is housed in the recently constructed University of Florida Genetics Institute with modern facilities for bioinformatics, genomics, proteomics and a full service transgenic and knockout mouse facility. In addition to being an active member of the Center, the primary academic appointment will be in a relevant department (Departments of Molecular Genetics and Microbiology, Neurology or Neuroscience). Candidates with a Ph.D. and/or M.D. and relevant postdoctoral experience should send their curriculum vitae, names of three references, and a brief description of research interests to: **Dr. Laura P.W. Ranum, Center for NeuroGenetics, Department of Molecular Genetics and Microbiology, University of Florida, College of Medicine, Gainesville, FL 32610-3610. E-mail: neurogenetics-facultysearch@health.ufl.edu** as well as apply online to **website: https://jobs.ufl.edu/applicants/jsp/shared/Welcome_css.jsp**; **position number 00026738**. For further information about the center, visit our **website: <http://www.neurogenetics.med.ufl.edu>**. Review of applications will begin immediately, with search committee determinations beginning circa January 1, 2013. The search may remain open until the position is filled.

UF is an Equal Opportunity Institution with a strong commitment to excellence through diversity.

POSTDOCTORAL FELLOW in Analysis and Modeling of Social Networks

The Center for Complex Networks and Systems Research (**website: <http://CNetS.indiana.edu>**) at Indiana University has an open postdoctoral position to study the diffusion of information in social networks. The appointment starts in January 2013 for one year and is renewable for up to two additional years. The ideal candidate will have a Ph.D. in computing or physical sciences; a strong background in analysis and modeling of complex systems and networks; and programming skills necessary to handle big data and large-scale simulations. To apply, send curriculum vitae as well as the e-mail addresses of three references to **CNetS, e-mail: tgholbro@indiana.edu** or to: **919 E 10th Street, Bloomington, IN 47408, USA**. Applications received by 15 December 2012 will receive full consideration, but applications will be considered until the position is filled. *Indiana University is an Equal Opportunity/Affirmative Action Employer.*

POSITIONS OPEN



FACULTY POSITION Microbiology University of Connecticut-Storrs

The Department of Molecular and Cell Biology in the College of Liberal Arts and Sciences at the University of Connecticut seeks applicants for a nine-month **ASSISTANT PROFESSOR** tenure-track position in Microbiology, starting August 23, 2013 (Search #2013172). We are particularly interested in candidates working on microbiomes, host-microbe interactions, or the ecology and evolution of microbial communities. For details on the position, qualifications, and application instructions please visit **website: <http://www.jobs.uconn.edu>**. The University of Connecticut is an Equal Employment Opportunity/Affirmative Action Employer.

Chemical Biology Institute Yale University-Chemical Biology Institute

The Chemical Biology Institute, a cornerstone of Yale's new West Campus research enterprise, invites applications for tenure-track positions at the **ASSISTANT PROFESSOR** level to commence 1 July 2013. Faculty associated with the Chemical Biology Institute will hold primary appointments in any of several life science or physical science departments within the Faculty of Arts and Sciences, the School of Engineering and Applied Science, or the Yale School of Medicine. At this time, we seek candidates whose research interests and accomplishments align best with the Institute and the Department of Chemistry (**website: <http://www.chem.yale.edu/>**). Successful candidates will be creative teacher-scholars with reputations for outstanding research at the combined interface of chemistry, biology, and/or medicine, and must possess a Ph.D. in a relevant discipline. Applicants should create a profile at **website: <https://academicjobsonline.org/ajob/jobs/2261>** and upload a statement of research plans, curriculum vitae, and up to five reprints of published work(s). Applicants should also arrange for three references to upload their letters of recommendation. For further information, contact **Jessica Sorensen** at e-mail: jessica.sorensen@yale.edu or **PO Box 27392, West Haven, CT 06516-7392**. The deadline for the receipt of application materials is 26 December 2012. *Yale University is an Affirmative Action/Equal Opportunity Employer. Yale values diversity among its faculty, students, and staff and strongly encourages applications from women and underrepresented minorities.*

Help employers
find you. Post
your resume/cv.

Science Careers

From the journal *Science*



www.ScienceCareers.org

Faculty Positions in Computational Bioscience Research Center (CBRC) of the Computer, Electrical and Mathematical Sciences and Engineering Division at King Abdullah University of Science and Technology (KAUST)



The Computational Bioscience Research Center (CBRC) at King Abdullah University of Science and Technology (KAUST) invites applications for the faculty positions at all levels (Full, Associate, and Assistant Professor).

CBRC, <http://cbrc.kaust.edu.sa>, is part of the Computer, Electrical and Mathematical Sciences and Engineering Division (CEMSE) (<http://cemse.kaust.edu.sa/>). CBRC develops novel enabling bioinformatics methods and applies them in life science research. The activities of the Center are both in development of new methods and algorithms for computational biology and bioinformatics, their implementation on high performance computing platforms, and, their application in systems biology, microbiology, biotechnology and related fields. The focus of the CBRC is on modeling the key processes in the living cell so as to be able to explore the way cells react to different challenges. Bioinformatics research is motivated by and complemented with CBRC's internal and collaboratively conducted experimental work that helps refine and validate in silico-derived hypotheses potentially useful for various applications.

We are interested in applicants with the background primarily in mathematics, computer science, and engineering, though excellent candidates with life science backgrounds will be considered. The research focus of the candidates should be in one or more domains spanning computational biology, bioinformatics, systems biology, genomics, data integration, mathematical modeling, data mining, and artificial intelligence. Teaching interests may fall within the broad scope of the CEMSE division and, potentially, within Biological and Environmental Sciences and Engineering Division (BESE, <http://bese.kaust.edu.sa/>).

To apply for this position, please send a single PDF or word file containing: a cover letter, curriculum vitae, complete publication list, research plan, teaching statement, and contact information of four references to CBRC.recruitment@kaust.edu.sa with attention to Professor Vladimir Bajic.

Applications received by January 15, 2013 will receive full consideration and positions will remain open until filled.

About KAUST

King Abdullah University of Science and Technology (KAUST) is an international, graduate research university dedicated to advancing science and technology through interdisciplinary research, education, and innovation. Located on the shores of the Red Sea in Saudi Arabia, KAUST offers superb research facilities, generous assured research funding, and internationally competitive salaries, attracting top international faculty, scientists, engineers, and students to conduct fundamental and goal-oriented research to address the world's pressing scientific and technological challenges related to the sustainability of water, food, energy, and the environment.

www.kaust.edu.sa





**CHAIRPERSON
DEPARTMENT OF VETERINARY MICROBIOLOGY
AND PATHOLOGY
WASHINGTON STATE UNIVERSITY
PULLMAN, WA**

The College of Veterinary Medicine at Washington State University seeks a distinguished researcher and academic leader to be Chairperson of the Department of Veterinary Microbiology and Pathology (VMP) (<http://www.vetmed.wsu.edu/depts-vmp/index.aspx>). As one of the foremost pathology departments in the nation, VMP's mission is to enhance animal and public health through training veterinary medical students, graduate students and residents, conducting global outreach, and performing biomedical research in immunology, infectious diseases, food safety, genomics, and pathology. VMP's strong, extramurally funded research programs benefit from close collaborative ties with the USDA/ARS Animal Disease Research Unit, and other College of Veterinary Medicine entities including the Washington Animal Disease Diagnostic Laboratory, the newly founded Paul G. Allen School for Global Animal Health, and the School for Molecular Biosciences. VMP excellence in teaching is supported by the first-in-the-nation College Teaching Academy, whose mission is to enhance educational enterprises at all levels. The Chairperson's portfolio includes fiscal management of VMP, participation in and promotion of mentoring and professional development for faculty members, and fostering curricular development and scholarship in teaching. The successful candidate will have a record of academic leadership, productive, sustained, extramurally funded, internationally recognized research, and excellence in graduate education. Applicants must hold an earned doctorate in microbiology, immunology, pathology, veterinary medicine, medicine or a related discipline and be eligible for academic appointment at the level of Professor.

Review of applications will begin **January 7, 2013**. To apply or obtain more detailed information go to www.wsujobs.com. For questions or confidential expressions of interest about this position candidates may email or telephone **Ms. Sue Zumwalt** at szumwalt@vetmed.wsu.edu or 509.335.6027.

WSU is an EO/AA Educator Employer.



**Jiangsu Academy of
Agricultural Sciences**

**Open position as Deputy Director and Full Professor in the
Institute of Agricultural Facility and Equipment**

Jiangsu Academy of Agricultural Sciences (JAAS) is a professional agricultural research and extension institution that has been established since 1932. JAAS ranks at the top of provincial agricultural academies in China in terms of the comprehensive strength in agriculture. JAAS's headquarter and main research facilities are located in Nanjing, Jiangsu, China.

Currently, JAAS is seeking a deputy director with the rank of full professor in the area of agricultural facility and equipment researches. Applicant should have a commitment to scientific excellence and the enthusiasm, energy, and innovative thinking necessary to lead a dynamic institute with a broad and diverse portfolio. Applicant must possess a faculty position already beyond the assistant professor level in a university or the equivalent position in a research institution. In addition, the candidate should demonstrate excellent records of research accomplishment and has a command of bilingual language for English and Chinese, both in spoken and written.

Successful applicant will be offered a competitive package, including sufficient laboratory space, startup funding, relocation fee and competitive salary commensurate with experience, in addition to a housing allowance, and other employee benefits. Applicant can go to www.jaas.ac.cn for application details.

In addition, more information for other regular faculty positions from JAAS relevant to a variety of disciplines in agriculture is also available at www.jaas.ac.cn.

Contact information

E-mail: rsc-gbk@jaas.ac.cn; Tel: 086-25-84390037

UNIVERSITY of HOUSTON

COLLEGE OF PHARMACY

Senior Faculty Position in Toxicology

The Department of Pharmacological and Pharmaceutical Sciences, in collaboration with the Center for Nuclear Receptors and Cell Signaling, at the University of Houston is accepting applications for a senior level tenure-track faculty position in Toxicology at either the Associate Professor or Professor level. The search is focused on adding toxicological expertise in the research areas of drug-induced toxicity, nuclear receptors and regulation of drug metabolism, endocrine disruption, and developmental toxicology. Eligible candidates must have an earned doctoral degree, postdoctoral experience and a strong track record for establishing/maintaining an excellent extramurally-funded research program.

The successful candidate will be provided lab space in the new state-of-the-art facilities of the Center and will receive a generous start-up package through the State of Texas' National Research University Fund. Department faculty members teach in the Pharm.D. professional program and participate in departmental Ph.D. programs in Pharmacology and Pharmaceutics. The University of Houston is a Carnegie-designated Tier 1 public research university and a member institution of the world-renowned Texas Medical Center, which is home to major academic research institutions with basic and translational research programs in cancer, genomics/proteomics, cardiovascular medicine, and neuroscience.

Applications will be accepted beginning November 12, 2012, and search will continue until the position is filled. Interested individuals should send a letter of application, a curriculum vitae, a document describing his/her research program, and the names of three references with postal and e-mail addresses, telephone and FAX numbers electronically in PDF format to: Ming Hu, Ph.D., Chair, Search Committee, c/o ppsrx@uh.edu, University of Houston, College of Pharmacy, Houston, TX, 77204-5037. Web site: <http://www.uh.edu/pps/ppsrx/index.html>

The University of Houston is an Affirmative Action/Equal Opportunity employer. Minorities, women, veterans, and person with disabilities are encouraged to apply.

UNIVERSITY of HOUSTON

CENTER for NUCLEAR RECEPTORS and CELL SIGNALING



**Tenure-Track Assistant
Professor Position in Biochemistry**
Department of Biological Sciences

The Department of Biological Sciences at Oakland University invites applications for a candidate with a strong background in biochemistry, investigating key problems in **cellular metabolism**. Special consideration will be given to candidates studying enzyme or protein function using biochemical approaches. A PhD and at least two years of post-doctoral experience are required, in addition to strong research track record evidenced by publications. Laboratory space and a competitive startup package will be provided. The successful candidate is expected to develop a vigorous, extramurally funded research program, to teach effectively at the undergraduate and graduate levels, and to mentor undergraduate and graduate students (MS and PhD).

The Department of Biological Sciences (<http://www2.oakland.edu/biology/>) is a vibrant and growing department that places the highest priority on research excellence. The faculty have wide range of research interests, including inflammatory response, host-parasite interactions, metalloproteins, chromatin modifications, development of tubular organs, stem cells, flagellar motility, hypertension, oxidative damage in muscle, population dynamics and stream ecology. Oakland University is a state-supported institution of 20,000 students. It is located on a beautiful 1,600-acre campus in the heart of Oakland County, 25 miles north of Detroit.

Applications should be submitted by January 5, 2013. Applications should include a cover letter, curriculum vitae, detailed statement of research plans, teaching philosophy, 3 representative publications, and a list of 3 or more references. Application is set online at <http://academicjobs.oakland.edu/postings/447>. Inquiries should be addressed to: Arik Dvir, Chair, Department of Biological Sciences (dvir@oakland.edu).

Oakland University is an Affirmative Action/Equal Opportunity Employer and encourages applications from women and minorities.



Hiring Professors at All Ranks at South University of Science and Technology (SUSTC) Shenzhen, China

The South University of Science and Technology (SUSTC) invites applications and nominations for all ranks of tenured and tenure-track faculty members in the Division of Science, Division of Engineering and Division of Management & Finance.

SUSTC, officially established in April 2012, is a public institution funded by the municipal of Shenzhen, a special economic zone city in southern China. The University is accredited by the Ministry of Education, China and is a pioneer in higher education reform in China. Set on five hundred acres of wooded landscape in the picturesque Nanshan (South Mountain) area, the new campus offers an idyllic environment suitable for learning and scholarship. SUSTC engages in basic and problem-solving research of lasting impact to benefit society and mankind.

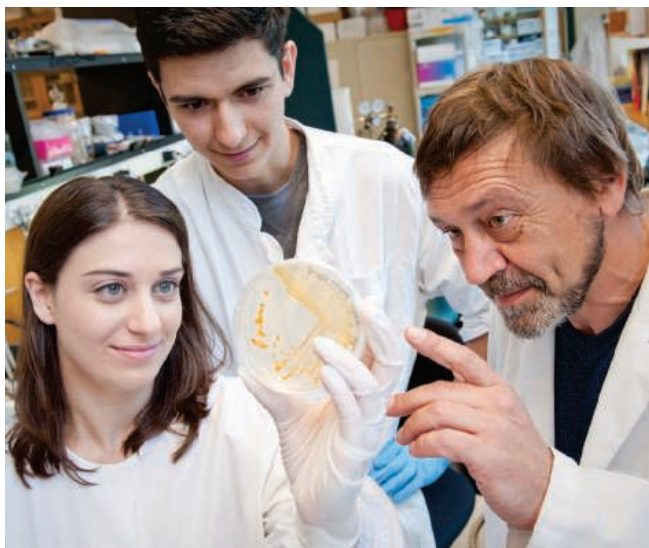
The Division of Science, Division of Engineering, and the Division of Management & Finance wish to hire faculty members at all ranks. Key areas include but not limited to: Neural and Cognitive Sciences, Biology and Gene Engineering, Modern Physics, Control and Modification of Materials, Nanoscience and Nanotechnology, Mathematics and Applied Mathematics, Molecular Chemistry and Catalysis, Large-Scale Computational Research, Robotics and Artificial Intelligence, Information Systems and Electronic Engineering, Modern Cities and Future Developments, Energy Sciences and Technology, Environmental Sciences, Financial Mathematics and Management Sciences. The Divisions especially encourage research that requires a multi-disciplinary approach. Experienced researchers whose interests do not fall within the above areas are invited to suggest new areas of research. **Cluster hiring is possible, with senior members accompanied by junior members in a group.**

The teaching language at SUSTC is English or Putonghua. The choice is made by the instructor. As we expect an international faculty, the majority of teaching materials and reference books will be in English and many classes will be conducted in English. With a very high faculty-to-student ratio, SUSTC is committed to delivering a student-centered education and encourages students to develop their innovative spirits. Students at junior and senior years are expected to participate in research in the Research Centers.

The University offers competitive salaries, fringe benefits including medical insurance, retirement and housing subsidy. Leading Professors, Chair Professors and Professors will be appointed with tenure. Associate Professors and Assistant Professors will be offered tenure-track contracts.

Send nominations, inquiries and applications to: hiring@sustc.edu.cn. All applications should include a CV and a detailed list of publications. **Those interested in cluster hiring should send CVs and publication lists as a group.** Evaluations will commence immediately and appointments will be made on a continuous basis. Additional information on SUSTC is available on the University homepage <http://www.sustc.edu.cn> and <http://english.sina.com/china/2012/0902/502496.html>.





College of Science Distinguished Graduate Fellowships

\$34,000 stipend, plus benefits and tuition remission for the study of a PhD
Five years support, given satisfactory progress toward PhD

Deadline to apply for the fellowships is February 1, 2013

Doctoral Programs: Biology | Chemistry and Chemical Biology | Mathematics
Physics | Psychology

For more information on how to apply, visit goo.gl/Yvelu

Northeastern University
College of Science



University of Pittsburgh

Assistant or Associate Professor in Bacterial Genomics

The Epidemiology Research Unit of the Division of Infectious Diseases, Department of Medicine, University of Pittsburgh, is recruiting a Bacterial Genomics Scientist with expertise in bacterial genomics, evolution, and pathogenesis to complement existing programs in epidemiology and molecular epidemiology of drug-resistant, vaccine-preventable, foodborne, and nosocomial bacterial diseases. The successful candidate will have expertise and a track record of research in areas such as microbial genomics and evolution, comparative genomics, functional bioinformatics, for studies investigating the emergence, transmission and spread of bacterial pathogens of public health importance. Backgrounds in transcriptomic and proteomic analyses are also desirable. The candidate should have a track record of research funding and will be expected to develop an independent, externally-funded research program by the end of a three-year start-up period. Candidates should have a Ph.D. in bacterial genomics or other relevant field and 2-5 years post-doctoral experience.

Interested candidates should send their CV, and the names of three references to **Lee H. Harrison, M.D., University of Pittsburgh, 521 Parran Hall, 130 DeSoto Street, Pittsburgh, PA 15261; E-mail: lharrison@edc.pitt.edu**.

The University of Pittsburgh is an Affirmative Action/Equal Opportunity Employer.

SYRACUSE UNIVERSITY

Departments of Biology and Chemistry

Assistant Professor of Biochemistry

The Departments of Biology and Chemistry at Syracuse University are soliciting applications for the joint position of Assistant Professor of Biochemistry. The successful applicant will have a Ph.D. in Chemistry, Biology or related areas and relevant postdoctoral experience. The candidate is expected to teach Biochemistry at all levels and develop a vigorous research program with strong extramural funding. The candidate will find an enthusiastic research environment with excellent facilities and many opportunities for collaboration in Biology, Chemistry, and Biomaterials at Syracuse University, and the adjacent SUNY campuses of the Upstate Medical University and Environmental Science and Forestry.

The College of Arts & Sciences is interested in candidates who have demonstrated commitment to excellence by providing leadership in teaching, research or service towards building an equitable and diverse scholarly environment. For details and to apply, go to www.sujobopps.com Job #070140.

Review of applications will begin November 30, 2012. For questions, please e-mail **Rob Doyle** (rpdoyle@syr.edu; **chair of the search committee**) or **Eleanor Maine** (emmaine@syr.edu).

The Chemistry and Biology Departments are committed to enhancing the diversity of its faculty and especially encourage applications from women, individuals with disabilities and members of underrepresented groups. Syracuse University is an Affirmative Action/Equal Opportunity Employer.



苏州大学

SOOCHOW UNIVERSITY

Research Positions in Nanotoxicology and Nanochemistry

The School of Radiation Medicine and Protection (SRMP) and School of Radiological and Interdisciplinary Sciences (RAD-X) of Soochow University Medical College in Suzhou, China, are seeking outstanding candidates for Postdoctoral Fellows, Associate and Full Professors in its **Division of Nanotoxicology and Nanochemistry**. Ongoing projects focus on nanotoxicology, cancer nanotechnology, and nanochemistry. **Specific areas** of interest include investigating biomedical effects of nanomaterials, development of functional nanomaterials for drug delivery and tumor therapeutics, analyses/detection of nanomaterials in living cells and animals.

Postdoctoral Candidates should have a PhD in the last 3 years and will join Full Professors' research groups in the fields listed above. Associate Professor Candidates should have a PhD and >3-year postdoctoral experience in the related fields and scholarly publication records. Full Professor Candidates should have demonstrated the ability to develop original and externally funded research programs. All candidates should have a command of spoken and written English.

Successful appointees will be offered an excellent package including sufficient lab space, start-up funding, relocation aid, competitive salary commensurate with experience, and other employee benefits.

Applicants should submit (i) a cover letter summarizing current research projects and future plans, (ii) a curriculum vitae, and (iii) names and contact info of 3 professional referees to: **SRMP and RAD-X Search Committee, Soochow University, Dushu Lake Campus, 199 Ren-Ai Road, Industrial Park, Suzhou 215123, China; Email: bxzhu@suda.edu.cn**

THE FACULTY OF BIOLOGY AND MEDICINE OF THE UNIVERSITY OF LAUSANNE, SWITZERLAND INVITES APPLICATIONS FOR THE FOLLOWING POSITION:

FULL PROFESSOR DIRECTOR OF THE DEPARTMENT OF FUNDAMENTAL NEUROSCIENCE

The Department of Fundamental Neuroscience at the University of Lausanne (<http://www.unil.ch/dbcm>) has been inaugurated recently. It intends to strengthen its research programme and develop a new research focus in molecular and cell-biological aspects of neuroscience. We therefore seek an outstanding researcher (PhD, MD or MD/PhD) as full professor and new director of the Department. The position requires a record of scientific excellence and management experience, as well as vision and the motivation to lead and shape a Department.

The future Director of the Department is expected to lead a strong, internationally competitive research programme, attract external funding and promote an interactive and synergistic research environment. She/he is expected to provide leadership in order to develop the Department of Fundamental Neuroscience into a centre of excellence in molecular and cell-biological aspects of neuroscience.

The Department is embedded in a highly active and expanding research community in the Lake Geneva area, offering interactions with strong neurobiology programmes at the Federal Institute of Technology (EPFL) and the University Hospital (CHUV) in Lausanne, as well as at the University of Geneva. It also forms part of a programme of excellence in research by the Swiss National Science Foundation (NCCR Synapsy). Future developments in the Department will benefit from an excellent infrastructure in a new building on the main campus of the University.

Further information may be obtained from Prof. Tafti (Medhi.Tafti@unil.ch), chair of the search committee.

The applications, in English, will include the curriculum vitae, the list of publications in which the five most significant ones are identified, a summary of the major discoveries (< 1 page), a short description of the present and future research programme (< 2 pages), and at least three names of referees. They should be sent via postal mail by January 23rd, 2013 for the attention of Prof. Béatrice Desvergne, Dean of the Faculty of Biology and Medicine, rue du Bugnon 21, CH-1011 Lausanne, Switzerland.



Seeking to promote an equitable representation of men and women among its staff, the University encourages applications from women.



SANTA FE INSTITUTE

Because our world isn't simple

Take On a Complex World. Inspire Others. Become a Complexity Scholar.



TO UNRAVEL THE COMPLEX SYSTEMS

most critical to our future — economies, ecosystems, conflict, disease, and human social institutions — a new kind of science is required, one that merges the riches of many disciplines, from physics and biology to the social sciences and the humanities.

For nearly 30 years the Santa Fe Institute, the locus of complexity science, has prepared the next generation's scholars to seek the theoretical foundations and patterns underlying our world's toughest problems.

Learn from the most respected minds in complexity science, where it all started. Become a Complexity Scholar at the Santa Fe Institute.

SCHOOLS

Complex Systems Summer School

June 2013, Santa Fe, New Mexico
Graduate students & postdoctoral fellows

Graduate Workshop in Computational Social Science and Modeling

June 2013, Santa Fe, New Mexico
Graduate students

Complexity and Modeling Program (C.A.M.P.)

July 2013, Massachusetts
High school students

FELLOWSHIPS AND INTERSHIPS

SFI Omidyar Fellowship

Ongoing
Postdoctoral fellows

NSF Research Experiences for Undergraduates

June-August 2013, Santa Fe, New Mexico
Undergraduate students

Project GUTS: Growing Up Thinking Scientifically

After-school programs in selected communities, various dates
Middle school students

GUTS y Girls

After-school programs in selected communities, various dates
Female middle school students

PROFESSIONAL DEVELOPMENT

Advanced Graduate Workshop in Computational Social Science & Modeling

June 2013, Santa Fe, New Mexico
Graduate students (by invitation only)

SFI Short Course on Complexity

September 2013 (two-and-a-half days)
Professionals (no math or science background required)

Introduction to Complexity

On-line course launching January 2013
General interest (no math or science background required)

Complexity Explorer

Website launch January 2013
On-line educational resource for teachers and students of complexity science

For eligibility, application deadlines, fees, tuition assistance information, and other details, see:

www.santafe.edu/education/



There's only one GALILEO GALILEI

Born in 1564, Galileo Galilei once contemplated a career in the priesthood. It's perhaps fortunate for science that upon the urging of his father, he instead decided to enroll at the University of Pisa. His career in science began with medicine and from there he subsequently went on to become a philosopher, physicist, mathematician, and astronomer, for which he is perhaps best known. His astronomical observations and subsequent improvements to telescopes built his reputation as a leading scientist of his time, but also led him to probe subject matter counter to prevailing dogma. His expressed views on the Earth's movement around the sun caused him to be declared suspect of heresy, which for some time led to a ban on the reprinting of his works.

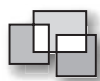
Galileo's career changed science for all of us and he was without doubt a leading light in the scientific revolution, which is perhaps why Albert Einstein called him the father of modern science.

Want to challenge the status quo and make the Earth move? At *Science* we are here to help you in your own scientific career with expert career advice, forums, job postings, and more — all for free. For your career in science, there's only one *Science*. Visit *Science* today at **ScienceCareers.org**.



For your career in science, there's only one **Science**

ScienceCareers.org



DEPARTMENT OF COMPUTER SCIENCE AND THE DONNELLY CENTRE UNIVERSITY OF TORONTO

The Department of Computer Science and the Donnelly Centre for Cellular and Biomolecular Research at the University of Toronto invite applications for a tenure-stream position in Computational Biology or Bioinformatics. The appointment is at the rank of Assistant Professor and will begin on July 1, 2013.

We seek outstanding applicants with demonstrated excellence in research at the highest level and with the potential for excellence in undergraduate and graduate teaching. Although we expect candidates to have a PhD and postdoctoral training in the computational sciences (computer science, computational biology and quantitative biology), exceptional candidates with recent or imminently-expected PhDs will be also considered.

The Department of Computer Science is an international leader in research and teaching, with recognized strength in most areas of computer science. The Donnelly Centre is an interdisciplinary research institute at the University of Toronto with the mandate to create a research environment that encourages integration of biology, computer science, engineering and chemistry, and that spans leading areas of biomedical research. The successful candidate will have the opportunity to take advantage of the University's strengths in biology and bioinformatics---and computational, medical and biological sciences more broadly---and to facilitate further interaction with other units. To facilitate such interactions, the successful candidate will hold a joint appointment in the Department of Computer Science (51%) and in the Donnelly Centre (49%).

Salaries are competitive with our North American peers and will be determined according to experience and qualifications. Toronto is a vibrant and cosmopolitan city, one of the most desirable in the world in which to work and live, and a major centre for advanced computer, medical and biological technologies with strong ties to the University.

Applicants should apply online at <http://recruit.cs.toronto.edu/>, and include curriculum vitae, a list of publications, a research and teaching statement, and the names and email addresses of at least three references. Other supporting materials may also be included. We will not accept applications submitted by post. If you have any questions regarding this position, please contact Sara Burns at recruit@cs.toronto.edu.

Review of applications will begin on **January 7, 2013** and continue until the position is filled. To ensure full consideration applications, should be received by February 4, 2013.

For more information on the Department of Computer Science see www.cs.toronto.edu and for the Donnelly Centre for Cellular and Biomolecular Research see www.thedonnellycentre.utoronto.ca.

The University of Toronto is strongly committed to diversity within its community and especially welcomes applications from visible minority group members, women, Aboriginal persons, persons with disabilities, members of sexual minority groups, and others who may contribute to the further diversification of ideas. All qualified candidates are encouraged to apply; however, Canadians and permanent residents will be given priority.

Assistant or Associate Professor (WOT) Environmental and Occupational Health Sciences Search # AA3319



The Department of Environmental and Occupational Health Sciences at the University of Washington invites applications and nominations of outstanding individuals for up to two 12-month, full-time (100% FTE) tenure-eligible faculty positions at the rank of Assistant Professor or Associate Professor (WOT), with research interests in toxicology. One successful candidate will assume the Sheldon Murphy Endowed Chair. It is anticipated that interviews will begin in January of 2013, and that the appointment will begin in September 2013.

Applicants with research interests in all areas of toxicology will be considered, including but not limited to systems and computational toxicology, immunotoxicology, toxicologic pathology, epigenetic/genetic toxicology, molecular toxicology, neurotoxicology, risk assessment, reproductive and developmental toxicology, and gene-environment interactions. Interactions with faculty in related environmental health sciences disciplines are expected.

The Department's mission includes contributing to the prevention of occupational illness and injury in Washington State workers. The Department and the University have a long history of fostering successful collaboration among these disciplines in research, classroom teaching, and service to the community. Faculty members collaborate across the School of Public Health and other Schools and Colleges at the University of Washington. The current toxicology program has robust research and graduate training programs with a key emphasis on applying molecular, cellular, computational modeling, and functional behavioral approaches to solve toxicology questions.

The Department seeks to augment this current expertise in toxicology and to increase its ability to secure external research support. Successful candidates for these positions must have a PhD or equivalent in toxicology, environmental health sciences or other related biomedical or health science fields. Candidates who have post-doctoral experience, can demonstrate evidence of an externally-funded research program and independent and collaborative research potential, have interest and ability in teaching at the graduate and undergraduate levels, and a record of peer reviewed publications commensurate with experience are particularly encouraged to apply.

To apply, please provide a curriculum vitae, a personal statement of experience and interest in teaching, research and service, and names, with contact information, for at least four professional referees, via email or regular mail to: **Search Committee Chairman, Search # AA3319, Department of Environmental & Occupational Health Sciences, University of Washington, Box 357234, Seattle, WA 98195-7234; toxsrch@uw.edu.**

Inquiries should be directed to **Professor Michael Morgan** at the above address. Applications received by **December 23, 2012**, will receive priority consideration. The position will remain open until filled. Further information about the department can be found at: <http://depts.washington.edu/envhlth/> The Mission Statement and Strategic Plan for the School of Public Health may be found at <http://sph.washington.edu/about/mission.asp>.

The UW School of Public Health is committed to a diverse academic community. We view diversity as essential to our mission, for more information please see the following website: <http://www.washington.edu/diversity/>.

University of Washington faculty engage in teaching, research and service. The University of Washington is an Affirmative Action, Equal Opportunity Employer. The University encourages applications from women, minorities, individuals with disabilities and covered veterans.

WEBINAR
Now available
on demand.



FACTS & FICTION

Careers in Industry and Academia

Trying to figure out the next step in your career? Join us for a roundtable discussion that will look at facts and fiction surrounding academic and industry career options for PhD-level scientists. Get some nuts and bolts advice on how to research career options, what questions to ask, and how to best prepare for various careers.

- Do industry and academic careers require different skill sets?
- Do industry jobs have better compensation? Less autonomy?
- Do academic scientists have less work/life balance?

For answers view our roundtable discussion for free at:

ScienceCareers.org/webinar

Science Careers

From the journal *Science*



Produced by the *Science*/AAAS Business Office.



Join the Conversation!

Twitter is a great way to connect with AAAS members and staff about the issues that matter to you most. Be a part of the discussion while staying up-to-date on the latest news and information about your personal member benefits.

**Follow us @AAASmember
and join the conversation
with #AAAS**



MemberCentral.aaas.org



UNIVERSITY OF CENTRAL FLORIDA

College of Medicine

Orlando, FL

Associate Dean for Research College of Medicine

The College of Medicine at the University of Central Florida in Orlando, Florida, invites applications and nominations for the position of Associate Dean of Research.

The University of Central Florida is a rapidly growing metropolitan research university with more than 56,000 students, an operating budget of \$1.2 billion, extramural research funding of \$133 million and the highest Carnegie research ranking. UCF is committed to innovative community partnerships, world-class research with local impact, and the integration of technology and learning.

The College of Medicine was established in 2006 and is one the newest medical schools in the nation. The college includes undergraduate and graduate programs in the broad field of biomedical sciences and biotechnology. The successful biomedical research program in the Burnett School of Biomedical Sciences is poised to expand with the addition of new biomedical research facilities at the new Lake Nona biomedical research, clinical, and education cluster in the southeastern region of Orlando. The college serves as an anchor for this innovative and rapidly growing Lake Nona Medical City, a complex of world class hospitals and leading edge research facilities including the Sanford-Burnham Institute for Biomedical Research.

Reporting to the Dean, the Associate Dean for Research serves as the chief officer responsible for establishing a world-class research enterprise at the College of Medicine, promoting investigator-initiated scholarship and facilitating opportunities to increase grants and contracts from external sources. The Associate Dean will facilitate basic science, translational, clinical, and medical education research within the college and promote interactions with other colleges, centers, and institutes within and outside of the university.

UCF seeks an accomplished scientist and a visionary research leader with a track record of building successful research programs. The successful candidate will possess an earned doctorate or equivalent terminal degree and credentials that merit appointment at the rank of professor with tenure. It is highly desirable that the candidate demonstrate proven academic accomplishments as reflected by significant funding and publications in scientific journals. Leadership experience, excellent written and oral communication skills, commitment to collaborative working relationships with various constituencies, strong support of diversity, and a global perspective for past and current trends in life science research is also desired.

Witt/Kieffer, an executive search firm specializing in healthcare and higher education, has been retained by the University of Central Florida College of Medicine to assist in identifying and recruiting the successful Associate Dean for Research. We appreciate receiving recommendations/nominations of potential candidates. You may be assured that all nominations will be handled with the utmost of professional courtesy and confidentiality. Candidates who choose to self-nominate, should submit their curriculum vitae to the e-mail address listed below. Application materials, including a letter indicating the applicant's interest, experience and qualifications for the position, a curriculum vitae, and the names, addresses, telephone numbers and e-mail addresses of three references (who will not be contacted without permission) must be submitted electronically (MSWord strongly preferred) to:

Anne Zenzer, Senior Vice President, Witt/Kieffer
2015 Spring Road, Suite 510
Oak Brook, Illinois 60523
annez@wittkieffer.com 630/990-1370

Applications will be accepted until the position is filled.

UCF is an equal opportunity, affirmative action employer and especially encourages the candidacies of women, members of racial and ethnic minorities, and persons with disabilities. All searches and documents are subject to the Sunshine and public records laws of the State of Florida.

WITT / KIEFFER



AAAS is here – helping scientists achieve career success.

Every month, over 400,000 students and scientists visit ScienceCareers.org in search of the information, advice, and opportunities they need to take the next step in their careers.

A complete career resource, free to the public, *Science Careers* offers a suite of tools and services developed specifically for scientists. With hundreds of career development articles, webinars and downloadable booklets filled with practical advice, a community forum providing answers to career questions, and thousands of job listings in academia, government, and industry, *Science Careers* has helped countless individuals prepare themselves for successful careers.

As a AAAS member, your dues help AAAS make this service freely available to the scientific community. If you're not a member, join us. Together we can make a difference.

To learn more, visit aaas.org/plusyou/sciencecareers



For your career in science, there's only one

Science

Introducing myIDP: A career plan customized for you, by you.

- The first and only online app that helps scientists prepare their very own individual development plan.
- Recommended by leading professional societies and the NIH.
- Developed by scientists at FASEB, UCSF, and the Medical College of Wisconsin in collaboration with AAAS and Science Careers, with support from the Burroughs Wellcome Fund.



Visit the website and
start planning today!
myIDP.sciencecareers.org



Open positions in the Department of Chemistry:

- Analytical Chemistry / Natural Product Chemistry
- Theoretical Chemistry / Computational Chemistry
- Molecular Biochemistry

Educational minimum requirements:

- BSc and MSc in Chemistry,
- Doctorate in Science,
- International experience (e. g. Postdoc).

Job description: full time

We expect:

- a. Research experience documented by original publications in refereed journals
- b. Willingness to teach in one of the above mentioned areas

**Application deadline:
December 28th, 2012**

Complete applications should be sent,
per email only, to:
wbaumann@uniandes.edu.co



Senior Faculty Position

Climate Change and Sea Level Rise Initiative

Old Dominion University seeks a senior level faculty member in any discipline related to climate change and sea level rise to lead its Climate Change and Sea Level Rise Initiative (CCSLRI). The goal of the CCSLRI is to foster research, education and outreach about the potential impacts of climate change and sea level rise on metropolitan communities that are situated at or close to sea level. Old Dominion University is a dynamic research-extensive public institution located in the coastal metropolitan Hampton Roads region of Virginia, a popular recreation area with a population of 1.7 million. ODU serves almost 25,000 students, including more than 6,000 graduate students, with over 5,000 students in residence on the Norfolk campus.

The CCSLRI involves a broad range of faculty from across the University, including the sciences, engineering, social sciences, education, business and health sciences (see <http://www.odu.edu/ao/research/ccslri/>). The successful candidate will be an effective leader and advocate for the Initiative, a proponent of inter- and cross-disciplinary research, and will be expected to lead the CCSLRI faculty through example in collaborative scholarly and teaching activities.

Applicants should possess an appropriate terminal degree and an academic record that merits a tenured appointment at the rank of associate or full professor in one of the academic departments within the University. A successful record in research and grant writing is required, as is evidence of effective leadership and the ability to interact and communicate clearly with internal and external communities.

Applications and nominations should be sent electronically to: **CCSLRI Search Committee, attention of Judy Bowman (jb Bowman@odu.edu), 222 Koch Hall, Norfolk, VA 23529**. Applicants should include a letter of interest that addresses the Initiative's goals, a curriculum vitae, and three professional references with email addresses and phone numbers provided. Review of applications will begin December 1, 2012; the search will remain open until an appointment is made.

Old Dominion University is an affirmative action, equal opportunity institution and requires compliance with the Immigration Reform and Control Act of 1986.



POSITIONS OPEN



FACULTY POSITION in Nanotechnology/Drug Delivery at UNC-Chapel Hill

The University of North Carolina (UNC) Eshelman School of Pharmacy is seeking outstanding candidates to fill a 12-month tenure-track position of **ASSISTANT/ASSOCIATE PROFESSOR**. The selected candidate will serve in the Division of Molecular Pharmaceutics and the Center for Nanotechnology in Drug Delivery and will be eligible for membership in the UNC Lineberger Comprehensive Cancer Center and the Carolina Institute for Nanomedicine. Startup funds consistent with rank and experience of the candidate have been reserved. Ideal candidates will demonstrate broad expertise, creativity, and a strong record of publication in polymer chemistry, nanomedicine, drug delivery, and therapeutics. A Ph.D. degree in Engineering, Pharmaceutical Sciences, Chemistry, or related discipline and a clear potential to establish an independent research program that contributes to the School are required. Applications should be submitted at **website: <http://unc.peopleadmin.com/postings/8668>**.

Women and members of minority groups are encouraged to apply. The University of North Carolina at Chapel Hill is an Equal Opportunity Employer.

FACULTY POSITION in Physiological Ecology or Ecological Genetics Department of Biological Sciences Texas Tech University Lubbock, Texas USA

The Department of Biological Sciences at Texas Tech University seeks applicants for a tenure-track **ASSISTANT PROFESSORSHIP** to begin in the 2013–2014 academic year. We seek an outstanding scientist working on either the relationship of structure to function (Physiological Ecology), the relationship of genes to structure and/or function (Ecological Genetics), or the integration of both fields within a broad ecological and evolutionary context. Candidates using experimental, comparative, and/or genome-wide approaches to major questions in any biological system are encouraged to apply. The successful candidate will be expected to supervise an independent research program that will attract extramural funding, to provide research training for graduate and undergraduate students, and to teach in their area of specialty at the undergraduate and graduate levels.

Texas Tech University is growing into one of the premier research institutions in Texas, using support from Texas' National Research University Fund, and is dedicated to the goal of building a culturally diverse faculty committed to teaching and working in a multicultural environment. The Department of Biological Sciences has historical strengths in organismal biology, ecology, evolution, behavior, and systematics. The successful candidate will enjoy working in a collaborative, integrative, and supportive environment for scientific productivity and interaction.

Application materials should include curriculum vitae, three representative publications, statements of research and teaching interests, and the names and contact information for at least three references. A Ph.D. in the Biological Sciences is required and postdoctoral experience is encouraged. To apply, please go to **website: <http://jobs.texasstate.edu/postings/49867>**.

Application review will begin on December 15, 2012 and continue until the position is filled. Questions can be addressed to e-mail: william.resetarits@ttu.edu. For further information about the department and graduate programs, see **website: <http://www.biol.ttu.edu/>**.

The entities of the Texas Tech University System are Equal Opportunity Employers and employ without regard to sex, race, color, national origin, religion, age, disability, genetic information, status as a disabled or Vietnam era veteran, or other protected classes.

POSITIONS OPEN



POSTDOCTORAL FELLOWSHIPS

The Geophysical Laboratory, Carnegie Institution of Washington, invites applications for postdoctoral fellowships. The Geophysical Laboratory emphasizes interdisciplinary experimental and theoretical research in fields spanning geoscience, microbiology, chemistry, and physics. The Laboratory supports world-class facilities in high-pressure research; organic, stable isotope and biogeochemistry; mineral physics and petrology; and astrobiology.

Please visit **website: http://www.glcw.edu/employment/Postdoctoral_Positions** to view a list of required materials and application instructions. Also, see **website: <http://www.glcw.edu/>** for a listing of personnel, current research interests, and major facilities.

Completed applications for Carnegie fellowships should be submitted by January 15, 2013.

The Geophysical Laboratory is an Equal Opportunity Employer.

ASSISTANT PROFESSORS OF BIOLOGY State University of New York at Geneseo

State University of New York at Geneseo Department of Biology invites applications for two tenure-track faculty positions at the rank of Assistant Professor to begin in August 2013.

The College strives to provide a diverse learning environment in which to prepare students for an increasingly multicultural society and interconnected world. For further information about SUNY Geneseo, please see our home page at **website: <http://www.geneseo.edu>**.

Required Qualifications: A Ph.D. degree and postdoctoral experience. Candidates should have a demonstrated interest in undergraduate education and the potential to develop a productive research program that includes opportunities for undergraduate students.

Position #1: We invite applications from individuals trained in microbiology or a microbiology-related field. Teaching responsibilities include Microbiology lecture and laboratory and participation in core courses of the department (General Biology, Ecology, Genetics, and/or Cell Biology).

Position #2: We invite applications from candidates who are broadly trained in the area of cell and developmental biology and have experience working on animal systems. Teaching responsibilities include Developmental Biology lecture and laboratory and Cell Biology.

Applications must be made online at **website: <https://jobs.geneseo.edu>**. Please attach a cover letter, curriculum vitae including a list of relevant coursework, a statement of teaching philosophy, and a statement of research interests that includes a plan to apply for extramural funding. In addition, three letters of recommendation and up to three recent reprints should be mailed separately to either the: **Micro or Devo Search Committee, SUNY Geneseo, Biology Department, 1 College Circle, Geneseo, NY 14454**. Review of applications will commence January 15, 2013. All applicants are subject to drug and criminal background checks.

SUNY Geneseo is an Affirmative Action/Equal Opportunity/Equal Access Employer committed to recruiting, supporting, and fostering a diverse community of outstanding faculty, staff, and students. The College actively seeks applications from women and members of underrepresented groups.

POSITIONS OPEN

FACULTY POSITIONS in Pharmacology and Toxicology University of Mississippi Medical Center

Applications are invited for two tenure-track faculty positions and one non-tenure-track teaching position in the Department of Pharmacology and Toxicology at the University of Mississippi Medical Center. Applicants considered for the tenure-track positions at **ASSISTANT, ASSOCIATE, or FULL PROFESSOR** must have a Ph.D. and/or M.D. degree and postdoctoral research experience in Pharmacology and can participate in our Medical and Dental teaching programs but are expected to maintain an extramurally funded research program. Special consideration will be given to candidates with currently funded research programs in: pharmacogenomics or proteomics, obesity or diabetes, signal transduction, neuropharmacology or cerebral vascular disorders. The non-tenure-track position would be well suited for an experienced pharmacologist primarily interested in Medical Education. The institution has strong research programs in cardiovascular, renal, cancer and behavioral neuroscience with many opportunities for collaboration in these areas. New faculty members will receive competitive salaries, excellent startup packages and access to LC/MS, Genomics, Cell sorting, 2-photon/Confocal Microscope Core facilities. Additional information about the department and its faculty can be found at our **website: <http://pharmacology.umc.edu/>**. Jackson, the state capital of Mississippi, offers small city/suburban living with a moderate climate, low housing costs, and good schools. Applicants should send a curriculum vitae, a statement of research interests, previous and current extramural research funding, and the names of at least three references to: **Dr. Richard J. Roman, Department of Pharmacology University of Mississippi Medical Center, 2500 North State Street, Jackson, MS 39216-4505. E-mail: rroman@umc.edu**. *Equal Opportunity Employer, Minorities/Females/Persons with Disabilities/Veterans.*

Stop
searching
for a job;
start your
career today.

Science Careers

From the journal *Science*



www.ScienceCareers.org

MARKETPLACE

Widely
Recognized
Original &
Guaranteed

KlenTaq1

8¢/u
Truncated
Taq DNA
Polymerase
Withstand 99°C

US Pat #5,436,149 e-mail: abpeps@msn.com
Call: AB Bioscience, LLC 1•800•383•3362
Fax: 314•968•8988 www.abpeps.com



More scientists agree — we
are the most useful website.

www.ScienceCareers.org